Swee-Leong Kok
Neil White
Nick Harris

Free-Standing Thick-Film Piezoelectric Cantilevers - Energy Harvesting

Design, Fabrication and Characterisation

ABSTRACT

DESIGN, FABRICATION AND CHARACTERISATION OF FREE-STANDING THICK-FILM PIEZOELECTRIC CANTILEVERS FOR ENERGY HARVESTING

by Swee-Leong, Kok

Research into energy harvesting from ambient vibration sources has attracted great interest over the last few years, largely due to the rapid development in the areas of wireless technology and low power electronics. One of the mechanisms for converting mechanical vibration to electrical energy is the use of piezoelectric materials, typically operating as a cantilever in a bending mode, which generate a voltage across the electrodes when they are stressed. Traditionally, the piezoelectric materials are deposited on a non-electro-active substrate and are physically clamped at one end to a rigid base, which serves as a mechanical supporting platform. In this research, a three dimensional thick-film structure in the form of a free-standing cantilever incorporated with piezoelectric materials is proposed. The advantages of this structure include minimising the movement constraints on the piezoelectric, thereby maximising the electrical output and offering the ability for integration with other microelectronic devices. A series of free-standing composite cantilevers in the form of unimorphs were fabricated and characterised for their mechanical and electric properties. The unimorph structure consists of a pair of silver/palladium (Ag/Pd) electrodes sandwiching a laminar layer of lead zirconate titanate (PZT). An extended version of this unimorph, in the form of multimorph was fabricated to improve the electrical output performance, by increasing the distance of the piezoelectric layer from the neutral axis of the structure. This research also discusses the possibility of using an array of free-standing cantilevers in harvesting vibration energy in a broader bandwidth from an unpredictable ambient environment.

i

Contents

List of Figures

List of Tables

Acknowledgements

First and foremost, I would like to thank my PhD supervisor, Prof. Neil White for his ideas and guidance throughout my project. Thanks also go to my co-supervisor, Dr. Nick Harris for his helpful comments in my work.

My sincere gratitude also goes to Dr. Andy Cranny and Dr. Darryl Cotton for showing me the thick-film processing techniques. I appreciate Dr. Steve Beeby and Dr. Russel Torah for allowing me to use the shaker for characterising the samples. I am also thankful to Prof. Alun Vaughan and Prof. Michael Kraft for their comments and suggestions.

I am indebted to Prof. Martyn Hill and Dr. John Atkinson for their generosity in giving me a temporary office space to work in and granting me access to thick-film facilities in the Faraday Building after the fire incident at the clean room and Mountbatten building in Nov. 2005.

Besides that, I would like to take this opportunity to thank my fellow colleagues and friends, Dr. John Tudor, Dr. Peter Glynne-Jones, Somphop Rodamporn, Dr. Dibin Zhu, Ivo Ayala, Dr. Elena Koukharenko, Ghaithaa Manla, Dr. Siti Ahmad, Noreha Abdul Malik, Dr. Neil Grabham, Alex Weddell, Dr. Geoff Merrett, Dr. Andrew Frood, Pedro Barbosa, Adam Lewis and many others in Electronic Systems and Devices Group, who have either been involved directly or indirectly in my project and particular making the lab a friendly and enjoyable place to work in.

Last but most importantly, I owe special thanks to my parents and family members for their encouragement and support in whatever I believe in, without which my PhD would not have been possible.

Nomenclature

Symbol	Unit	Description
ε_T	F/m	permittivity at constant stress
ε_0	F/m	permittivity of vacuum
ε_{33}^T	F/m	permittivity of a piezoelectric material
κ	kg/s^2	spring constant of a spring-mass-damping system
ρ	kg/m^3	total density
ρ_e	kg/m^3	density of electrode
ρ_p	kg/m^3	density of PZT
σ	N/m^2	stress
δ	dimensionless	strain
ζ	dimensionless	damping ratio
ζ_e	dimensionless	electrical damping ratio
ζ_m	dimensionless	mechanical damping ratio
ζ_T	dimensionless	total damping ratio
v_i	dimensionless	coefficient related to boundary conditions
v^E	dimensionless	Poisson's ratio at constant or zero electric field
ω	Hz	driving angular frequency
ω_n	Hz	angular natural frequency
ω_r	Hz	angular resonant frequency
A	m^2	area of piezoelectric material
a_{in}	m^2	base acceleration level
b	kg/s	generic damping factor
b_e	kg/s	electrical damping for a spring-mass-damping system
b_m	kg/s	mechanical damping for a spring-mass-damping system
C^T	F	capacitance of a piezoelectric material
C_p	F	capacitance of a piezoelectric material
$\boldsymbol{D}$	C/m^2	charge density
D	N/m	bending modulus per unit width
d	m	distance from neutral axis to the centroid of piezoelectric layer
d_{ij}	C/N	piezoelectric charge constant at i-polarisation and j-stress applied direction
E	N/C	electric field
E_{eff}	%	energy conversion efficiency

e_e	N/m	elastic modulus for electrode layer
e_p	N/m	elastic modulus for piezoelectric layer
e_T	N/m	total elastic modulus for a composite structure
f_a	Hz	antiresonant frequency of a piezoelectric ceramic
f_r	Hz	resonant frequency of a piezoelectric ceramic
g_{ij}	Vm/N	piezoelectric voltage coefficient at i-polarisation and j-stress applied direction
h_e	m	electrode thickness
h_p	m	piezoelectric thickness
k	dimensionless	coupling factor of piezoelectric cantilever
K_{33}^T	dimensionless	relative dielectric constant at constant stress
k_{31}	dimensionless	coupling factor of piezoelectric material
l	m	free-standing length
l_b	m	total beam length
M	kg	lump mass of a spring-mass-damping system
M_m	kg	proof mass
m_b	kg	total cantilever mass
m_{eff}	kg	effective mass at the tip of a cantilever
P	W	output power in rms value
Q_m	dimensionless	*Q*-factor of a piezoelectric material
Q_T	dimensionless	*Q*-factor of a cantilever structure
R	Ω	resistive load
r	dimensionless	ratio of driving frequency to natural frequency
s_E	m^2/N	elastic compliance at constant electric field
s_{ii}^D	m^2/N	elastic compliance at constant displacement ($i =1$ along its length; $i = 3$ along its thickness)
s_{ii}^E	m^2/N	elastic constant at constant electric field along its length
T_c	°C	Curie Temperature
V	V	output voltage in rms value
Y	m	amplitude base excitation
$y(t)$	m	base displacement of a spring-mass-damping system
$\dot{y}(t)$	m/s^2	base velocity of a spring-mass-damping system
$\ddot{y}(t)$	m/s^2	base acceleration of a spring-mass-damping system
$z(t)$	m	relative displacement of a spring-mass-damping system
$\dot{z}(t)$	m/s	velocity of a spring-mass-damping system
$\ddot{z}(t)$	m/s^2	acceleration of a spring-mass-damping system
Z_m	Ω	impedance of a piezoelectric material

Abbreviations

µTAS	Micro Total Analysis Systems
CVD	Chemical Vapour Deposition
FoM_V	Figure of Merit for performance comparison of energy harvesters
IDE	Interdigitated Electrode
IDT	Interdigitated
MEMS	Micro-Electro-Mechanical System
NPD	Normalised Power Density
PVDF	Poly(vinylidene Fluoride)
PZT	Lead Zirconate Titanate
RF	Radio Frequency
SEM	Scanning Electron Microscope
SFM	Scanning Force Microscopy
SPIDA	Solder Paste Inspection Data Analyst
SU-8	Epoxy-based negative photoresist

"We should be taught not to wait for inspiration to start a thing. Action always generates inspiration. Inspiration seldom generates action"

Frank Tibolt

Chapter 1   Introduction

1.1 Overview of The Technology

With the advancement in the areas of wireless technology and low-power electronics, a pervasive system [1] is made possible. This system is referred to a world where computational devices are embedded in the environment for intelligent buildings and home automation [2], autonomous vehicles [3] and also possible to be implanted in human bodies such as the one in body sensor networks for health monitoring [4]. To develop a totally autonomous system, however, traditional batteries, with limited life-span have to be replaced with energy harvesters, which can provide clean and renewable electrical energy sources.

Vibration-based energy harvesting is one of the attractive solutions for powering autonomous microsystems, due to the fact that, vibration sources are ubiquitous in the ambient environment. Basically, the vibration-to-electricity conversion mechanism can be implemented by piezoelectric [5], electromagnetic [6], electrostatic [7], and magnetostrictive [8] transductions. In this book, piezoelectric transduction is investigated due to its high electrical output density, compatibility with conventional thick-film and thin-film fabrication technologies and ease of integration in silicon integrated circuits.

Typically, piezoelectric materials are fabricated in the form of a cantilever structure, whereby stress is induced by bending the beam configuration in an oscillating manner and generating electric charges on its electrodes, as a result of the piezoelectric effect [9]. They are widely used as sensors and actuators [10, 11]. In recent years,

piezoelectric materials are advancing into another level of development whereby they are used to provide an alternative for powering wireless sensor nodes through vibrations within the environment [5, 12, 13].

Typically, the piezoelectric materials are deposited on a non-electro-active substrate such as alumina, stainless steel or aluminium. They are physically clamped at one end to a rigid base and free to move at the other end. The presence of the substrate does not contribute directly to the electrical output, but merely serves as a mechanical supporting platform, which constrain the movement on the piezoelectric materials and poses difficulties for integration with other microelectronic devices. In order to minimise the constraint, a cantilever structure, which is free from external support or attachment to a non-electro-active platform is proposed. This structure would be in free-standing form consists of only the active piezoelectric materials and electrodes, and would be able to be stressed to generate charges similar to the traditional cantilever structure.

Micro scale free-standing structures in the form of cantilever are commonly fabricated by using thick-film, thin-film and silicon micromachining technology [14]. However, thin-film and micromachining involves complex and expensive processes such as chemical vapour deposition and photolithography. Furthermore, the structures fabricated in these technologies generally are small (a few micrometers in length and width, and less than 1 μm thick) [15], therefore usually producing very low electrical output power (in order of nano-watts) and operate at high level of vibration (in order of kilohertz). The technology used for fabricating free-standing devices depends on the application, for example, in bio-molecular recognition [16], thin-film and micro-machining technologies are used to fabricate cantilevers with sub-micron dimensions. Thick-film technology is preferable to be used for fabricating bigger structures with thicknesses greater than 50 μm, and typically with area from a few mm^2 to a few cm^2, which is the size in between bulk devices and thin-film devices. Thick-film technology can be used to fill the gap between these technologies.

There are a number of challenges in the research of designing, fabricating and characterising free-standing thick-film piezoelectric cantilevers for energy harvesting. Firstly the research requires the understanding of the process conditions and limitation of thick-film technology particularly for fabricating three-dimensional structures. Thick-

film technology involves processes which are hostile and destructive to ceramic free-standing structures e.g. high contact force (> 1 N) during screen-printing, high air flow curtain (> 50 l min^{-1}) in multi-zone furnace and high thick-film processing temperature (> 800 °C). The thermal expansion coefficient mismatch between electrode and piezoelectric materials could also pose a problem in fabricating straight and flat cantilever. Besides that, the mechanical properties of thick-film ceramic materials are notoriously brittle and fragile which is poor to withstand the stress induced when the structure is operated in bending mode.

The target to meet the minimum electrical energy requirement for powering the microsystem is another surmounting challenge. Typically, a ceramic cantilever structure has high mechanical Q-factor at around 150, therefore, in order to harvest maximum electrical energy, the resonant frequency of the device has to match the ambient vibration sources. The unpredictable nature of ambient vibration sources intensifies the challenges toward making thick-film free-standing structures as a useful ambient energy harvester. All of these challenges will be addressed and suggested solutions to the issues will be discussed in detail in this work.

1.2 The Scope of the Book

This book is discussing about the design, fabrication and characterisation of robust and miniature (< 5 cm^3) thick-film piezoelectric energy harvesters, in the form of free-standing cantilever structures for the application of energy harvesting.

The scope of the book covers the mechanical design of a cantilever structure. Investigations into the effect of the neutral axis of the structure on the overall electrical output performance will be carried out. The maximum stress on the film and the deflection on the tip of the cantilever will be estimated in order to fabricate a robust free-standing structure. The electrical output of the device will also be estimated and verified with experimental results. Conventional thick-film technology will be explored to a greater extent in fabricating three dimensional structures by means of a sacrificial layer technique adopted from micromachining technology. A suitable sacrificial layer will be identified, which would be able to withstand high temperature thick-film processing environment and does not degrade the thick-film piezoelectric properties.

Finally, the prototype of the free-standing structure is characterised and maximised so that the devices would be able to operate at low level of ambient vibration and able to generate electrical energy which meet the minimum requirement for powering a microsystem.

1.3 The Book Structure

This book is divided into three main parts. Chapter 2 and 3 form the first part of the discussion about the technology, which includes a literature review of piezoelectricity, thick-film technology application and fabrication methods, and the design of free-standing energy harvesting device. The second part of the book is discussed in Chapter 4, about the fabrication techniques and the improvement method for fabricating robust thick-film free-standing cantilever. The final part of the book is presented in Chapters 5 – 8, dealing with the characterisation of the free-standing structures, optimisation of electrical output and developing a multi-frequency structure for wider bandwidth operation.

Chapter 2 introduces the background of piezoelectricity and its applications particularly in energy harvesting. The enabling technology for fabricating piezoelectric energy harvesters based on thick-film technology is also discussed. Thick-film technology, from the evolution to the standard processing technique is briefly introduced in this chapter, this follows by discussing the advantages of free-standing structures and the possibility of fabrication process.

Chapter 3 addresses the issues of energy harvesting design. Beam theory is used to estimate the natural frequency of the structure. The influence of the distance from the centroid of the piezoelectric material to the neutral axis of the structure in stress, deflection and electrical output is also discussed. Simulation results of finite element analysis with ANSYS are compared with analytical calculation results.

Chapter 4 explains the fabrication process, which combines conventional thick-film and sacrificial layer techniques in fabricating a free-standing structure. The process flow for fabrication is listed in this chapter. Fabrication steps that were taken to enhance free-standing structures are explained.

Chapter 5 presents the experimental results of piezoelectric materials characterisation using Berlincourt (direct) and resonant measurement method for determining the properties of the PZT materials. Comparison is made between a clamped and unclamped sample to verify the analytical model developed by other researchers.

Chapter 6 discusses the results of testing a unimorph free-standing structure under harmonic base excitation. The mechanical and electrical properties of the piezoelectric cantilever having different lengths are characterised with and without a proof mass attached to the end of the structure. The efficiency of energy conversion is compared between cantilevers with different lengths and proof masses.

Chapter 7 describes multimorph cantilever structures. These structures are an extension of the unimorph structure arranged in a multi-layer fashion. Experimental results reveal an improved performance compared to the unimorph structure. Two polarisation modes are studied; series and parallel. The electrical outputs from both of these configurations are measured and discussed in the chapter.

Chapter 8 considers an alternative approach for wide-bandwidth operations. An array of multi-cantilevers is designed to operate in multi-frequency environments, with the intention to harvest energy in a broader frequency spectrum. Experiment results of multi-frequency response are presented and discussed in this chapter.

Chapter 2   Literature Review

2.1 Introduction

The research in designing and fabricating free-standing thick-film piezoelectric devices for the application of energy harvesting involves the understanding of the mechanics of vibrating cantilever structures, the mechanic-to-electric conversion mechanism, thick-film materials and fabrication processes. This chapter will give an overview of all the fundamental knowledge which makes up the back-bone of this book.

This chapter is divided into four main topics: piezoelectricity, vibration energy harvesting, thick-film technology and free-standing structures. In order to understand the interesting phenomena of mechanical to electrical energy conversion, piezoelectricity is first reviewed. This is followed by a few examples of its applications, with the main focus on ambient energy harvesting. The relevant progress in energy harvesting technology will be discussed in detail.

The piezoelectric materials are usually fabricated in the form of a cantilever structure. Electrical energy is produced when the cantilever operates in bending mode at resonant frequency. The cantilever can be fabricated into micro-scale by thin-film and micro-machining technology but as the physical size decreases, the natural frequency of the structure increases, which is not desirable for ambient energy harvesting. An alternative for fabricating cantilever-type energy harvester is by using thick-film technology, where the piezoelectric materials are usually printed on a substrate such as stainless steel and need to be manually clamped at one end to form a cantilever. In most cases, these devices are attached with a proof mass in order to operate at lower vibration levels,

which make the whole device bulky (in a range of millimetres and with thickness around 50 µm).

Cantilevers in the form of free-standing structures are one solution for the above mentioned issues. In free-standing form, the piezoelectric materials are more flexible to move and there are other advantages which will be discussed in this chapter.

2.2 Piezoelectricity

Piezoelectricity is the ability of certain crystals to generate a voltage when a corresponding mechanical stress is applied. The piezoelectric effect is reversible, where the shape of the piezoelectric crystals will deform proportional to externally applied voltage.

Piezoelectricity was first discovered by the brothers Pierre Curie and Jacques Curie in 1880. They predicted and demonstrated that crystalline materials like tourmaline, quartz, topaz, cane sugar, and Rochelle salt (sodium potassium tartrate tetrahydrate) can generate electrical polarization from mechanical stress. Inverse piezoelectricity was mathematically deduced from fundamental thermodynamic principles by Lippmann in 1881. Later the Curies confirmed the existence of the inverse piezoelectric effect [17].

(a)   (b)   (c)
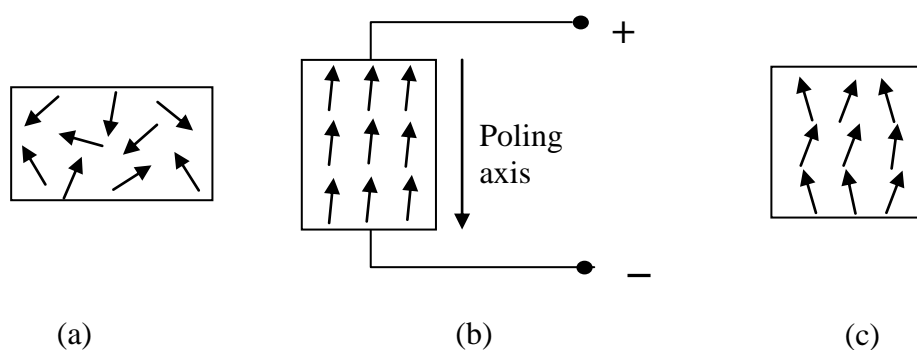
Figure 2-1: Schematic diagram of the electrical domain: (a) before polarisation, (b) during polarisation and (c) after polarisation.

A piezoelectric crystal is built up by elementary cells consisted of electric dipoles, and dipoles near to each other tend to be aligned in regions called Weiss domains. These domains are randomly distributed within the material and produce a net polarisation as shown in Figure 2-1 (a), therefore the crystal overall is electrically neutral.

For the material to become piezoelectric, the domains must be aligned in a single direction. This alignment is performed by the poling process, where a strong field is applied across the material at the Curie temperature (a temperature above which, the piezoelectric material loss its spontaneous polarization and piezoelectric characteristics, when external electric field is not applied). The domains are forced to switch and rotate into the desired direction, aligning themselves with the applied field (Figure 2-1 (b)). The material is then cooled to room temperature, while the electric field is maintained. After polarisation, when the electric filed is removed, the electric dipoles stay roughly in alignment (Figure 2-1 (c)). Subsequently, the material has a remanent polarisation. This alignment also causes a change in the physical dimensions of the material but the volume of the piezoelectric material remains constant.

2.2.1 Constituent Equations of Piezoelectricity

One thing in common between dielectric and piezoelectrics is that both can be expressed as a relation between the intensity of the electric field *E* and the charge density $\mathcal{D}$. However, beside electrical properties, piezoelectric interaction also depends on mechanical properties, which can be described either by the strain, δ or the stress, σ. The relations between $\mathcal{D}_i$, E_k, δ_{ij}, and σ_{kl} can be describe in a strain-charge form of constitutive equation as,

$$\begin{bmatrix} \delta_{ij} \\ \mathcal{D}_i \end{bmatrix} = \begin{bmatrix} s^E_{ijkl} & d_{ijk} \\ d_{ikl} & \varepsilon^T_{ik} \end{bmatrix} \begin{bmatrix} \sigma_{kl} \\ E_k \end{bmatrix} \tag{2-1}$$

Vector $\mathcal{D}_i$ (C/m^2) and E_k (N/C) are tensors of three components and the stress σ_{kl} (N/m^2) and the strain δ_{ij} (m/m) are tensors of six components. d_{ikl} (C/N) is the piezoelectric charge constant and its matrix-transpose d_{ijk}, s^E_{ijkl} (m^2/N) is the elastic compliance at constant electric field (denoted by the subscript *E*) and ε^T_{ik} (F/m) is the permittivity at constant stress (denoted by the subscript *T*).

8

The anisotropic piezoelectric properties of the ceramic are defined by a system of symbols and notations as shown in Figure 2-2. This is related to the orientation of the ceramic and the direction of measurements and applied stresses/forces.
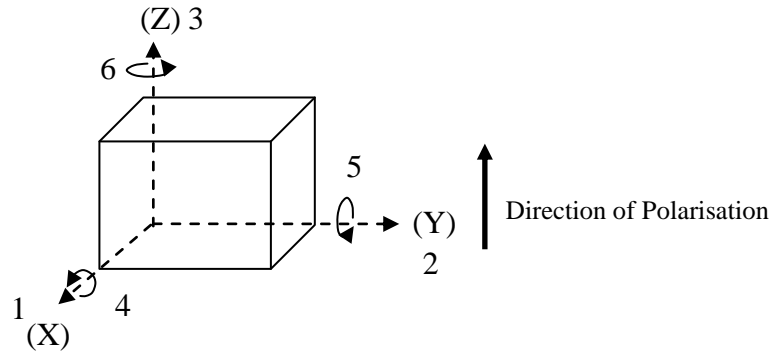
Figure 2-2: Notation of piezoelectric axes.

A cantilever piezoelectric can be designed to operate in either d_{31} or d_{33} modes of vibration depending on the arrangement of the electrodes [18]. d_{31} is a thickness mode polarisation of plated electrode on the piezoelectric materials, with stress applied orthogonal to the poling direction, as shown in Figure 2-3 (a). d_{33} mode on the other hand, can be implemented by fabricating interdigitated (IDT) electrodes on piezoelectric materials for in-plane polarisation where stress can be applied to the poling direction, as shown in Figure 2-3 (b).
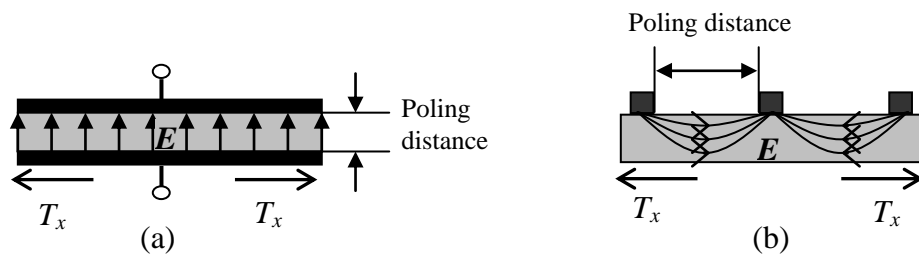
Figure 2-3: Cross-sectional view of piezoelectric configuration mode, (a) d_{31} and (b) d_{33}.

2.2.2 *Piezoelectric Material Measurement Methods*

Generally there are two categories of piezoelectric material measurements methods: static and dynamic measurement methods. The static method is implemented by either directly applying force to the material and observing the charge generation or by applying constant electric field and observing the dimension change, while the dynamic method is using alternating electrical signal at high frequency to observe the frequency responses of the material [19].

Static piezoelectric measurement can be made by either direct or indirect methods. The direct method, also known as Berlincourt method, is conducted by applying a known force to a piezoceramic sample and the charge generated is measured. The relationship between the generated charge and applied force is the piezoelectric charge coefficient as given in equation (2-2).

$$d_{ij} = \frac{\text{Short circuit charge density in } i \text{ direction}}{\text{Applied stress in } j \text{ direction}} \quad \frac{[\text{C}]}{[N]} \tag{2-2}$$

$$d_{ij} = \frac{\text{Strain developed in } j \text{ direction}}{\text{Applied field in } i \text{ direction}} \quad \frac{[\text{m}]}{[V]} \tag{2-3}$$

The subscripts *i* and *j* are the notations for poling direction and the applied stress direction respectively as according to the Figure 2-2. A poled piezoelectric material produces a voltage of the same polarity as the poling direction for compressive force and on the other hand, voltage in the opposite direction is produced when tensile force is applied. This method is the simplest way to measure the d_{33} coefficient by using standard laboratory equipment [20]. The indirect method (or converse method) is an opposite technique, where voltage is applied to generate deformation to the piezoceramic dimensions (without changing the material volume). The relation of applied field and developed strain is given in equation (2-3). When a voltage of opposite polarity is applied to the piezoceramic, the material will be compressed and voltage of the same polarity will induce an expansion along the poling axis.

Resonant frequency measurement is one of the dynamic methods used to determine the piezoelectric and elastic properties of the ceramics. Since frequencies are very easily

and accurately measured, this method provides a good basis for measuring the properties of piezoelectrics [19]. This method involves the measurement of the resonant, f_r and antiresonant, f_a frequencies which are influenced by the dimensions of the material and the clamping condition. When excited at the resonant frequency, the ceramic will resonate with greater amplitude which corresponds to the lowest impedance and follow by an antiresonant frequency, where the amplitude of the oscillation become minimum, which corresponds to the highest impedance in the circuit as shown in Figure 2-4.
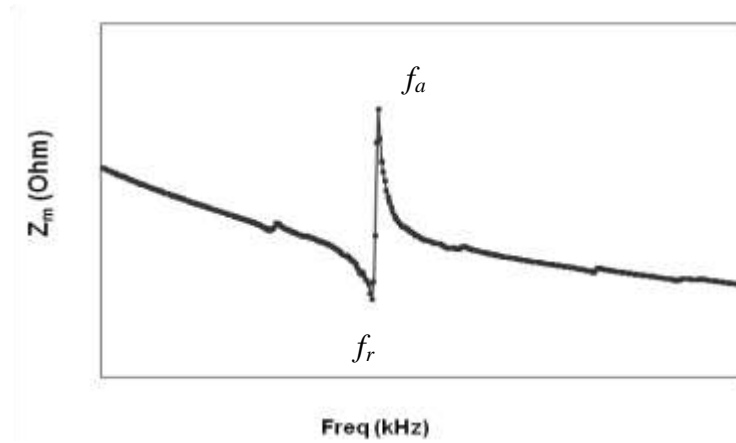
Figure 2-4: Impedance of a piezoelectric ceramic at resonance.

As the thickness of the samples was many times smaller than their widths and lengths ($h < w/50$ and h $< l/100$), this method is suitable for measuring the piezoelectric constants related to transverse modes, where the direction of polarisation is perpendicular to the direction of the applied stress. The transverse piezoelectric charge coefficient is given as [19]

$$d_{31} = \frac{1}{2l_b f_r} \sqrt{\frac{\varepsilon_{33}^T}{\rho\left\{1 + \frac{8}{\pi^2}\left(\frac{f_r}{2\Delta f}\right)\right\}}} \tag{2-4}$$

This is related to the resonant frequency, f_r, the difference between resonant and antiresonant frequencies, Δf, the length of piezoelectric material, l_b, the density, ρ, and the permittivity of the piezoelectric materials. ε_{33}^T is the permittivity of the material, and usually compared with the permittivity of vacuum, ε_0 (8.85×10^{-12} F/m) and described in a form of relative dielectric constant at constant stress, K_{33}^T. This value is related to

11

the dimensions (thickness, *h* and area, *A*) of the piezoelectric material and its capacitance, C^T (at constant or no stress) as

$$K_{33}{}^T = \frac{\varepsilon_{33}{}^T}{\varepsilon_0} = \frac{C^T h}{\varepsilon_0 A} \tag{2-5}$$

The effectiveness of energy conversion between electrical and mechanical is indicated by the coupling factor, which can be determined using

$$k_{31} = \frac{d_{31}}{\sqrt{\varepsilon_{33}^T s_{11}^E}} \tag{2-6}$$

where s_{11}^E is the elastic compliance at a constant electrical field of the material, which is the inverse of Young's modulus, is measured at constant electric field (denoted as superscript *E*) and along its length (denoted as subscript *11*) and can be estimated as

$$s_{11}{}^E = \frac{1}{\rho \left(2 l_b f_r \right)^2} \tag{2-7}$$

Once the coupling factor is known, the constant displacement elastic compliance, $s_{11}{}^D$ (m²/N) can be calculated, which is related to the elastic compliance at constant electric field at a normalisation factor of coupling coefficient as

$$s_{11}{}^D = s_{11}{}^E \left(1 - k_{31}{}^2 \right) \tag{2-8}$$

Other important piezoelectric properties are piezoelectric voltage coefficient, g_{31} (Vm/N), which is defined as the ratio of the charge coefficient to the permittivity of the material,

$$g_{31} = \frac{d_{31}}{\varepsilon_{33}{}^T} \tag{2-9}$$

and the *Q*-factor of the piezoelectric material, Q_m, can be determined by measuring the equivalent resistance (minimum impedance, Z_m) at the resonant frequency [21],

$$Q_m = \frac{1}{2\pi f_r C^T Z_m} \left(\frac{f_a{}^2}{f_a{}^2 - f_r{}^2} \right) \tag{2-10}$$

2.2.3 Piezoelectric Materials

There are a wide variety of piezoelectric materials. Some naturally exist in the form of crystals like Quartz, Rochelle salt, and Tourmaline group minerals. Some poled polycrystalline ceramics like barium titanium, and lead zirconate titanate, PZT, and polymer piezoelectric materials like polyvinylidene fluoride, PVDF and polyimide can be manufactured and easily integrated with MEMS [9].

Commercially, piezoelectric materials are manufactured in bulk form. They are fabricated from a combination of ceramic materials (in short piezoceramics) and pressed in a high temperature ($1100 - 1700^0$C) to form a solid poly-crystalline structure. The raw material to fabricate bulk piezoelectric is in powder form. The powder is then pressed and formed into desired shapes and sizes, which is mechanically strong and dense [21]. In order to make these bulk ceramics into piezoelectric materials, electrodes are deposited onto their surface either by screen printing or vacuum deposition, and poled with electric fields of 2-8 MV·m^{-1} in an oil bath at a temperature of 130 - 220 ^{0}C [22]. Bulk piezoceramics are attractive for their high electromechanical efficiencies and high energy densities. However, bulk piezoceramics tend to be relatively thick (greater than 100 μm), which will not be sensitive and need higher energies to actuate their structures, besides that they are difficult to be processed into thickness below 100 μm, therefore limit their application in Micro-Electro-Mechanical System (MEMS) . Furthermore they need to be attached to certain parts of the MEMS structures using mechanical or adhesive bonding, which is tedious and not cost effective. MEMS devices which require piezoelectric structures with features below 100 μm would usually be fabricated using thin and thick film technologies.

Piezoelectric polymer materials are attractive in fabricating flexible devices. They have much higher piezoelectric stress constants and low elastic stiffness which give them advantages in producing high sensitivity sensors compared to brittle piezoceramics. However, these materials have lower piezoelectric charge constant and are not favourable to fabricate device for electrical power generation. Polyvinylidene fluoride (PVDF) is a common piezoelectric polymer material, which was discovered by Kawai [23]. It is lightweight, tough, and can be cut to form relatively large devices. The earlier form of PVDF was in polymer sheet, which is difficult to be shaped in micro-scale and

they are usually processed with a punching technique based on a micro-embossing technique which is described in the literature [24]. With the development of PVDF thin-film technology, micro-structures can be fabricated as reported by Arshak *et al* [25]. The fabrication process involved drying and curing at low temperature of around 170 °C, and was able to produce d_{33} of 24 pC/N[1] [26]. An alternative to PVDF is polyimide, a high temperature piezoelectric polymer, which can maintain its piezoelectric properties at temperature up to 150 °C as reported by Atkinson *et al* [27].

Film piezoceramics have the advantages that lie between bulk and polymer piezoelectric materials. Although film piezoceramics do not have piezoelectric activity as high as bulk piezoceramics, however, for certain applications where a device thickness has to be fabricated less than 100 μm, film piezoceramics are more favourable for their fabrication compatibility with micro scale devices. Films can be deposited directly on to a substrate, using a deposition technique that is more precise and with higher resolution. The processing temperature of film piezoceramics is in between bulk piezoceramics and piezoelectric polymers (800 °C – 1000 °C), which make it possible to be integrated with semiconductor technology. Film piezoceramics basically can be fabricated with thin- and thick-film technologies. Thin-film technologies involve physical vapour deposition, chemical vapour deposition, and solution deposition, which fabricate films with typical thickness less than 5 μm. For thicker films (10 μm – 100 μm), thick-film technology is preferable. The technology involves a screen printing method, where each layer of ceramic thick film will be printed on a substrate followed by drying and curing processes.

2.2.4 *Lead Zirconate Titanate (PZT)*

Research and development in high performance piezoelectric ceramic had attracted great attention since the discovery of barium titanium oxide in 1940 [28]. This was followed by the discovery of lead titanate zirconate (PZT) in 1950s by Bernard Jaffe [29]. Compared to barium titanium oxide, PZT has a higher Curie point, higher total electric charge, and higher coercive voltage. PZT can be processed in bulk, thin-film, thick-film, and polymer forms in applications suited to their individual characteristics.

Thick-film PZT materials can be classified as 'hard' and 'soft', according to their coercive field during field-induced-strain actuation and Curie temperature [30]. A 'hard' piezoceramic has larger coercive field (greater than 1 kV/mm) and higher Curie point (T_C > 250 °C) compared to 'soft' piezoceramic, which has moderate coercive field (between 0.1 and 1 kV/mm) and moderate Curie point (150 °C < T_C < 250 °C) . Examples of 'hard' PZTs are Pz26 from Ferroperm Piezoceramics [22] and PZT-401 from Morgan Electroceramics [31]. Their typical applications are high power ultrasonics for cleaning, welding and drilling devices. Their distinctive characteristics include high mechanical factor, high coercive field, and low dielectric constant, which make them capable to be used in underwater applications and high voltage generators.

Compared to its counterpart, 'Soft' PZTs have lower mechanical Q-factor, higher electromechanical coupling coefficient, and higher dielectric constant, which are useful to fabricate sensitive receivers and applications requiring fine movement control, for instant in hydrophones and ink jet printers. Other applications ranging from combined resonant transducers (for medical and flow measurements) to accelerometer and pressure sensors [32]. Examples of soft PZTs are Pz27 and Pz29 from Ferroperm Piezoceramics. Pz27 and Pz29 have similar properties as PZT-5A and PZT-5H respectively from Morgan Electroceramics [31] (Appendix A).

2.3 Piezoelectric Applications

The applications of piezoelectric materials can be categorised into sensors, actuators, transducers and generators depending on the type of piezoelectric effect. Sensors make use of the direct piezoelectric effect, transforming mechanical energy into measurable voltage signal. If the output power from this conversion is large enough to power microelectronic devices, it can therefore be used as a microgenerator. Actuators transform electrical into mechanical energy by means of the inverse piezoelectric effect. Finally, transducers use both effects to operate as single devices.

One of the earliest applications of piezoelectric devices was in the area of sonar. They were developed during World War 1 in 1917 in France by Paul Langevin *et al* [33]. It was used as an ultrasonic submarine detector which consisted of a transducer made of

thin quartz crystals glued between two steel plates, and a hydrophone to detect the returned echo.

The successful practical use of piezoelectricity in sonar created intense development interest in piezoelectric devices. Over the next few decades, new piezoelectric materials and new applications for those materials were explored and developed, for instance, in 1927 Morrison and Horton demonstrated the Quartz crystal clock [34], which had been developed into various modern day applications such as computers, calculators, digital watches and mobile phones.

With the rapid development in micro-fabrication technology, microscopic devices based on piezoelectric materials were able to be fabricated. One of the earliest examples is the piezoelectric cantilever developed by Blom *et al* [35]. They used ZnO as the piezoelectric material to sputter on CVD (Chemical Vapour Deposition) SiO_2. Later, Lee *et al* [36] used the method to develop a piezoelectric acoustic transducer for the application of highly sensitive micro-phone and micro-speaker.

Due to piezoelectric direct energy conversion between the electrical domain and the mechanical domain and thus prompt response (~ns), the application of piezoelectric materials has expanded into the detection of atomic masses. Itoh *et al* [37] had developed the first self-excited force-sensing micro-cantilever for dynamic scanning force microscopy (SFM). The devices have two piezoelectric ZnO layers on a SiO_2 film. One of the layers was utilised for excitation and detection of the lever and the other for its static deflection. Yi *et al* [38] reported both experiment and theoretical investigations of the resonance frequency change of a piezoelectric unimorph cantilever due to the mass loaded at the tip of the cantilever, which is possible for bio-sensing applications.

As the piezoelectric activity in some materials has greatly improved over time, the electrical energy significantly increased and the idea of energy harvesting became popular. One of the earliest piezoelectric energy harvesting systems was developed by Umeda *et al* [39] based on mechanical impact using a piezoelectric transducer. However, the details of the materials used to fabricate the transducer were not discussed. From their initial experiment, they dropped a 5.5 g steel ball bearing from 20 mm onto a piezoelectric transducer which consisted of a 19 mm diameter, 0.25 mm

16

thick piezoelectric ceramic bonded to a bonze disc of 0.25 mm thick with a diameter of 27 mm. They found that the optimum efficiency of the impact excitation approach is 9.4 % into a resistive load of 10 kΩ with most of the energy being returned to the ball bearing which bounces off the transducer after the initial impact.

The interests in energy harvesting increased with advances in wireless technology and low power electronics. Piezoelectric materials are used to fabricate micro-generators which are able to capture the ambient vibration energy surrounding the electronics and converting this into usable electrical energy to power microelectronic devices. The application of energy harvesting is not limited to the ambient environment; it is also possible to harvest energy from human body. One such example is a shoe-mounted piezoelectric developed by Shenck *et al* [40]. They explored two methods, one of which is by harnessing the energy dissipated in bending the ball of the foot, using a flexible, multi-laminar PVDF bimorph stave mounted under the insole. The second one is to harness foot strike energy by flattening curved, pre-stressed spring metal strips laminated with a semi-flexible form of piezoelectric PZT under the heel, consisting of two back-to-back single-sided unimorphs. The PVDF transducer produced an average power of 1.3 mW when driving a 250 kΩ load at a 0.9 Hz walking pace, while the PZT transducer produced an average power of 8.4 mW in a 500-kΩ load at the same walking pace.

The examples given above are by no means an exhaustive list of piezoelectric applications. The range of piezoelectric materials applications are far too large to be covered in this work, therefore to suit the purpose of the study, piezoelectric materials fabricated in the form of cantilevers for the application of vibration energy harvesting will be discussed in detail.

2.4 Vibration Energy Harvesting

Piezoelectric is one of the four general types of mechanical-to-electrical energy conversion mechanisms for harvesting vibration energy [41]. The other three are electromagnetic [6], electrostatic [7] and magnetostrictive [8]. With the improvement of piezoelectric activity, the PZT piezoelectric materials (traditionally used to fabricate sensing devices) are becoming popular in fabricating micro-power generators for the

application of embedded and remote systems [42]. Micro-generator is the term often used to describe a device which produces electrical power in micro-Watt scale, while energy harvester is a more general term for describing a device which produces power derived from external ambient sources (e.g. solar, vibration, thermal and wind energy). Both of these terms will be used interchangeably in this book where appropriate.

The vibration energy harvesting of piezoelectric materials is based on the concept of shunt damping to control mechanical vibration [43], however, rather than dissipating the energy through joule heating, the energy is used to power some electronic devices.

In order to estimate the output power from a vibration energy harvester, analytical models have been developed over the years. A generic energy conversion model followed by a specific conversion model for piezoelectric will be discussed in the following section.

2.4.1 *Generic Mechanical-to-Electrical Conversion Model*

One of the earliest general models for energy harvesters was proposed by William and Yates [44]. The model is represented as a single-degree-of-freedom linear mass-spring-damper system as illustrated in Figure 2-5.
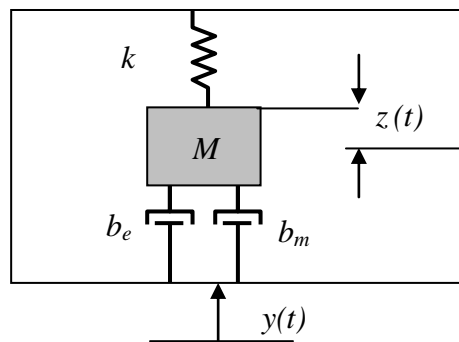
Figure 2-5: A schematic diagram of a spring-mass-damper system of a piezoelectric FSD, based on the model developed by Williams et al [44].

When the system with lump mass, *M* is excited with a displacement of *y(t)* relative to the system housing, a net displacement *z(t)* is produced and the generic equation derived from Newton's second law can be written as in equation (2-11), with the assumption

that the source of the vibration is unlimited and unaffected by the system. The general single degree of freedom model can be written as,

$$M\ddot{z}(t) + \left(b_e + b_m\right)\dot{z}(t) + \kappa z(t) = -M\ddot{y}(t) \tag{2-11}$$

where κ is the spring constant. For a piezoelectric device, the damping effect of the system is related to its induced damping coefficient, b (with subscripts e and m referring to electrical and mechanical damping respectively), which can be written in relation to damping ratios, ζ and undamped natural frequency, ω_n as,

$$b_{e,m} = 2M\omega_n\zeta_{e,m} \tag{2-12}$$

As the system undergoes harmonic motion relative to the base with external excited displacement $y(t) = Y\sin(\omega t)$, there is a net transfer of mechanical power into electrical power. By solving the equation (2-11) and $P = \frac{1}{2}b_e\dot{z}$ (electrical induced power), the magnitude of the generated electrical power can be written as,

$$P = \frac{M\zeta_e\omega^3\left(\dfrac{\omega}{\omega_n}\right)^3 Y^2}{\left[2\zeta_T\left(\dfrac{\omega}{\omega_n}\right)\right]^2 + \left[1-\left(\dfrac{\omega}{\omega_n}\right)^2\right]^2} \tag{2-13}$$

where ζ_T is the total damping ratio ($\zeta_T = \zeta_e + \zeta_m$), and ω is the base excited angular frequency and Y is the amplitude of vibration. When the device is operated at its resonant frequency ω_n, maximum power can be produced and equation (2-13) is simplified to,

$$P_{max} = \frac{M\zeta_e a_{in}^{\ 2}}{4\omega_n\left(\zeta_e + \zeta_m\right)^2} \tag{2-14}$$

where a_{in} is input acceleration from vibration source ($a_{in} = \omega_n^2 Y$). This equation shows that input acceleration is the major factor for increasing the output power from the piezoelectric FSDs. By maintaining the frequency of the vibration source to match the

natural frequency of the device, the electric power generated by the device is proportional to the square of the source acceleration.

2.4.2 Analytical Model of Piezoelectric Harvester

Although the mass-spring-damper system with lumped parameters is more suitable to represent a simple electromagnetic vibration-to-electric energy conversion model, it gives an insight of a general mechanism of mechanical to electrical transduction model which include piezoelectric transduction.

A more specific piezoelectric energy harvester model, where the mechanism of piezoelectric transduction due to the constitutive relations according to equation (2-1) is taken into account, has been proposed by duToit *et al* [45], with an additional term related to undamped natural frequency, ω_n, piezoelectric charge constant, d_{33} and output voltage, v being added to the single-degree-of-freedom equation (2-11). However, the model does not give a clear picture of optimum load resistance at resonant frequency. An improved model by Roundy *et al* [12] suggested an analogous transformer model representing the electromechanical coupling, while the mechanical and the electrical domains of the piezoelectric system are modelled as circuit elements, as shown in Figure 2-6.
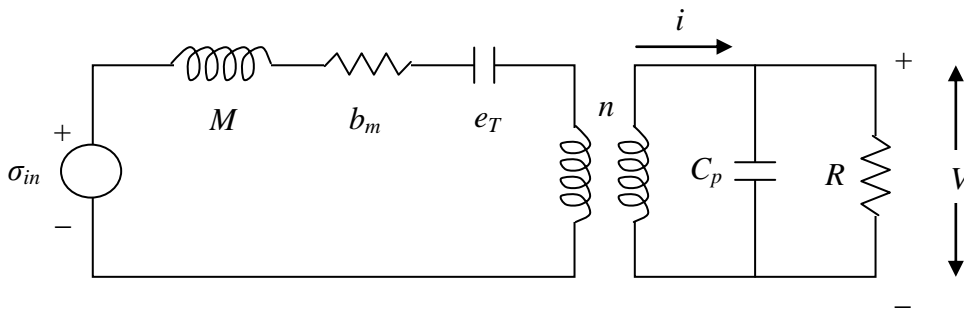
Figure 2-6: A diagram of an analogous circuit for a piezoelectric vibrated device with a resistive load.

The mechanical domain of the equivalent circuit consists of inductor, resistor and capacitor which represents the mass of the generator, M, the mechanical damping, b_m, and mechanical stiffness, e_T respectively. At the electrical domain, C_p is the capacitance

of the piezoelectric and R is the external resistive load, while n is the equivalent turn ratio of the transformer which is proportional to the piezoelectric charge constant d_{31}. V is the voltage across the piezoelectric and i is the current flow into the circuit, which are analogues to the stress and the strain rate respectively. The output voltage at resonant frequency derived from the model is,

$$V = \frac{-j\omega \dfrac{e_p d_{31} h_p B}{\varepsilon} a_{in}}{\left[\dfrac{1}{RC_p}\omega_r^2 - \left(\dfrac{1}{RC_p} + 2\zeta_T\omega_r\right)\omega^2\right] + j\omega\left[\omega_r^2\left(1+k^2\right) + \dfrac{2\zeta_T\omega_r}{RC_p} - \omega^2\right]} \qquad (2\text{-}15)$$

where j is the imaginary number, ω is the driving frequency (Hz), ω_r is the fundamental resonant frequency of the cantilever (Hz), E_T is the elastic constant for the composite structure (N/m^2), d_{31} is the piezoelectric charge coefficient (C/N), h_P is the thickness of the piezoelectric material, ε is the dielectric constant of the piezoelectric material (F), B is a constant related to the distance from the piezoelectric layer to the neutral axis of the structure, ζ_T is the total damping ratio, k_{31} is the piezoelectric coupling factor and C_P is the capacitance of the piezoelectric material. The root mean square (rms) power is given as $|V|^2/2R$, therefore from equation (2-15), the rms value of power transferred to the resistive load can be written as,

$$P = \frac{1}{\omega_r^2} \frac{RC_P^2\left(\dfrac{e_t d_{31} h_P B}{\varepsilon}\right)^2 a_{in}^2}{\left(4\zeta_T^2 + k_{31}^4\right)\left(RC_P\omega_r\right)^2 + 4\zeta_T k_{31}^2\left(RC_P\omega_r\right) + 4\zeta_T^2} \qquad (2\text{-}16)$$

More complex models have been developed by Erturk and Inman [46, 47]. Instead of a single-degree-of-freedom model, they had developed a distributed parameter electromechanical model which incorporates Euler-Bernoulli beam theory with the piezoelectric constitutive equation. The detail of this model will not be discussed in this research work. However, both models agree to a certain extent that at resonant frequency, the output power is proportional to the square power of the piezoelectric charge coefficient, the elasticity of the cantilever, the thickness of the piezoelectric material and the effective mass of the cantilever, all but the first of which are controllable by design. It is also found that the input acceleration from base excitation,

a_{in} ($a_{in} = \omega_n^2 Y$) plays an important part in output power generation. However, for the application of energy harvesters, the acceleration level from an ambient vibration source is a natural phenomenon, which is not controllable. Therefore the energy harvester has to be designed to suit the specific application, though the model gives a good estimation for the potential power generation.

2.4.3 Cantilever-Based Piezoelectric Energy Harvesters

The most common piezoelectric energy harvesters are in the form of a cantilever, due to its simple geometry design and relative ease of fabrication. The structures usually consist of a strong flexible supporting platform with one end fixed to the base on the substrate. Piezoelectric materials are deposited on either one side (unimorph) or both sides (bimorph) of the platform with the intention to strain the piezoelectric films and generate charges from the piezoelectric d_{31} effect. This bending mode operation is effectively generating electrical energy when they are exposed to continuous harmonic vibration sources.

The flexible supporting platform is not electrically active but acts as a mechanical support to the whole structure. It can be stainless steel, aluminium plate or micromachined silicon depending on the fabrication process and the scale of the device. One of the earliest examples using stainless steel as the supporting platform was developed by Glynne-Jones *et al* [5]. They developed a cantilever with a tapered profile as shown in Figure 2-7, in order to produce constant strain in the piezoelectric film along its length for a given displacement. The generator was fabricated by screen-printing a layer of PZT-5H with a thickness of 70 μm on both sides of a stainless steel beam with length 23 mm and thickness 100 μm to form a bimorph cantilever. The device was found to operate at its resonant frequency of 80.1 Hz and produced up to 3 μW of power when driving an optimum resistive load of 333 kΩ.

Another example using stainless steel as the centre supporting platform was developed by Roundy *et al* [48]. Instead of a tapered profile, they simplified their model into a rectangular cantilever with constant width. Based on the model, a prototype micro-generator was fabricated in a form of bimorph structure which consisted of two sheets of PZT attached to both sides of a steel centre shim. The structure with total size of

about 1 cm^3 included a proof mass attached at the tip of the cantilever as shown in Figure 2-8 (a) was excited at 100 Hz with an acceleration magnitude of 2.25 m/s^2. A maximum output power of abut 70 µW was measured when driving a resistive load of about 200 kΩ. An improved version of the prototype was developed with a cantilever with total length of 28 mm, width 3.2 mm and PZT thickness of 0.28 mm, attached with proof mass of length 17 mm, width 3.6 mm and height 7.7 mm as shown in Figure 2-8 (b), produced a maximum power of 375 µW when excited to its resonant frequency of 120 Hz at an acceleration of 2.5 m/s^{-2} [12].

An example of micromachined silicon MEMS cantilever has been developed by Jeon *et al* [15], as shown in Figure 2-9. The cantilever was fabricated by depositing a membrane layer of silicon oxide, a layer of zirconium dioxide which acts as a buffer layer, sol-gel deposited PZT layer and a top interdigitated Pt/Ti electrode on silicon substrate. A proof mass can be added to the cantilever by spin-coating and patterned with a layer of SU-8 photoresist. The beam is releasing by undercutting the silicon substrate using a vapour etching process. The cantilever with a dimension of 170 µm x 260 µm was found to have a fundamental resonant frequency of 13.9 kHz, which was able to generate an electrical power of 1 µW at a base displacement of 14 nm when driving a resistive load of 5.2 MΩ.

In another study, Sodano *et al* [49] compared the efficiencies of three piezoelectric materials: PZT, Quick Pack (QP) actuator and Macro-Fiber Composite (MFC) as shown in Figure 2-11. The PZT material was PSI-5H4E piezoceramic obtained from Piezo System Inc with a length of 63.5 mm and width 60.32 mm. The QP actuator is a bimorph piezoelectric device developed by Mide Technology Corporation, with length 101.6 mm and width 25.4 mm. It was fabricated from a monolithic piezoceramic material embedded in an epoxy matrix, which is ready to be clamped at one end to form a cantilever. The MFC prototype was developed by NASA, consists of thin PZT fibres embedded in a Kapton film with length 82.55 mm and width 57.15 mm and connected with an interdigitated electrode (IDE) pattern. Both the brittle PZT material and the flexible MFC were bonded on a 0.0025 in. aluminium plate and clamped at one end. From their experiment, they found that the PZT performed better than the other two prototypes, with an efficiency of 4.5 % compared to 1.75 % for MFC prototype at resonant frequency. However, their research interest was at the time aimed at recharging

nickel metal hydride batteries and they did not report on the maximum output power of the prototypes.

Recently, Wang *et al* [50] made an improvement to the cantilever structure by separating two plates of PZT to form an air-spaced cantilever as shown in Figure 2-10, which increases the distance between the piezoelectric layer and the neutral plane thus increasing the output voltage generation. The two PZT plates were formed by adhering PZT sheets (Piezo System, Inc) with thickness of 127 μm on both sides of an aluminium plate. Both of the PZT plates with length 7 mm were separated at 221 μm from its middle plane to the neutral plane and attached with proof mass with dimension 16 x 9.2 x 0.31 mm. The device was tested with a speaker with a consistent sinusoidal signal maintained with commercial accelerometer. An output of 32 mV/g was measured at its resonant frequency of 545 Hz.
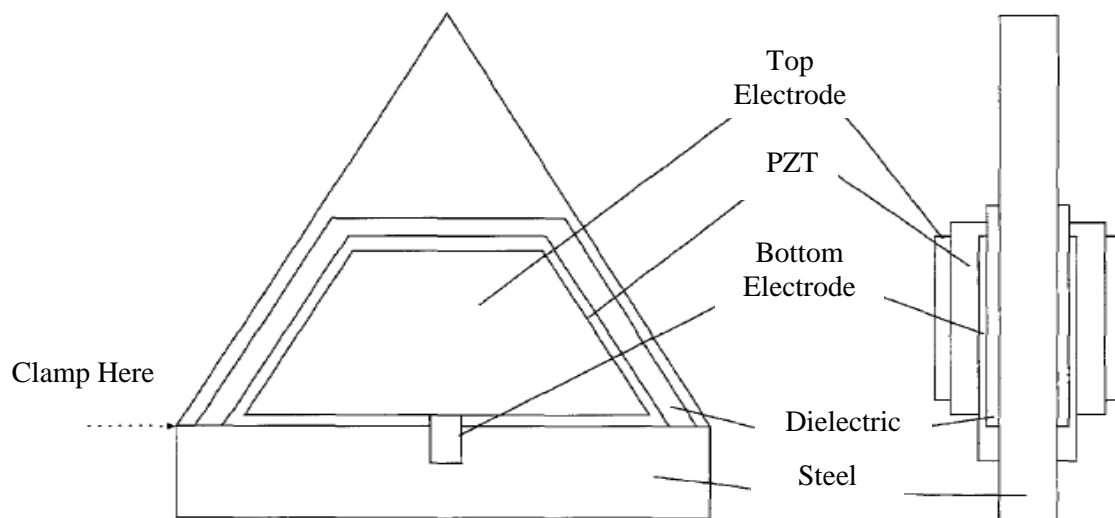
Figure 2-7: Design of prototype generator (after [5]).

24

<table>
<tr><td>(a)</td><td>(b)</td></tr>
</table>
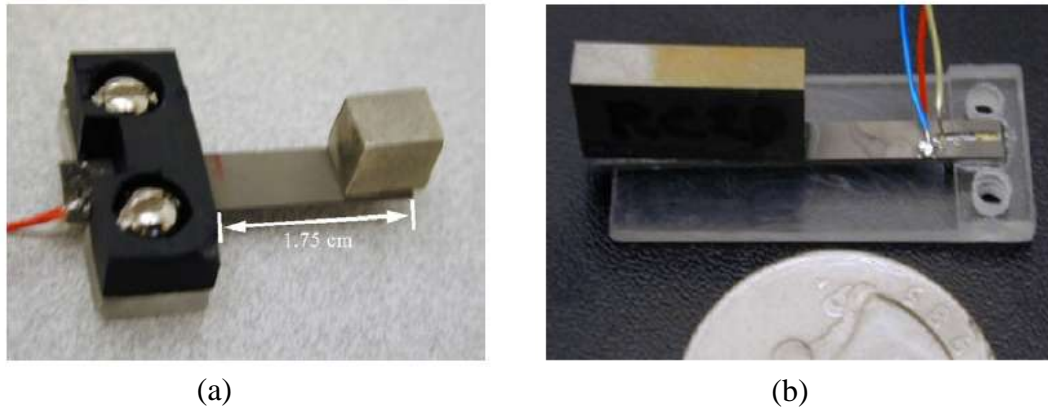
Figure 2-8: (a) A rectangular cantilever microgenerator prototype (b) An improved version (after [12]).
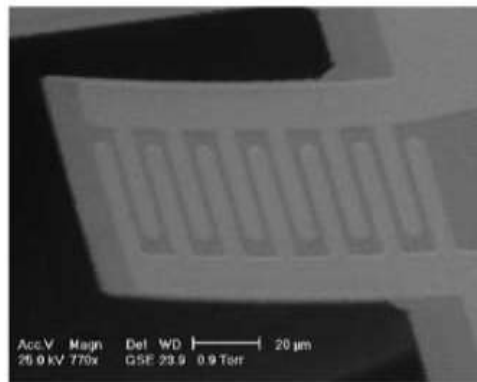
Figure 2-9: MEMS micromachined IDE pattern cantilever (after [15]).
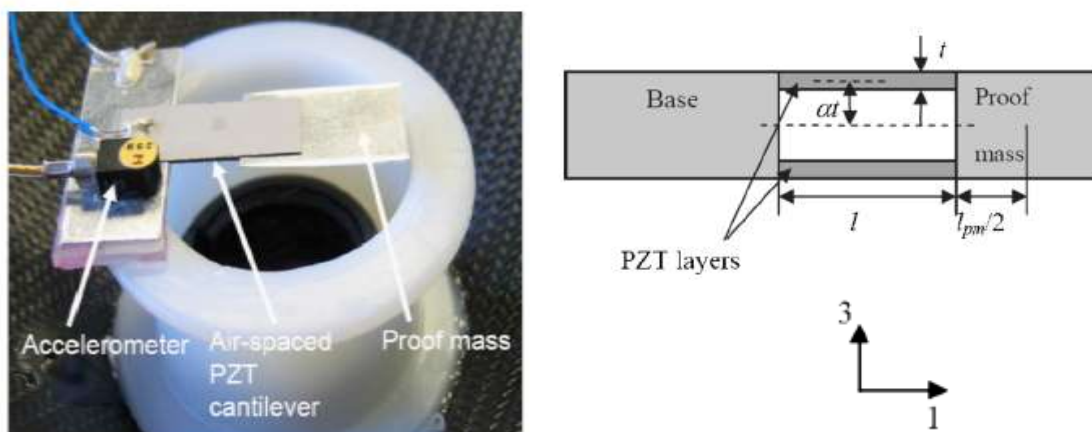
Figure 2-10: Schematic structure of the vibration energy harvester based on air-spaced piezoelectric cantilevers (after [50]).

25

(a)

(c)

(b)
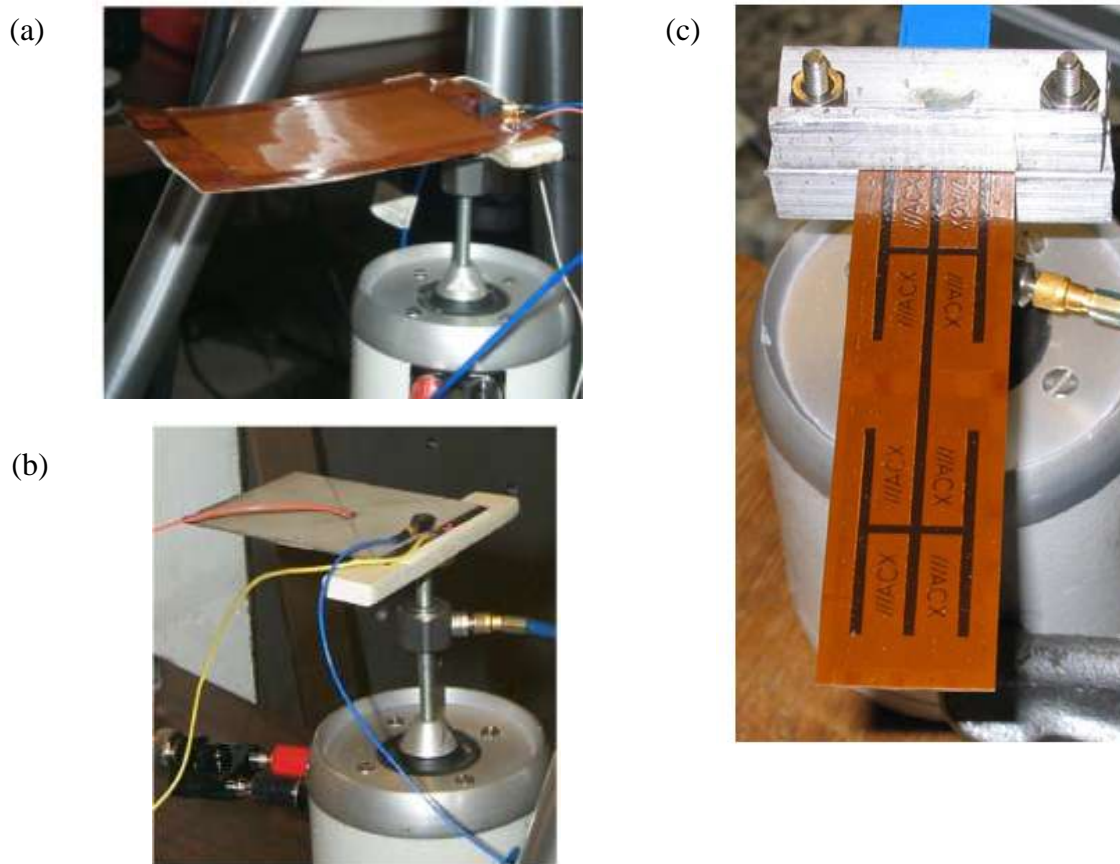
Figure 2-11: Cantilever configuration of a MFC plate (a), a PZT plate (b) and a Quick Pack actuator (c) (after [49]).

2.4.4 Performance Comparison

Over the years, many micro-generator prototypes have been fabricated. The most common vibration energy harvester is based on an electromagnetic principle because at present, the output powers produced by electromagnetic generators are greater than piezoelectric and electrostatic based generators. However, with recent improvement in piezoelectric activity in PZT and the ability to be incorporated within simple cantilever structures, which is relatively easy to be fabricated and integrated with microelectronic systems, piezoelectric methods are an attractive alternative for future investigation.

Each of the energy harvesters was being claimed to demonstrate better performance in one way than another. The most common comparison merit is the electrical output power density. Although power density comparison can give an idea of the performance of an energy harvester, it does not explain the influence of the excitation source. As according to Equation (2-14), the output power of a resonant device is closely dependent on the amplitude of an excitation source. However, to make the comparison meaningful, all the energy harvesters have to be excited at a fixed vibration characteristic (e.g. adjust acceleration level at resonant frequency of the tested devices to give a fixed vibration amplitude), which is impossible as the size of the energy harvesters range from micro to centimetre scales depending on the fabrication technology. Micro-scale devices are more sensitive to micro-scale vibration amplitudes (a few nano- to micrometer), while centimetre scale devices do not show their optimum performances if excited at these same levels, therefore it is not appropriate to make a comparison in terms of power density.

There are other alternative ways to compare the energy harvesters in a more universal metric, for example, a normalised power density (NPD) suggested by Beeby *et al* [6], in which the power density is divided by the source acceleration amplitude squared. Volume figure of merit, FoM$_V$, suggested by Mitcheson *et al* [51], measures the performance as a percentage comparison to its maximum possible output for a particular device. The maximum possible output is proportional to the resonant frequency of the device to the power of three and the overall size of a device with an assumption that the device (with a proof mass) has the density of gold, occupying half of the total volume and the other half is room for displacement,

$$FoM_V = \frac{\mathrm{Measured\,Power\,Output}}{\frac{1}{16}Y_0\rho_{AU}Vol^{4/3}\omega^3} \tag{2-17}$$

A few recently published experimental results of fabricated energy harvesters are listed and summarised in Table 2.1. The table is divided into three sections according to the mechanism of power conversion. Each of the micro-generator is identified by the first author and the year of the publication.

Table 2-1: Comparison of a few key experimental energy harvesters.

Micro-generator	Power (μW)	Freq (Hz)	Volume* (cm^3)	Input Acceln (m/s^2)	NPD (kgs/m^3)	FoM$_V$ (%)
Piezoelectric						
Glynne-Jones, 2000 [52]	3	80.1	70	NA	NA	NA
Roundy, 2003 [53]	375	120	1.0	2.5	60	1.65
Tanaka, 2005 [54]	180	50	9	1	20.5	0.26
Jeon, 2005 [15]	1.0	1.4×10^4	2.7×10^{-5}	106.8	3.2	1.10
Fang, 2006 [26]	2.16	609	6.0×10^{-4}	64.4	0.9	1.44
Reilly, 2006 [55]	700	40	4.8	2.3	28.2	1.25
Lefeuvre, 2006 [56]	3.0×10^5	56	34	0.8	1.42×10^4	81.36
Ferrari, 2006 [57]	0.27	41	0.188	8.8	0.018	0.01
Mide, 2010 [58]	8.0×10^3	50	40.5	9.8	2.1	0.16
Electromagnetic						
Ching, 2000 [59]	5	104	1	81.2	7.6×10^{-4}	7.82×10^{-4}
Li, 2000 [60]	10	64	1.24	16.2	0.03	0.01
Williams, 2001 [61]	0.33	4.4×10^3	0.02	382.2	1.1×10^{-4}	4.8×10^{-5}
Glynne-Jones, 2001 [62]	5.0×10^3	99	4.08	6.9	26.1	1.49
Mizuno, 2003 [63]	4.0×10^{-4}	700	2.1	12.4	1.24×10^{-6}	2.26×10^{-8}
Huang, 2007 [64]	1.44	100	0.04	19.7	0.09	0.07
Beeby, 2007 [6]	46	52	0.15	0.6	884	24.8
Torah, 2008 [65]	58	50	0.16	0.6	1.0×10^3	29.4
Ferro Solution, 2008 [66]	1.08×10^4	60	133	1	84.4	0.36
Perpetuum, 2009 [67]	9.2×10^4	22	130.7	9.8	7.33	0.85

	Electrostatic					
Tashiro, 2002 [68]	36	6	15	12.8	0.015	0.017
Mizuno, 2003 [63]	7.4×10^{-6}	743	0.6	14	6.3×10^{-8}	1.9×10^{-9}
Arakawa, 2004 [69]	6.0	10	0.4	4.0	0.96	0.68
Despesse, 2005 [70]	1.0×10^{3}	50	18	8.8	0.7	0.06
Miao, 2006 [71]	2.4	20	0.6	2.2×10^{3}	8.0×10^{-7}	0.02
Basset, 2009 [72]	0.06	250	0.07	2.5	0.15	4.9×10^{-3}

* Device size does not include the electrical possessing and storage circuits

NA = Data is not available from literature

2.5 Thick-Film Technology

Thick-film technology is distinguished from other fabrication technologies by the sequential processes of screen-printing, drying and firing (curing). Screen-printing is possibly one of the oldest forms of graphic art reproduction and traditionally silk screen printing was used to transfer patterns to printable surface such as clothes, ceramics, glass, polyethylene and metals [10].

The process is ideal for mass production with the ability to produce films of 10-50 μm thick in one print whilst other deposition and printing techniques require many hours of processing to achieve the same thickness. Limitations of conventional screen-printing are feature size and geometry with a minimum line width and separation distance around 100-150 μm.

2.5.1 Evolution of Thick-Film Technology

Thick-film technology is traditionally used to manufacture resistor networks, hybrid integrated circuits, and other electronic components [73]. In the past two decades, research in thick-films has been extended to include sensing capabilities [74]. One of

the prominent applications of thick-film as a sensing element was as a strain gauge [75, 76].

One of the earliest piezoelectric devices fabricated with thick-film technology was reported by Baudry in 1987 [77]. Following on from the discovery of high piezoelectric activity materials such as lead zirconate titanate (PZT) brought thick-film technology to another level of development, where it is possible to fabricate micro-generators for embedded and remote systems [78].

Thick-film micro-generators are commonly fabricated in the form of a cantilever to harvest energy from bending mode as discussed in the previous section. Another example of a thick-film generator is based on the thermoelectric principle. This type of generator can be fabricated from high Seebeck coefficient materials such as bismuth telluride, which has the potential to convert body temperature changes into useful electric power sources [79]. However, the development of the generator is still in an early stage to investigate the feasibility for implantable biomedical applications.

There are many other interesting applications which need acceptable acoustic outputs for instance in micro-fluidic application for carrying out chemical and biological analysis, which is known as micro total analysis systems (μTAS) or "Lab on a Chip" [80]. Thick-film technology was used in fabricating multi-layered resonators for use as a micro-fluidic filter to separate particles within the fluid by ultrasonic standing waves.

2.5.2 Standard Fabrication Process

Piezoelectric paste is the main component in thick-film technology. It is a composite of finely powdered piezoelectric ceramic dispersed in a matrix of epoxy resin which was applied as a film onto a substrate by scraping with a blade [81]. Alternatively, thick-film piezoelectric materials can be made into a form of water-based paint as described by Hale [81]. The piezoelectric paint consists of polymer matrix to bind PZT powder and cured at ambient temperature. One of the advantages of this paint is able to spray on flexible substrate materials and has found application in dynamic strain sensors.

The basic equipment used for processing screen-printed thick-film are the screen, screen printer, infrared dryer and multi-zone furnace. A typical thick-film screen is made from a finely woven mesh of stainless steel, polyester or nylon. For optimum accuracy of registration and high resolution device printing, a stainless steel screen is preferred. The screen is installed in a screen printer, which is necessary for accurate and repeatable printing. The screen printer consists of a squeegee, screen holder and substrate work-holder. Before a printing process is started, the gap between substrate and screen is adjusted to be around 0.5 mm to 1 mm, depending on the screen material and the resolution required for the print (a bigger gap is necessary for flexible materials such as polyester screen, and also as a requirement for higher definition printing).

The substrate work-holder is aligned according to the printing pattern on the screen. Once the setting is correct, a printable material (paste / ink) is then smeared across the pattern on the screen as shown in Figure 2-12(a). A squeegee is then brought in contact with the screen with applied force, which deflects the screen (Figure 2-12(b)) and the paste is drawn through by surface tension between the ink and substrate and deposits on the substrate under the screen which is rigidly held by the substrate holder as shown in Figure 2-12 (c).
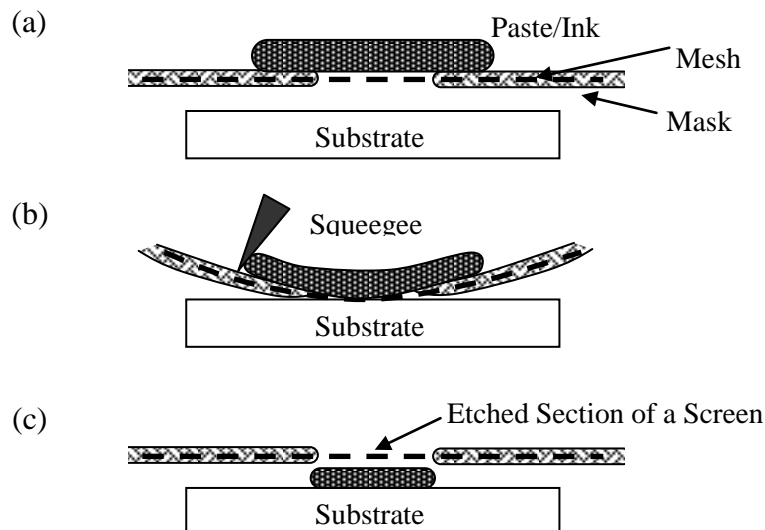
Figure 2-12: Thick-film screen printing steps.

After screen-printing, an irregular surface pattern caused by the screen mesh appears on the wet print surface. Therefore before the drying process, the printed layer needs to be

left to settle for about 10 minutes otherwise a uniform device thickness will not be achieved. The drying process is carried out in an infra-red belt conveyor or a conventional box oven at a temperature around 150 °C for 10–15 minutes. The function of the drying process is to remove the organic solvents by evaporation from the wet print and retain a rigid pattern of films on the substrate. Normally, the thickness of the film will be reduced by up to half of its original printed thickness after the drying process. A thicker film can be formed by printing another layer of film directly onto the dried film. The next stage of the process is co-firing, where the dried films are annealed in a multi-zone belt furnace. This is to solidify the composite of the films which consist of glass frit and active particles (e.g. PZT). During the process, the glass melts and binds the active particles together and adheres to the substrate.

The main concerns for piezoelectric thick-film fabrication are to produce films that are uniform in thickness, crack-free, have high mechanical density, are reproducible, and with high piezoelectric performance. Reproducible and high piezoelectric performance can be achieved by formulating correct paste composition. The curing or co-firing temperature is crucial as well to determine piezoelectric properties of the films, while screen-printing with correct squeeze pressure and snap height can control the film thickness and uniformity. Screen mesh and emulsion thickness are also important to determine deposition resolution and quality of prints.

2.6 Thick-Film Free-Standing Structures

Conventionally, thick-films are printed in layers onto a suitable substrate material, and the subsequent device is considered as a single entity [78]. With some materials such as piezoelectrics, optimum electromechanical characteristics can be only obtained when a thick-film piezoelectric material (piezoceramic) is unconstrained in its direction of displacement when a force (or voltage) is applied [82]. To achieve this, the piezoceramic needs to be free-standing (or free supporting) from the surface of a substrate.

A free-standing structure is defined as one that stands alone, or on its own foundation, free of external support or attachment to a non-electrical-active platform. These

structures can be of a variety of forms, from simple cantilevers to complex combination structures like honeycombs as shown in Figure 2-13.

The wide acceptance for the integration of microelectronics and micromechanical systems (MEMS), has been the main drivers leading to the requirements of free-standing micromechanical devices. These micro-scale free-standing structures have been fabricated with a combination of thin-film and silicon micromachining technologies [14].

Thick-film technology, however, has not received significant attention compared to its competitor technologies. One of the main reasons is because piezoceramics are considered too fragile to form free-standing structure. Circular membranes (a form of free-standing structure), fabricated with thick-film technology for use as pressure sensor, were possibly the first of this kind to be reported [83].
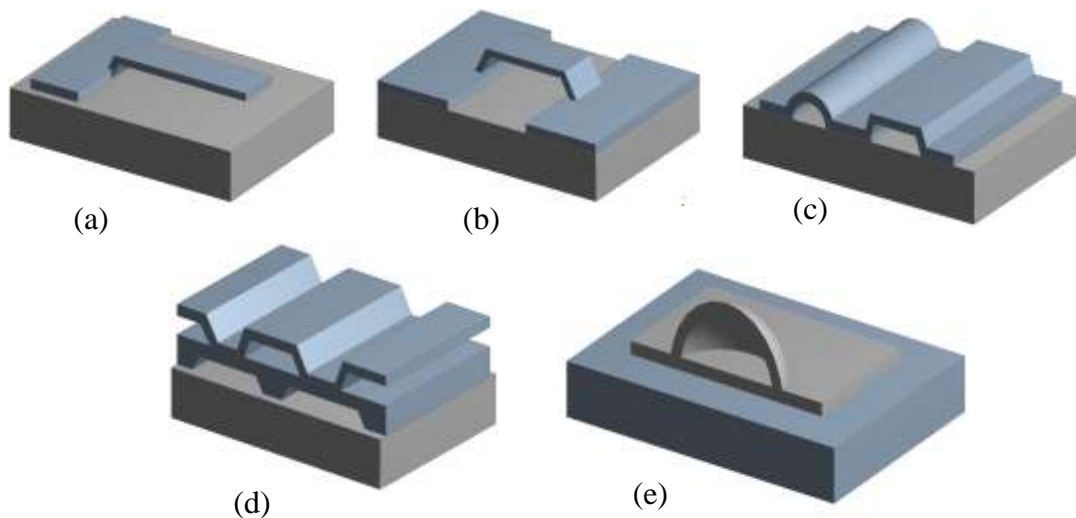
Figure 2-13: A few examples of free-standing micromechanical structure [83]: (a) cantilever, (b) bridge, (c) tunnel, (d) honeycomb, and (e) dome.

2.6.1 The Advantages of Thick-Film Free-Standing Structure

One of the potential advantages of thick-film free-standing structures is its ability to provide a support structure upon which other sensing materials can be deposited. These structures are three-dimensional micromechanical structures and are analogous to silicon micro-machined MEMS devices [10]. The main difference is that thick-film free-standing structures are formed without the supporting platforms, which are passive mechanical elements that do not directly contribute to the generation of electrical energy. It is therefore desirable for them to be thin and flexible.

Free-standing thick-film devices are multi-layered structures comprising only screen-printed piezoelectric materials and electrodes. Their mechanical (e.g. *Q*-factor and elastic constants) and electrical properties (piezoelectric coefficients and coupling factor) can be measured in the absence of the supporting platform. The piezoelectric charge constant, d_{33}, can be directly measured using the Berlincourt method, rather than being inferred indirectly as with measurements on clamped films [82, 84].

Free-standing thick-film structures can be fabricated using mass-production methods and do not need to be assembled manually, unlike some other devices described in the literature [5, 48, 49]. It is therefore possible to create quite complex structures with a series of relatively simple fabrication steps, for instance a multi-cantilever structure (which will be discussed in Chapter 8). They can also be integrated with other thick-film layers and microelectronic components, thereby offering an interesting alternative to micromachined MEMS.

The electrical connectivity of piezoelectric materials within a multi-layered composite structure, without the hindrance from non-electro-active centre shim, is also another attractive feature for a free-standing structure. This feature enables a multimorph structure to operate flexibly as either current source or voltage source depending on the demand of the resistive load. The detail of multimorph operation will be discussed in Chapter 7.

2.6.2 Conventional Fabrication Techniques

Standard micromachining techniques involve the process of transferring a pattern from a master mask to another surface on a substrate, usually silicon. The pattern protects some areas of the substrate during the chemical etching process and is selectively removed by a further chemical etching process in later stages [85]. There are two major classifications of micromachining techniques; bulk-micromachining and surface-micromachining [14].

Bulk micromachining technique is primarily using accurate and precise machining of a relatively thick substrate. This technique involves either etching silicon in all crystallographic directions at the same rate (isotropic wet etching) or removing silicon at a rate that depends on the orientation of the crystal lattice structure and the doping level (anisotropic wet etching), to shape desired patterns. A silicon micromachined accelerometer [86] and a micro generator based on cantilever structures [26] are examples of devices fabricated with bulk micromachining. The fabrication process is show in Figure 2-14.

Step 1: Functional films preparation.

Step 2: Functional films patterning and silicon slot etching.

Step 3: Silicon deep etching at the bottom side.

Step 4: Cantilever release by RIE.

Step 5: Metal mass fabrication on the cantilever.
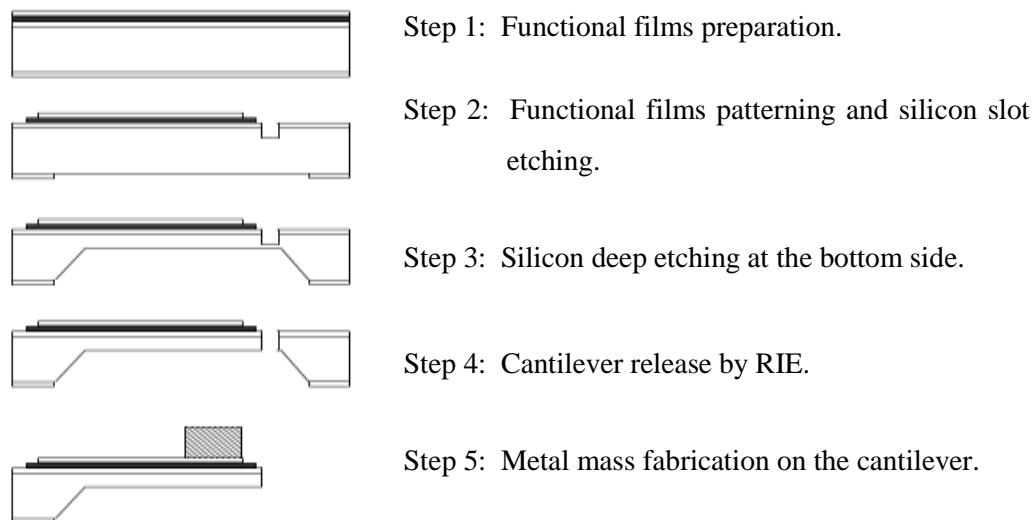
Figure 2-14: Micromachining process for fabricating a cantilever structure [26].

35

The greatest advantage of micromachining techniques is its capability to integrate the micromechanical structures with electronic circuits with higher reliability. However, this process is relatively expensive and involves complex fabrication steps. Furthermore, chemicals used in the process are harmful to the environment if a proper waste management is not implemented.

In contrast to bulk micromachining, surface micromachined features are built up, layer by layer on a surface of a substrate. Usually sacrificial layer techniques are used where the active layers which are the eventual moving structures are deposited on temporary rigid platforms. The platforms will then be removed, usually by etching away the materials. These platforms are called 'sacrificial layers', since they are 'sacrificed' to release the materials above them. Unlike bulk micromachining, where a silicon substrate is selectively etched to produce free-standing structures, surface micromachining is based on the deposition and etching of different structural layers on top of the substrate. Therefore the substrate's properties are not critical. Expensive silicon wafer can be replaced with cheaper substrates, such as glass, and the size of the substrates can be much larger compared to those used in bulk micromachining. The sacrificial layer for surface micromachining could be silicon oxide, phosphosilicate glass or photoresist. Figure 2-15 shows the fabrication steps of surface micromachining in building a free-standing structure.

Step 1: Insulation layer deposition

Step 2: Sacrificial layer deposition

Step 3: Anchor hole etching follow by polysilicon deposition and patterning

Step 4: Sacrificial layer etching and releasing a free-standing structure
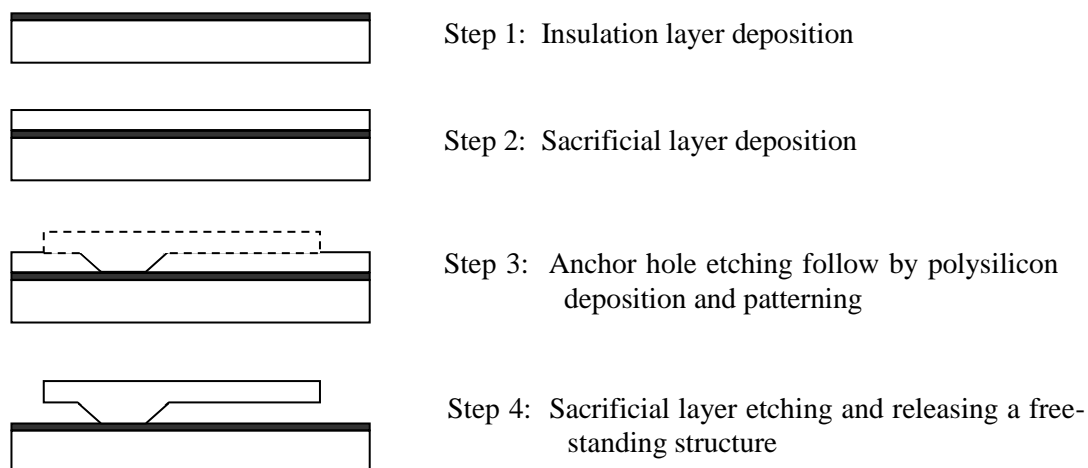
Figure 2-15: Fabrication steps of surface micromachining based on sacrificial layer technique [14].

'Flip and bond' technique is another alternative for fabricating free-standing structures, developed by Papakostas [87]. It is a low temperature processing technique for fabricating polymer free-standing structures. As its name implies, the free-standing structures of this kind was made up from two independent parts which were fabricated separately and in the later stage, the parts would be combined together to make the desired free-standing structures. Figure 2-16 describes the steps of fabricating a free-standing structure with flip and bond technique. The fabrication steps begin with building two main structures in two different substrates (Step 1). They are the base and connection plate structures. The base structure is fabricated by printing silver-filled polymer conductor directly on top of alumina substrate. This structure acted as a spacer to separate the connection plate created at a later stage from the substrate, and also as the electrode pad for soldering. Flip and bond techniques offer a convenient and economic way to fabricate a thick-film based piezoelectric polymer free-standing structure. This low temperature technique can also be used to integrate with other silicon fabrication technique. However, the disadvantage is the technique involves manual assembly of the parts, which may not be precise.

Step 1:

Silver-filled polymer conductor

Sandwich layer of polymer piezoelectric layer in between polymer electrodes

Alumina Substrate

Polyimide Carrier

Step 2: Polyimide sheets carrying dried connection plate of silver-filled patterns were attached upside down on the spacer patterns, pressed by hand to achieve good contact and adhesion and cured on a hot plate for 60min at 150^0C

Step 3: Polyimide carrier was etched with O_2 in plasma. At the end of the process, a free-standing polymer thick-film cantilever structure on silicon or alumina was created.

Figure 2-16: Fabrication steps for a 'flip-and-bond' technique [87].

2.6.3 Thick-Film Sacrificial Layer Techniques

Thick-film free-standing structure can be fabricated by using sacrificial layer techniques as those used in the conventional thin-film processing technologies as described in section 2.6.2. One of the examples of fabrication incorporating sacrificial layer techniques is polymer free-standing structures based on SU-8 [88]. The structures were fabricated using Cu and lift-off resist as the sacrificial layers, where they were wet-etched at the final stage of the process. Piezoelectric polymer free-standing structures were fabricated by Atkinson *et al* [27], using piezoelectric polyimide as the active material and photoresist as the sacrificial layer. The process was based on conventional lithography and metallization techniques and the fabrication steps are shown in Figure 2-17.

	Step 1: Oxidation followed by sacrificial layer deposition
	Step 2: Lower electrode evaporation and patterning
	Step 3: Polyimide coating and top electrode patterning
	Step 4: Polyimide etching followed by sacrificial layer etching and finally releasing a free-standing structure
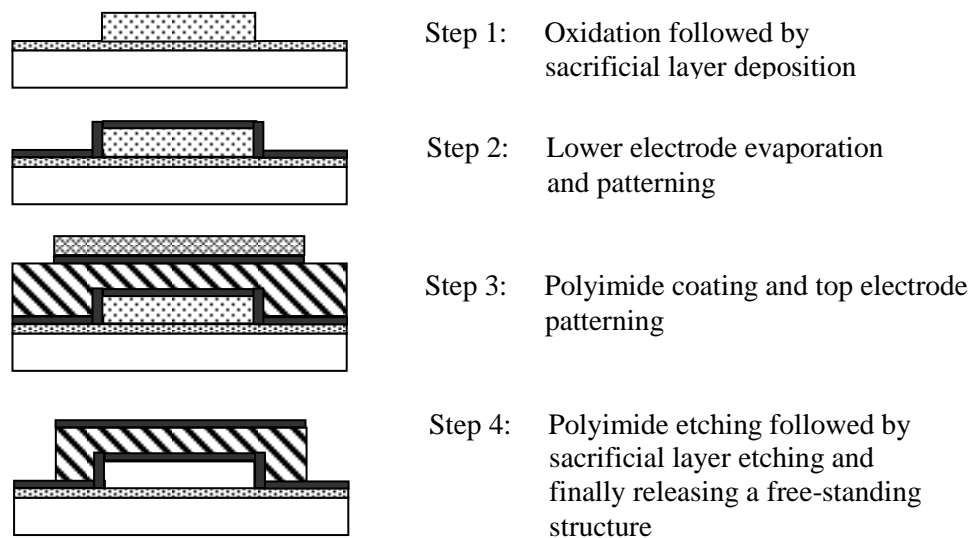
Figure 2-17: Piezoelectric polyimide free-standing structure fabrication steps [27].

Stecher [83] developed a thick-film free-standing structure by combining the processing of air and nitrogen fireable materials on the same substrate, where initially a carbon-like filler was printed and dried on those areas of the substrate for the structure to be free supporting at a later stage. The filler has to prevent the successively printed dielectric from being bonded to the substrate. This was followed by a second step where the

dielectric material is printed on top of the filler and parts of the substrate, where the part that printed on the substrate will form a rigid base to support the free-standing structure.

The dried paste is then co-fired in a nitrogen atmosphere. The nitrogen must be used because the filler must not be burnt out before the glass-ceramic has sintered. The process is repeated to form a multilayer composite film. Finally, the composite film is co-fired in an air environment, where the carbon filler acting as a sacrificial layer is burnt out without residues, releasing a composite thick-film free-standing structure. The fabrication steps are shown in Figure 2-18.

Step 1: Carbon-like filler printing

Step 2: Electrode and PZT layers print on top of the filler and fired in nitrogen environment

Step 3: Fire in air environment to burn carbon-like filler
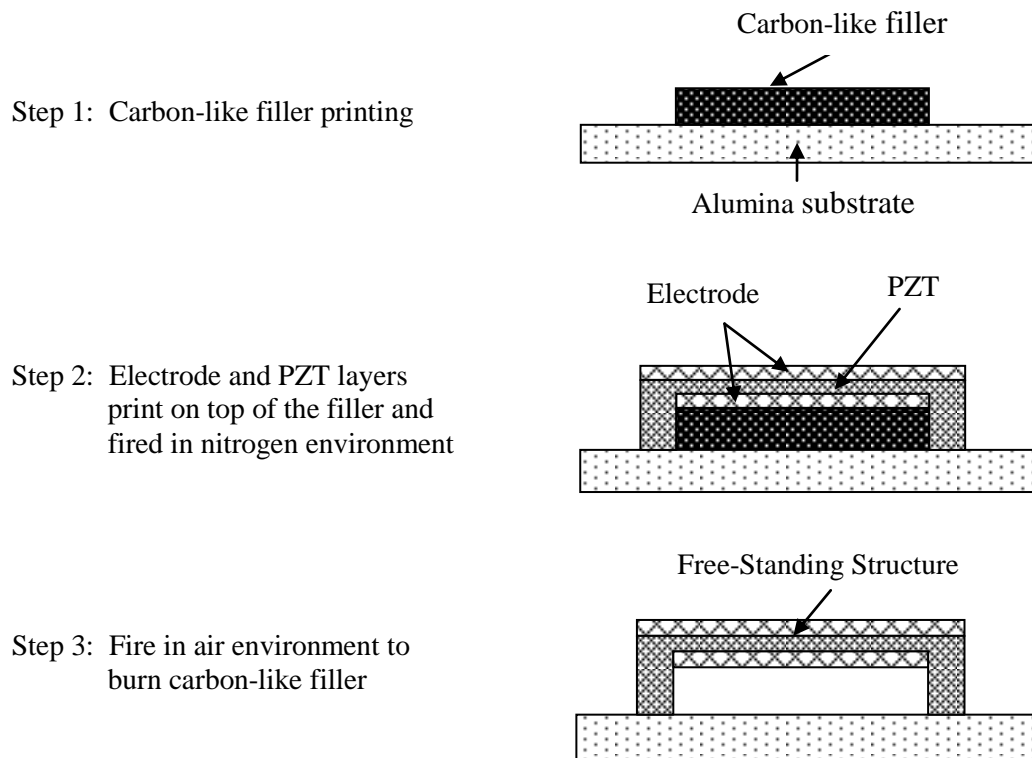
Figure 2-18: Fabrication steps for thick-film sacrificial layer technique.

2.7 Conclusion

Free-standing structures in the form of a cantilever are interesting features which find application in sensing and actuating. Incorporated with high piezoelectric activity materials like PZT, the structures can be operated as micro-generators for powering low power microelectronic devices. The micro-generators can be modelled as a single-degree-of-freedom mass-spring-damper system, where the electrical output power can be estimated and improved with optimised designs. Conventionally, free-standing structures were fabricated with thin-film and silicon micro-engineering technologies. Thick-film technology, however, has not received significant attention compared with its competitor technologies, for fabricating free-standing structures. One of the main reasons for this is because piezoceramics are considered too fragile to form free-standing structures. In this work, studies on the free-standing structures fabricated by thick-film technology will be presented.

Chapter 3   Free-Standing Cantilever Structure Designs

3.1   Introduction

Making the reality of ambient vibration energy harvesting using thick-film free-standing structure is very challenging. Some of the challenges include, fabricating a robust piezoceramic structure, ensuring the structure resonates with the vibration sources, solving the problem of unpredictable ambient vibrations and meeting the minimum electrical energy requirement.

First and foremost the characteristics of potential vibration sources from the environment have to be investigated before any energy harvester device can be designed. Once the vibration sources are identified, energy harvesters can be tailored to suit that specific environment. Besides that, the design of the energy harvesters has to be based on the limitation of the fabrication technology (in this case, thick-film technology) and the physical constrains of the real device (e.g. the maximum allowed displacement and stress before the device fails to respond accordingly or is broken) in order to fabricate a robust piezoceramic structure.

The output voltage and electrical power are the crucial factors in making the device useful. For this reason, the multimorph structure was developed to enhance the electrical performance of the device. Besides improving the electrical energy output, the multimorph can be deployed as either current source or voltage source depending on the

electrode configuration. Multimorph free-standing structures will be discussed in detail in Chapter 6.

Last but not least, the unpredictable ambient vibrations are addressed in Chapter 7. The unpredictable pattern of vibration can result in total failure for a high *Q*-factor structure like the piezoceramic structure. To use a single cantilever structure alone will not solve the problem for ambient energy harvesting. Employing an array of cantilevers with different frequencies however is one way to tackle this issue.

In this chapter, a piezoelectric unimorph cantilever structure model is discussed. The main objective is to estimate the mechanical and electrical performance of the model by simulation and theoretical calculation. The model is a sandwiched structure of electrode-PZT-electrode, which has a neutral axis near to the centre plane of the piezoelectric material. The calculated results from the model will then be compared to finite element method simulation results to validate the model.

3.2   Ambient Vibration Sources

Ambient vibration sources are ubiquitous around us, which can be either natural (e.g. earthquake) or man-made (e.g. machinery). For the purpose of this research, predictable man-made vibration sources are considered. These vibrations can be ranging from high level such as those produced by jet engines to low level such as those produced by home electrical appliances. The focus of this research is on low lever vibrations because they exist in a wider range of applications, are easy available and ready to be used for power generation.

A few typical low level vibration sources were measured with an accelerometer and portable data acquisition system (USB measurement module and laptop). The digitised time data were processed offline with FFT and presented in frequency domain as shown in Figure 3-1. The acceleration and the resonant frequency of the sources can be directly obtained from the data, while the excited amplitude of the vibration can be obtained by dividing the acceleration level over angular frequency squared. For example a microwave casing has a peak resonant frequency at around 100 Hz with an acceleration level of 0.7 m/s^2. This gives an amplitude of 1.72 μm. A stationary car with engine

capacity of 1000 cc vibrates at around 30 Hz and when accelerated at 1.23 m/s^2 was calculated to produce 33.5 μm of vibration amplitude.
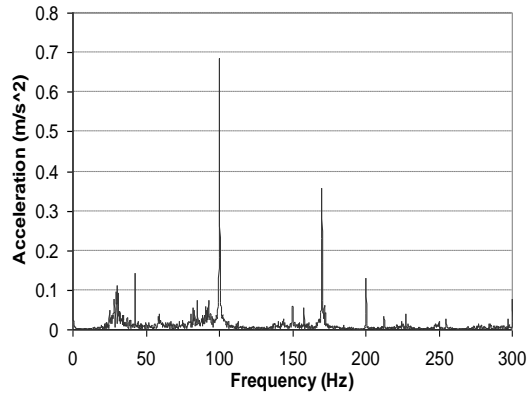
Microwave Casing
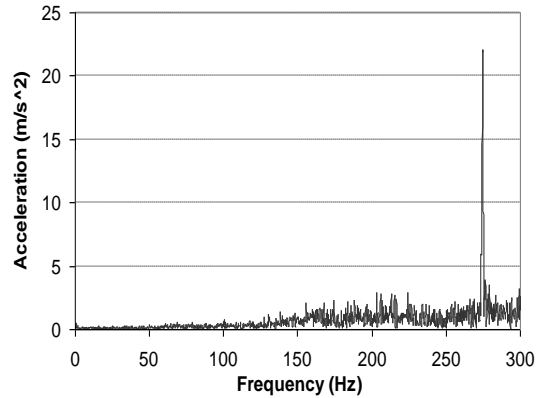
Blender Casing
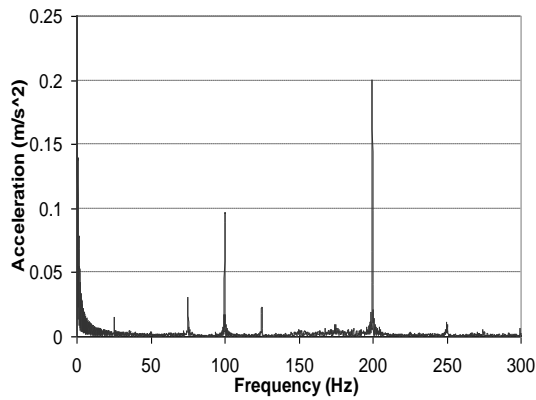
Kitchen ventilation Fan at Lower Speed
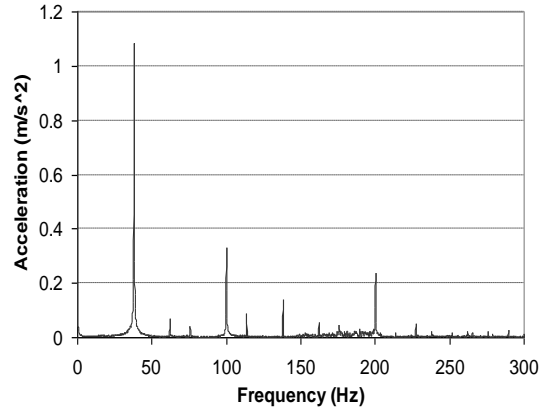
Kitchen ventilation Fan at Higher Speed
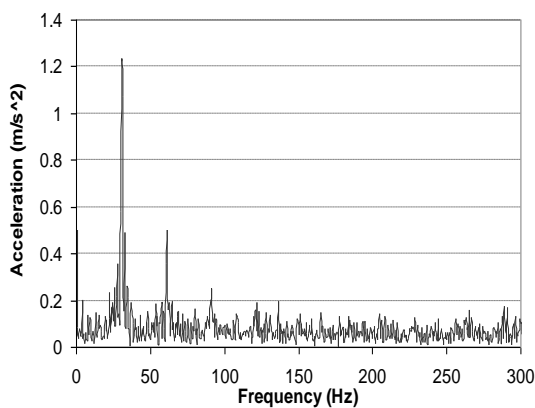
Stationary Car with Engine Switched On
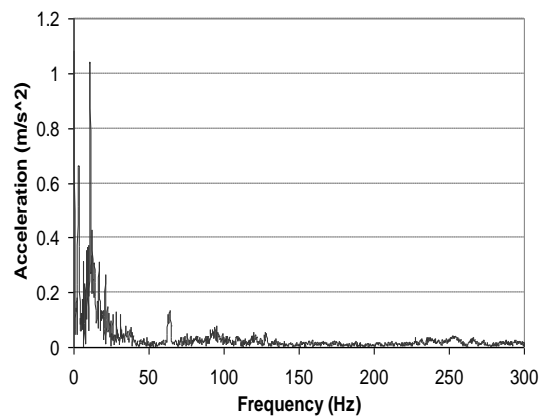
Bus Travelling at Moderate Speed

Figure 3-1: Typical low level ambient vibration sources.

Table 3-1 shows the summary of all measured vibration sources in terms of fundamental resonant frequencies, acceleration magnitude and calculated excited amplitudes. Generally, the results show that, the vibrations available around us are at low level with frequencies lower than 500 Hz and at an acceleration of around 1 m/s^2 (0.1 g).

Table 3-1: Summaries of Measured Vibration Sources.

Vibration Sources		Acceleration (m/s^2)	Frequency (Hz)	Amplitude (μm)
Blender (Casing)		21.8	275	7.32
Microwave (Casing)		0.68	100	1.72
Refrigerator (coil) (x-direction)		0.09	100	0.21
Kitchen ventilation fan	Speed I	0.2	200	0.13
	Speed II	1.1	38	19
Kitchen door when closed		0.42	433	0.06
Desktop PC	Normal operation	0.21	543	0.018
	Running CD ROM	0.26	154	0.28
Laptop	Normal operation	0.26	90.2	0.081
	Running CD ROM	0.66	43.2	0.896
Knock on wooden table		0.3 – 0.4	400 - 800	0.016 – 0.063
Lift [*]		0.078	7.3	37.1
Vending machine		0.12	100	0.29
Bus [**]	Stationary	0.37	111	0.75
	Travelling at moderate speed	1.04	10.8	226
Car[***] (1000 cc)	Engine	1.23	30.5	33.5
	Near to radiator	0.16	29.5	4.66
	Near to headlight	0.23	29.5	6.64
	Bonnet	0.18	29.5	5.18
	Dashboard	0.04	30	1.07
	Roof	0.26	29.5	7.54

Notes:
[*]*Lift just about to stop at higher level.*
[**]*The vibration was measured on the upper floor of a double decker bus.*
[***]*Stationary measurement.*

3.3 The Design Considerations

The design features and dimensions of a thick-film free-standing structure have to be based on the constraints imposed by thick-film technology. The minimum feature which can be printed is about 100 μm in length and depends on the mesh density of a screen-printing mask and also the properties of the thick-film pastes. The minimum thickness of the cantilever structure that can be produced is governed by the particle size of the pastes being used (e.g PZT, which is typically 0.8 – 2 μm). There is no definite upper limit of thickness for the PZT film that can be produced, but films with thickness greater than 200 μm would be inferior compared to bulk piezoelectric ceramics for the same thickness.

The free-standing cantilever structure is designed to be operated in an ambient vibration environment, where the first natural frequency mode of the cantilever has to be matched with the frequency of ambient vibration sources, which are generally lower than 500 Hz. In order to achieve low resonant frequency level, the dimensions of the cantilever can be adjusted and a proof mass can be added to fine-tune the natural frequency of the structure to suit the desired application. However, at low vibration frequency, the excited amplitude of the cantilever is inversely proportional to the resonant frequency squared. This will translate into a relatively big deflection and stress on the cantilever. A thick-film ceramic structure is relatively brittle and fragile; therefore the cantilever structure has to be designed to operate within the limit of stress that the structure can withstand.

The smaller the feature size of the energy harvester the better it is for miniature system integration. However, there is another issue that must be considered which is that the output electrical energy reduces as the size of the generator decreases. Therefore an optimum design is needed to trade-off between the electrical energy output and the compactness of the device.

After considering all the physical limitations of a ceramic free-standing structure, the next step is to optimise the performance of the energy harvester in order to produce useful electrical energy for powering microsystem. An open circuit output voltage is an important indicator to determine the practical usage of the device. For most of the

electronic applications, usually the AC voltages generated by a micro-generator are converted to usable DC voltage. In this conversion, diodes are normally used for simple full wave direct rectification, which need a minimum forward voltage of 300 mV for each diode to operate. The minimum voltage was able to be reduced to 150 mV by replacing the diodes with active switches in a four stages voltage multiplier circuit as studied by Saha *et al* [89]. A few tens of micro-watts of electrical power are needed for powering ultra low-power electronics, MEMS sensors and RF communications system. As reported by Torah *et al* [65], 58 μW of power is needed to power an accelerometer based micro-system.

3.4 Theoretical Analysis of Multilayer Structures

Generally, the base excited harmonic motion is modelled as a spring-mass-damper system with the equation of motion [90],

$$M\ddot{x} + b(\dot{x} - \dot{y}) + \kappa(x - y) = 0 \tag{3-1}$$

where y denotes the displacement of the base and x the displacement of the mass from its static equilibrium position. The vibration body is assumed to have a harmonic motion,

$$y(t) = Y \sin \omega t \tag{3-2}$$

By defining the relative displacement $z = x - y$. The magnitude of the displacement and acceleration can be derived as,

$$Z = \left\{ \frac{r^2}{\sqrt{\left[(1 - r^2)^2 + (2\zeta r)^2 \right]}} Y \right\} \tag{3-3}$$

$$\ddot{Z} = \left\{ \frac{1}{\sqrt{\left[(1 - r^2)^2 + (2\zeta r)^2 \right]}} \ddot{Y} \right\} \tag{3-4}$$

and the phase difference is,

$$\phi = \tan^{-1}\left(\frac{2\zeta r}{1 - r^2} \right) \tag{3-5}$$

where r and ζ is the frequency and damping ratio respectively as,

$$r = \frac{\omega}{\omega_n} \qquad (3\text{-}6)$$

$$\zeta = \frac{c}{2M\omega_n} \qquad (3\text{-}7)$$

3.4.1 Natural Frequency of a Unimorph Cantilever

From the Bernoulli-Euler equation derivation, a thin cantilever beam with one end clamped and the other end free, the natural transverse vibration can be written as,

$$f_i = \frac{v_i^2}{2\pi\sqrt{2}}\left(\frac{h}{l_b^2}\right)\sqrt{\frac{e_T}{\rho}} \qquad (3\text{-}8)$$

where v_i is a coefficient related to boundary conditions, h is the total thickness of the cantilever beam, l_b is the length of the cantilever beam, e_T is the resultant elastic modulus and ρ is the density of the structure. However, for a more detail analysis on each layer of the structure, the Bernoulli-Euler equation can be derived in a term related to bending modulus (Appendix B) as,

$$f_i = \frac{v_i^2}{2\pi d_b^2}\sqrt{\frac{D}{m_w}} \qquad (3\text{-}9)$$

where m_w is the mass per unit area. The coefficient, v_i of the first three modes are:

$$v_1 = 1.875104$$
$$v_2 = 4.694091$$
$$v_3 = 7.854757 \qquad (3\text{-}10)$$

The natural frequency of a multilayer cantilever consists of piezoelectric and electrode can be calculated accurately, if the thicknesses of the piezoelectric layer, h_p and electrode layer, h_e are known. Assume that the lengths of the piezoelectric and electrode are similar to the beam length, l_b and thickness of upper electrode and lower electrode are h_e. The mass per unit area of the cantilever for a unimorph as shown in Figure 3-2 is

$$m_w = \rho_p h_p + 2\rho_e h_e \tag{3-11}$$
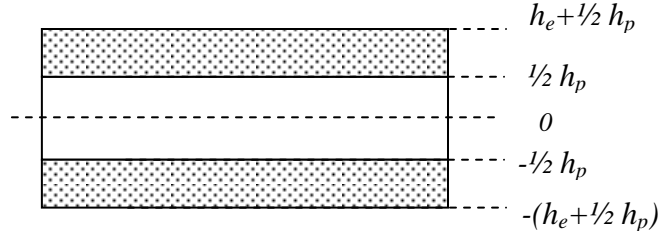
Figure 3-2: A cross-sectional view of a unimorph structure.

The bending modulus per unit width, *D* of the unimorph cantilever is given by [91],

$$D = \sum_{i=1}^{n} e_i \int (h - h_N)^2 dh \tag{3-12}$$

where e_i is the elastic modulus for the particular layer (e_e denotes elastic modulus for electrode layer and e_p denotes elastic modulus for piezoelectric layer), *h* is the thickness of a particular layer of the structure and h_N is the neutral axis from the reference point, "*0*". For simplification to estimate the natural frequency of a symmetrical unimorph cantilever, the neutral axis is assumed to be coincident with the centroid of the PZT layer. Therefore, the bending modulus per unit width for a unimorph structure as shown in Figure 3-2 is,

$$
\begin{aligned}
D_{unimorph} &= \int_{-(h_e + \frac{1}{2}h_p)}^{-\frac{1}{2}h_p} e_e(z)^2 dz + \int_{-\frac{1}{2}h_p}^{\frac{1}{2}h_p} e_p(z)^2 dz + \int_{\frac{1}{2}h_p}^{h_e + \frac{1}{2}h_p} e_e(z)^2 dz \\
&= e_p \left[\frac{z^3}{3} \right]_{-\frac{1}{2}h_p}^{\frac{1}{2}h_p} + 2e_e \left[\frac{z^3}{3} \right]_{\frac{1}{2}h_p}^{h_e + \frac{1}{2}h_p} \\
&= e_p \left\{ 2 \left(\frac{\frac{1}{8}h_p^3}{3} \right) \right\} + 2e_e \left\{ \frac{\left(\frac{1}{2}h_p + h_e \right)^3}{3} - \frac{\frac{1}{8}h_p^3}{3} \right\} \\
&= \frac{1}{12}e_p h_p^3 + \frac{2}{3}e_e \left(h_e^3 + \frac{3}{4}h_p^2 h_e + \frac{3}{2}h_p h_e^2 \right)
\end{aligned}
\tag{3-13}
$$

The first mode natural frequency of the unimorph structure can be calculated by substituting equations (3-11) and (3-13) into (3-9),

$$f_N = \frac{0.1615}{l_b^2} \sqrt{\frac{e_p h_p^3 + 8e_e\left(h_e^3 + \frac{3}{4}h_p^2 h_e + \frac{3}{2}h_p h_e^2\right)}{\rho_p h_p + 2\rho_e h_e}} \tag{3-14}$$

Lower resonant frequency is desirable for miniature integrated system. However, as size scales down, resonant frequency scales up, therefore additional proof masses are needed to be attached at the end of the cantilever to further reduce the resonant frequency of the cantilever. The natural frequency for a cantilever with proof mass, f_M can be obtained by comparing with resonant frequency for a cantilever without proof mass as,

$$f_M = f_N \sqrt{\frac{m_{eff}}{m_{eff} + M_m}} \tag{3-15}$$

where M_m is the additional proof mass and m_{eff} is the effective mass at the tip of the cantilever, which is given by [92],

$$m_{eff} = 0.236\rho_b w_b h_b l_b = 0.236 m_b \tag{3-16}$$

where ρ_b, w_b, h_b and l_b are density, width, total thickness and total length of the beam and m_b is the total beam mass,

$$m_b = w_b l_b \left\{\rho_e(h_{e1} + h_{e2}) + \rho_p h_p\right\} \tag{3-17}$$

The total mass at the tip of a cantilever when attached with a proof mass, M_m is therefore,

$$M_{eff} = M_m + m_{eff} = 0.236 w_b l_b \left\{\left(\rho(h+h) + \rho h\right) + \frac{M_m}{0.236 w_b l_b}\right\} \tag{3-18}$$

3.4.2 *Location of Neutral Axis of a Unimorph Cantilever*

(a)   (b)
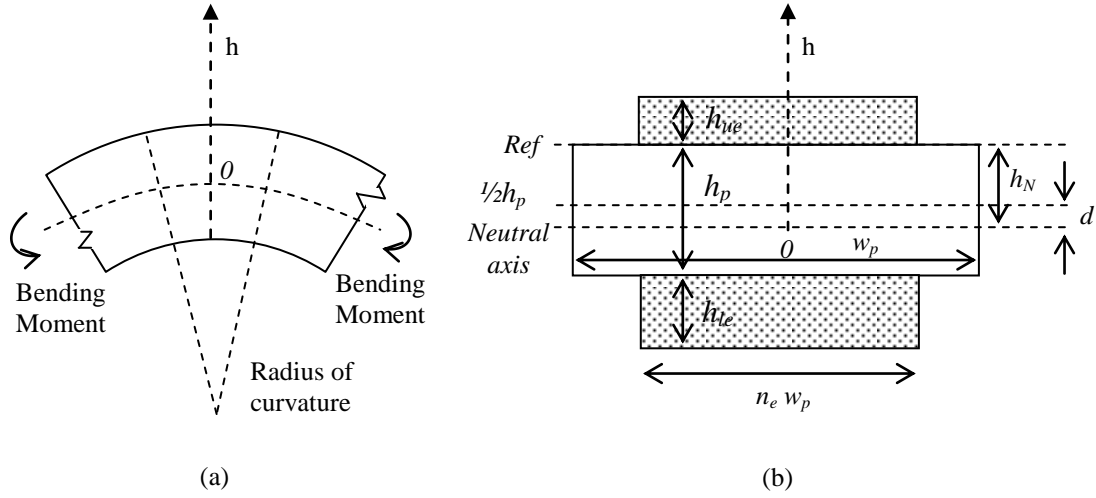
Figure 3-3: (a) Side view of Bending beam with bending moment and radius of curvature, (b)Transformed cross-section of a composite unimorph beam, with PZT layer width, w_p and transformed electrode width of $n_{ep}w_p$.

A bending beam is subjected to tension and compression proportional to the distance above and below the neutral axis respectively as shown in Figure 3-3(a). There is no resultant force acting on the cross section at the neutral axis and the stress, σ_x is the multiplication of elastic modulus, e, curvature, κ and the distance from the neutral axis, y. Since E and κ are nonzero, therefore,

$$\int_A \sigma \, dA = -\int_A e\kappa h \, dA = \int_A h \, dA = 0 \tag{3-19}$$

A composite beam can be analysed with the transformed-section method [93], where the cross section of a composite beam is transformed into an equivalent cross section of an imaginary beam that is composed of only one material, with elastic modular ratio,

$$n_{ep} = \frac{e_e}{e_p} \tag{3-20}$$

Therefore the distance of the neutral axis from a reference point as shown in Figure 3-3(b) can be derived as,

$$h_N = \frac{\sum_{i=1}^{n} h_i A_i}{\sum_{i=1}^{n} A_i} \tag{3-21}$$

where h_i is the distance from the reference point to the centre of each layer of the material and A_i is the area of the i-th layer of the structure. The distance from the centroid of PZT layer to the neutral axis is therefore,

$$d = \frac{1}{2}h_p - \frac{h_p^2 + n_{ep}\left(h_{e1}^2 - h_{e2}^2 + 2h_p h_{e1}\right)}{2\left\{h_p + n_{ep}\left(h_{e2} + h_{e1}\right)\right\}} \tag{3-22}$$

We can see from Equation (3-22) that, if the thickness of the upper electrode is similar to the lower electrode, $h_{e1} = h_{e2}$, the neutral axis is located at the centre of the PZT layer, therefore, $d = 0$. This will give a zero resultant stress, which will be discussed in the following section.

3.4.3 Maximum Allowed Stress
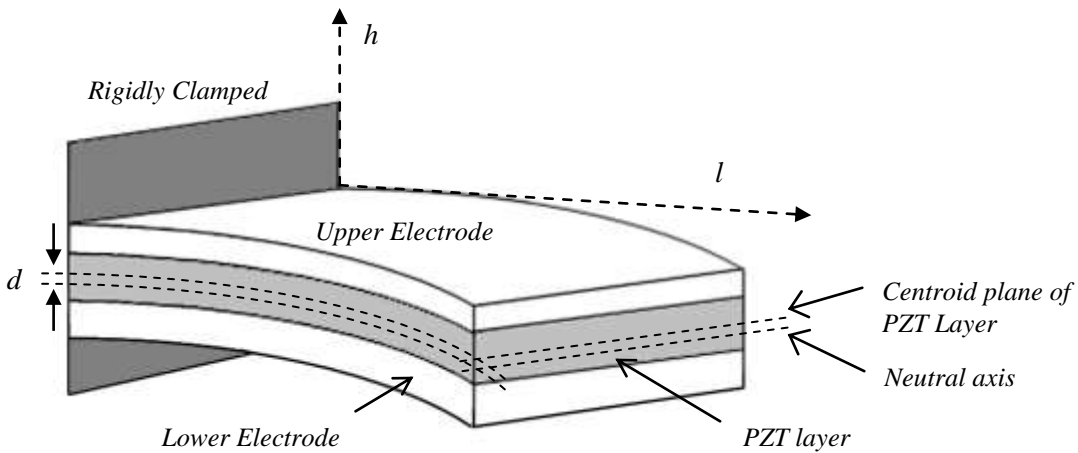
Figure 3-4: Bending beam of unimorph structure.

The resultant stress on the clamped area of a beam for each layer of a unimorph is proportional to the input moment divided by the inertia across the length of the beam as,

$$\sigma_l = \frac{1}{l_b} \int_0^{l_b} \frac{M(l)d}{I_{unimorph}} dl \tag{3-23}$$

To find the exact value of stress of each layer of the material, the moment inertia of the beam, I_b has to be defined. The transformed cross-section of a unimorph is redrawn in Figure 3-5 with parallel-axis passing through the centroid of the beam.
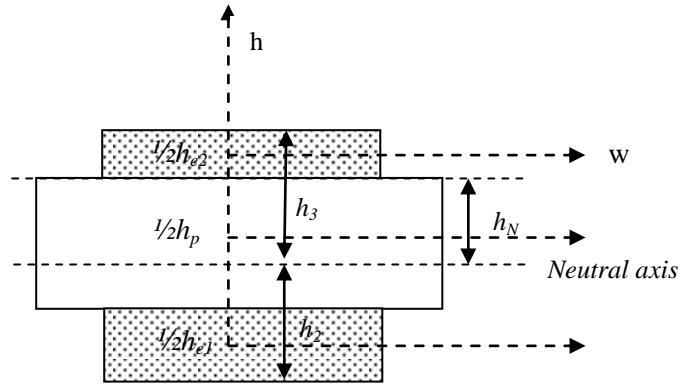
Figure 3-5: Parallel-axis for a transformed cross-section of a unimorph.

From the parallel-axis theorem for the moment of inertia [93]

$$I = \int_{-\frac{1}{2}h}^{\frac{1}{2}h} (h+d)^2 dA = \int_{-\frac{1}{2}h}^{\frac{1}{2}h} h^2 \, dA + 2d \int_{-\frac{1}{2}h}^{\frac{1}{2}h} h \, dA + d^2 \int_{-\frac{1}{2}h}^{\frac{1}{2}h} dA \tag{3-24}$$

where d is the distance from the centroid of the layer to the neutral axis of the structure and A is the cross-section area of the layer. The integration of the second term at the right hand side of equation (3-24) is zero, therefore, the total moment of inertia for a unimorph as shown in Figure 3-5 is,

$$I_{unimorph} = \left\{ \frac{1}{12} wh_p^3 + wh_p \left(h_N - \frac{1}{2} h_p \right)^2 \right\} + n_{ep} w \left\{ \frac{1}{12} \left(h_{e1}^3 + h_{e2}^3 \right) + he_1 \left(h_2 - \frac{1}{2} h_{e1} \right)^2 + h_{e2} \left(h_3 - \frac{1}{2} h_{e2} \right)^2 \right\}$$

$$\tag{3-25}$$

where n_{ep} is the elastic modular ratio as defined in equation (3-20). By substituting $h_2 = h_p + h_{e1} - h_N$ and $h_3 = h_N + h_{e2}$ in equation (3-25), we get

$$I_{unimorph} = w\left(\frac{1}{3}h_p^3 + h_p h_N^2 - h_p^2 h_N\right) +$$

$$wn_{ep}\left(\frac{1}{3}\left(h_{e1}^3 + h_{e2}^3\right) + h_N^2\left(h_{e1} + h_{e2}\right) + h_N\left(h_{e2}^2 - h_{e1}^2 - 2h_{e1}h_p\right) + h_{e1}h_p\left(h_p + h_{e1}\right)\right)$$

$$(3\text{-}26)$$

If the neutral axis is passing through the PZT centroid, $h_N = \frac{1}{2}h_p$ and the upper electrode and lower electrode are made of same material and with same thickness, $h_{e1} = h_{e2} = h_e$, equation (3-26) can be simplified as

$$I_{unimorph} = w\left\{\frac{1}{12}h_p^3 + n_{ep}\left(\frac{2}{3}h_e^3 + \frac{1}{2}h_p^2 h_e + h_e^2 h_p\right)\right\} \qquad (3\text{-}27)$$

Comparing equation (3-27) to the bending modulus per unit width in equation (3-13), we get

$$I_{unimorph} = \frac{Dw}{e_p} \qquad (3\text{-}28)$$

The input moment as a function of length from the clamped area of a beam, $M(x)$ is

$$M(x) = M_{eff}\left(\ddot{y} + \ddot{z}\right)\left(l_b - l\right) \qquad (3\text{-}29)$$

By substituting equation (3-4), (3-18) and (3-28) into (3-23), we get

$$\sigma_l = \frac{0.118 e_p l_b^2 d\left\{\left\{\rho_e\left(h_{e1} + h_{e2}\right) + \rho_p h_p\right\} + \dfrac{M_{pm}}{0.236 w_b l_b}\right\}\ddot{y}}{D_{unimorph}}\left\{1 + \frac{1}{\sqrt{\left[\left(1 - r^2\right)^2 + \left(2\zeta r\right)^2\right]}}\right\}$$

$$(3\text{-}30)$$

We can see from equation (3-30) that the resultant stress is proportional to the distance from the neutral axis, and therefore the thicknesses of the upper and lower electrodes are very critical in determining the resultant stress of the beam. The equation also shows that the width of the cantilever does not affect the resultant stress, though there is a practical limit to the size of the width. A beam with a small ratio of width to its thickness when subjected to shear force will be twisted and become unstable and is therefore not suitable to be operated as a resonant device.

Maximum stresses are produced on the upper and lower electrodes compared to the PZT layer when the beam is vibrating. Thus the elastic modulus of the electrodes has to be high in order to support the brittle ceramic layer at the centre of the structure.

3.4.4 Maximum Allowed Deflection

Thick-film free-standing structures are realised by elevating part of the film from the substrate, therefore limiting the deflection of the cantilever to a height constrained by the fabrication process. The maximum deflection of the cantilever has to be known so that the maximum dimension of the cantilever can be designed to suit the fabrication process.

The deflection, z of a piezoelectric cantilever beam with no connection between its electrodes can be described by differential equation of the deflection curve as [93],

$$\frac{d^2 z}{dl^2} = \frac{M(l)}{e_T I_{unimorph}} \tag{3-31}$$

where e_T is the resultant elastic modulus of PZT and electrode layers. The total stress in the composite structure is the sum of the stresses in the PZT layer and the electrode layer multiplied by their relative cross-sectional areas. Hence the resultant elastic modulus can be derived as,

$$e_T = (1 - A_p)e_e + A_p e_p \tag{3-32}$$

where A_p is the area ratio of the PZT layer to the total cross-sectional area of the composite beam. Solving equation (3-31) for a beam attached with proof mass, we get,

$$z = \frac{M_{eff}(\ddot{y} + \ddot{z})l_b^3}{3e_T I_{unimorph}} \tag{3-33}$$

Substituting equation (3-5), (3-18), (3-28) and (3-32) into (3-33), we get,

$$z = \frac{0.236l_b^4 \left\{ \left(\rho_e(h_{e1} + h_{e2}) + \rho_p h_p \right) + \dfrac{M}{0.236w_b l_b} \right\} \ddot{y}}{3 \left\{ 1 + (n_{ep} - 1) \left(\dfrac{h_p}{h_{e1} + h_{e2} + h_p} \right) \right\} D_{unimorph}} \left\{ 1 + \frac{1}{\sqrt{(1 - r^2)^2 + (2\zeta r)^2}} \right\} \tag{3-34}$$

3.4.5 Estimated Output Voltage

The output voltage for a piezoelectric cantilever can be estimated with equation (2-15) deduced from the Roundy's dynamic model [12] (Appendix C). Although the model is oversimplified, it does give a reasonably good approximation of the amount of voltage generated.

At resonant frequency, equation (2-15) can be simplified as,

$$V = \frac{3}{4} \frac{je_T d_{31} h_p d a_{in}}{\varepsilon \, l_b^2 \left\{ \varsigma_T \omega_r^2 - j \left[\dfrac{\omega_r^2 k_{31}^2}{2} + \dfrac{\varsigma_T \omega_r}{RC_p} \right] \right\}} \tag{3-35}$$

where e_T is the resultant elastic modulus as defined in equation (3-32) and d is the distance from the centroid of the layer of PZT to the neutral axis of the structure as defined in equation (3-22).

3.5 Analysis and Discussion on Calculation Results

A cantilever as shown in Figure 3-6 with standard dimensions as summarised in Table 3-2 is used to verify the model as derived in section 3.4. The standard parameters for the calculation are also incorporated into the same table.
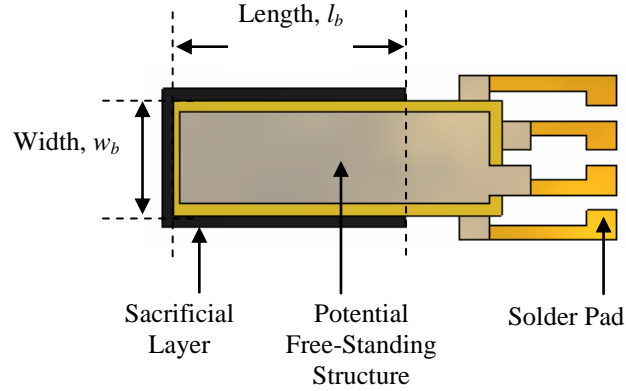
Figure 3-6: Diagram of a multimorph cantilever structure. The theoretical model was based on a unimorph sandwiched structure of PZT, lower and upper electrodes.

Table 3-2: Standard dimensions of a cantilever used to verify theoretical model.

Dimension		Unit	Value
Length	l_b	mm	18
Width	w_b	mm	9
PZT thickness	h_p	μm	80
Lower electrode thickness	h_{e1}	μm	15
Upper electrode thickness	h_{e2}	μm	20
PZT density	ρ_p	kg/m^3	7400
Electrode density	ρ_e	kg/m^3	10900
Base excitation	A_{in}	m/s^2	10
PZT elasticity	e_e	GPa	116
Electrode elasticity	e_p	GPa	60
Piezoelectric charge constant (magnitude)	d_{31}	pC/N[1]	50
Dielectric permittivity	e_{33}^T	nF/m[1]	4

The calculation takes into account of the effect of cant

56

ilever length on the mechanical damping, coupling factor and matching resistive load. These parameters were measured experimentally in Chapter 6 and were used to fit in the model.

Mechanical damping involves complex damping loss factors (which will be discussed in Chapter 6), but for a good approximation, the mechanical damping ratio is proportional to the length of the cantilever as shown in Figure 3-7 (a). Typically a proof mass is attached at the end of a cantilever in order to reduce the resonant frequency and induce greater stress on the structure, which increases the mechanical damping of the structure. Figure 3-7 (b) shows the experimental results of the mechanical damping ratio for a standard cantilever with the dimensions as shown in Table 3-2. It seems that changing the proof mass has a greater effect on damping ratio than changing the beam length. For example, doubling the proof mass increases the damping ratio by nearly an order of magnitude more than the effect that doubling the beam length has on damping ratio.

(a)   (b)
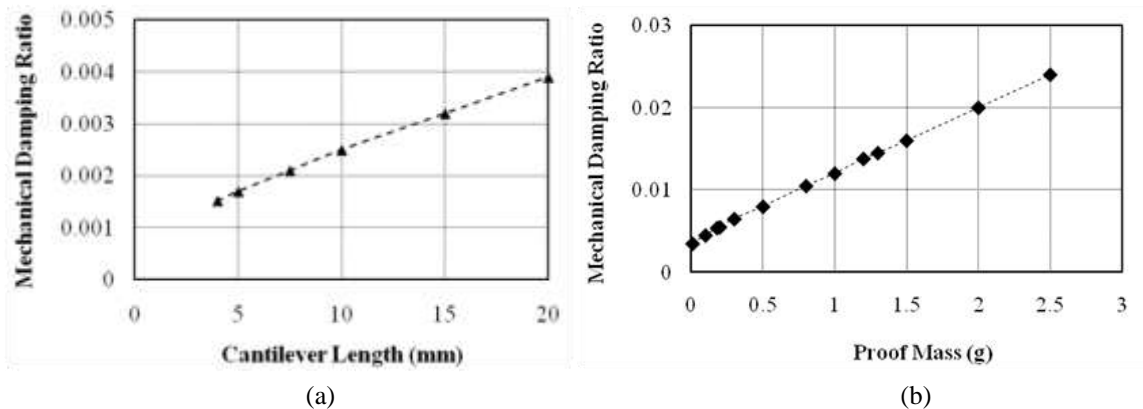
Figure 3-7: Experimental data of mechanical damping ratio as a function of cantilever length (a) and proof mass (b). The dotted lines are a fitting line to illustrate that the mechanical damping ratio is proportional to the cantilever and proof mass.

As the mechanical damping ratio increases, the electrical damping will increase to match the mechanical damping. Figure 3-8 (a) shows the experimental results of optimum resistive load, which is proportional to the length of the cantilever and shows a similar effect on the mechanical damping ratio to that of changing the length. The presence of proof mass, however, does not produce a linear effect on optimum resistive load. Figure 3-8 (b) shows that the optimum resistive load level off at about 240 kΩ.

Figure 3-9 shows the dependence of the structural coupling factor of the piezoelectric cantilever on the length and proof mass. The detail of the discussion will be presented in Chapter 6.

(a)   (b)
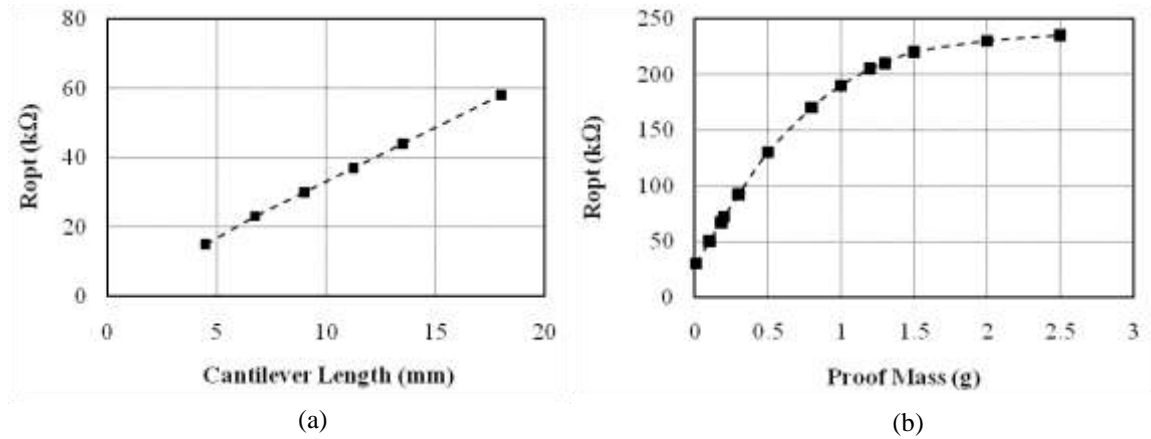
Figure 3-8: Experiment data of optimum resistive load as a function of cantilever length (a) and proof mass (b). The dotted lines illustrate the change of optimum resistive load at resonant frequency.

(a)   (b)
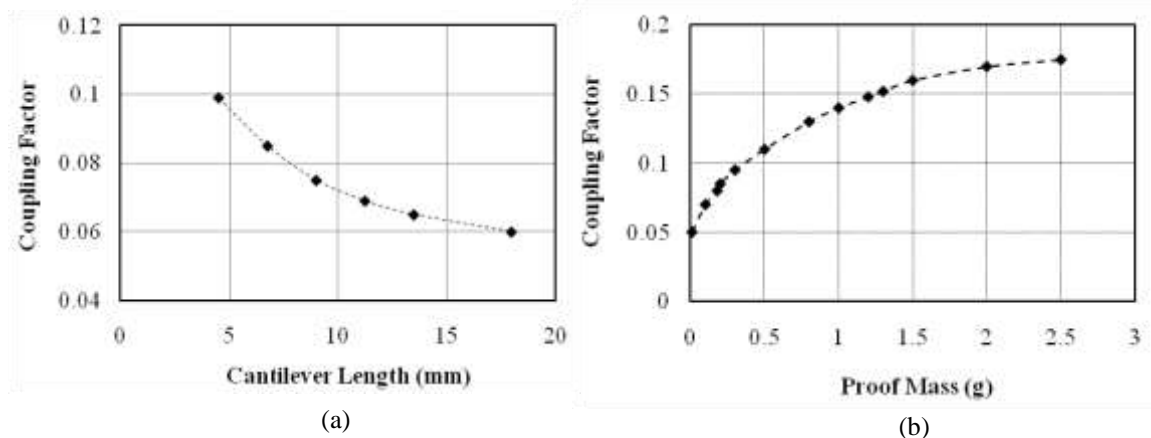
Figure 3-9: Experimental data of structural coupling factor as a function of cantilever length (a) and proof mass (b) at resonant frequencies. The dotted lines illustrate the curve fittings of the experimental data.

The cantilever designs were based on the maximum allowed stress and deflection of the structure. From the experiment results in Chapter 7, the ceramic cantilever can withstand up to a maximum stress of about 115 MPa. The deflection is limited by the gap between the free-standing structure and substrate, which is 2 mm as expected from fabrication outcome.

Figure 3-10 (a) and (b) shows the dependence of maximum stress and deflection respectively on the cantilever length. Two conditions of mechanical damping ratio are compared in the calculation. One is calculated with experimental damping according to Figure 3-7 (a) and the other one is calculated with fixed value of damping ratio of 0.0037. If 115 MPa is taken as the upper limit of the maximum stress allowed, theoretically the cantilever can have a length up to 850 mm before it breaks, with the assumption that the damping ratio increases proportionally with length. For a damping ratio fixed at 0.003, however, the maximum allowed length of the cantilever is 148 mm.

In the case of limitation on gap height at 2 mm, the allowed length of the cantilever is about 25 mm, for the assumption case, however a shorter cantilever is allowed at 23 mm if the damping ratio is fixed at 0.0037. These calculation results show that, a slight change of mechanical damping ratio can lead to a large change of stress and displacement of a free-standing structure, therefore an accurate experimental damping ratio value is important in determining the length of the structure to meet the operation restrictions. From the assumption that the damping ratio increases proportionally with length, the maximum allowed cantilever length is 25 mm for a base excitation at 10 m/s^2.

(a)   (b)
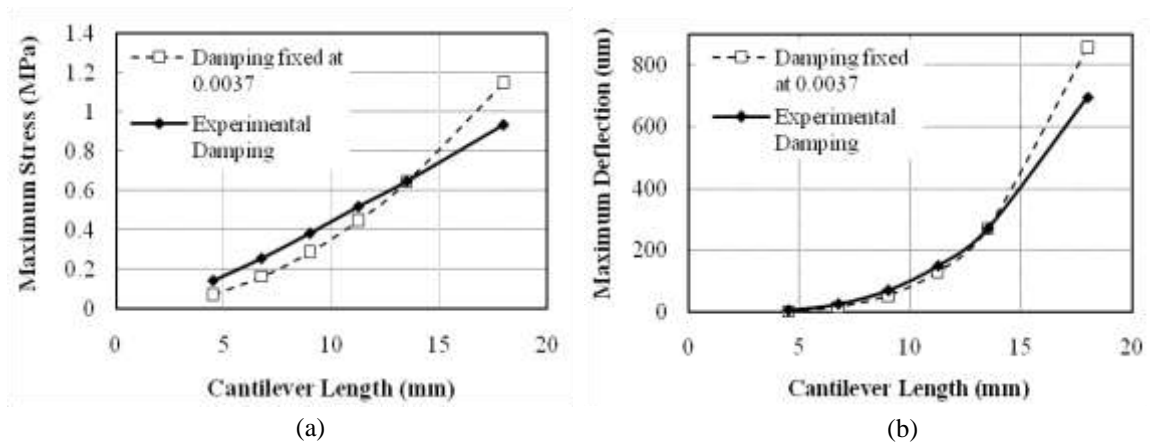
Figure 3-10: Theoretical calculation of cantilever length variation effect on maximum stress (a) and maximum deflection for two cases (b); one with damping fixed at 0.0037 and the other one is the value measured from experiment as shown in Figure 3-7 (a).

Figure 3-11 shows that at a constant resistive load (20 kΩ), the output power is proportional to the cantilever length for a constant damping ratio at 0.0037. However, in reality, damping increases with cantilever length resulting in vibration amplitude losses in the process, hence reducing the electrical output power.

It is desirable to keep the mechanical damping ratio as low as possible to increase the electrical energy output. However, the mechanical damping is an inherent property of the cantilever structure which is difficult to control. One of the ways to increase the electrical energy is by matching the cantilever of different lengths with the optimum resistive load accordingly. The calculated results of the experimental damping case when driving with constant resistive load at 20 kΩ is re-plotted in Figure 3-12 to compare with the outputs when the devices are driving at the optimum resistive load according to experiment results as shown in Figure 3-8 (a). Figure 3-12 shows that the output power generated when driving with optimum resistive load (58 kΩ) increases by a factor of 2 compared to the same device when driving with constant resistive load at 20 kΩ.
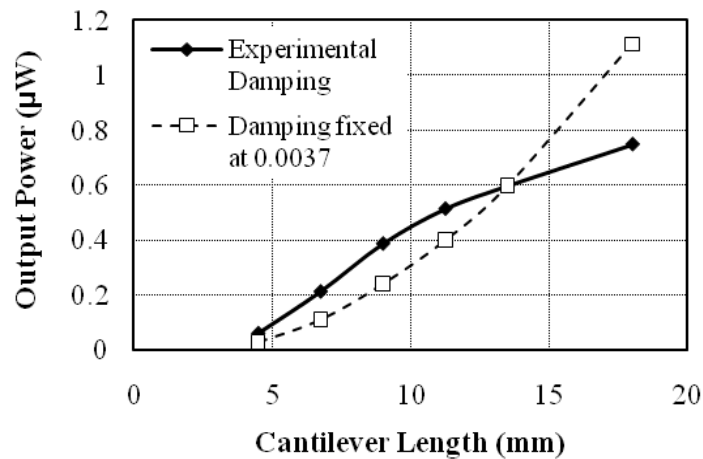
Figure 3-11: Theoretical calculation of the cantilever length variation effect on output power at a constant resistive load of 20 kΩ.
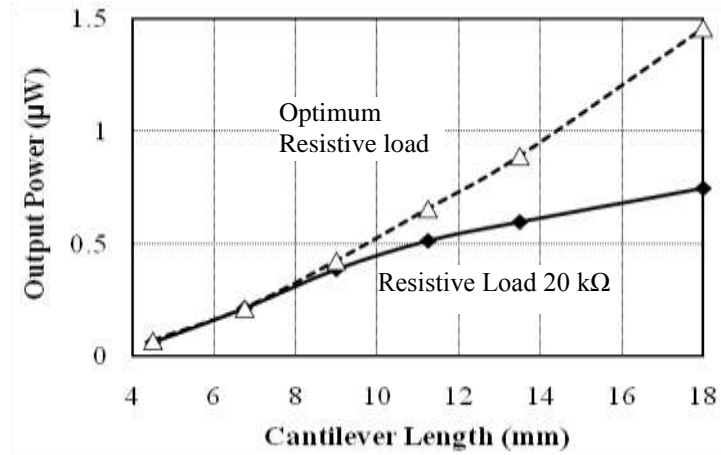
Figure 3-12: Theoretical calculation of the output power as a function of cantilever length when driving resistive loads; at optimum resistive load and constant resistive load at 20 kΩ.

According to equation (3-30), the resultant stress on the PZT is proportional to the distance from the neutral axis of the structure to the centroid of the material, *d*. When both the upper and lower electrodes have the same thickness, the centroid and the neutral axis coincide and zero resultant stress is produced, hence producing zero electrical output. Therefore, in order to generate electrical output, the thicknesses of the lower and upper electrodes have to be adjusted.

Two schemes of adjustments were studied; increasing the lower electrode thickness, h_{e1} while maintaining the upper electrode thickness, h_{e2} at 15 µm (condition-A). The other scheme is to vary the thickness of both electrodes but maintaining their total thickness at 36µm (condition-B). Figure 3-13 (a) shows that condition-B produces more stress than condition-A at the same excitation level. The deflection of the cantilever decreases as condition-A was applied, as shown in Figure 3-13 (b). This is because the stiffness of the structure is increased when the total thickness of the structure is increased hence higher excitation level is needed to maintain the deflection of the cantilever. In the case shown in Figure 3-13 (b), the excitation level, however is maintained at 10 m/s^2, therefore the maximum deflection is decreased when the thickness of lower electrode is increased. Whilst condition-B, which has constant total electrode thickness displayed a slight increase in deflection as the lower electrode thickness increases.

(a)   (b)
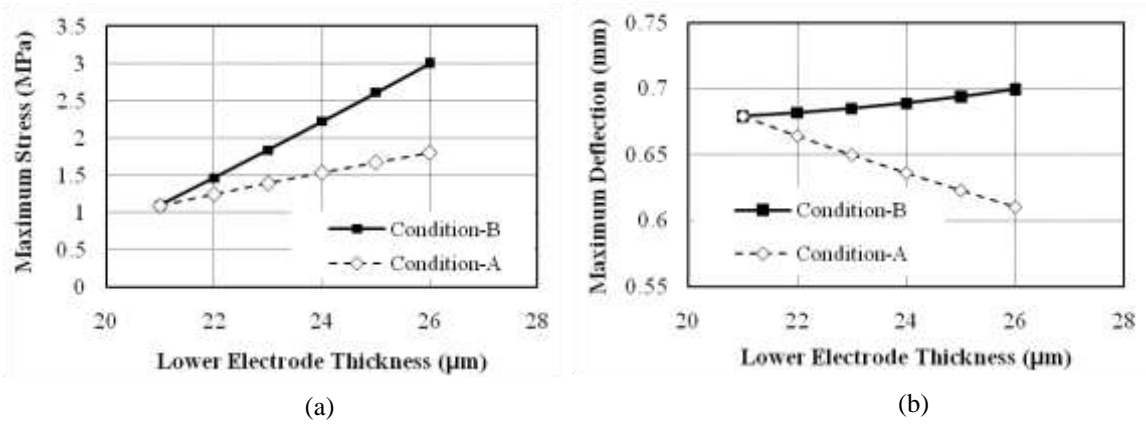
Figure 3-13: Theoretical calculation of the lower electrode thickness variation effect on maximum stress (a) and maximum deflection (b) on two conditions; one with constant upper electrode h_{e2} at 15 µm (condition-A) and another one with constant total thickness at 116 µm (condition-B).

According to equation (3-35), the output voltage increases proportionally to the distance, d, therefore the performance of output voltage is in a similar pattern to the one displayed by the production of maximum stress. As can be seen from Figure 3-14 (a), the changing rate of output voltage is greater for condition-B compared to condition-A, which becomes significant at higher electrode thickness differences between upper and lower electrodes. Figure 3-14 (b) shows an improvement of output power for condition-B by a factor of 7 when an adjustment was made to the thickness of the lower electrode from 21 µm to 26 µm while maintaining the total thickness of the electrodes at 36 µm.

At a constant base excitation input, the stress on the PZT layer decreases as the piezoelectric material thickness increases, as shown in Figure 3-15. This is because the distance, d, does not change with increased thickness of PZT but increases the stiffness of the cantilever; therefore greater base excitation input is needed to maintain the stress level on the structure.

(a)   (b)
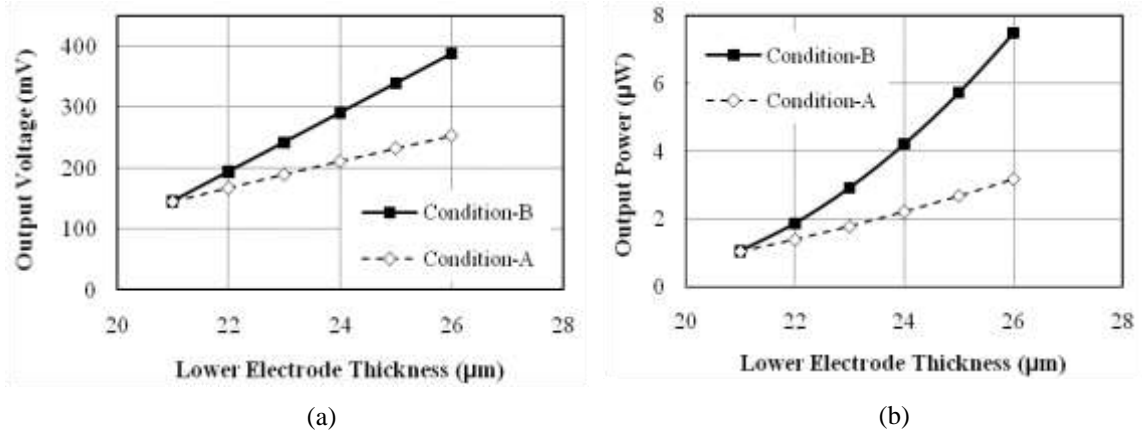
Figure 3-14: Theoretical calculation of the condition-A (constant upper electrode) and –B (constant total thickness) effect on output voltage (a) and output power (b).
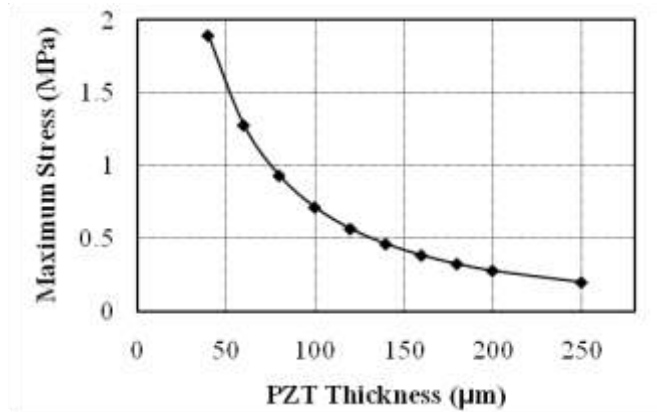
Figure 3-15: Theoretical calculation of the PZT thickness variation effect on maximum stress induced on the structure at a constant base excitation.

The output power does not increase significantly with increased PZT thickness. Although the output voltage is proportional to the PZT thickness according to equation (3-35), however, the stiffness of the structure increases with the thickness of the PZT. As the stiffness increases, the natural frequency of the structure increases, which reduces the amplitude of the cantilever deflection. This will reduce the stress induced on the structure, hence impedes the performance on the electrical output. Figure 3-16 shows that the output power level reach limiting values of approximately 1.05 µW.
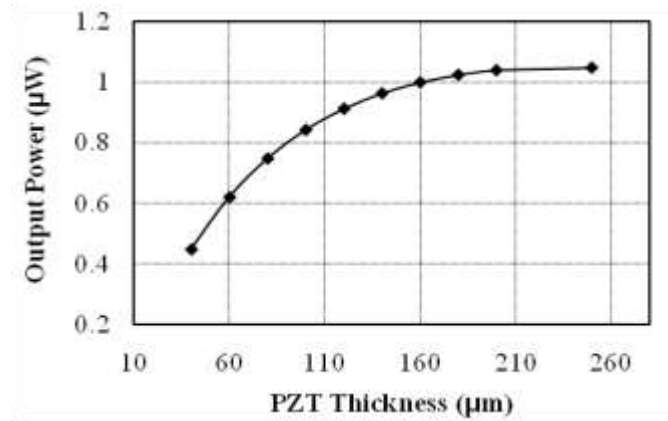
Figure 3-16: Theoretical calculation of the PZT thickness variation effect on output power.

Another way to increase the stress, deflection, output voltage and output power is by increasing the base excitation level. The maximum deflection of the cantilever tip is proportional to the base excitation input as shown in Figure 3-17. At a constant damping ratio of 0.0037, a base excitation of 30 m/s^2 will induce a cantilever acceleration level to 5010 m/s^2 according to equation (3-4). At this level of acceleration, a cantilever of length 18 mm is calculated to produce a maximum stress of 2.8 MPa and a deflection of 2 mm, which reach its maximum allowed deflection of the design.
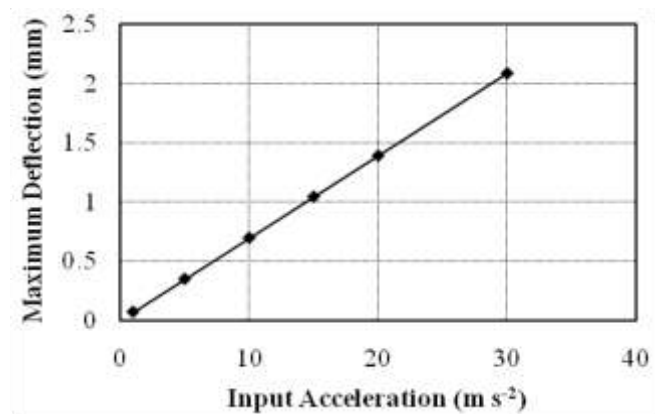
Figure 3-17: Theoretical calculation of the base input acceleration effect on maximum deflection for a cantilever with length 18 mm.

The output voltage increases linearly with base input acceleration. An increment of acceleration level from 10 m/s^2 to 30 m/s^2 will produce output voltages from 122 mV to 367 mV, as shown in Figure 3-18 (a). This gives an increment with a factor of 9.5 for the output power from 0.7 μW to 6.7 μW, as shown in Figure 3-18 (b).

(a)   (b)
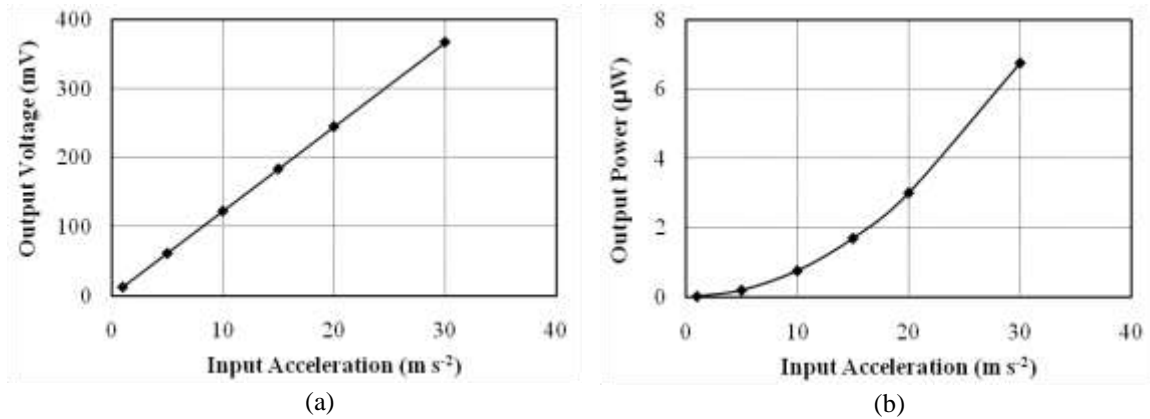
Figure 3-18: Theoretical calculation of the base input acceleration effect on output voltage (a) and output power (b) for a cantilever with length 18 mm at resonance.

If the mechanical damping ratio is assumed to be constant at 0.0037 regardless of the damping caused by mass, the maximum stress and deflection is increased proportionally with the proof mass. In reality, however, the mechanical damping ratio increases with proof mass and therefore impede the development of stress and deflection on the structure. The maximum stress and deflection were found to level off at about 10 MPa and 7.3 mm respectively, when a proof mass of greater than 1.5 g was attached to the tip of the cantilever.

Figure 3-19 shows the maximum deflection of the cantilever having a length of 18 mm when excited to an acceleration of 10 m/s^2. The dotted line shows that the maximum deflection is proportional to the proof mass when calculated at a fixed damping at 0.0037, whilst the solid line shows the maximum deflection base upon experimental damping ratio according to Figure 3-7 (b). At an acceleration level of 10 m/s^2, the allowed proof mass for a cantilever of length 18 mm is 0.1 g to meet the limitation of a gap height of 2 mm. The proof mass is allowed to increase to 0.5 g for a cantilever with shorter length at 13.5 mm for the same acceleration level.
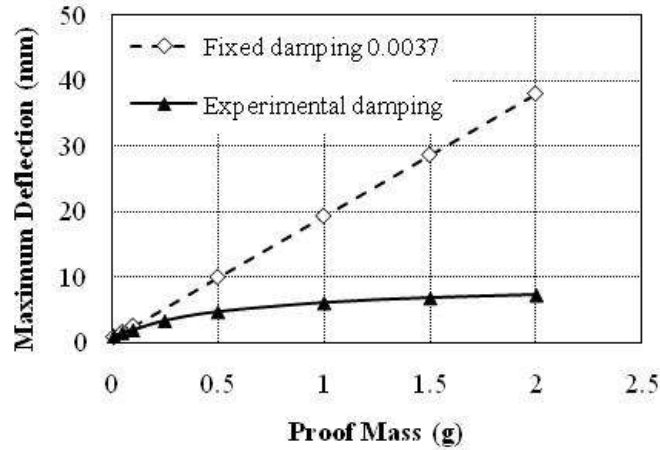
Figure 3-19: Theoretical calculation of the maximum deflection as a function of proof mass at an acceleration of 10 m/s^2 for two different cases; the dotted line is calculated with a fixed damping ratio at 0.0037 and the solid line is calculated base upon the experimental damping value according to Figure 3-7 (b).

The output voltage of the device increases rapidly if the mechanical damping ratio and the coupling factor are maintained at 0.0037 and 0.06 respectively as shown in Figure 3-20 (a). If the experimental value of damping ratio, optimum resistive load and coupling factor from Figure 3-7 (b) Figure 3-8 (b) and Figure 3-9 (b) are taken into account, the output voltage shows a saturation at 1.8 V when a proof mass greater than 1 g is attached at the end of the free-standing structure. The output power is increased to about 14.5 µW when a proof mass of 1 g is attached at the tip of the structure, however beyond this mass, the output power shows a slight decrease to 13.6 µW when a proof mass of 2 g is attached.

The output voltage and power of the device is dependent on the resistive load connected to the piezoelectric terminal. The estimated open circuit voltage is 560 mV for a cantilever with damping ratio of 0.0037 when excited to its resonant frequency at an acceleration level of 10 m/s^2, as shown in Figure 3-21 (a). An optimum output power of 1.5 µW is generated when it is driving a resistive load of 80 kΩ, as shown in Figure 3-21 (b). A few scenarios with different mechanical damping ratios for the same device were calculated to estimate the electrical output. These show that the lower the damping ratio the better the performance of the energy harvester. However, the mechanical damping is an inherent property of the cantilever structure which is very difficult to control. Therefore in order to improve the electrical output of the free-standing

structure, other feasible methods besides what have been discussed in this chapter need to be considered. One such method is the fabrication of a multimorph cantilever structure, which will be discussed in detail in Chapter 7.

(a)   (b)
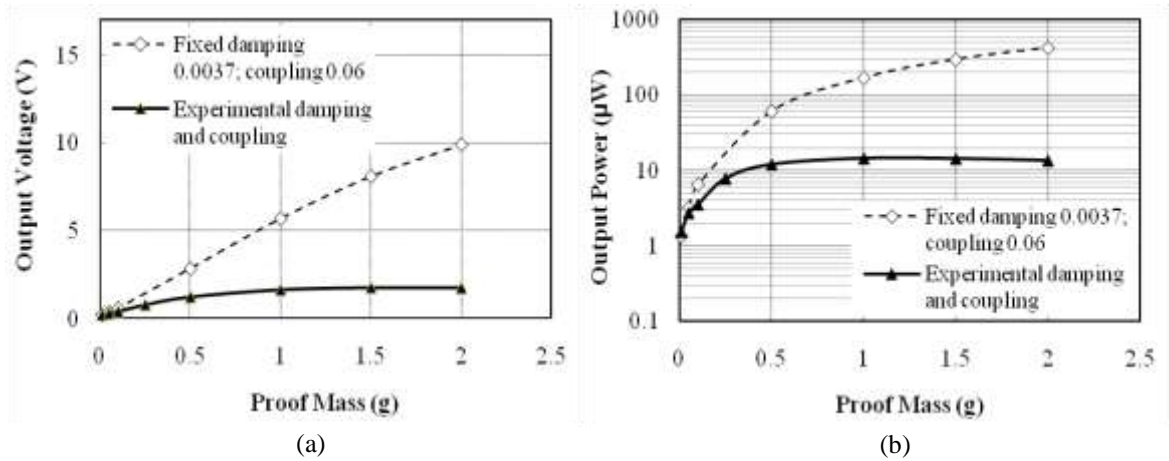
Figure 3-20: Theoretical calculation of the proof mass variation effect on output voltage (a) and output power for two scenarios (b): (1) Fixed values of damping at 0.0037 and coupling factor 0.06 and (2) Experimental values of damping and coupling factor.

(a)   (b)
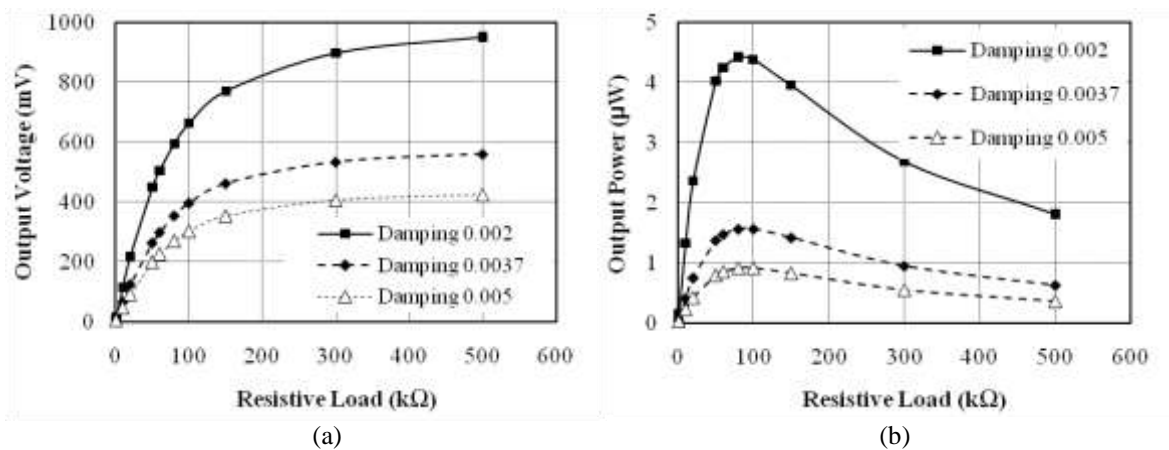
Figure 3-21: Theoretical calculation of the electrical output voltage (a) and output power (b) as a function of electrical resistive load for three different damping factors.

3.6 Computational Analysis

In reality, the beam of a thick-film free-standing cantilever is not perfectly straight and rigidly clamped at one end, but rather a structure which is standing or rising from the base of a substrate, forming an *S*-beam structure, as shown in Figure 3-22. This structure is a resultant of different thermal expansion coefficient between the PZT ceramic and the electrode materials, which are fabricated in a high temperature environment. Therefore, such a cantilever has a more complex structure and geometry and the use of finite element modelling (FEM) in order to analyse these structures is necessary. Accordingly, a series of finite element simulations was carried out by using harmonic response analysis with a commercial package ANSYS (www.ansys.com).

ANSYS is used to estimate the frequency response, stress and deflection produced when the cantilever structure is driven with base excitation under harmonic vibration in a direction normal to the base. The structure is purely mechanical and the piezoelectric coupling effect is not taken into account in the simulation. This situation is similar to an open circuit piezoelectric cantilever, and the main concern in this simulation is to investigate the mechanical properties of the structure related to the dimensions of the structure.

For simplification, a unimorph cantilever structure consisting of a sandwiched layer of upper electrode-PZT-lower electrode is designed with different dimensions and excited with different level of acceleration to investigate its performance.
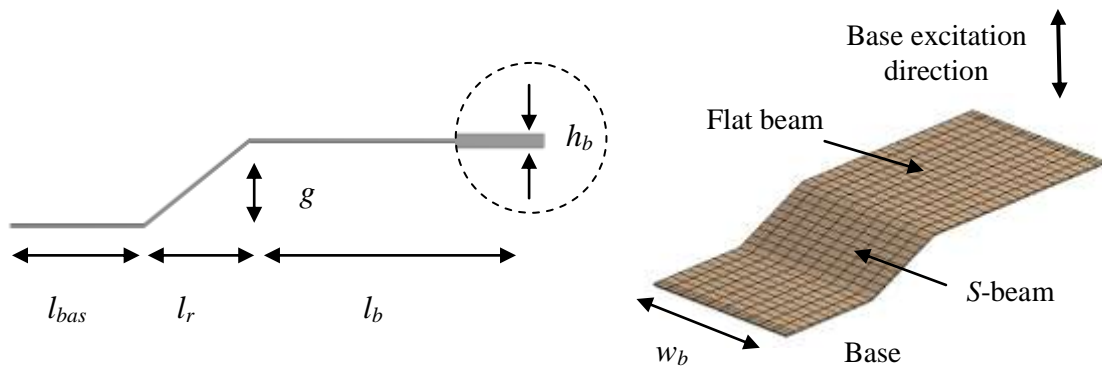
Figure 3-22: A schematic diagram of a unimorph cantilever (a) and a cantilever with mesh on used for simulation in ANSYS (b).

In order to compare with the analytical model, the actual beam length of an *S*-beam in the simulation is the sum of the rising area of the beam and the length of flat free-standing beam,

$$L = l_b + \sqrt{l_r^2 + g^2} \tag{3-36}$$

where *L* is the actual length of the *S*-beam, equivalent to the length of the analytical model, l_b is the length of the flat beam, l_r is the length of the rising part of the free-standing structure from the base connected to the straight beam and *g* is the gap height of the free-standing structure from the substrate.

The simulation parameters include the length, width, thickness, base acceleration and the proof mass, while the constants used in the simulation are the elastic modulus, poisson ratio and density of the material. Firstly, standard simulation parameters as in Table 3-3 are used followed by varying one parameter at a time starting with length while fixing the other parameters to calculate the resonant frequency, stress, deflection and cantilever tip acceleration.

The simulation results from a simple PZT cantilever structure will be compared with a sandwich layer of electrode-PZT-electrode. The purpose of the simulation is to investigate the effect of the geometry of a cantilever to the resonant frequency of the structure and with a focus on the PZT layer. The maximum stress, deflection and cantilever tip acceleration from the simulation is a useful guide for designing a workable free-standing structure.
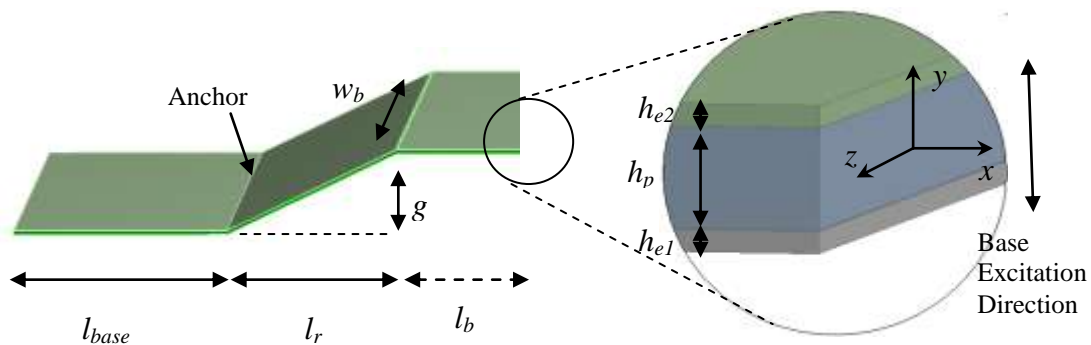
Figure 3-23: Diagram of multilayer cantilever structure.

Table 3-3: Initial parameter for ANSYS simulation.

	Parameter	Unit	Value
l_{base}	Base length	mm	5
l_r	Projection length for rising structure	mm	4
l_b	Free-standing length	mm	10
g	Free-standing height	mm	2
h_b	Beam thickness	μm	100
w_b	Beam width	mm	9
A_{in}	Acceleration amplitude	m/s^2	10
E_p	PZT Young's Modulus [31]	GPa	60
ρ_p	PZT Density [31]	kg/m^3	7400
β_p	PZT Poisson ratio [31]	dimensionless	0.35
E_e	AgPd Young's Modulus [94]	GPa	116
ρ_e	AgPd Density [94]	kg/m^3	10900
β_e	AgPd Poisson ratio [95]	dimensionless	0.38
ρ_{pm}	Density of Tungsten Proof Mass	kg/m^3	19250

The multilayer cantilever is designed with a sandwich layer of electrode-PZT-electrode as shown in Figure 3-23. The thickness of upper, h_{e2} and lower, h_{e1} electrodes are formed from similar material (AgPd) with a thickness of 15 μm for both layers. The thickness of the centre PZT layer, h_p is 70 μm thick, which make up a total thickness of 100 μm.

The cantilever structure is designed in such a way to suit the capability of thick-film fabrication technology and actual devices will be fabricated based on this model. The simulation results will then be compared with calculation results based on the model developed in a previous section and finally will be compared with experimental results in Chapter 6.

3.6.1 Modal Analysis

Although the free-standing structure is designed to be operated at low level vibration frequency, it is worth investigating the characteristics of the structure in higher order vibrational modes with regard to operational durability and optimisation. Four different conditions of cantilever were investigated; cantilever with length greater than width, cantilever with width greater than length, cantilever attached with proof mass of full width-wise coverage and cantilever with proof mass distribution focused on the centre of the tip.

Four modes of vibrations; fundamental, 2nd, 3rd and 4th, were generated from the ANSYS simulation. The results of the simulation are presented in the form of stress distributions, as shown in Figure 3-24 and frequency response plots, as shown in Figure 3-25. A cantilever with dimensions as shown in Table 3-3, resonated at a fundamental frequency of 192.3 Hz. The cantilever beam is purely moving in the transverse (up an down) direction, with maximum stress induced on the anchor of the cantilever. As the resonant vibration increases to 1211.2 Hz, a 2nd vibration mode occurs, where a movement of 2-degree-of-freedom is developed on the anchor and the area where the *S*-beam and flat beam are linked.

At higher vibration mode of 3rd order, a more complex wave-like propagation along the length of the structure is noticed. It involves a movement of torsional and longitudinal vibration modes which results in an elongation and side-way curving movement. This effect produces a maximum stress distribution toward the middle section of the *S*-beam and flat beam. This happens at around 3087.6 Hz, while 4th vibration mode occurs at 6803.6 kHz, which demonstrate a more complex wave-like movement and has a periodic distribution of stress along both sides of the cantilever.

At the fundamental vibration mode, a cantilever with width greater than length displayed a similar stress distribution pattern to the one with length greater than the width. At higher vibration modes, however, the side-ways transverse movement becomes prominent, as shown in Figure 3-26. It is noticed that, there are two peaks of maximum stress responses very close to each other at around 1192 Hz, as shown in Figure 3-27, which does not appear for the cantilever with length greater than width.

71

The 3rd and 4th vibration modes happen at about the same frequency as the one with longer length, at 3168.9 Hz and 6890.6 Hz respectively. The magnitudes of the stress are also similar between the two structures, which show that the width of the free-standing structure does not significantly improve or reduce the resonant frequency.

The simulation results verify that, by attaching a proof mass at the tip of a cantilever, the resonant frequency can be reduced while increasing the magnitude of stress induced on the structure, as shown in Figure 3-28. When a tungsten proof mass with dimensions of 2 mm $\times$ 9 mm $\times$ 1 mm and weight 0.35 g is attached, the first three vibration modes were reduced to 54.2 Hz, 837.2 Hz and 1386 Hz respectively. The stress distributions are similar to those without proof mass at fundamental resonant frequency but the magnitude of the induced stress is greatly increased. It is interesting to notice that, at 2nd resonant vibration mode, the stress distribution is concentrated on the flat beam and almost no stress is developed on the *S*-beam. This shows that in order to optimise electrical energy generation, piezoelectric material must be printed along the length of the cantilever and not just concentrated on the end of the clamped area.

The effect of proof mass distribution on the cantilever is significant at higher frequency mode as shown in Figure 3-30. In the simulation, a similar mass of 0.35 g but different dimensions of 2 mm $\times$ 3 mm $\times$ 3 mm was used. The fundamental resonant frequency of the cantilever with the distribution of mass focused on the centre of the cantilever tip is slightly lower than that spread across the width of the cantilever, at 53.1 Hz. The resonant frequency differences between these two settings become obvious when excited to higher frequency modes. The 2nd and 3rd resonant frequency modes happen at 662.5 Hz and 1034 Hz respectively.

The simulation results show that, at fundamental resonant frequency, the stress distribution of a cantilever is concentrated on the anchor area between the base and the free-standing structure, therefore, the structure has to be reinforced in this area. In order to generate optimum electrical output, piezoelectric materials have to be present through the length of the cantilever, as the maximum stress distribution is more toward the end of the cantilever at higher resonant frequency modes.
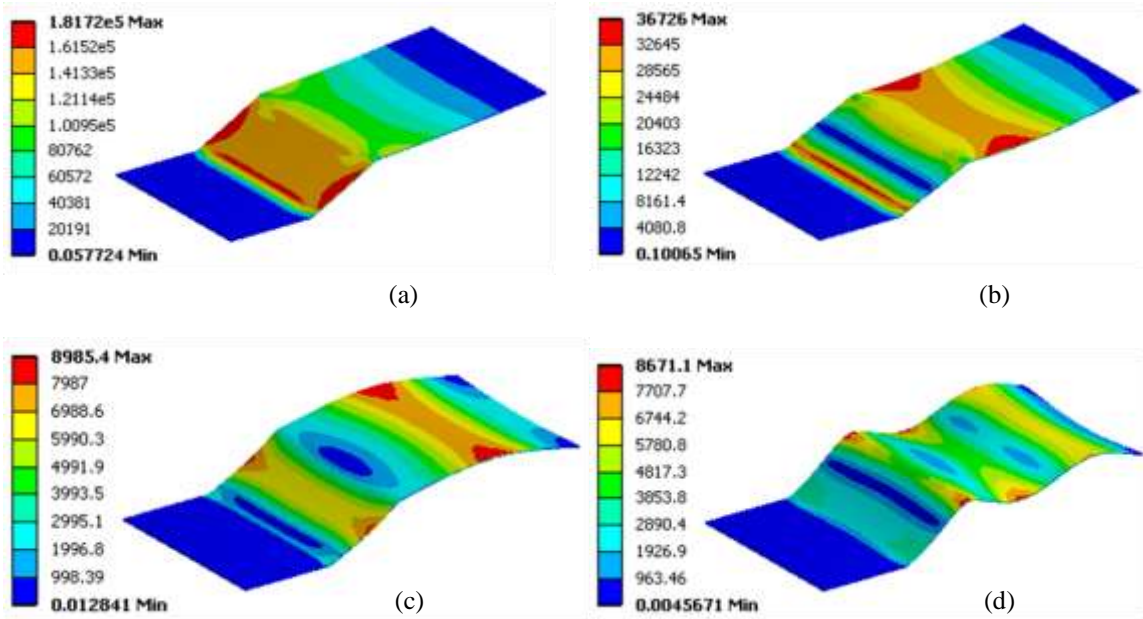
Figure 3-24: Contour plot of stress distribution of a cantilever with dimension as shown in Table 3-3 under fundamental (a), 2nd order (b), 3rd order (c) and 4th order (d) vibration modes.
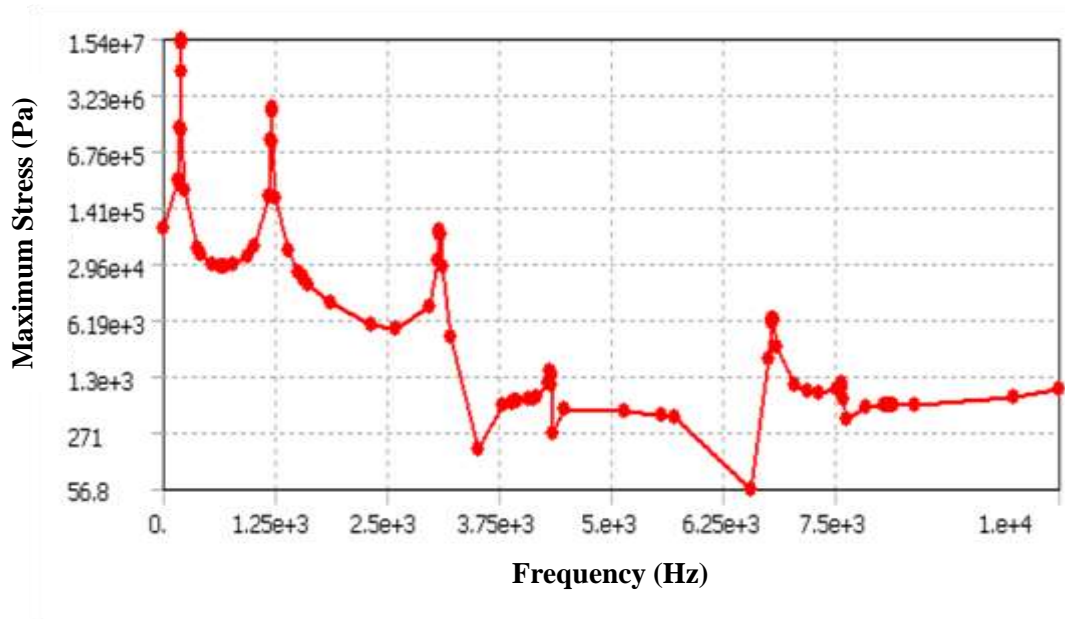
Figure 3-25: Diagram of maximum stress as a function of base excitation frequency for a cantilever having the dimension as shown in Table 3-3

73
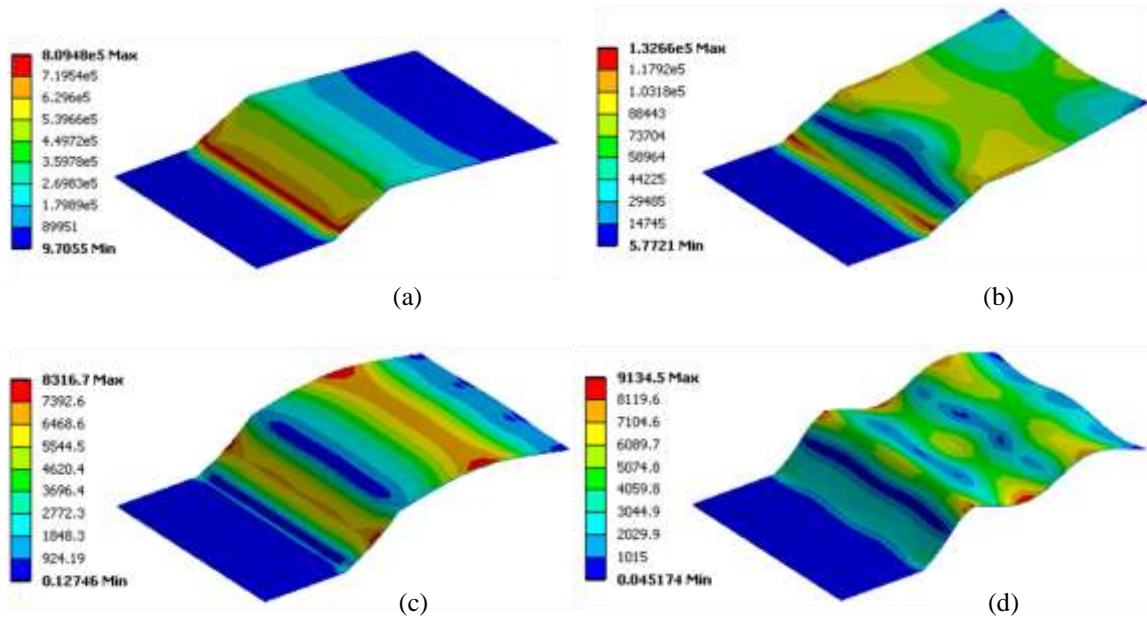
Figure 3-26: Contour plot of stress distribution of a cantilever beam having a width of 18 mm under fundamental (a), 2nd order (b), 3rd order (c) and 4th order (d) vibration modes.
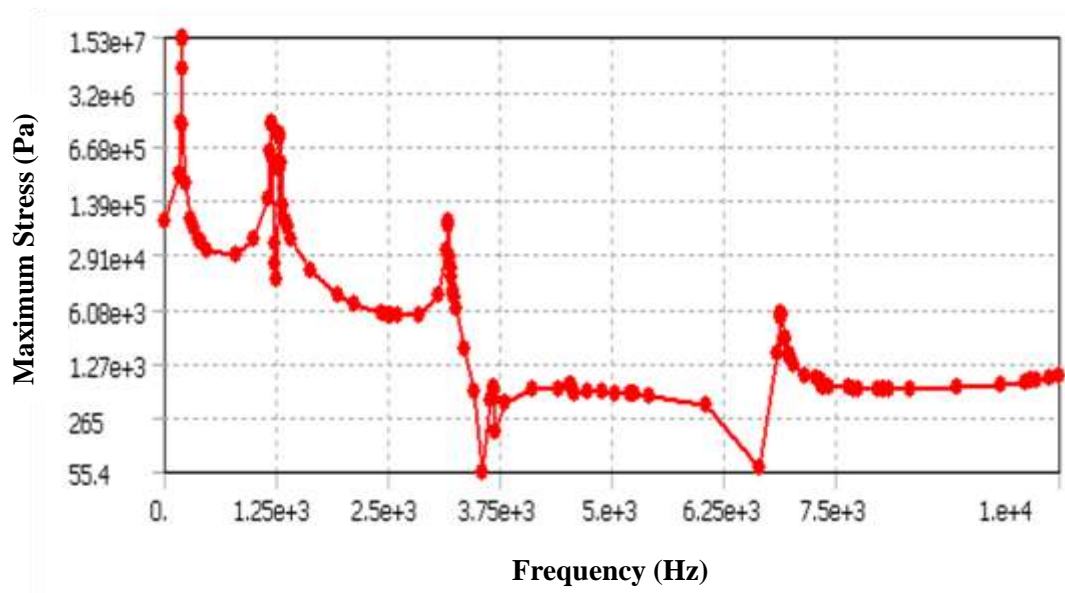
Figure 3-27: Diagram of maximum stress as a function of base excitation frequency for a cantilever having a width of 18 mm.
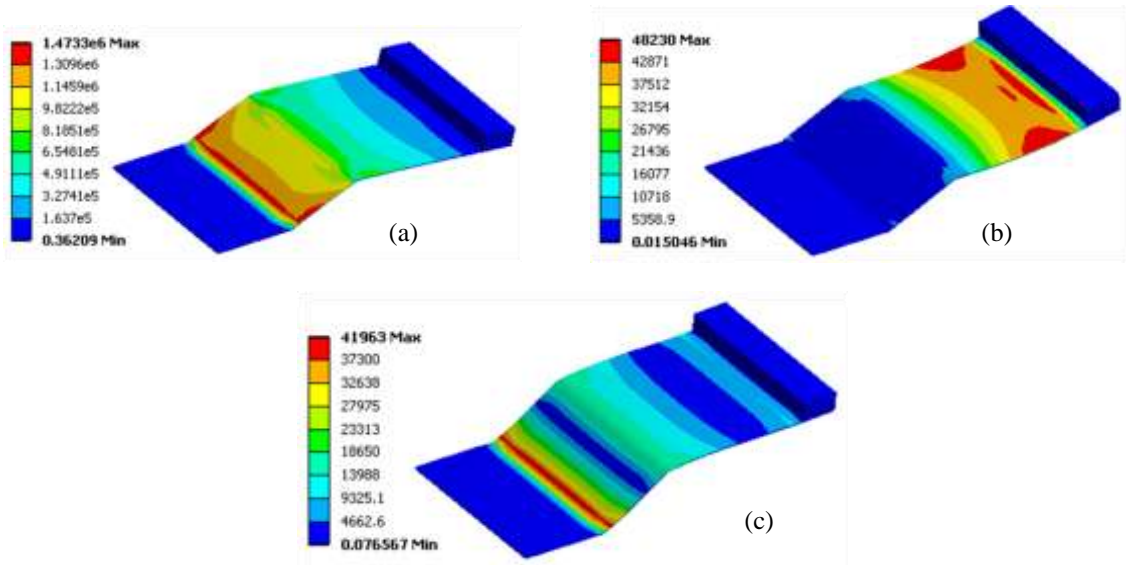
Figure 3-28: Cantilever with full-width-coverage tungsten proof mass; contour plot of stress distribution of a cantilever beam attached with the proof mass for fundamental (a), 2nd order (b) and 3rd order (c) vibration modes.
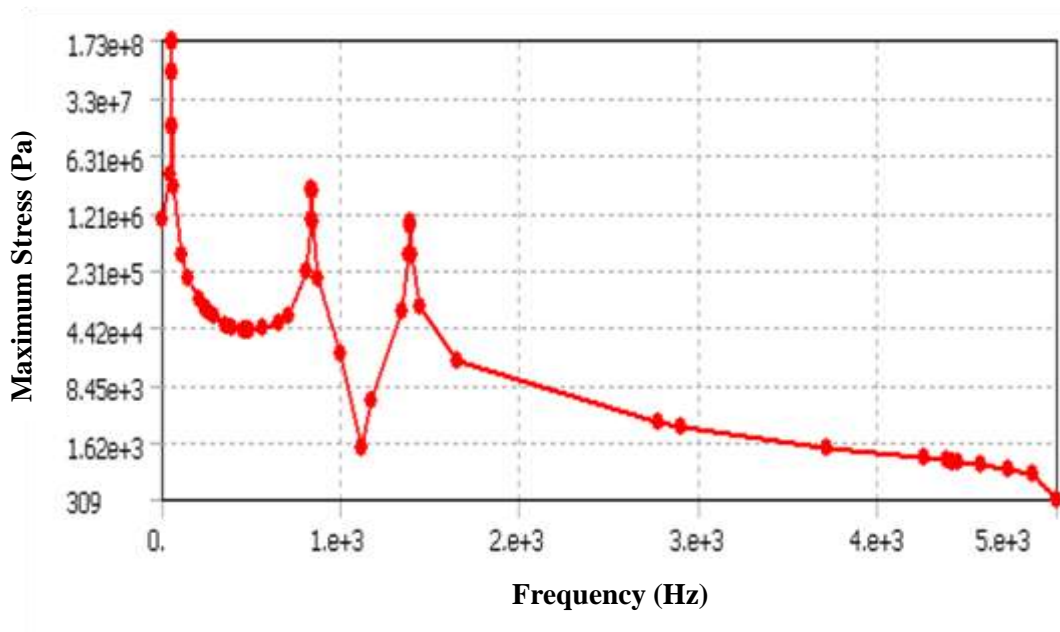
Figure 3-29: Diagram of maximum stress as a function of base excitation frequency for a cantilever attached with full-width-coverage proof mass.
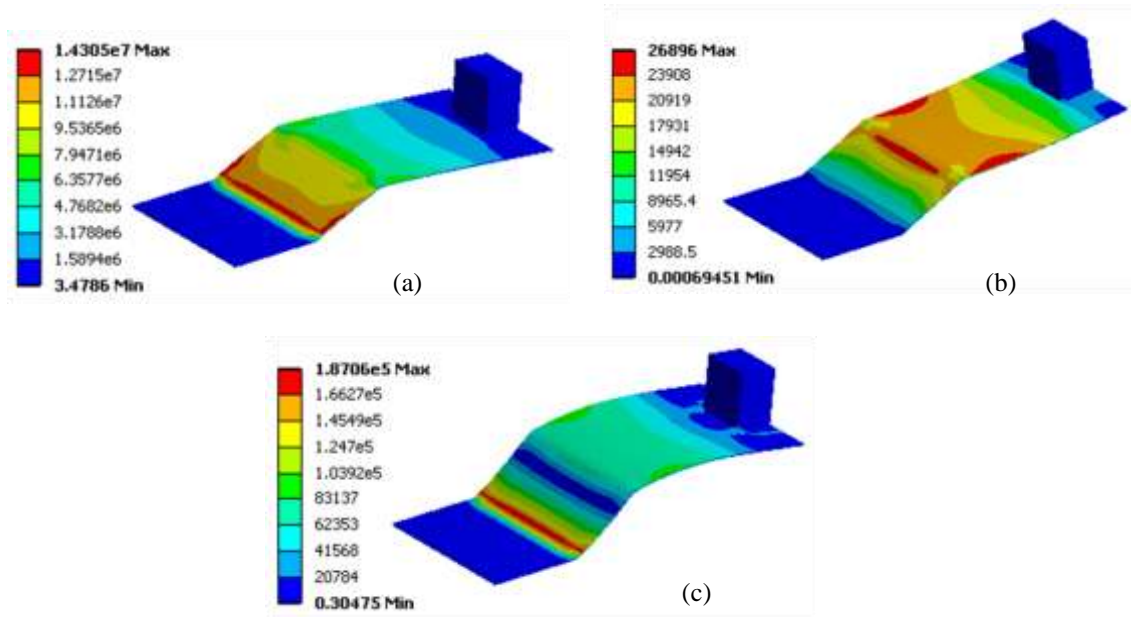
Figure 3-30: Contour plot of stress distribution of a cantilever beam attached with full-width-coverage proof mass for fundamental (a), 2nd order (b), 3rd order (c) and 4th order (d) vibration modes.
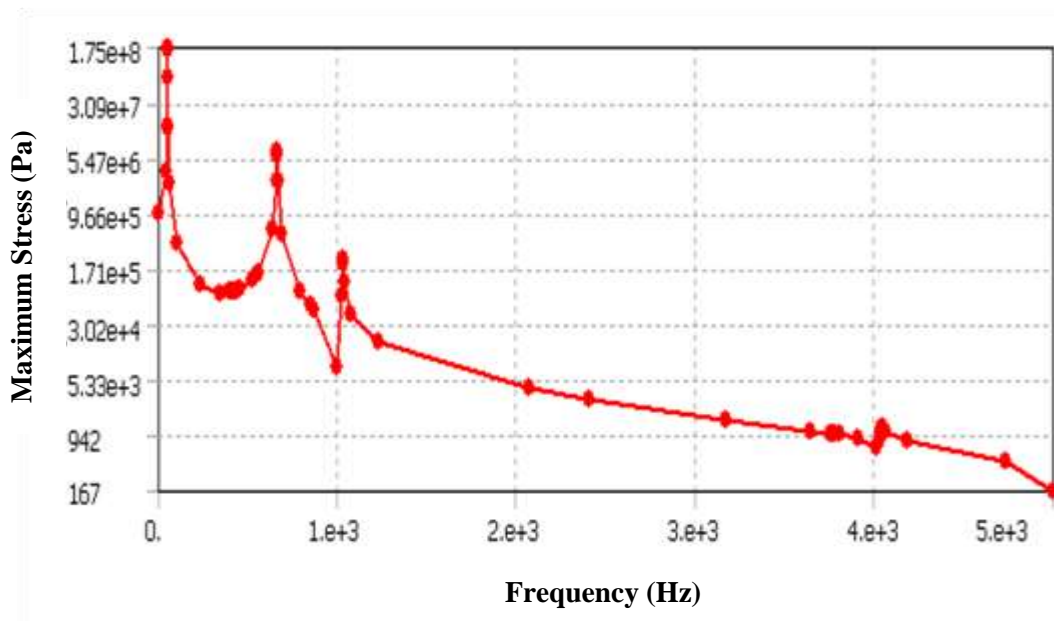
Figure 3-31: Diagram of maximum stress as a function of base excitation frequency for a cantilever attached with full-width-coverage proof mass.

3.6.2 Comparison with Calculation Results

The simulation results of the multilayer composite structure are compared with a single layer PZT with similar thickness of 100 μm. Figure 3-32 (a) verifies that the natural frequency of a cantilever is inversely proportional to the square of the cantilever length. The flexural rigidity of the beam changes as Ag/Pd electrodes are added. A change in stiffness directly affects the frequency of the beam's vibrations. The natural frequency difference between the composite structure and single layer structure becomes less significant when the length of the structure increases.

The calculation results, based on a composite structure according to equation (3-14), shows a slight difference compared to the simulation results. For a cantilever length of 5 mm, the calculated natural frequency is 2.19 kHz, while the simulated natural frequencies for the composite and single structure are 2.48 kHz and 1.71 kHz.

The stress, deflection and acceleration on the tip of the cantilever are directional responses as a resultant from the base excitation, as shown in Figure 3-23. The y-direction indicates translation motion while x-direction indicates longitudinal (elongation) motion. As the effect on z-direction is minimal compared to x- and y-directions it is therefore ignored. Figure 3-32 (b) shows that the acceleration at the tip of the cantilever for both composite structure and single material structures are almost similar. This is because the resonant frequency of the composite cantilever increases while the deflection decreases compared to a single material structure, and therefore produces a constant acceleration. Both the composite and single material structure are accelerated by a factor of about 200 compared to their base excitation levels, for a cantilever length of 5 mm. The acceleration level decreases to a factor of 130 when the cantilever length increases to 20 mm. The difference between calculation and simulation results is significant for a shorter cantilever. This is because the calculation results are based on a straight and flat cantilever model, whereas the simulation results are based on elevated cantilever model. Hence, at a shorter length the *S*-beam of the simulation model plays a significant role in determining the tip acceleration, which is not considered in the theoretical model.

The deflection of the cantilever can be estimated from the *y*-direction deformation from the ANSYS simulation results. The deflection difference between composite and single material structures is significant when the length of the structure increases. These simulation results verify the fact that as the length of a cantilever structure increases, the resonant frequency decreases. Once the resonant frequency is reduced, the cantilever would experience a greater magnitude of deflection at a constant acceleration level. For a cantilever of length 20 mm, a single material structure produces as much as three times the magnitude of deflection produced by a composite structure as shown in Figure 3-32 (c). This shows that the electrode layers which are stiffer than PZT play an important role in reducing the deformation of the structure when excited to its resonance.

As both of the structures were excited with the same excitation level, the maximum stresses on *x*-direction for both structures are similar, as shown in Figure 3-32 (d). These simulation results show that a material with higher elastic modulus can be added on the outer layer of the composite structure in order to protect the more fragile and brittle piezoelectric material from overstress at the centre of the composite structure, since the stress increases with the distance from the neutral axis to the centroid of the material.

From the ANSYS simulation results for a single material structure (consists of PZT) and a multilayer structure (consists of PZT and Ag/Pd electrodes), it can be concluded that the natural frequency and the maximum deflection of a cantilever structure depends on the elasticity of the individual layer.

The theoretical calculation results for a composite structure are in a good agreement with the ANSYS simulation results for a composite structure. This verifies that the model developed in section 3.4 is reasonable good to be used to estimate the performance of a free-standing cantilever, therefore will be used in the following chapter.

(a)

(b)

(c)

(d)
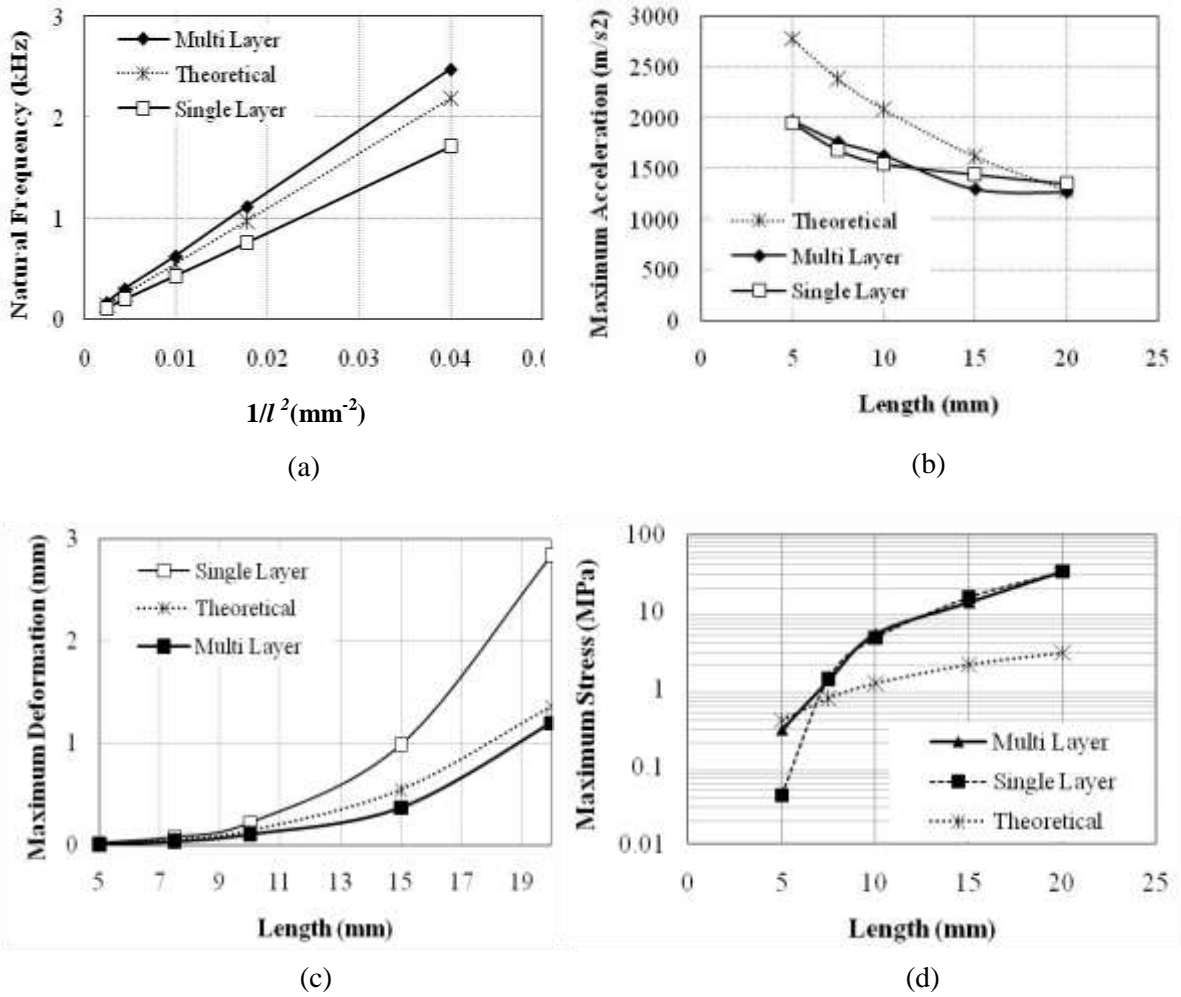
Figure 3-32: Comparison between ANSYS simulations and theoretical calculation results on its natural frequency (a), maximum cantilever tip acceleration (b), maximum stress (c) and maximum deformation on the tip of the cantilever (d).

3.7 Screen Printing Design

A free-standing cantilever structure as shown in Figure 3-33 was designed with various length from 5 mm to 20 mm with a fixed width at 10 mm. The effective length of the free-standing structure is the part where it is printed above the sacrificial layer. The sacrificial layer is deliberately designed to be 1 cm wider peripherally than the actual part of the free-standing structure, in order for it to be dissipated effectively when co-fired at high temperature. The lower and upper electrodes are designed to be 0.5 mm narrower peripherally than the piezoelectric material. This is to give a leeway for printing tolerance, preventing a short connection between upper and lower electrodes.
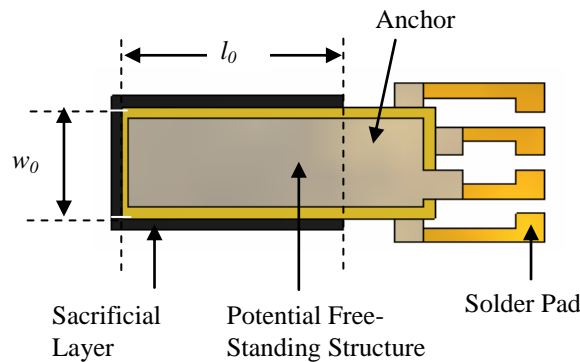
Figure 3-33: A free-standing cantilever structure design layout.

Each layer of the composite structure was designed with Autodesk Inventor software (www.autodesk.com) and converted separately into photo-plotter format (eg. Gerber, HPGL, DXF or DWG) which would than translate into a patterned thick-film printing screen. The layout of the sandwiched composite free-standing structure is shown in **Error! Reference source not found.** (a). In total, five printing screens are needed to fabricate a sandwiched layer composite structure. The lower electrode screen can be reused for printing the upper electrode by rotating the screen through 180°. In this research, an IDE cantilever structure will also be investigated, and only one extra screen with an IDE pattern is needed as shown in **Error! Reference source not found.** (b).
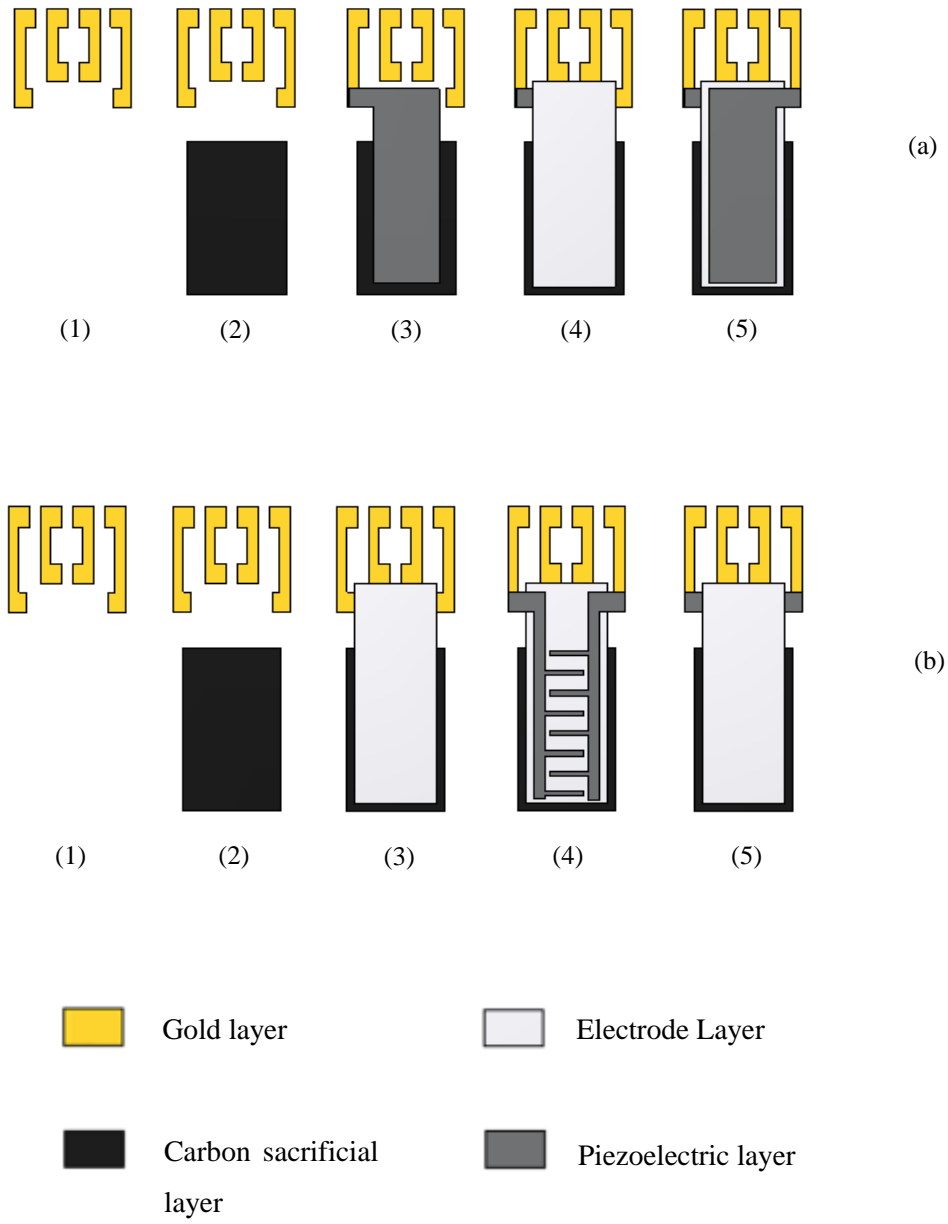
Figure 3-34: Layouts of a plated electrode (a) and an IDE cantilever structure (b).

3.8 Conclusion

There are a few challenges in designing a free-standing structure for energy harvesting. One of which is the natural frequency of the structure, which has to be matched to the vibration sources in order to harvest maximum energy. Since thick-film materials are brittle, it is very important to know the maximum allowed stress.

If the structure is overstressed, it would fail to operate accordingly and might lead to fracture. Small and compact are desirable features for miniature energy harvester, however a cantilever structure needs some room to manoeuvre and therefore the maximum displacement of the cantilever has to be determined so that the structure can move freely in a confined space. A useful energy harvester has to produce up to a certain level of voltage and electrical power suitable for microelectronic devices. The challenge of fulfilling these requirements is enormous especially for miniature thick-film devices. The first step toward making a thick-film free-standing micro-generator a reality is by computational simulations and analytical calculations. Overall, the calculation results are in relatively good agreement with the simulation results.

Chapter 4   Processing of Thick-Film Free-Standing Devices

4.1 Introduction

Generally, piezoceramic thick-film fabrication steps are in sequence starting from paste formulation, screen-printing deposition, drying and co-firing and finally poling process. The major difference for this study is to apply sacrificial layer techniques to fabricate thick-films in three dimensional free-standing forms. The fabrication technique involves a one-step air co-firing technique, where the active members of the structure were co-fired together with the electrodes in an air environment.

One of the disadvantages of thick-film lead zirconate titanate (PZT) materials is their brittleness which makes them too fragile to form free-standing structures. Therefore silver/palladium (Ag/Pd), which is more ductile, was chosen to form the electrode. It also acts as the support platform for the ceramic layers to form a robust free-standing structure.

Ag/Pd electrodes were printed as planar plate and interdigitated (IDT) patterns on the PZT layers for two purposes; one of which was to study the electrical outputs from the d_{31} and d_{33} piezoelectric effects. Another reason was to use them as a tool to investigate the consequences of the composite film fabrication process with two materials of different thermal expansion coefficient.

4.2 Fabrication Materials

The ingredients for fabricating thick-film free-standing micro-generators consist of PZT pastes, carbon pastes, conductor pastes and base substrate.

General purpose thick-film pastes are available commercially for fabricating passive circuit elements such as conductors, dielectrics and resistors. However, special purpose thick-film pastes for fabricating micro-generators are not available commercially at the present time; therefore customized pastes have to be made in-house. Carbon pastes were also formulated in-house, similar to that described by Birol *et al* [96] for low temperature co-fired ceramic (LTCC) technology. These were used as the sacrificial layer for fabricating the free-standing structures.

There are a range of electrode pastes available commercially. Typically used thick-film electrode pastes are gold, silver, and silver/palladium pastes. However, not all of the electrode pastes are suitable for high temperature co-firing with PZT, since problems such as electro-migration can occur which can degrade the piezoelectric activity in the PZT materials.

A range of substrates can also be used to fabricate free-standing devices. As the free-standing cantilever structures do not need physical support for bending mode operation, the substrate material is therefore not critical in determining the properties of the devices. However, the substrate has to be able to withstand the high temperatures used in the processing of thick-film materials.

4.2.1 Lead Zirconate Titanate (PZT) Pastes

The main ingredient for thick-film piezoceramic pastes are PZT powder, high temperature permanent binder, low temperature temporary binder and solvent. These special formulised pastes using PZT as the functional material have been reported in [97, 98].

Typically, the PZT powders sinter at a temperature higher than 800 °C in order to produce high piezoelectric activity material. Lead borosilicate glass is used as the

permanent binder. It is often available in the form of powder, also known as glass frit. During the co-firing process the glass melts and binds the PZT particles together and later forms solid composite films once cooled down to a lower temperature. These films adhere firmly to the substrate. The presence of glass modifies the mechanical properties as well as the piezoelectric properties of the film. Therefore, it is important to mix PZT powder and glass frit in correct proportions. If the percentage of glass frit is more than necessary, hence reducing the PZT powder loading, then this will result in a lower piezoelectric activity. Polymer binders are also used as the permanent binder for fabricating flexible structures [99], which are generally cured at lower temperature (typically 100 – 200 °C) with an infra-red dryer.

Temporary binders such as organic polymers together with solvents such as pine oil (or terpineol) are used to make thixotropic pastes, which can easily pass through the printing screen. They also serve to hold the paste together during the drying process, and are eventually evaporated off during the firing stage. Excessive solvent, however, will result in a smeared print and reduced definition of the printed geometry.

The thickness that can be produced for PZT thick-films ranges from a few microns to hundreds of microns. The minimum film thickness is governed by the particle size of PZT, which is typically 0.8 – 2 μm. There is no definite upper limit of thickness that can be produced, but films with thickness greater than 200 μm is suitable to be fabricated with bulk piezoelectric materials for higher piezoelectric activity.

4.2.2 Carbon Pastes

A carbon paste, similar to that described by Birol *et al* [100] for the purpose of producing low temperature co-fired ceramic (LTCC) technology, was used as the sacrificial layer for the free-standing structure. Graphite was chosen because it can be fully burnt out in air at a temperature above 800 °C (Figure 4-1) and is therefore compatible to the piezoceramic sintering temperature.
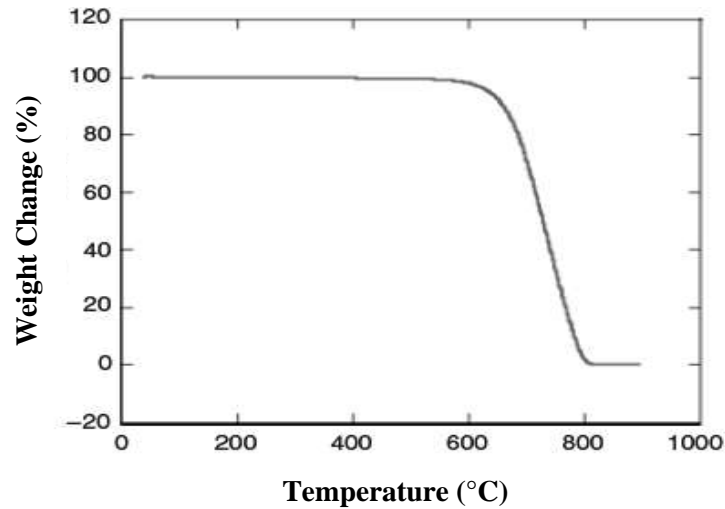
Figure 4-1: Thermogravimetric analysis (TGA) of graphite heated in air at 10 °C/min [100].

One of the advantages of using carbon as the sacrificial layer is that carbon burns in the air producing carbon dioxide, which is not toxic in small amounts and is considered environmentally advantageous over thin-film and silicon processes for fabricating free-standing structures.

4.2.3 Electrode Pastes

Silver/palladium (Ag/Pd) pastes are commonly used in fabricating electronic components such as hybrid microcircuits, passive electronic components (e.g. multilayer capacitors), multichip modules and packaging for integrated microcircuits [94].

Silver (Ag) is widely used in the electronics industry for its high electrical conductivity (or low electrical resistivity of 1.59×10^{-8} Ωm). The major weakness of Ag is the electromigration effect in humid conditions under potential bias. Silver also has poor solder leach resistance. These problems can be minimised by adding palladium (Pd) to Ag to make an alloy system.

The melting temperature for the Ag/Pd system can be modified by adjusting the ratio (atomic) of the metals in the system of the solid-solution formation. The solidus and liquidus increasing in temperature monotonically from Ag to Pd ($T_m^{Ag} = 692^0C$, $T_m^{Pd} = 1552^0C$) [94]. For low firing process at around 1000 °C, a solution with 85% of Ag and 15% of Pd is used to formulate the paste. Usually the Ag/Pd thick-film conductors are fritted with borosilicate or similar glass phases which are used to bond the metal particles to the surface of the alumina substrate on firing.

The other alternative electrode material is gold (Au). Apart from its relatively high cost, gold can be made as an excellent electrode paste. It exhibits better wire bondability and migration resistance compared to Ag. Gold is usually added with Pt or Pd to form alloys for thick-film applications to improve solderability with Sn/Pb solder. The properties of the electrode materials are summarised in Table 4-1.

Although Au is better than Ag/Pd, the trade off between the cost of fabrication and performance makes Ag/Pd preferable as the electrode material. Conversely, due to the use of high temperature solders to connect the thick-film terminals, Au is a better candidate for the soldering pad material.

Table 4-1: Comparison of material properties for silver, palladium and gold [94].

Metal	Density (g/cm^3)	Melting Temperature (°C)	Electrical Resistivity ($\times 10^{-8}$ Ωm, 298 K)	Thermal Expansion Coefficient ($\times 10^{-6}$/K)	Thermal Conductivity (W/mK, 300 K)	Young's Modulus (GPa)
Silver, Ag	10.5	961	1.59	19.2	429	76
Palladium, Pd	12	1825	10.8	11.2	71.8	112
Gold, Au	19.3	1063	2.35	14.2	317	80

4.2.4 Substrate Materials

The substrate is the essential material acting as a base on which films or layers of thick-film material are deposited and processed to build a whole device. Some bulk ceramics need to be adhered to the substrates to make them function as a complete device. The substrates for bulk ceramic devices are usually rough, big and strong enough to provide support to thick piezoceramic (ranging from hundreds of microns to millimetres thick).

The choice of a substrate for thick and thin-film devices is critically dependent on the process of fabrication. There are a few substrates that are suitable for thick-film devices such as alumina, silicon, stainless steel, polymer and glass.

In this study, alumina is used as the substrate for processing PZT thick-film. Alumina is used because it can withstand the high temperatures used for thick-film processing, which can reach up to 1000^{0}C. It has a thermal expansion coefficient that is comparable to most thick-film pastes. Besides that, it offers good adhesion for printed layers and is rigid enough to withstand the tensile stress of shrinking thick-film pastes after the curing process. It is also known as a hermetic material, where it can prevent moisture seeping into it, which can reduce the quality of the thick-film layers during firing. Compared to other substrates, it is relatively low-cost and can be used for mass production.

4.3 Thick-Film Printing Process

One layer of sacrificial carbon is printed first on an alumina substrate. The film was then dried in an infra-red dryer at 150 °C for 10 minutes. A second layer of film (which can be either Ag/Pd or PZT) is then printed over the sacrificial layer with part of the film covering the alumina substrate as shown in Figure 4-2. This creates a step between the sacrificial layer and the upper film layer, with a height equal to the thickness of the carbon layer. Therefore the sacrificial layer is preferred to be as thin as possible to ensure the film above the sacrificial layer is properly connected between the base and the potential free-standing structure.

A sequence of printing and drying is repeated for each layer of the films to make a multi-layer composite structure. The resultant film was strongly bonded to the substrate and was not easily pulled off during a standard tape peel test.

For composite films of thickness greater than the printing paste can achieve (>50 µm), especially for electrode layer, it is necessary to use a brush to smear the pastes across the area where the step is to ensure that the electrode is properly connected to the free-standing structure.
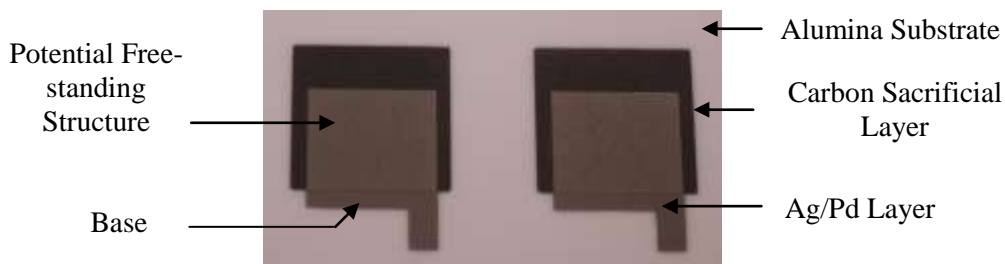
Figure 4-2: A photograph of Ag/Pd films printed on carbon sacrificial layers.

4.4 Three-Dimensional Co-Firing Technique

Conventionally, each layer of thick-film in a composite structure is printed, dried and fired individually before another layer of film is printed on them, and usually this process is carried out in an air environment.

This process, however, is not possible for fabricating a 3-Dimensional structure. This is because once the carbon sacrificial layers are burnt out in air, the thick-films would be released as free-standing structures. These structures are too brittle and fragile to be printed on with another layer. One solution for this issue is to fire the thick-films in a nitrogen environment to retain the carbon sacrificial layer while the process of printing, drying and firing is repeated for fabricating a multilayer structure, similar to that described by Stecher [83].

Co-firing is a technique whereby multiple layers are printed and dried before being fired once as a complete structure, but for devices containing PZT, each successive firing

results in lead evaporation, altering the chemical composition away from the stoichiometric optimum and leading to a reduction in piezoelectric activity [101]. Therefore, this suggests that multilayers of composite thick-films printed on carbon sacrificial layers can be co-fired together in an air environment, without the need to fire each layer separately in a nitrogen environment. This one-step co-firing method not only improved the piezoelectric activity in the material but also reduced the complexity of the process and hence reduced the cost of the fabrication.

Typical co-firing profile temperatures for thick-film layers on silicon as described by Glynne-Jones *et al* [102] are in the range of 750 °C to 1000 °C. Films at a low co-firing temperature of 750^{0}C exhibited poor sintering, whilst at temperatures above 800 °C the films show acceptable adhesion and sintering. However, co-firing at higher temperature (> 900 °C) is undesirable because it may causes free-standing structures to be more brittle and prompt cracking.

In order to completely burn out the carbon sacrificial layer, co-firing temperatures have to be set above 800 °C. This temperature is conducive to the curing temperature of PZT films. The quality of a piezoelectric thick-film can be compared by measuring its piezoelectric charge constant, d_{33}. A study by Torah *et al* [20] showed that the values of d_{33} for samples co-fired at peak temperature of 800 °C were not much different from those co-fired at peak temperature of 1000 °C. At 800 °C, the value of d_{33} was measured at about 110 pC/N whilst at 1000 ^{0}C it increased a little to 169 pC/N.

Due to the differences in coefficients of thermal expansion of PZT and Ag/Pd, pre-stress will be induced in these layers [103]. Ag/Pd material has a higher thermal expansion coefficient and therefore expands with a faster rate compared to PZT film when they are co-fired, and contracts faster when they are allowed to cool to room temperature at the end of the fabrication process, which leads to stress gradients. The effect of the pre-stress is essential in forming a free-standing structure by extending and bending the material from the anchor area where the base and the free-standing structure meet. The adverse effects of the process are the formation of cracks and warping on the structures. However, these issues can be rectified by techniques which will be discussed in this chapter.

4.5 Co-firing Process

A multi-zone furnace is used to set the desirable co-firing profile for fabricating the devices. The multi-zone furnace consists of 8 zones with heating coils which can be controlled to set desirable temperatures in each zone. The furnace is also fitted with 5 air curtains which control the air flow vertically downward for maintaining the temperature while the fabrication process is running. Fabrication samples are placed on a conveyor belt with controllable speed, which is important in setting co-firing profiles.

In this study, three co-firing profiles were used with similar total co-firing process time of 45 minutes but different peak temperatures of 550 °C (denoted as 550 Profile), 850 °C (850 Profile) and 950 °C (950 Profile) as shown in Figure 4-3. The objective is to identify the best co-firing profile for fabricating robust free-standing cantilevers and with high piezoelectric performance, which can be compared by the piezoelectric constant, d_{33}.

The air flow was set to 50 l/min, 40 l/min, 5 l/min, 40 l/min, and 50 l/min in five sequential zones respectively. The higher air flows at both ends of the furnace act as a curtain to prevent drastic change of temperature and also provide uniform air circulation inside the furnace. The air flow in the middle zone of the furnace was set to an appropriate level for burning carbon and co-firing process.
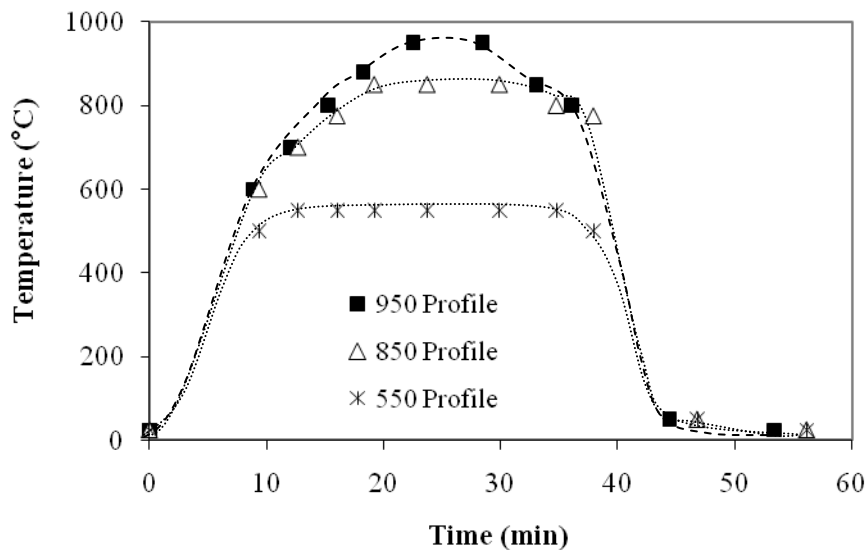
Figure 4-3: Three different co-firing profiles for fabricating free-standing structure.

4.6 Experiment Results and Discussion

A few experiments have been carried out to investigate the structure of thick-film free-standing cantilever as a result of different co-firing profiles and fabrication sequence of PZT-Ag/Pd. Another experiment where Ag/Pd was printed in an IDT pattern exploiting the piezoelectric effect of d_{33}, was used as a mean to investigate the role of the Ag/Pd material in supporting free-standing structure. Finally, multilayer composite structures of PZT-Ag/Pd were fabricated with improvements to produce robust and flat cantilevers.

4.6.1 Effect of PZT-Ag/Pd Fabrication Sequence

There are a few problems faced by piezoceramic free-standing structures. One of which is thermal shock, which may result in structures cracking as an effect of rapid temperature change during the co-firing process. For a thick-film printed directly on a substrate, the thermal shock can be reduced as the expansion and contraction of the film is prohibited as it is rigidly clamped to the substrate. PZT films are not able to be free-standing by themselves as shown in Figure 4-4 (a), where the films broke off from the base after the carbon sacrificial layer burnt out.

Figure 4-4 (b) shows that Ag/Pd films were able cope with rapid temperature change in holding together the film as part of a free-standing structure but the rates of expansion and contraction of the materials are relatively fast therefore they collapse and adhere to the alumina substrate after the carbon film burnt out forming a wave-like structure. These experiments conclude that none of the materials is able to be free-standing by itself.

Composite free-standing structures consisted of sandwich layers of piezoceramics and Ag/Pd conductors were investigated. Because the structure consists of two different materials with two different coefficients of thermal expansion, increasing or decreasing the processing temperature will produce a surface stress on the structure and thus create a pronounced bending. The direction of bending depends on the arrangement of the layers between ceramics and conductors.

(a)   (b)
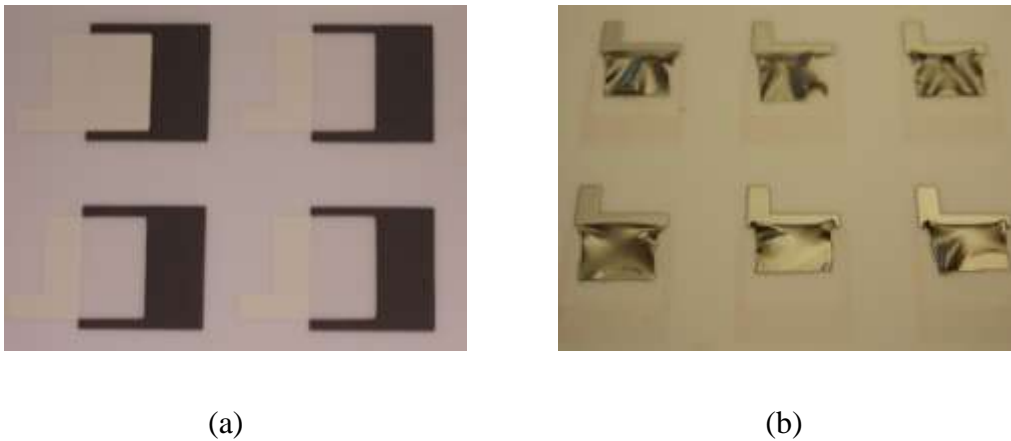
Figure 4-4: Photographs of failed free-standing structure comprising only (a) PZT and (b) Ag/pd materials.

Composite films with Ag/Pd printed as the bottom layer and PZT as the top layer were co-fired at 850 °C, produced a free-standing structure which bend inward to the substrate as shown in Figure 4-5 (a). This is because the thermal expansion coefficient for the conductor is greater than for the ceramic, therefore expansion of the conductor is faster than the ceramic at high temperature in the furnace. However, once the composite films were cooled to room temperature at the end of the process, the conductors contract faster than the ceramic and cause the structure to bend inward. Composite films with the arrangement the other way round produced a free-standing structure which bends outward from the substrate as shown in Figure 4-6 (a).

A sequence of composite films with Ag/Pd conductor as the bottom layer was co-fired together with the carbon sacrificial layer to release the structure. The resultant of the arrangement of Ag/Pd-PZT-Ag/Pd (A-P-A) collapsed inward to the substrate but with a higher rising angle. An extension series of composite layers of A-P-A-P produced side-way curving structures as shown in Figure 4-5 (c). Composite layers of A-P-A-P-A seem to be able to pull the films away from the substrate due to the complex combination of expansion and contraction of the composite films.

(a)

(b)

(c)

(d)
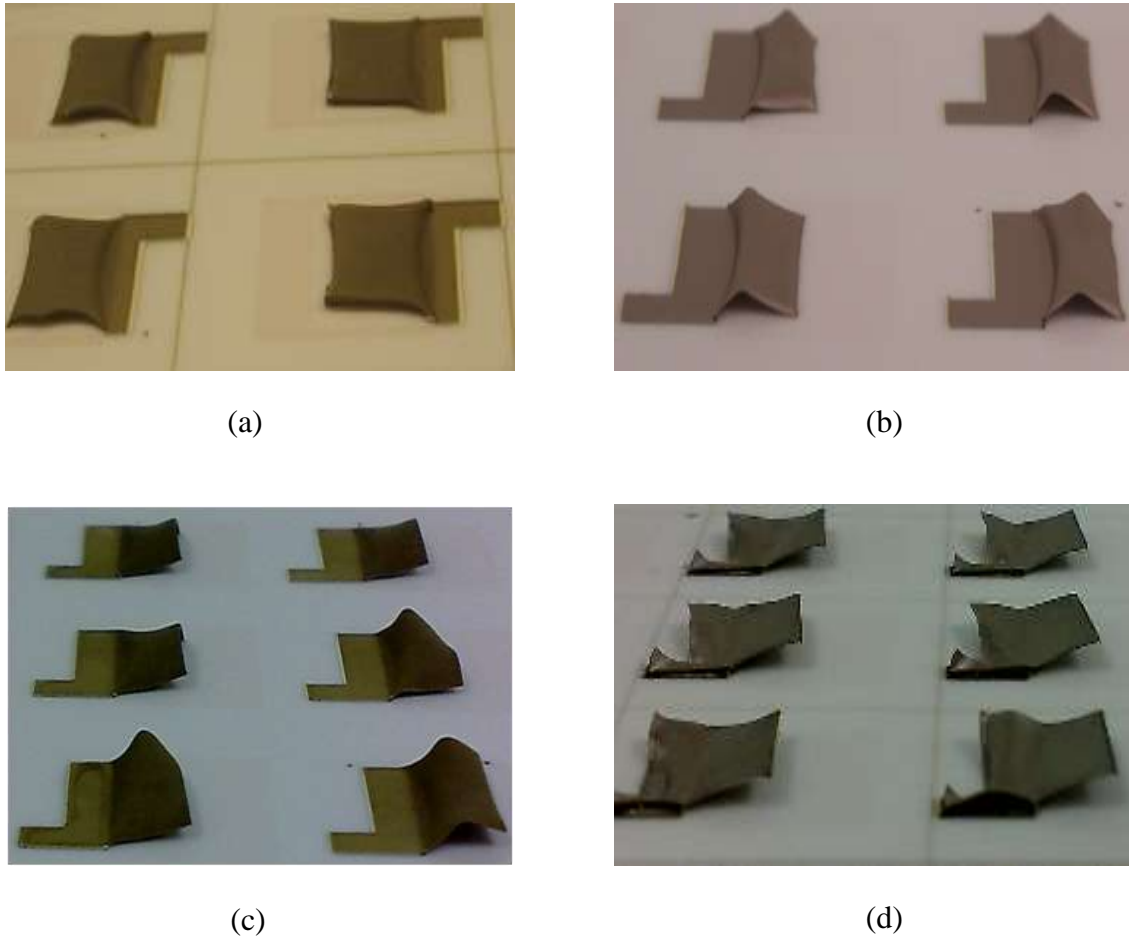
Figure 4-5: Composite structures of Ag/Pd conductors and PZT ceramics printed in sequence and co-fired together: (a) conductor-ceramic (A-P), (b) conductor-ceramic-conductor (A-P-A), (c) conductor-ceramic- conductor-ceramic (A-P-A-P) and (d) conductor-ceramic-conductor-ceramic-conductor (A-P-A-P-A).

In another experiment, a sequence of film printed with PZT layers as the bottom layer and followed by a layer of Ag/Pd results in an upward bending structure as shown in Figure 4-6. This is because the thermal expansion coefficient of the conductor is greater than the ceramic layer, therefore the upper layer of conductor contracts faster than the lower layer of ceramic when cooled down to room temperature at the end of the co-firing process. This effect caused the structures to be pulled away from the substrate. There is also a sign of curl effect at both sides of the free-standing structure.

A smoother surface for the free-standing structures was obtained when more layers of film were printed and co-fired together. Figure 4-6 (a) shows the result of fabrication

with a series of films of PZT-Ag/Pd-PZT-Ag/Pd (P-A-P-A). Therefore, it can be concluded that free-standing structures with PZT as the bottom layer act as an important factor to raise the structure away from the substrate.

(a)   (b)
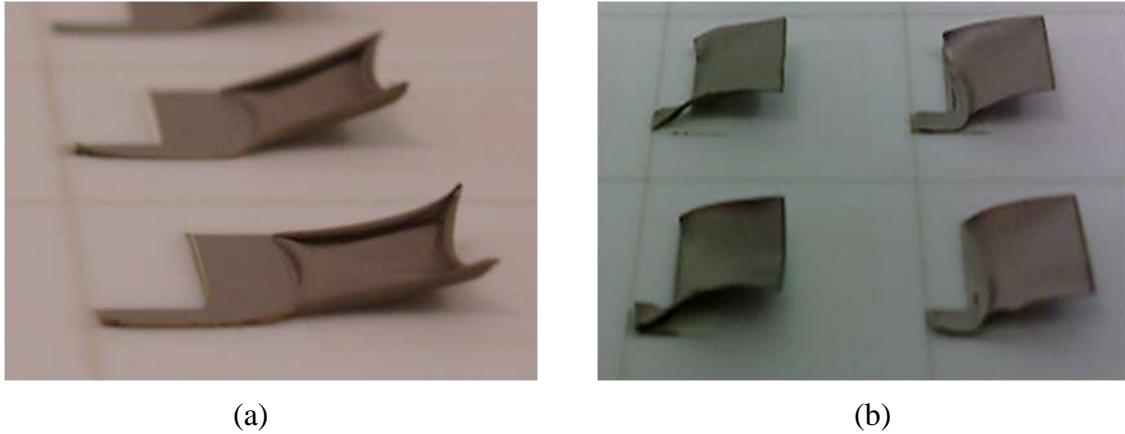
Figure 4-6: (a) Composite structures of PZT ceramics as the lower layer followed by printed Ag/Pd conductors and co-fired together, (b) Composite of ceramic-conductor-ceramic-conductor.

4.6.2 *Effect of Air-Flow and Co-Firing Profile*

In another experiment, free-standing structures with longer cantilever beams were designed and fabricated in a multilayer manner. PZT layers were designed 1 mm longer in perimeter compared to electrode layers.

A series of composite samples printed in the sequence of PZT-Ag/Pd-PZT-Ag/Pd-PZT (PAPAP) were co-fired with 850 Profile. Figure 4-7 shows a sign of rising from the base but fail to maintain the height at the end of the structure and fall back onto the substrate. This maybe because the rate of the contraction and expansion of the bi-material are slow in an arrangement with very little air passage, therefore at the end of the co-firing process the gravity force becomes more dominant than the residual stress of the bi-material structure and hence bends downward to the substrate.

This experiment concludes that air flow plays an important role in fabrication of free-standing structures.

Adhered to substrate
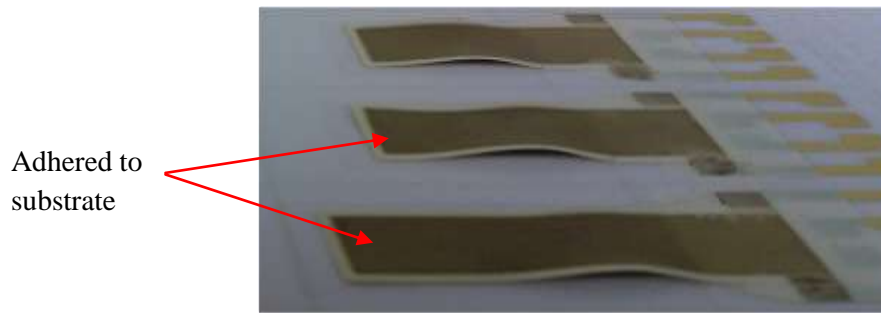
Figure 4-7: A photograph of failure free-standing structure fabricated with reduced air flow.

In another experiment with lower co-firing temperature at 550 °C (Figure 4-3), the samples were found to be free-standing before the carbon sacrificial layer completely burnt off. This resulted in a free-standing structure as shown in Figure 4-8. The films were released from the substrate to form free-standing structures because the polymer binder of the sacrificial layer was burnt out at 550 °C but the thick-films were not properly cured, therefore the structures were fragile and easily broken.

Carbon Residual
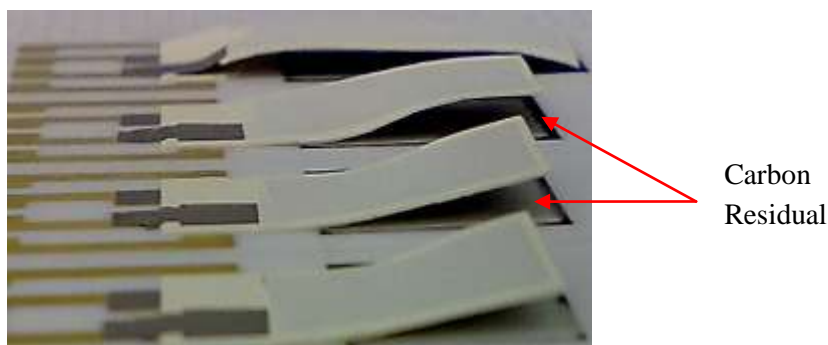
Figure 4-8: Thick-film co-fired with 550 Profile.

Samples co-fired with 850 Profile were found to be more robust as shown in Figure 4-9 (a). As the temperature of the co-firing was increased to 950 °C, a sign of electro-migration from Ag/Pd to PZT layer can be observed as the structures turned to a darker colour as shown in Figure 4-9 (b). It also shows signs of cracks especially near to the base of the structure which was a result of stress caused by the surface tension after the fabrication process.

<table>
<tr><td>(a)</td><td>(b)</td></tr>
</table>
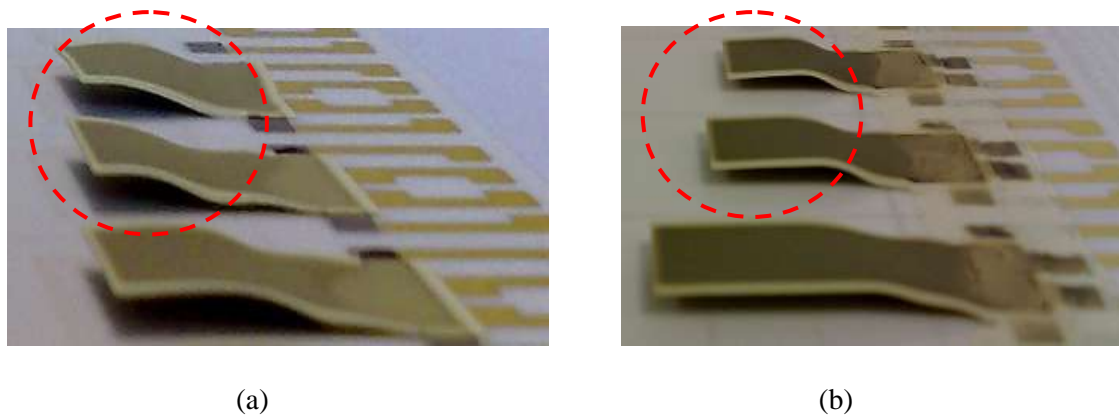
Figure 4-9: Thick-film co-fired with: (a) 850 and (b) 950 Profile.

In another experiment, the printed films were arranged in an upside-down manner and the fabrication results showed no significant difference from the right-side-up arrangement. This meant that the pre-stress introduced by the thermal expansion is greater than the gravitational effect, which is not a significant factor in influencing the gap height of the structure. The height of the free-standing structure from the base is dependent on the gap between the two alumina substrates as shown in Figure 4-10. Three small alumina substrates of thickness 0.6 mm are stacked together to make a total gap height of about 2 mm (includes air gaps between alumina substrates). The experiment results also showed that, at the end of co-firing process, the films did not adhere to the covering substrate, but left some trace of glass binder on its surface.
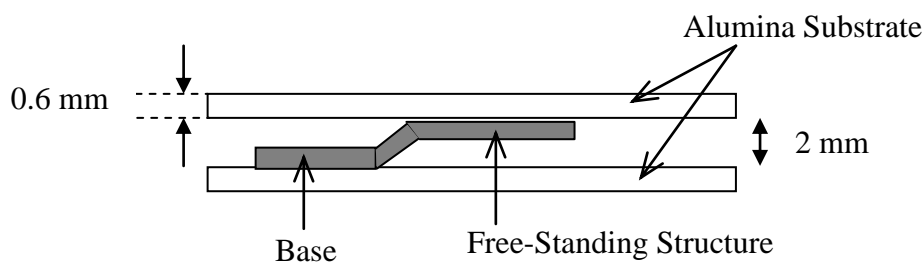
Figure 4-10: Schematic diagram of an arrangement of alumina substrates with a gap of 2 mm.

4.6.3 Investigation on the Structure Support Role of Ag/Pd Using Interdigitated Electrode (IDE)

The Ag/Pd (ESL 9633B) pastes were used to print electrodes as well as support layers for the fragile ceramics. A layer of IDT patterned Ag/Pd electrode was printed over PZT ceramic layers as shown in Figure 4-11 (a). The films were then co-fired together at 850 °C. Figure 4- (b) shows the result of the co-firing process, where the lower layer of ceramics broke off and adhered firmly to the substrate. The free-standing structures were seen to be only supported by the IDT electrodes. The free-standing structures were curved side-ways, because of different thermal expansion between conductors and ceramics. As the temperature cooled to the room temperature at the end of the co-firing process, the conductors contracted faster than the ceramics and pulled them together to make a 'U' curved free-standing structure.

(a)

Ag/Pd IDT Electrode

PZT ceramic

Carbon Sacrificial Layer

(b)

PZT ceramic layer makes a 'U' curve at width-length

PZT ceramic is broken at the free-standing rising area, connected only by IDT electrodes

PZT ceramic is firmly adhered to alumina substrate
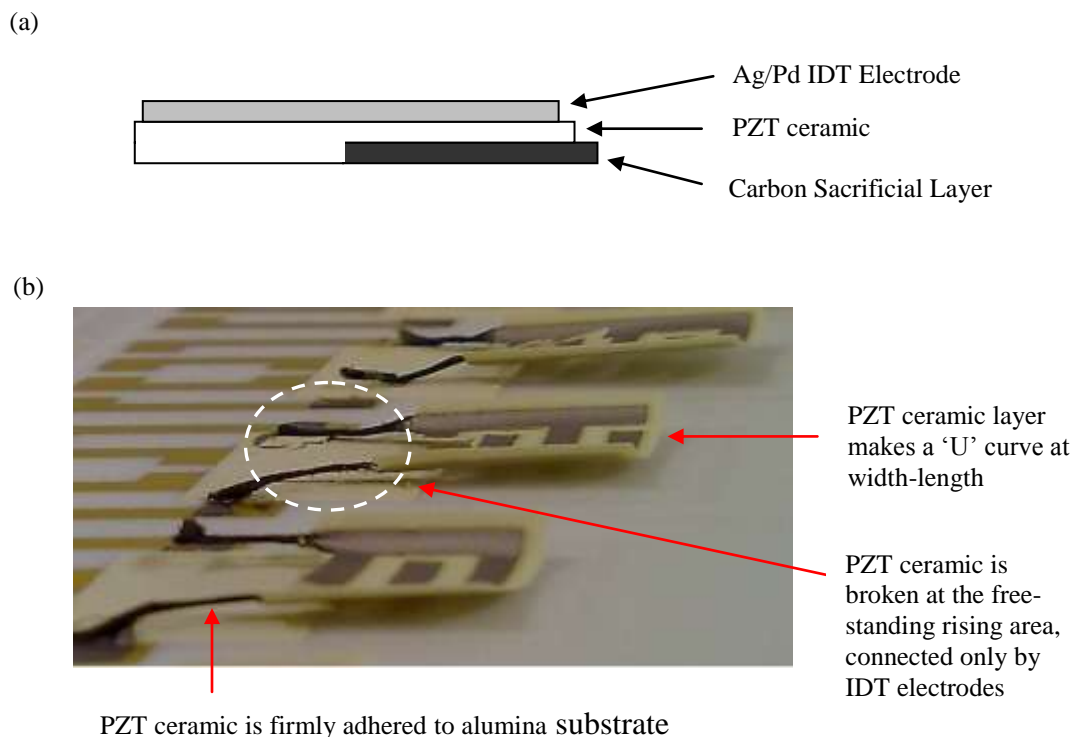
Figure 4-11: IDT patterned electrode on ceramic-conductor composite structure: (a) schematic diagram of a conductive layer printed on seven layers of ceramic; (b) fabrication results.

A layer of ceramics printed over the IDT conductors was able to enhance the structure as shown in Figure 4-12. An *S*-beam and flat beam structures were clearly formed, but there were cracks in the ceramics at the anchor area, which connected to the base.

Therefore, this can be concluded that ceramics are playing two roles, one of which is to protect the conductor layers from burning in high temperature and the other role is to have a flattening effect on the free-standing structures. The ceramics, however, are brittle and not strong enough to withstand the thermal shock which will result in cracking. In order to prevent this issue, a layer of Ag/Pd was printed prior to the IDT electrodes as shown in Figure 4-13. This metal layer acts as a mechanical support platform for the brittle PZT cermet structure.
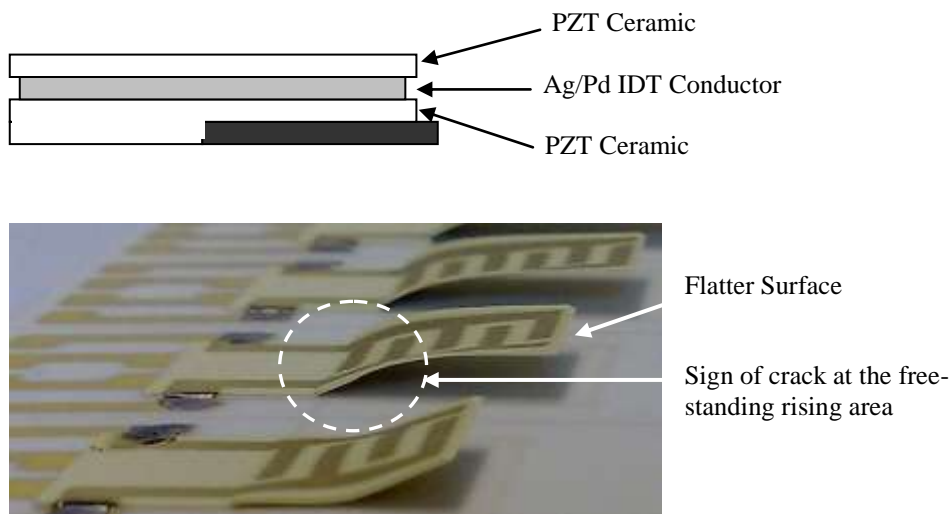
Figure 4-12: Enhanced structures with a layer of ceramic printed over Ag/Pd IDT conductors.
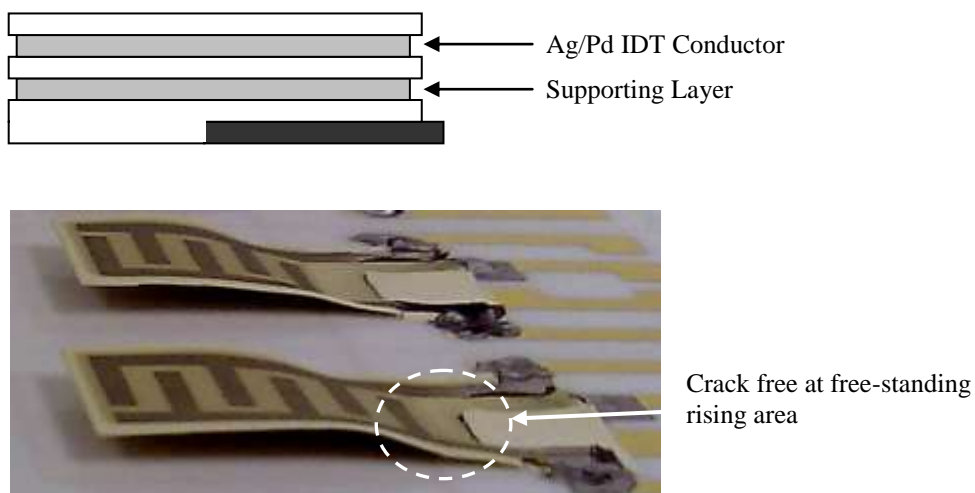
Figure 4-13: A layer of Ag/Pd as supporting layer can prevent the cermet from cracking after co-firing.

4.6.4 Multilayer PZT-Ag/Pd

At a co-firing profile with peak temperature of 850 °C, the upper and lower layer of Ag/Pd conductors suffer warping effects and peeled off from the surface of the ceramics as shown in Figure 4-14. This is because the lower electrodes tend to pull the structures down while the upper layers pulled the structure the opposite way as an effect of different thermal expansion coefficient between ceramics and electrodes.
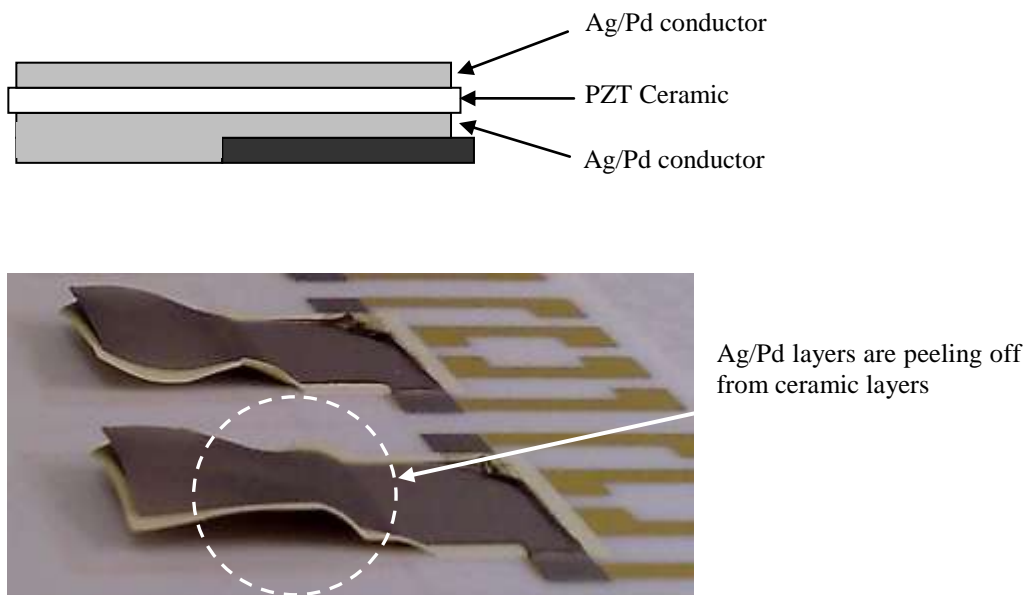
Figure 4-14: Upper and lower electrodes peeling off from ceramic layers.

The warping effect was minimised by covering the bottom Ag/Pd conductor with a layer of PZT, and the resultant of fabrication is shown in Figure 4-15. However, the structure is not flat; they can be seen to be curved side-ways to form a "U" shaped structure and pulled the structures off the substrate.

The structures can be further improved by covering the upper Ag/Pd electrode with another layer of PZT. The resultant structures are flatter and adhered firmly to the substrate as shown in Figure 4-16. This experiment established that PZT ceramic film is effectively acting as a protective layer to prevent Ag/Pd conductors from suffering warping effects at high temperatures.

Ag/Pd Electrode

PZT Ceramic

Carbon Sacrificial Layer

Ceramic pulling off
from substrate

Curving side-way
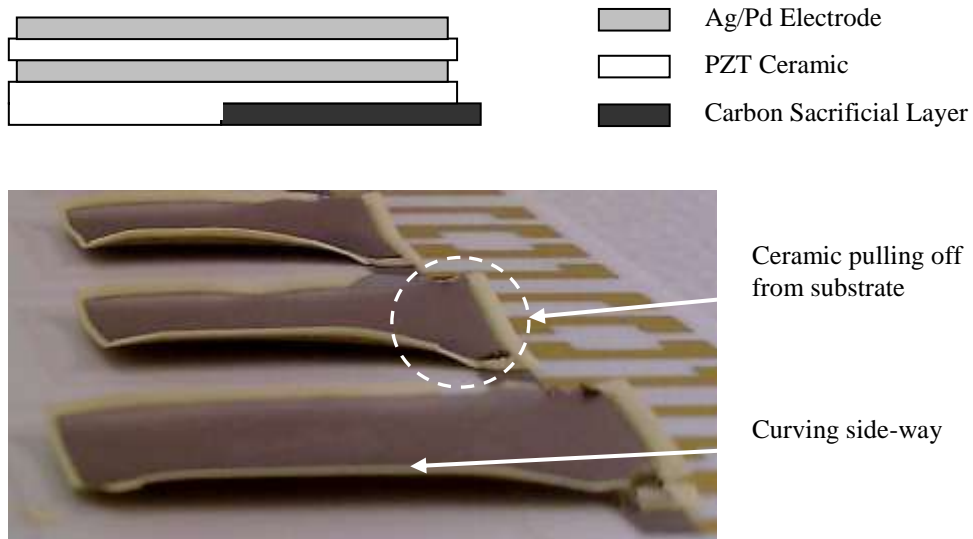
Figure 4-15: Composite films of ceramic-electrode-ceramic-electrode which curve side-way and
pull off from substrate.

Ag/Pd Electrode

PZT Ceramic

Carbon Sacrificial Layer

Ceramic is adhered
firmly to the substrate

Flat Beam Structure

S-Beam Structure
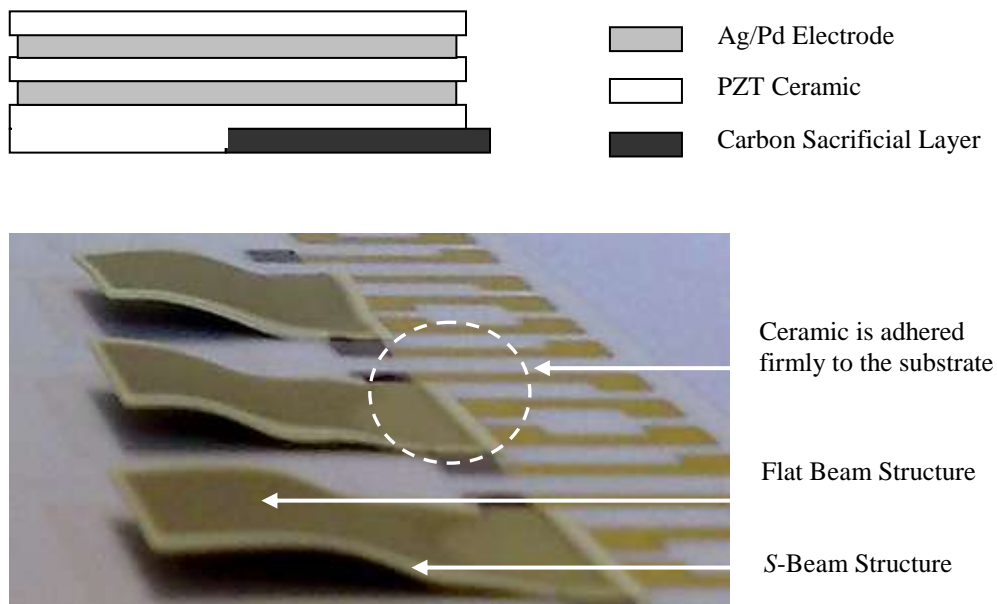
Figure 4-16: Flatter free-standing structures as a result of protective films of ceramic printed on
both upper and lower side of the structures.

101

4.7 Final Fabricated Samples and Polarisation

The composite free-standing structures with different length were fabricated. Longer structures formed distinctive features of *S*-beam and flat beam, which are raised to an angle of about 45° from the base to form flat cantilever beams at a height of 2 mm from the substrate as shown in Figure 4-17. There are signs of warping effects on the exposed Ag/Pd layer, peeling off from the substrate near to the solder pads. This problem can be solved by covering with a layer of PZT to protect them from exposure to high processing temperatures.
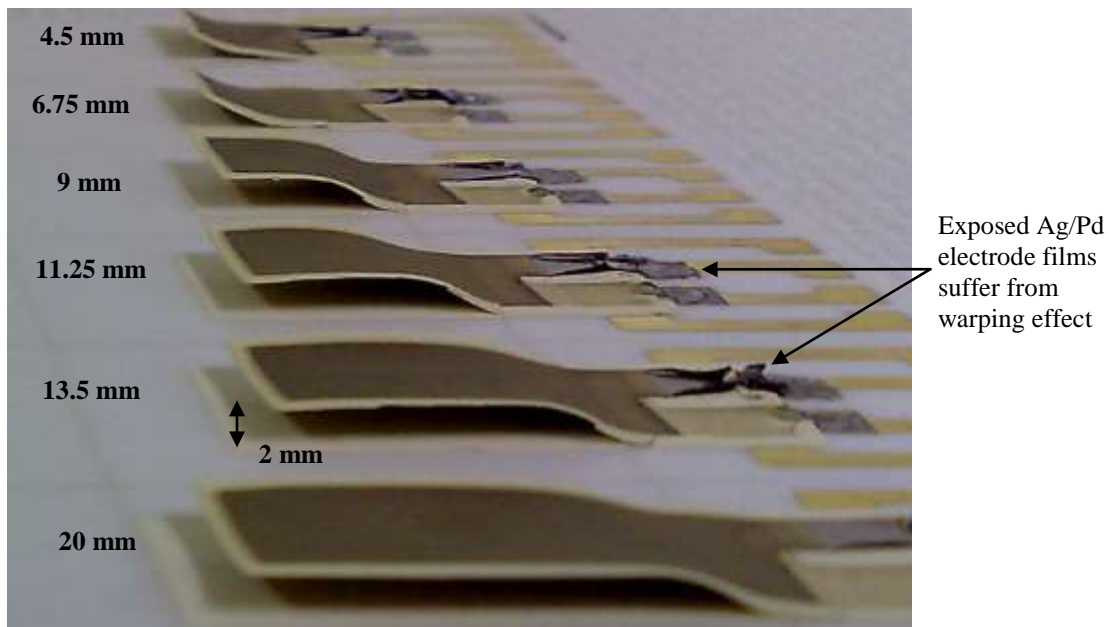
Figure 4-17: Photograph of fabricated samples of free-standing cantilever with different lengths with a gap height of 2 mm.

Due to the high thermal expansion coefficient of Ag/Pd material, a shrinkage of 10 % from the original design size was noticed, as shown in Figure 4-18. A few samples with no additional layer of PZT covering on the upper electrode were also fabricated to investigate their mechanical and electrical properties. These samples appear to be slightly indented at the spine of the cantilever making a 'U' shaped free-standing cantilever as shown in Figure 4-19.

(a)   (b)
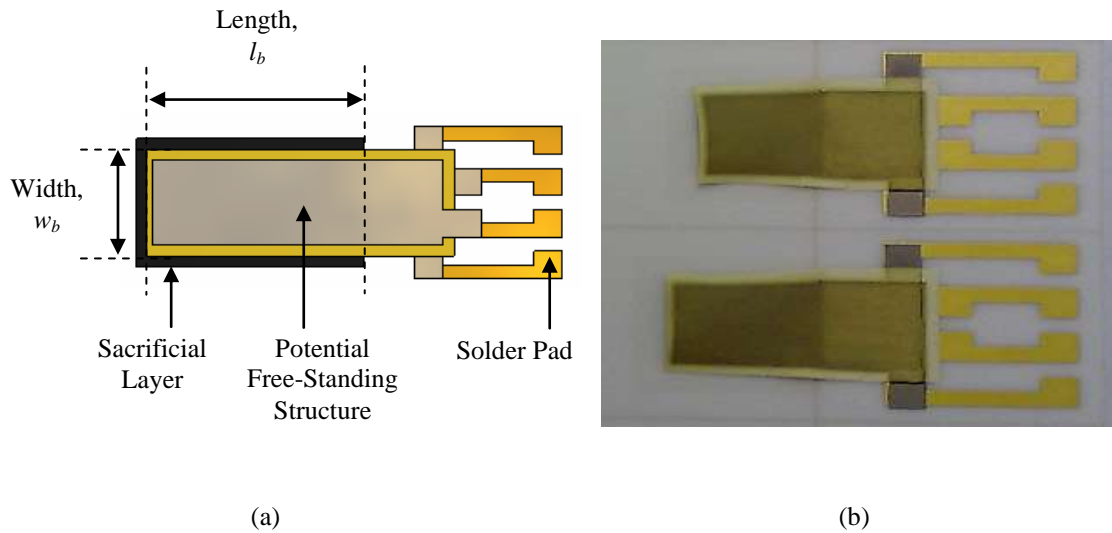
Figure 4-18: Photographs of free-standing structures: a) original designed model, with length, l_0 and width, w_0; b) samples of fabrication outcome.

Top View   Side View
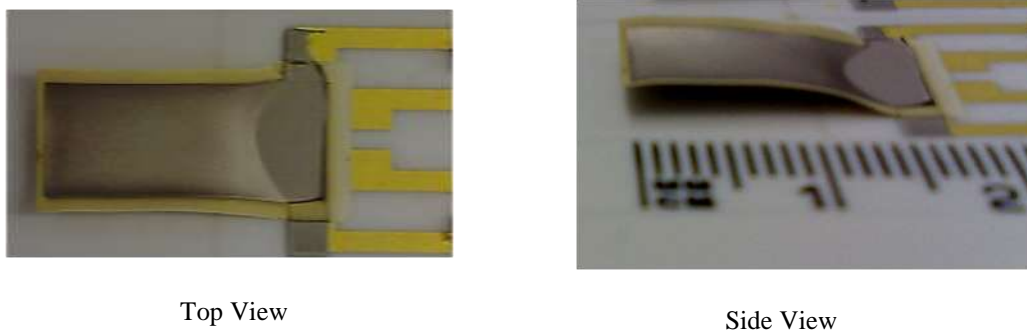
Figure 4-19: Sample A1 with no additional PZT covers on the upper electrode.

Polarisation is the final fabrication step, which is needed to induce remnant polarisation in piezoceramic materials before they are piezoelectric. An electric field up to several MV/m (typically 2-5 MV/m) is applied to the upper and lower electrodes of the sandwich structure, at an elevated temperature (typically 80-150 °C). The electric field is applied for around 30 minutes, and the sample is allowed to cool down to room temperature for another 30 minutes before the electric field is removed. This is to prevent the sample from depolarising below the Curie temperature. The influence of poling conditions such as poling temperature, poling electric field and poling duration on piezoelectric properties of thick-film PZT had been studied by Dargie *et al* [104].

The experimental results showed that a higher piezoelectric charge coefficient, d_{33} was measured at a higher polarisation temperature of 150 °C. Combining with polarisation field strength of 2.5 MV/m, a maximum value of coefficient was obtained at about 200 pC/N. Further increments of the electric field strength did not show any improvement in the piezoelectric activity.

Some of the plated and IDE fabricated samples were polarised to further investigate their mechanical and electrical properties in the following chapters. A set-up of the polarisation is shown in Figure 4-20. The samples were polarised with different field strengths at a constant temperature of 200 °C on a hot-plate. It was found that, the piezoelectric layer suffered electrical short circuits when it was polarised with an electric field strength greater than 5 MV/m. Therefore, all the samples were polarised at slightly lower field strengths to prevent the high voltage from damaging the device. All the successful polarised samples are listed in Table 4-2.
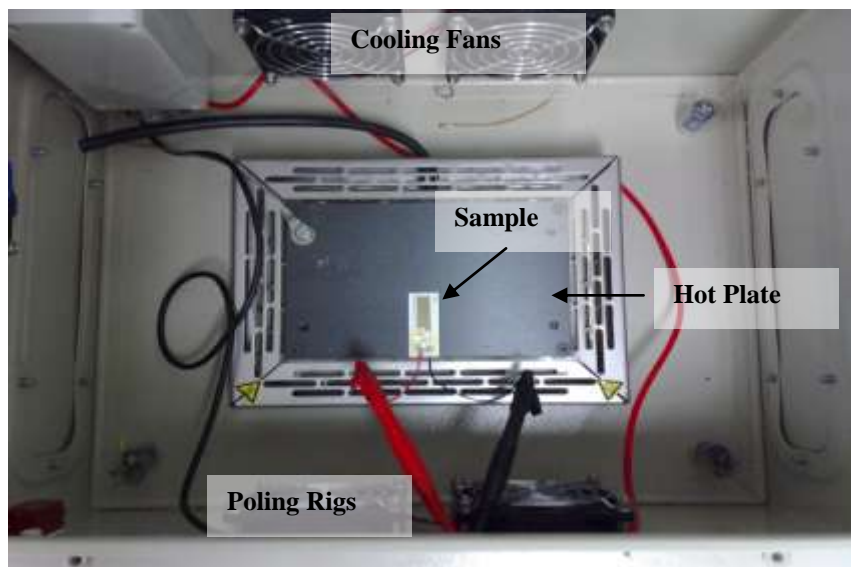
Figure 4-20: Polarisation set-up.

Table 4-2: Summary of Polarised Samples.

Sample	Geometry			Poling			Process
	Length (mm)	Width (mm)	Total Thickness * (um)	V(V)	Temp (^{0}C)	Time (min)	
A1	13.5	9	114	180	200	30	2PZT + 2S/P + 4PZT + 2S/P
B1	11.25	9	114	180	200	30	2PZT + 2S/P + 4PZT + 2S/P
C1	6.75	9	135	200	200	30	
C2	9	9	135	200	200	30	2PZT + 2S/P + 4PZT + 2S/P + 2PZT
C3	13.5	9	135	200	200	30	
C4	18	9	135	200	200	30	
D1	4.5	9	124	220	200	30	
D2	6.75	9	124	220	200	30	
D3	9	9	154	220	200	30	2PZT + 2S/P + 4PZT + 2S/P + 1PZT
D4	11.25	9	124	220	200	30	
D5	13.5	9	124	220	200	30	
D6	18	9	124	220	200	30	
IDa1	9	9	208	300	200	30	2PZT + 2S/P + 4PZT + 2S/P + 2PZT

Note:
2PZT + 2S/P denotes a process of printing and drying two layers of PZT followed by print and dry two layers of silver/palladium.
All the samples are co-fired with Profile 850.

4.8 Conclusion

A one-step air co-firing technique was used to fabricate free-standing structures, where the different thermal expansion coefficient between the conductors and cermets was exploited.

The method was based on a combination of conventional thick-film technology and a sacrificial layer technique. A carbon sacrificial layer was printed on a substrate followed by a series of prints of PZT pastes and Ag/Pd pastes one after another and co-fired together at a peak temperature of 850 °C in a multi-zone furnace with a constant air flow. At the same time that the carbon sacrificial layer was burnt out, the composite films were sintered, resulting in solid and firm free-standing structures which were released at the end of the process, as a result of pre-stress effect.

The resultant PZT cermets were found to be brittle and fragile, and were not able to establish on their own. From the experiments, the Ag/Pd conductors were found to be able to support the cermets structures, besides acting as the electrodes. Higher thermal expansion coefficient compared to the PZT piezoceramic is the major weakness of Ag/Pd conductor. As the rate of expansion and contraction of Ag/Pd conductors are faster than the cermet, the films suffer from warping effect after a co-firing process. This problem was solved by printing an additional layer of PZT cermet on each of the exposed areas at the lower and upper electrode layers.

The fabricated free-standing structures were in the form of an elevated free-standing structure with a gap height of 2 mm and a flat beam extended from the *S*-beam. The overall structures were shrunk by about 10 % from the original design. Finally the samples were polarised to increase the piezoelectric activity in the PZT layers.

Chapter 5   Piezoelectric Materials Characterisations

5.1   Introduction

Five series of samples as described were characterised; A, B, C, D and IDa. Samples A, B, C and D are multilayer cantilever structures with plated electrodes, while sample IDa is a cantilever with interdigitated (IDT) electrodes. Each series of samples was fabricated in the same way, but with slight differences in the printing process as summarised in Table 4-.

Firstly, the thickness of the samples was measured with a Solder Paste Inspection Data Analyst (SPIDA) system. SPIDA is a non-contact, optical inspection and measurement system designed for measuring wet or dry solder paste deposits, which is suitable to measure the thickness of thick-films deposited on rigid substrates.

In order to investigate the structural and electrical properties of the piezoceramic samples, the free-standing part of the samples were detached from the base. In this condition, the samples are flexible and easier to handle. The surface and structural properties of the free-standing piezoceramic samples were inspected using a Scanning Electron Microscope (SEM) at magnifications of 300, 800 and 4000. Two series of samples similar to sample D but co-fired at different profiles with peak temperatures of 850 °C and 950 °C were also inspected. These samples were also measured for their piezoelectric charge constant, d_{33} using the Berlincourt method. A dynamic measurement method, however, requires an external excitation voltage to produce the

measurement; therefore the samples have to be connected to the electrode pads adhered on the substrate. The measured electrical properties of the unclamped (free-standing) piezoceramic will be compared with clamped samples to verify the theory developed by Torah *et al* [82] and Steinhausen *et al* [84].

5.2 Thick-Film Dimensions Measurement

The thickness of the films was measured using a Solder Paste Inspection Data Analyst (SPIDA) system, Z-Check 700 S (www.timco-worldwide.com), as shown in Figure 5-1 (a) is a non contact inspection and measurement system designed for measuring solder paste deposits, adhesive glue, component placement and a wide range of related electronic assembly applications.

The SPIDA system consists of a glade table where samples are positioned and inspected under a video camera with a magnification of up to 160. With the assistance of a laser pointer, the thickness of the thick-film sample can be calculated by measuring the different between the "high point" and "low point" of the light as shown in Figure 5-1 (b). The calculation is performed on the captured video image by image processing software provided by the manufacturer.

Film thickness is dependent on the viscosity of the thick-film paste, the coarseness of the screen mesh, the screen emulsion thickness and the adjustable printing gap between substrate and screen. Two 12 inch × 12 inch screens with different mesh coarseness (defined by the density and thickness of the mesh filaments) and different emulsion thicknesses were used for printing the PZT ceramics and the electrodes. A screen with a wider mesh opening of 250 meshes (number of wires per inch) and emulsion thickness of 25 μm was used for printing the PZT ceramics, whilst a smaller opening mesh (325 wires per inch) and 20 μm thick emulsion was used for finer printing of the electrodes.

Since gold is more expensive then Ag/Pd, it is not used as the electrode material. However, the electrode pad that provides electrical connection to the device requires a high temperature solderable material; therefore a thin layer of gold is used for this component of the design. Besides playing a role as an electrode, the Ag/Pd layer also acts as the physical support platform for the free-standing structure. Two printed-dried

layers of Ag/Pd are necessary to provide this physical support. The electrodes (gold and Ag/Pd) do not contribute to the piezoelectric activity in the structure and therefore it is desirable that they are thin, which can be realised by printing using screens with higher mesh densities. Thinner and finer electrodes can produce higher definition of print which is important when fabricating multilayer structures as well as reducing the overall cost of fabrication.

Monitor screen

Video camera with magnificent up to ×40

White Light source

Device under measurement

Laser pointer

(a)

"High point" of the laser light

"Low point" of the laser light

Z = 0.064   Thickness readings

(b)
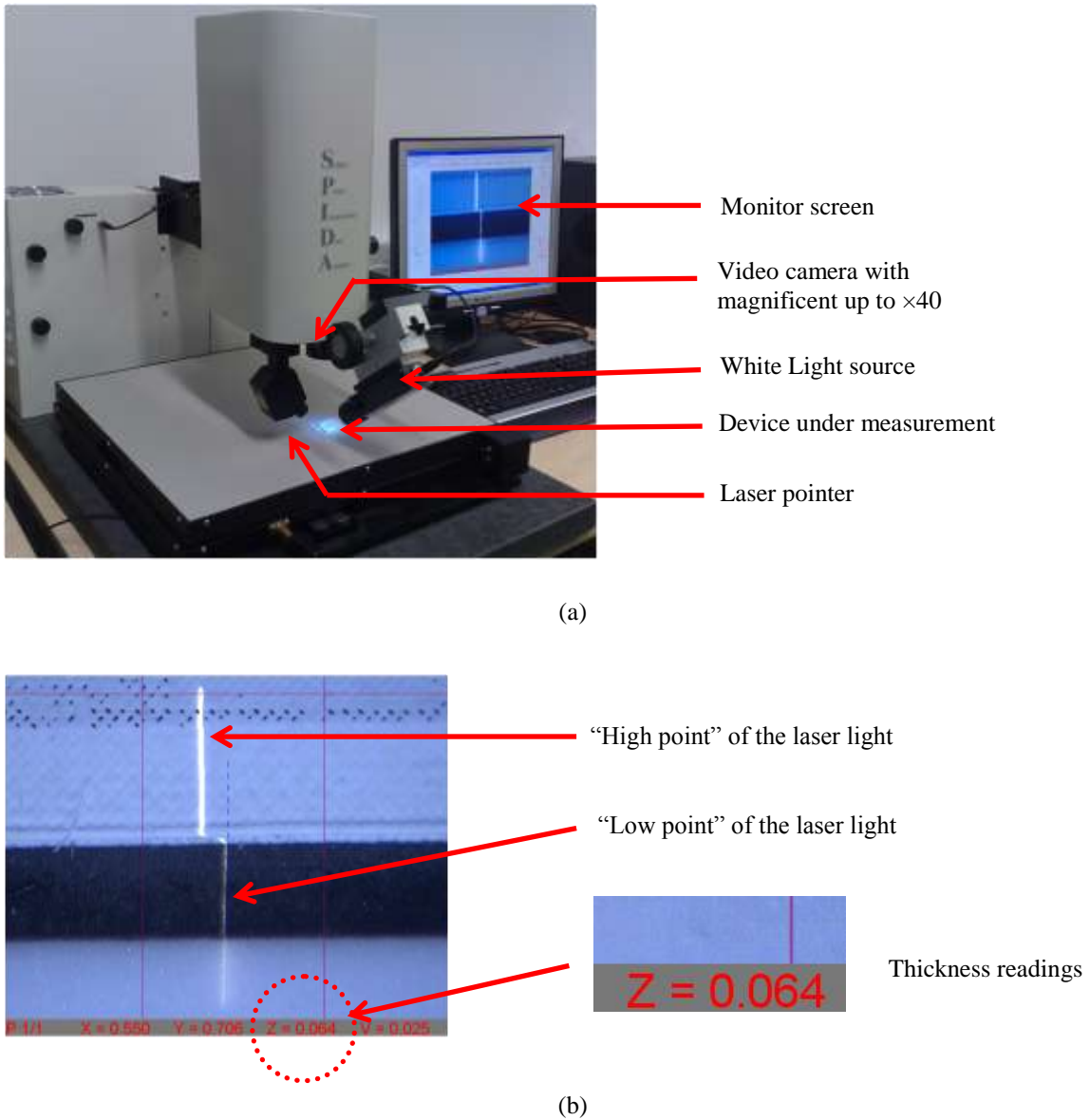
Figure 5-1: Photographs show: (a) A SPIDA system set-up and (b) a thick-film sample under inspection.

The thickness of the films is an important parameter when predicting the mechanical and electrical performance of the device, especially the PZT and the Ag/Pd electrode layers. Three samples for each device were measured after co-firing at 850 °C, the average thicknesses of the devices are listed in Table 5-1.

Table 5-1: Thick-film thickness measured with SPIDA system.

Thick-Film Material	Process	No. of Layer	Average Thickness (µm)
Gold (ESL 8836)		1	12
Ag/Pd (ESL 9633B)	Co-fired at 850 °C	1	12
		2	20

The thicknesses of four samples for each of the device were measured before and after co-firing. The effective thickness to be taken into account when predicting the mechanical and electrical performance of a free-standing structure is the thickness after co-firing, which suffers a reduction of around 10% compared to the thickness before they are co-firing. Figure 5-2 shows the thickness of PZT as a function of the number of layer for two conditions; printed-dried and printed-dried-co-fired. The plot shows that the thickness of the printed-dried films increases linearly with the number of layers. However, when the films were co-fired, the overall thickness decreases which becomes significant as the number of layers increases. For instance, eight layers of printed-and-dried PZT produced a thickness of about 125 µm, which reduced to 112 µm after co-firing at 850 °C as shown in Figure 5-2.
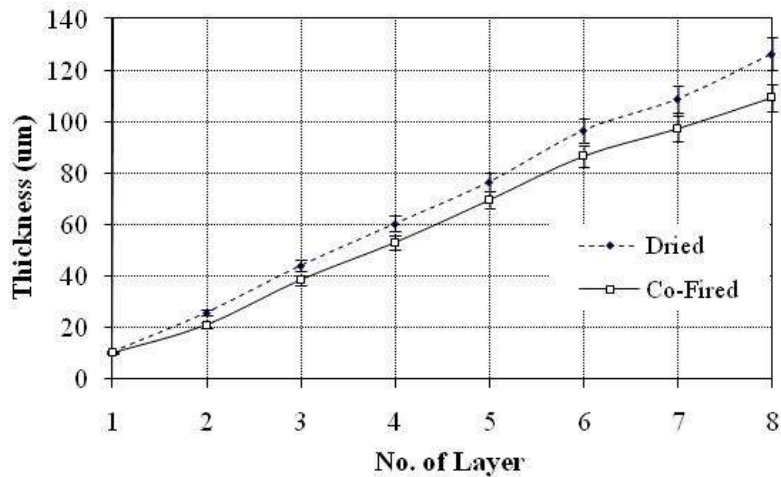
Figure 5-2: PZT thickness before and after co-firing.

5.3 Thick-Film Free-Standing Samples under SEM Inspection

Multilayer composite structures with five sections of laminar PZT and four layers of Ag/Pd, printed in a sequence of PZT-Ag/Pd-PZT-Ag/Pd-PZT-Ag/Pd-PZT-Ag/Pd-PZT were examined. Figure 5-3 shows SEM images of two multilayer samples co-fired with temperature profiles with peaks at 850 °C and 950 °C.

The fabrication process has a very important influence over the formation of microstructure and hence the mechanical and electrical properties of the piezoceramic materials. From the SEM micrographs at a magnification of 300 it can be seen that, sample co-fired at 850 °C profile produced Ag/Pd layers which are in a relatively uniform shape and have a definite separation between the electrode and PZT layers, compared to sample co-fired with 950 °C profile. One of the risks of co-firing at high temperature is the electron migration from electrode to PZT layers, which may reduce the capacity of polarisation of the PZT material.

The population of pores and void spaces for both samples are rather similar when inspected under a magnification of 800. The voids are formed by intercrystalline boundaries between the piezoceramic and electrode layers, and spaces between the grains, which range from several to several tens of micrometers. The presence of the

111

voids is largely due to the nature of the screen-printing process and the size of the granules used in the thick-film paste formulation. They are responsible for the reduction of fracture strength [105] and capacity of polarisation, which explains why some piezoelectric material samples experienced internal short circuits when polarised above an electrical field strength of 3 MV/m, as discussed in the previous chapter.

(a)

(d)

(b)

(e)

(c)

(f)
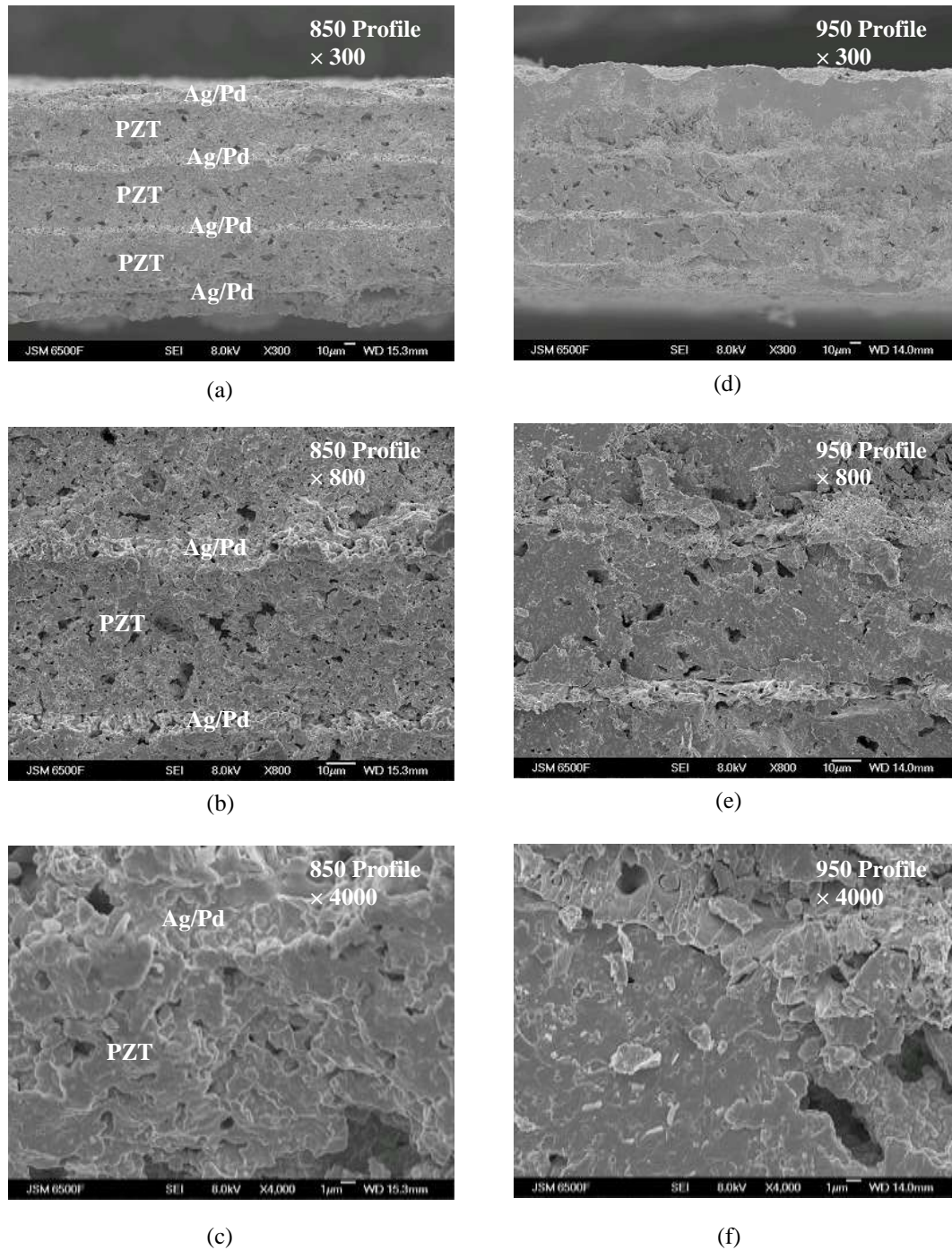
Figure 5-3: SEM micrographs of samples co-fired at 850 °C and 950 °C under magnification of ×300, ×800 and ×4000.

As sintering temperature increases from 850 °C to 950 °C, the adhesion of granules was improved as shown in Figure 5-3 (f), therefore increasing the density of the material. A denser piezoceramic typically has higher piezoelectric activity. At higher temperature, however, the Ag/Pd expands and contracts faster when cooled to room temperature. This effect results in deformation of the electrode layer and may weaken the overall structure.

5.4 Resonant Measurement

The resonant measurement method is commonly used to measure piezoelectric properties of the bulk material. However, it is not suitable for the measurement of piezoelectric properties of thick-film PZT when it is printed on a substrate due to mechanical clamping effects of the substrate [82]. Hence, a non-clamped thick-film in free-standing form is an alternative solution as a tool to characterise the thick-film piezoelectric properties. The properties that were measured were constant electric field elastic compliance, s_{11}^E, constant displacement elastic compliance, s_{11}^D, coupling factor, k_{31}, piezoelectric charge coefficient, d_{31}, piezoelectric voltage coefficient, g_{31} and mechanical quality factor, Q_m of the piezoelectric materials.

Before calculating relevant piezoelectric parameters, the capacitance (at constant stress or stress free) of the devices was measured. This was carried out with an LCR meter at 1 kHz (Wayne Kerr). Sample D series which were polarised at a higher dc voltage of 220 V produce higher capacitance compared to sample C series which were polarised at 200 V. A plot of capacitance against the dimensions of the material for both samples, as illustrated in Figure 5-4, shows a linear relationship between the capacitance and the ratio of area to the thickness of the materials, which is in a good agreement with equation (2-5). From the extrapolation of the graph in Figure 5-4, the average value of permittivity, ε_{33}^T of sample C series can be calculated as 4 nF/m and sample D series as 4.3 nF/m.
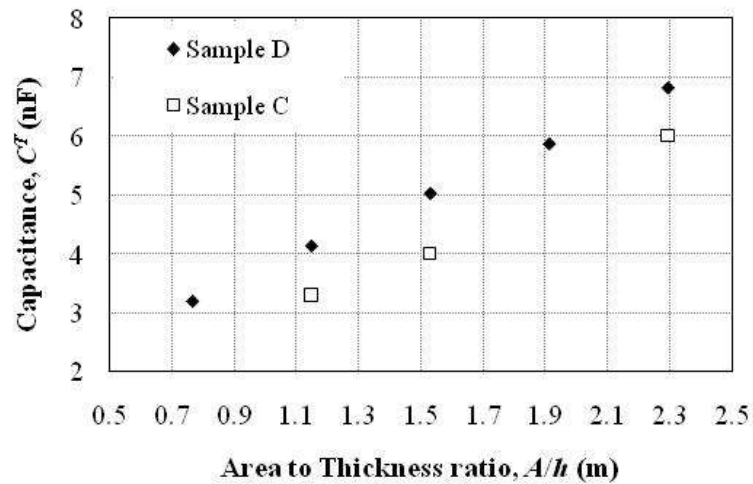
Figure 5-4: Comparison of sample D and C series for the value of capacitance over the ratio of area/thickness (with ± 5% error).

The resonant and antiresonant frequencies that correspond to the minimum and maximum impedances of the materials are important variables to determine the piezoelectric constants of the materials. The frequency response of the samples was measured by using Network/Spectrum Analyser (HP 4195A) between 100 kHz to 500 MHz. The resonant and antiresonant frequencies for sample D series can be identified by the magnitude of the impedance as shown in Figure 5-5.

There are a few possible modes of vibration in the range of 120 kHz to 280 kHz: lateral, longitudinal and thickness modes. For all the samples of series C and D, the thickness vibration mode is not significant compared to the lateral and longitudinal modes. This is due to the fact that the length and the width of the samples are more than 50 times bigger than their thickness.

The lateral vibration mode was observed for samples D1 and D2 which is about 180 kHz, however, the lateral mode diminishes as the length of the sample increases which can be see in sample D3 – D5 as shown in Figure 5-5. The resonant frequency of the longitudinal mode for sample D1 is about 240 kHz and reduced to about 185 kHz for sample D5. From equation (2-4), the average value of d_{31} for sample D series is about 33.9 pC/N.

114
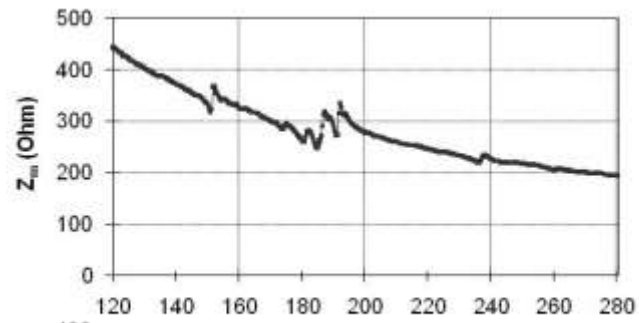
Sample D1

Sample D2
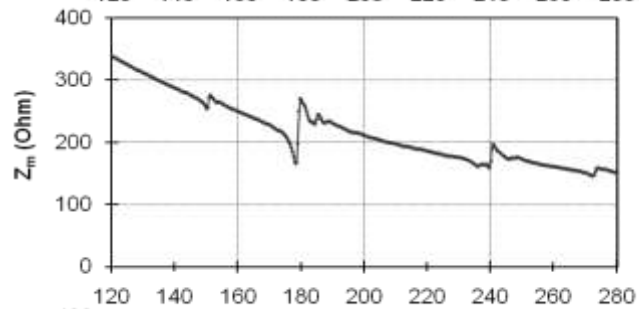
Sample D3
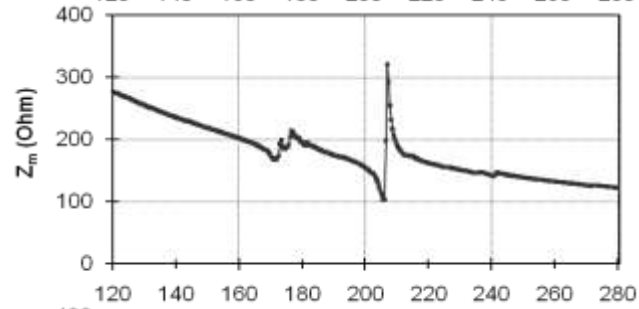
Sample D4
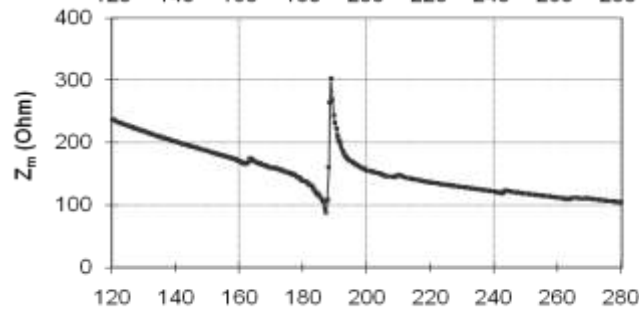
Sample D5
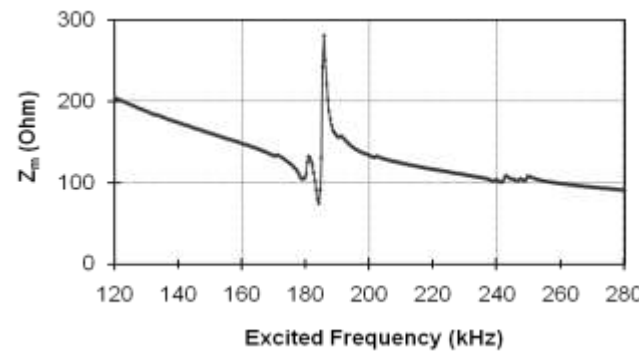
Figure 5-5: Frequency response for sample D1, D2, D3, D4 and D5, corresponds to their impedance.

Similar to the case of sample D series, Figure 5-6 shows the frequency response for sample C series. Sample C2, which has a square dimension displays two significant vibration modes. One of which is the lateral mode, at a resonant frequency of 165 kHz and the other one is the longitudinal mode, which happens at around 235 kHz. For sample C1, with its length smaller than its width, the lateral mode occurs at the resonant frequency similar to sample C2, at 165 kHz, due to the fact that their dimensions are almost similar which results in poor output from longitudinal vibration mode. As the length of the sample increases and becomes larger than its width (sample C3), the longitudinal vibration mode becomes prominent which happens at a resonant frequency of 178 kHz, while the lateral mode diminishes as the length of the sample increases. The resonant frequency is inversely proportional to the length of the material, as shown in Figure 5-7, which is in good agreement with equation (2-4). The average value of d_{31} for sample C series is 24 pC/N, which is slightly smaller than sample D series.
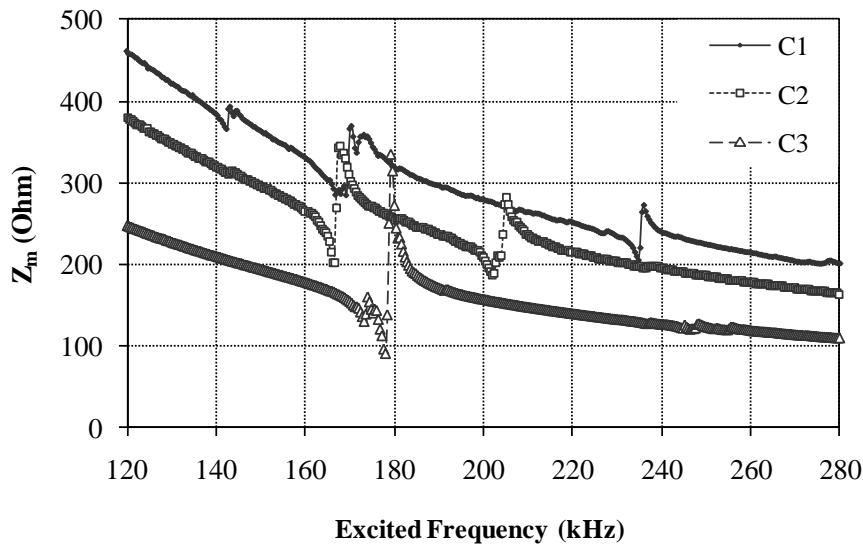
Figure 5-6: Frequency response for sample C series.

The longitudinal resonant frequencies of sample D and C series are inversely proportional to the length of the structure as indicated in Figure 5-7, which is consistent with equation (2-7). The elastic compliances at constant electric field, s_{11}^{E} for sample D ranges from 5.48×10^{-12} m^2/N to 12.9×10^{-12} m^2/N and ranges from 5.85×10^{-12} m^2/N to 13.4×10^{-12} m^2/N for sample C series, with the assumption that, the density of PZT type-5H is 7400 kg/m^3 [31].
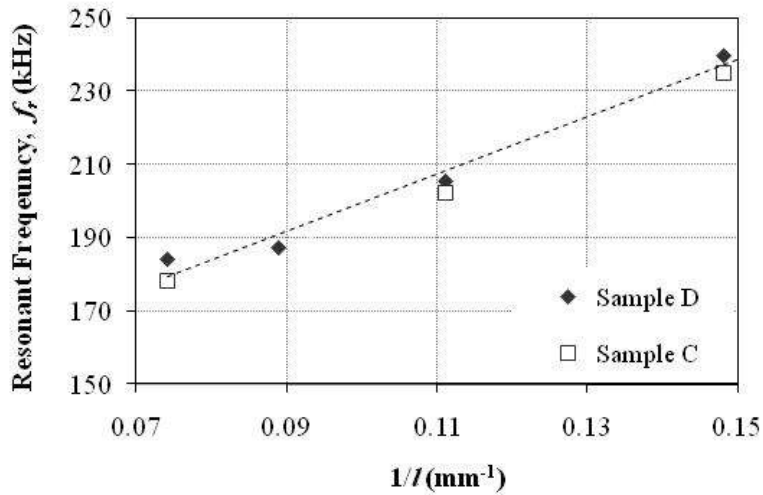
Figure 5-7: Resonant frequency as a function of inverse of cantilever length.

The coupling factor for the material can be estimated by substituting the measured values of d_{31}, ε_{33}^T and s_{11}^E into equation (2-6). Figure 5-8 shows that the coupling factor increases with length of the materials. For example, the coupling factor for sample D series increases from 0.127 at a length of 6.75 mm to 0.216 at a length of 18 mm, while sample C series has a slight reduced coupling factor of 0.12 at a length of 6.75 mm and increases to 0.192 at a length of 13.5 mm.
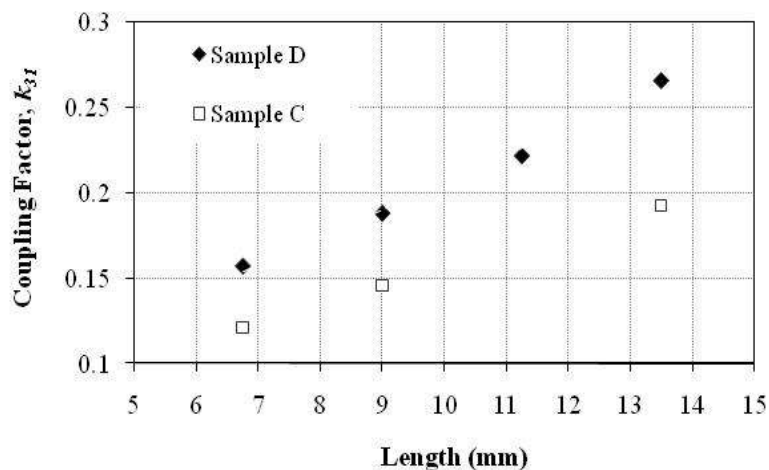
Figure 5-8: Coupling factor of sample D and C series as a factor of material length.

From equation (2-8), the constant displacement elastic compliance, s_{11}^D for sample D series ranges from 5.1×10^{-12} m²/N to 12.6×10^{-12} m²/N, while that for sample C series

117

ranges from 5.63×10^{-12} m^2/N to 13.3×10^{-21} m^2/N. The piezoelectric charge coefficients calculated from equation (2-9) for samples D and C series range from 9.38×10^{-3} Vm/N to 11.4×10^{-3} Vm/N and 8.3×10^{-3} Vm/N to 9.1×10^{-3} Vm/N, respectively.

As expected, the impedance reduces as the length of the material increases as shown in Figure 5-9. The minimum impedance (impedance at resonant frequency) is proportional to the ratio of thickness to the area of the material. The impedances at resonant frequency were measured for evaluating the mechanical quality factor, Q_m of the materials according to equation (2-10). The mechanical quality factor for the samples was calculated and plotted in Figure 5-10. On average both samples have a Q-factor, Q_m of the order of 120. The experimental results obtained by the resonant measurement method for all the piezoelectric properties are summarised in Table 5-2.
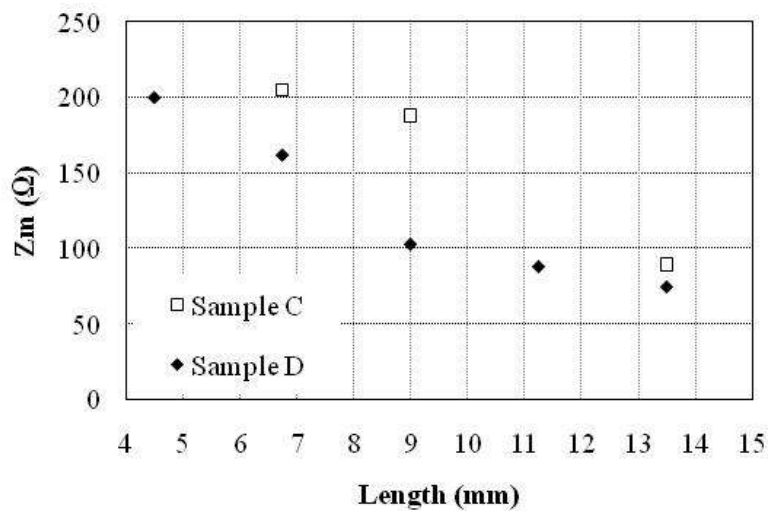
Figure 5-9: The impedance at resonance is proportional to the ratio of thickness to the area of the material.
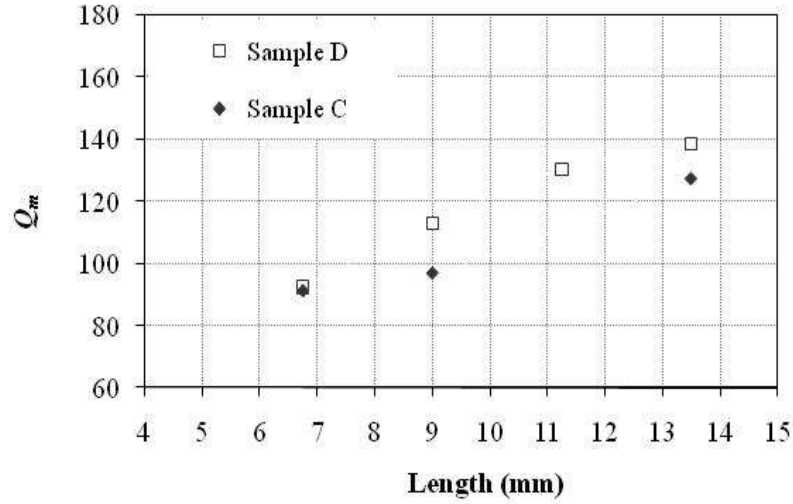
Figure 5-10: Mechanical quality factor, Q_m for sample C and D series.

Table 5-2: Summary of measurement results from resonant measurement method for sample C and D series.

Piezoelectric Constant			C			D			
			C1	C2	C3	D2	D3	D4	D5
Constant electric field elastic compliance	s_{11}^E	$\times 10^{-12}$ m²/N	13.4	10.2	5.9	12.9	9.9	7.6	5.5
Constant displacement elastic compliance	s_{11}^D	$\times 10^{-12}$ m²/N	13.3	10.0	5.6	12.6	9.5	7.2	5.1
Permittivity	ε_{33}^T	$\times 10^{-9}$ F/m	2.9	2.6	2.6	3.6	3.3	3.1	3.0
Relative dielectric constant	K_{33}^T	dimensionless	325	295	295	4.8	372	347	336
Coupling factor	k_{31}	dimensionless	0.12	0.15	0.19	0.16	0.19	0.22	0.27
Piezoelectric charge coefficient	d_{31}	$\times 10^{-12}$ C/N	-29	-26	-21	-39	-32	-25	-22
Piezoelectric voltage coefficient	g_{31}	$\times 10^{-3}$ Vm/N	-8.3	-9.1	-9.1	-9.4	-10.3	-11.0	-11.4
Impedance at resonance	Z_m	Ω	205	188	90	162	103	88	75
Mechanical quality factor	Q_m	dimensionless	99	89	125	100	103	138	130

5.5 Direct Measurement (Berlincourt Method)

The piezoelectric charge coefficient, d_{33} can be measured directly with a commercial Berlincourt piezometer system (www.piezotest.com), as shown in Figure 5-11 (a). The piezoelectric specimens were obtained by detaching the free-standing part of the samples from their base on the substrate. The specimens were then inserted in between a loading contact of the piezometer system as shown in Figure 5-11 (b). A continuous alternating force is applied on the specimen resulting in production of charges, corresponding to the d_{33} piezoelectric effect. The magnitude of the measurement result is a ratio of short circuit charge density over the applied stress, according to equation (2-2).

<table>
<tr><td>(a)</td><td>(b)</td></tr>
</table>
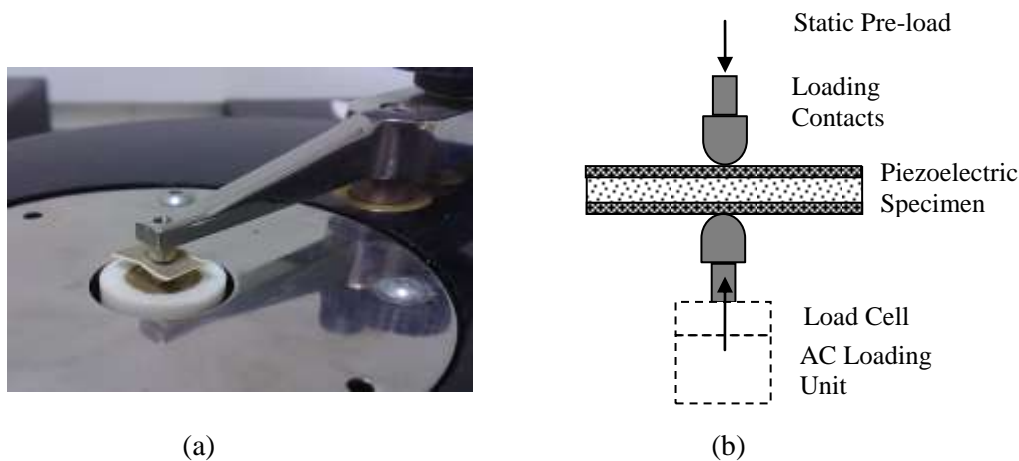
Figure 5-11: A photograph (a) and a schematic diagram (b) showing a piezoelectric specimen being measured with the Berlincourt measurement method.

5.5.1 Effect of Substrate Clamping

Conventionally, thick-film piezoelectric materials are printed on a rigid support substrate. This rigidly clamps the films to the substrate and imposes a deformation restriction on the lower surface of the films when stress is applied as shown in Figure 5-12. There are a few possible types of mechanical clamping for a film printed on a substrate [84]; one of which is where the piezoelectric film is mechanically bonded with an inactive substrate. With the presence of the substrate, an interfacial stress occurs between the printed piezoelectric film and the substrate and causes the measured effective piezoelectric coefficient d_{33} to reduce from the true value [82]. This is because

of the influence of the d_{31} component in the film when a deformation of the structure occurs.
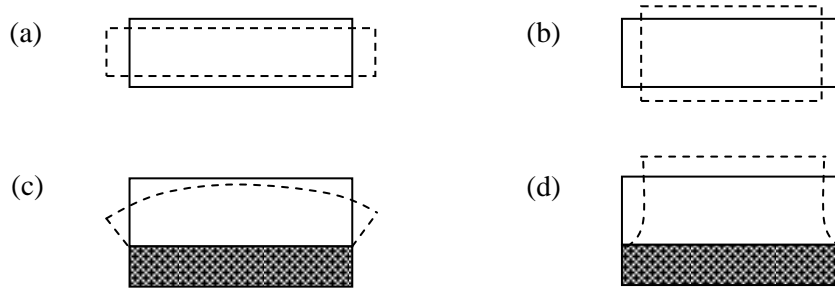
Figure 5-12: Diagram of a free-standing film in expansion (a) and contraction (b) compared to a clamped film in expansion (c) and contraction (d).

Theoretical analysis [82] shows that a reduction of measured d_{33} is inevitable for a clamped sample according to

$$d_{33(clamped)} = d_{33(unclamped)} - 2d_{31}\left[\frac{\left(\dfrac{v_{substrate}}{e_{substrate}}\right) + s_{13}^{E}}{s_{11}^{E} + s_{12}^{E}}\right] \tag{5-1}$$

By substituting the parameters for the properties of an alumina substrate and a clamped thick-film as listed in Table 5-3 into equation (5-1), the unclamped d_{33} can be estimated, which is slightly more than 80% compared to the measured value of a clamped sample.

Another problem associated with the determination of d_{33} is the fact that the system of substrate-piezoelectric film acts as a natural bending element. Therefore, to determine d_{33} correctly, the change in thickness of a specimen between two opposite points at the upper and the lower side of the sample must be measured [84].

Free-standing films are not completely free from the clamping effect: for example, the electrode itself may cause a mechanical clamping. However the thickness of the electrodes is much smaller than the piezoelectric films and furthermore the elasticity of Ag/Pd electrode is greater than the piezoelectric film, therefore the clamping effect of the electrode-PZT can be neglected [84].

Table 5-3: Parameters for 96 % alumina substrate [82].

Parameter			Value
Poisson ratio	$v_{substrate}$	dimensionless	0.25
Young's modulus	$e_{substrate}$	$\times 10^9$ Pa	331
	s_{11}^E	$\times 10^{-12}$ m^2/N	16.4
Elastic compliance	s_{12}^E	$\times 10^{-12}$ m^2/N	-4.78
	s_{13}^E	$\times 10^{-12}$ m^2/N	-8.45

5.5.2 *Decay of d₃₃ over Time*

The measured piezoelectric charge coefficient decayed as a continuously varying stress was applied to the materials. This is a common phenomenon for piezoelectric materials and arises because of several factors, including the presence of a defective interface layer, which can give rise to the backswitching of domains [106].

A series of experiments were carried out to determine d_{33} for clamped and unclamped samples. A clamped sample, as shown in Figure 5-13 (a), was printed directly on an alumina substrate without a carbon sacrificial layer. The sample was fabricated with the process similar to sample D series, as described in Table 4-. The only difference is that the sample was not covered with a non-active PZT layer on both sides of the electrodes. This clamped sample will be compared with an unclamped sample similar to those of sample D series.

The measurements were taken at two different periods of time; one of which was taken just after the samples had been polarised and the other was taken after six months following polarisation. Comparisons were also made on d_{33} with two different co-firing profiles, 850 °C and 950 °C, for unclamped samples, as shown in Figure 5-13 (b).

Multilayer Films

Substrate

Score Line

(a)

Multilayer Films

Detached

Tweezer

Exposed Electrode

(b)
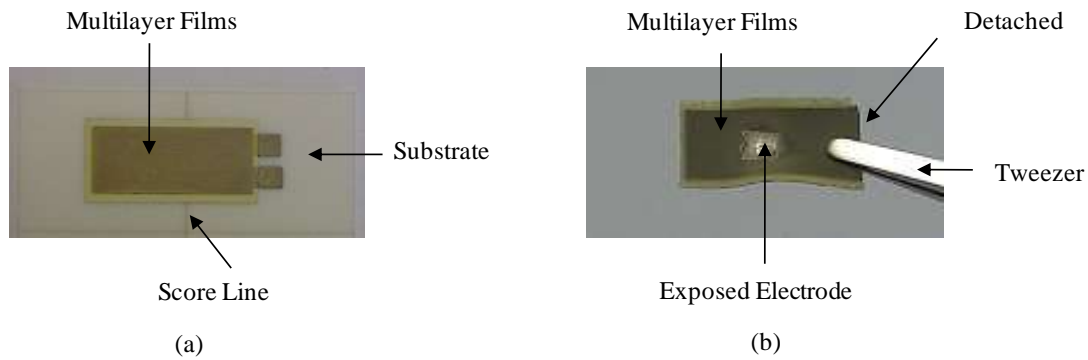
Figure 5-13: Photographs of (a) a clamped sample printed across a score line on a substrate and (b) an unclamped sample held with a pair of tweezers.

Figure 5-14 shows the d_{33} measurement results for the clamped sample at a continuous alternating mechanical force of 0.25 N at 110 Hz for 15 minutes at two conditions; one of which is taken just after polarisation and the other one is taken after six months from the first measurement. At the beginning of the measurement, a d_{33} value of 42 pC/N was measured which gradually dropped to 31 pC/N after 15 minutes. At the second measurement, 6 months after polarisation, the initial value decreased to 32 pC/N and after 15 minutes of continuous application of alternating force, the value decreased further to 22 pC/N, which shows a decaying rate of 29 % over a period of 6 months.
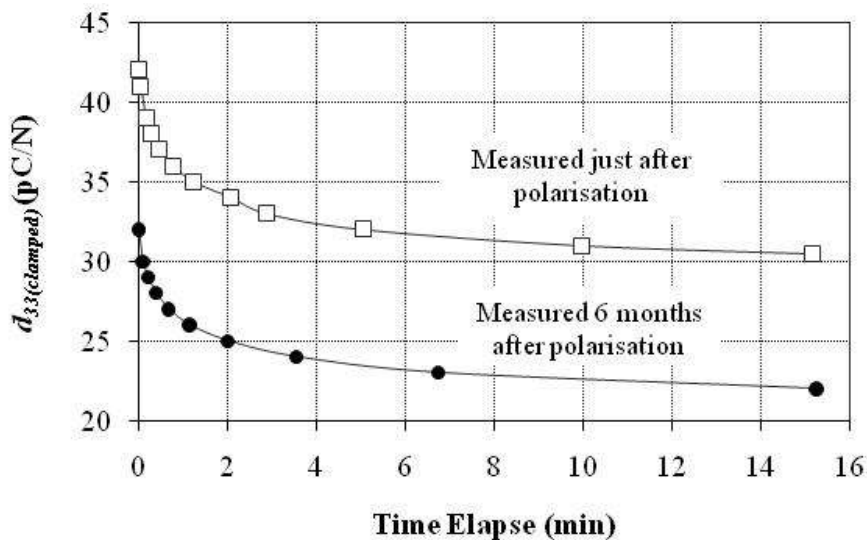
Figure 5-14: d_{33} as a function of time elapsed over 15 minutes for measurements taken just after polarisation and six months after polarisation for a clamped sample.

The measured value of d_{33} for a free-standing sample, similar to those of sample D series, is shown in Figure 5-15. The d_{33} of the sample decays from 78 pC/N to 55 pC/N as a continuous dynamic force is applied for 15 minutes. After a period of 6 months, the measured d_{33} decays from 48 pC/N to 35 pC/N for the same dynamic force, which corresponds to a decay rate of 36 %.

In another experiment, a comparison was made between unclamped (free-standing) samples co-fired at 850 °C and 950 °C. The initial value of d_{33} for the sample co-fired at 950 °C is 116 pC/N, which is more than a factor 1.5 greater than the value measured for the sample co-fired at 850 °C. After 8 hours of continuous application of dynamic force, the values of d_{33} for both of the samples decrease to 88 pC/N and 51 pC/N respectively, which correspond to decay rates of 24 % and 32 %. This verified that piezoelectric materials co-fired at a peak temperature of 950 °C perform better than those co-fired at 850 °C.

In the same way as samples C and D series, the piezoelectric properties of a sample fabricated at a co-firing profile of 950 °C was measured and incorporated into Table 5-4. The measurement results are compared with sample co-fired at 850 °C and commercial bulk PZT material.
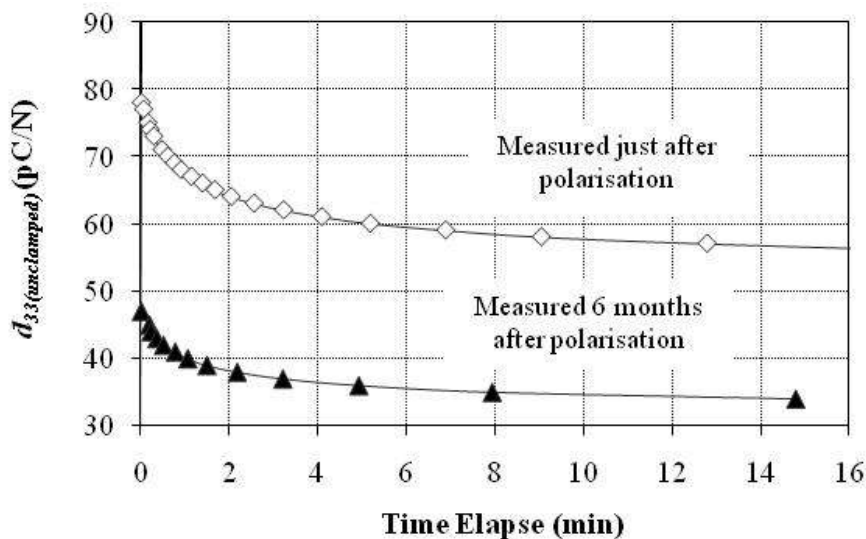
Figure 5-15: d_{33} as a function of time elapsed for an unclamped sample just after polarisation and six months after polarisation.
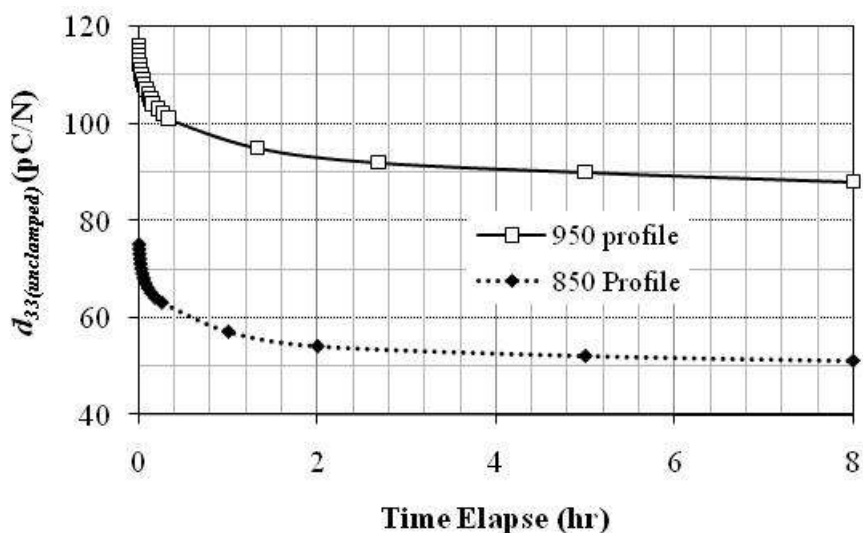
Figure 5-16: The d_{33} value as a function of time elapsed for free-standing samples co-fired at 850 °C and 950 °C.

Table 5-4: Summary of measurement results for fabricated samples at standard 850 °C and 950 °C in comparison with bulk PZT from Morgan Electroceramics Ltd.

Piezoelectric Constant			Co-firing profile		Bulk PZT-5H [31]
			850 °C	950 °C	
Constant electric field elastic compliance	s_{11}^E	$\times 10^{-12}$ m^2/N	8.4	7.11	17.7
Constant displacement elastic compliance	s_{11}^D	$\times 10^{-12}$ m^2/N	8.31	6.96	15.5
Coupling factor	k_{31}	dimensionless	0.126	0.145	0.35
Relative dielectric constant	K_{33}^T	dimensionless	336	617	3250
Piezoelectric charge coefficient	d_{31}	$\times 10^{-12}$ C/N	-19	-28.6	-250
	d_{33}	$\times 10^{-12}$ C/N	53	82	620
Piezoelectric voltage coefficient	g_{31}	$\times 10^{-3}$ Vm/N	-6.73	-5.24	-6.7
	g_{33}	$\times 10^{-3}$ Vm/N	17.8	21.2	21.9
Mechanical quality factor	Q_m	dimensionless	130	98.1	65

5.5.3 Comparison between Clamped and Unclamped Samples

Figure 5-17 shows the measurement results of d_{33} for clamped and unclamped samples. Both of the samples were fabricated with the same process and co-fired at 850 °C. Initially, the value of d_{33} for the unclamped and clamped samples was measured at 53 pC/N and 28 pC/N respectively after 8 hours of continuous application of dynamic force. Six months after polarisation, the values reduced to 35 pC/N and 20 pC/N respectively, which correspond to decay rates of 34 % and 29 %.

The d_{33} difference between the unclamped and clamped samples is 47 % when they were measured just after polarisation and 43 % when measured 6 months after polarisation. When substituting the measured value of d_{33} for clamped samples at 28 pC/N and unclamped samples at 53 p/N into equation (5-1), the value of d_{31} is calculated as -18.8 pC/N, which is very close to that listed in Table 5-4. It can therefore be concluded that the experimental results are in good agreement with the estimation from equation (5-1).
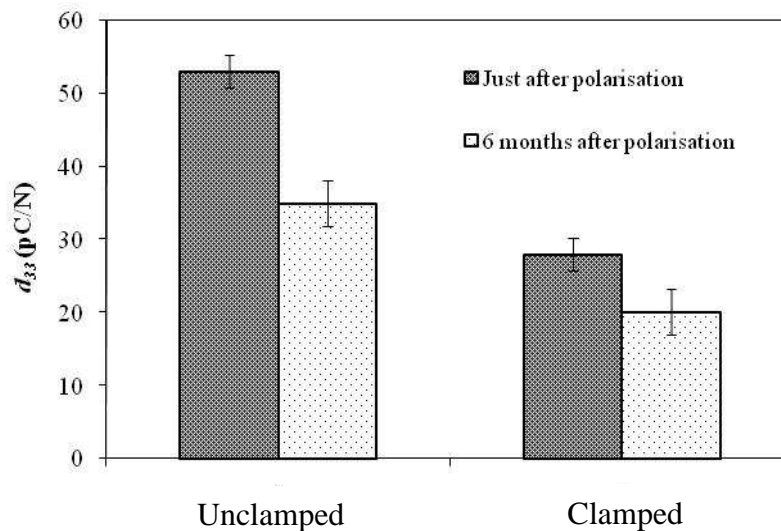
Figure 5-17: Comparison of d_{33} value between unclamped (free-standing) samples and clamped sample.

5.6 Conclusion

A free-standing structure is an excellent tool for measuring thick-film piezoelectric properties. Both the direct (Berlincourt method) and resonant measurement methods can be used to measure the piezoelectric properties, which are difficult to implement for traditional thick-film devices when clamped on a substrate. The experiment results show that a sample co-fired at a peak temperature of 950 °C performed better than those co-fired at 850 °C. However, higher processing temperatures may cause the electrode layers to deform and weaken the overall structure. The experiment results also verify that the value of d_{33} for a clamped sample is influenced by the value of d_{31} as a consequence of the clamping effect.

Chapter 6   Testing under Harmonic Base Excitation

6.1 Introduction

The D series free-standing samples fabricated with the process parameters shown in Table 4- were used to test under harmonic base excitation. The composite structures were fabricated in the sequence of PZT-Ag/Pd-PZT-Ag/Pd-PZT as shown in Figure 6-1. The centre PZT layer which forms the functional part was sandwiched between two Ag/Pd electrodes which were used for polarising, while the upper and lower PZT layers act as protection to the Ag/Pd electrodes during the fabrication process. Since only the centre PZT layer is polarised, it can therefore be considered as a unimorph structure similar to the one described in [107] and analogous to piezoelectric materials printed on a substrate.
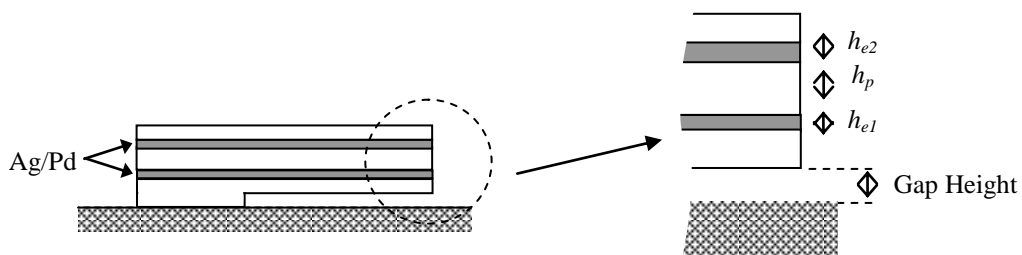
Figure 6-1: Diagram of a free-standing unimorph cantilever structure.

The unimorph structures were used as a tool to characterise the PZT incorporated cantilever structure for their mechanical and electrical properties such as natural frequency, *Q*-factor, damping ratio and coupling factor by observing the electrical output. The D series free-standing structures (Figure 6-2) with dimensions as shown in Table 6-1 were used in the investigation.

(a)   (b)
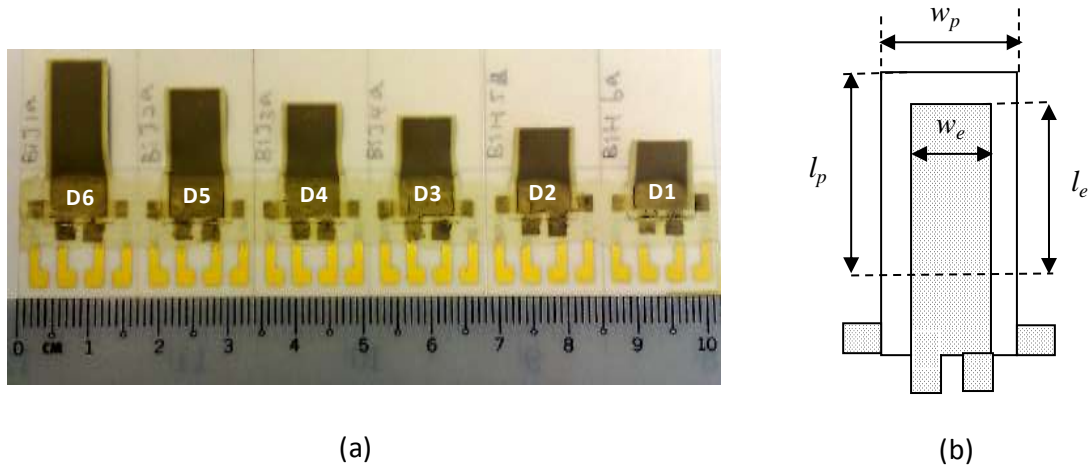
Figure 6-2: Free-standing cantilever samples; (a) photograph and (b) the dimensions of a sample.

Table 6-1: Dimensions (in mm) of samples shown in Figure 6.2.

Parameter	Sample					
	D1	D2	D3	D4	D5	D6
Free-standing Length, l_p	4.5	6.75	9	11.25	13.5	18
Free-standing Width, w_p	9	9	9	9	9	9
PZT Thickness, h_p	0.055	0.055	0.055	0.055	0.055	0.055
Lower Electrode Thickness, h_{e1}	0.02	0.02	0.02	0.02	0.02	0.02
Upper Electrode Thickness, h_{e2}	0.012	0.012	0.012	0.012	0.012	0.012
Non-active layer Thickness	0.0125	0.0125	0.0125	0.0125	0.0125	0.0125
Gap between cantilever and substrate	2	2	2	2	2	2

In another experiment, a sample with interdigitated electrodes (IDE) was characterised to investigate the electrical output. The open circuit voltage of an IDE cantilever operated in a bending mode is given by,

$$V_{33} = h_{IDT}\, \sigma \left(\frac{d_{33}}{\varepsilon_T} \right)$$

(6-1)

where h_{IDT} is the poling distance between two abjection fingers as shown in Figure 2-3 (b). According to equation (6-1), the IDE patterned cantilever performs better than the plated cantilever in term of voltage output, as the gap between two adjacent electrodes can be unlimited which will give an unlimited voltage output. However, higher polarisation voltages need to be applied to the PZT to achieve equivalent values of d_{33}. Another advantage of the IDE cantilever structure is that the d_{33} piezoelectric coefficient is more than double the size of the size of the d_{31} coefficient and so it is worth investigating the performance of this device in the d_{33} mode of operation.

6.2 Mechanical Properties of Cantilever Structure

The mechanical Q-factor is an important parameter to describe energy dissipated through vibration. The energy dissipation in the cantilever causes the stored mechanical energy to leak away and be converted into heat [108]. Generally the losses can be categorised as external and internal losses [109]. The external losses include loss in airflow and radiation of elastic wave at the support area, while the internal losses include surface loss and thermoelastic loss. The estimated total Q-factor of the system can be written as [110],

$$\frac{1}{Q_T} = \frac{1}{Q_{\text{support}}} + \frac{1}{Q_{air}} + \frac{1}{Q_{surface}} + \frac{1}{Q_{thermo}}$$

(6-2)

Q_{support} corresponds to the loss at the support of the cantilever, which is related to length and thickness. The energy loss through the support per oscillating cycle of a cantilever is given by [111],

$$Q_{\text{support}} \propto (l/h)^3$$

(6-3)

Air damping is related to air pressure, P_{air} and gas constant. At a constant air pressure, the Q-factor related to air damping is inversely proportional to the square of length of the cantilever, given by [112],

$$Q_{air} \propto (h/l)^2 \tag{6-4}$$

The surface loss which is mainly caused by surface stress [109], becomes dominant when the surface-to-volume ratio increases (thickness << length or width), and it is proportional to thickness and given by [108],

$$Q_{surface} \propto h \tag{6-5}$$

The rate of energy dissipation due to heat conduction produced when a beam is in oscillation, is inversely proportional to the product of the resonant frequency and the square of the cantilever thickness [109],

$$Q_{thermo} \propto 1/(f_r h^2) \tag{6-6}$$

The total Q-factor of the structures can be determined from an experiment by dividing the measured fundamental natural frequency of the structure, f_0, by the full width at half maximum electric output power, Δf, according to:

$$Q_T = 2\pi \frac{\text{Stored vibration energy}}{\text{Energy lost per cycle of vibration}} = \frac{f_0}{\Delta f} \tag{6-7}$$

The Q-factor is used to determine the performance of the free-standing structures. A higher value indicates a lower rate of energy dissipation relative to the oscillation frequency. For this reason, cantilevers with thin, narrow and long structures are required to design sensitive and low loss devices. The Q-factor can be used to estimate the damping ratio for free-standing structures, provided that the damping is smaller than 0.05, where the relation is,

$$\zeta_T = \frac{1}{2Q_T} \tag{6-8}$$

Damping ratio is an important parameter used to calculate piezoelectric properties, which will be discussed in section 6.4. The mechanical properties of a cantilever change with the addition of a proof mass at the tip of the beam. The sensitivity of the cantilever is inversely proportional to the additional mass as given by [113],

$$Q \propto \frac{m}{M_m} \tag{6-9}$$

where, m is the mass of the composite cantilever and M_m is the additional mass (proof mass).

6.3 Experimental Procedure

The samples were characterised on a shaker table operated in sinusoidal vibration over a range of different frequencies close to the resonant frequency of the unimorph cantilever beam. The acceleration level was maintained at a constant level by using a feedback system as shown in Figure 6-3 (a). The accelerometer in the shaker measures the actual value of frequency and acceleration level and is fedback into the control processor. A processed signal is then generated and amplified to drive the shaker to produce the desired acceleration level at a given frequency. The output voltage power from the device is driven into a programmable resistance load and subsequently converted to a digital signal and is measured with a National Instrument Sequence Test Programme.

In a further experiment, tungsten proof masses (of density 19.25 g/cm^3) were attached at the free-standing cantilever samples, in order to investigate the Q-factor, coupling factor, the efficiency of energy conversion and the maximum stress that the structure can withstand before it fails to perform accordingly. Four different dimensions of tungsten blocks with same thickness of 1 mm were used to investigate the mechanical and electrical performance of the piezoelectric cantilever. The proof masses are denoted as M1, M2, M3 and M4, with lengths and widths as shown in Figure 6-4.

In order to increase the total mass for the experiment, identical proof masses were stacked on top of each other and adhered with double-sided tapes. The tape is thin, in comparison to the thicknesses of the proof mass and the cantilever sample and does not

significantly contribute to the total mass. Furthermore, the experiments are conducted at a relatively low frequency ($\leq$ 500 Hz) and low acceleration level ($\leq$ 10 m/s^2), therefore the damping effect of the tape could be ignored.
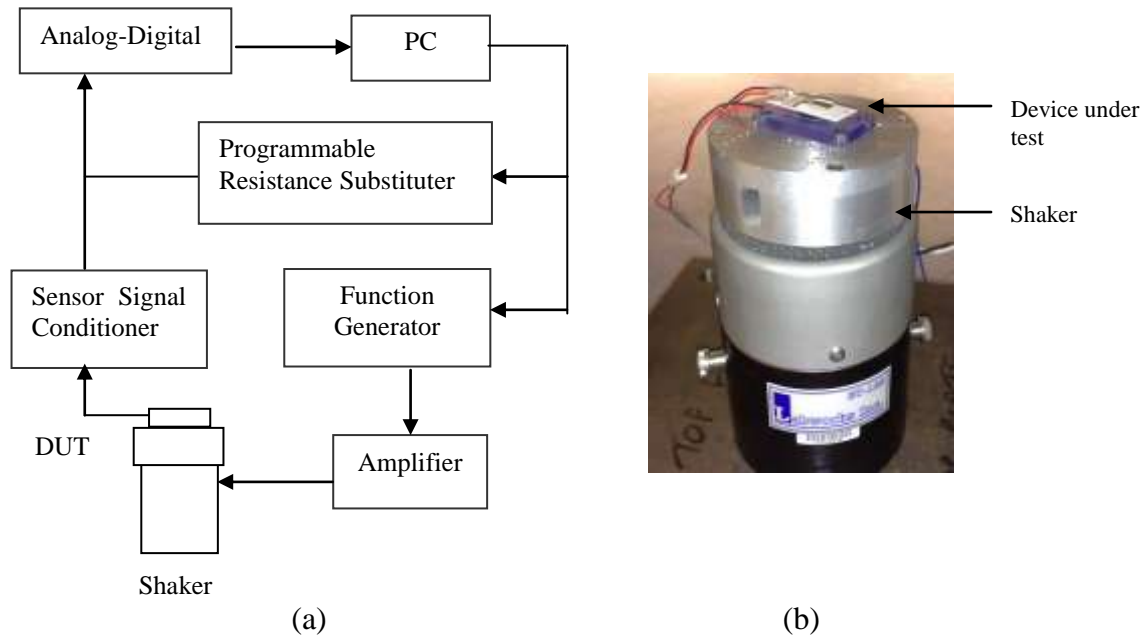
Figure 6-3: (a) Diagram of a sequence test system and (b) a shaker table where the device is being tested.
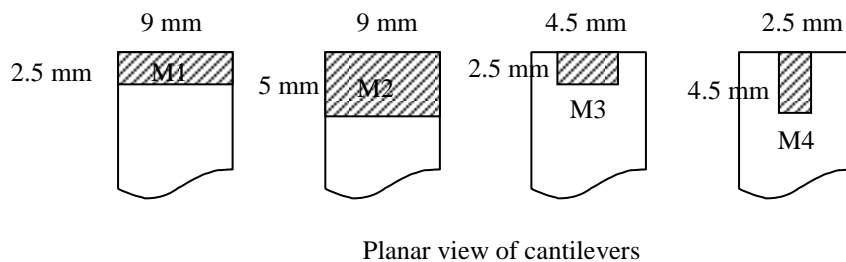
Figure 6-4: Schematic diagram of four different proof masses M1 – M4 (shaded) with the same thickness of 1 mm distributed on the tip of a cantilever.

6.4 Mechanical Characterisation

The mechanical properties of the composite free-standing cantilever samples were investigated and compared with the model developed in Chapter 3. The samples were tested under two conditions; unloaded and loaded with proof mass. The experimental results will be used to calculate the coupling factor and the energy conversion efficiency of the device.

6.4.1 *Excitation without Proof Mass*

Figure 6-5 shows a typical frequency response for the cantilevers. Those with a length of 18 mm (sample D6) have a resonant frequency of around 230 Hz, while shorter cantilevers, with a length of 4.5 mm, have a resonant frequency of about 2.3 kHz. Sample A1 and B1 were the initial batch of fabrication for series A and B respectively. Other samples in the same series could not be measured because of fabrication defects. C and D series were the improved version of the samples. Sample C series are printed with an additional layer of non-electro-active PZT layer compared with sample D series, as described in Table 4-, therefore the fundamental resonant frequency for sample C series is higher than sample D series. The natural frequency of sample A1 (with length 13.5 mm) and sample B1 (with length 11.25 mm) are within the natural frequency range of sample C and D series. This shows that the fabrication process was reasonably repeatable in producing uniform cantilever structures.
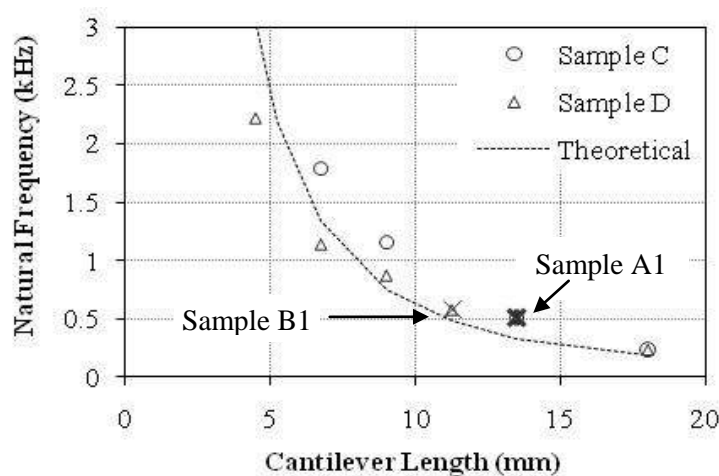
Figure 6-5: Experimental results in agreement with theoretical calculation for resonant frequency as a function of cantilever length.

The composite structure of sample D, with width 9 mm, length 1 cm, and total thickness of 196 μm was weighed at 0.11g. This gives an average density of 6240 kg/m^3. Sample C and D series were found to have a thickness of 208 μm and 192 μm respectively. Both samples D and C series were assumed to have the same density. Since the natural frequency structure is inverse proportional to the length of the cantilever structure, therefore the Young's modulus of the structure can be estimated by using equation (3-8). The calculated Young's modulus of sample C and D series are 3.78×10^{10} N/m^2 and 1.17×10^{10} N/m^2 respectively.

The total Q-factor, Q_T of the structure can be determined experimentally by exciting the free-standing structures over a range of frequencies close to the fundamental resonant frequency to determine the value of the full bandwidth at half maximum electrical output power, then substituting this value into equation (6-7). Figure 6-6 shows that the calculated values for Q_T of the samples lie in the range 120 to 215, with the largest value associated with sample D3, which is roughly a square shape. Shorter or longer cantilever lengths do not appear to exhibit the same Q-factor as those having a square structure. This is because shorter or longer cantilever structures suffer losses at different rates and with different dominant factors. The energy dissipation losses at the support are dominant for a shorter structure [108], while air damping losses become dominant for longer cantilever structure [114]. With the measured Q-factor value, the total damping ratio for the samples was calculated to be in the range of 0.002 to 0.005.
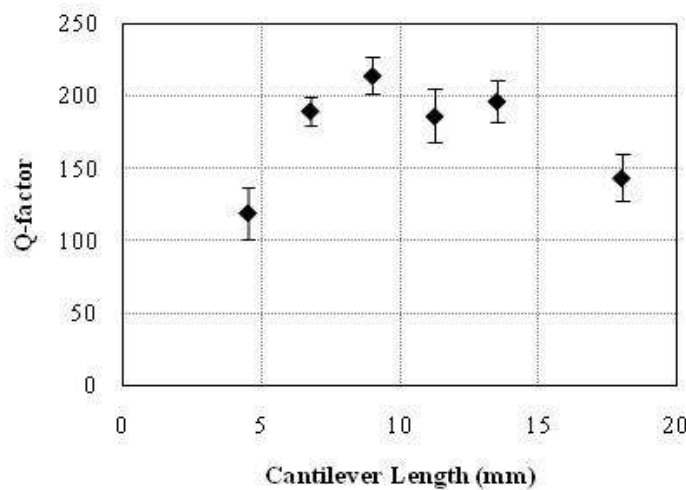
Figure 6-6: Q_T as a function of cantilever length.

6.4.2 Excitation with Proof Mass

Attaching additional proof masses to the cantilever beam can further reduce the resonant frequency. As an example, the natural frequency of sample D5 is reduced from 505 Hz to 68 Hz with proof masses of 2.22 g. as shown in Figure 6-7. The measurement results show that the natural frequency of the structure is not affected by the distribution of the proof masses.
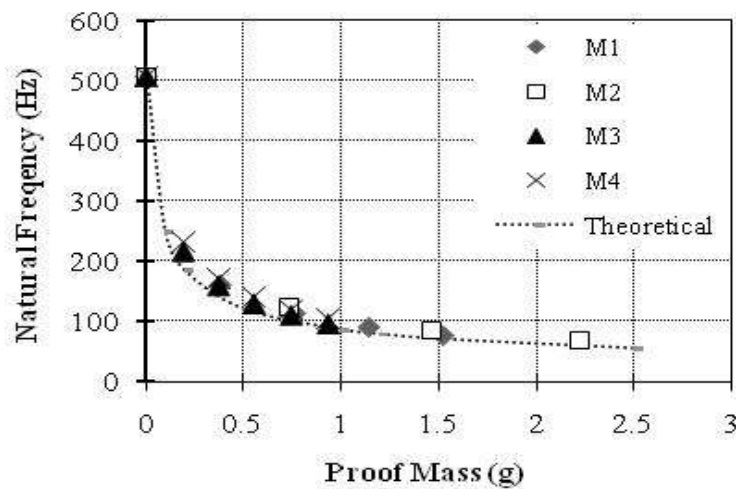
Figure 6-7: Experimental results in agreement with theoretical calculation for resonant frequency as a function of mass for sample D5 with length 13.5 mm.

The *Q*-factor of sample D5 was reduced from about 185 to about 30 when a proof mass of 2.2 g was attached as shown in Figure 6-8. The mechanical damping ratio obtained from the calculation by using equation (2-8) are in the range from 0.003 to 0.016 when a range of proof mass up to 2.2 g were attached to a cantilever of length 18 mm. The coupling factor appears to be increasing rather linearly with the proof mass from 0.06 to about 0.2, as shown in Figure 6-9.
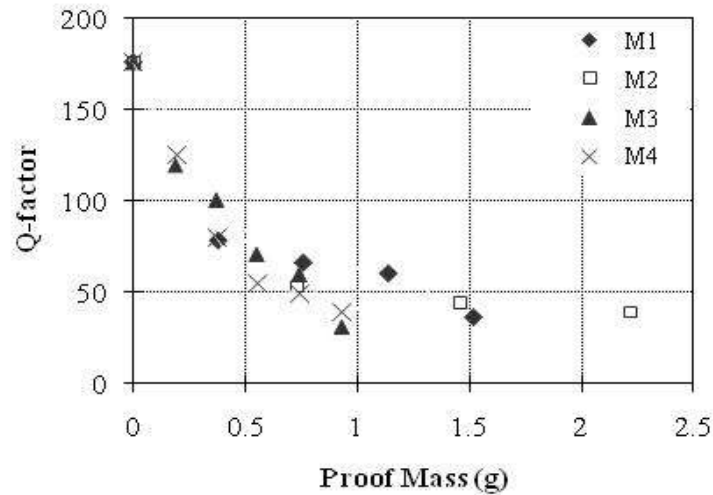
Figure 6-8: Q_T as a function of mass for sample D5 for four different proof mass distributions.
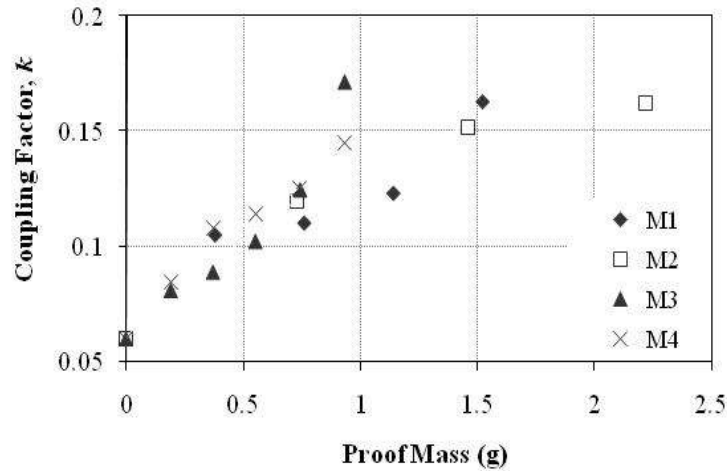
Figure 6-9: Coupling factor as a function of mass attached to a cantilever with length 18 mm.

6.5 Electrical Characterisation

The same series of samples was used to investigate the electrical output performance from the piezoelectric cantilever structures. A modest electrical power output (a few nano-watts) was produced when the composite unimorph structure was operated in its bending mode. The output power is affected by the distance from the centroid of the piezoelectric material layer to the neutral axis of the composite cantilever, d. The samples used in the experiment have a d value of 6 μm, which was calculated from equation (3-22) by using the parameters in Table 6-1 and with the assumption that the

137

elastic moduli for the Ag/Pd electrode and PZT layer are 116 GPa and 60 GPa respectively.

The electrical output power from the devices was measured by connecting the lower and upper electrodes to a programmable load resistance and then converting the voltage into a digital signal to be measured with a National Instruments Sequence Test programme. A series of different experiments was carried out to investigate the output power as a function of cantilever length, electrical load resistance, proof mass and input acceleration level.

The mechanical damping factor is a property of the system which is difficult to control. However, the electrical damping factor can simply be varied by using different resistive load. As can be seen from equation (2-16), once the resistive load is matched with the mechanical damping, maximum energy is transferred from the mechanical to the electrical domain.

6.5.1 Excitation without Proof Mass

By careful selection of resistive loads, the electrically induced damping can be adjusted so that it is equal to the mechanical damping. Once the optimal resistive load is obtained, maximum output power is produced. Figure 6-10 shows the experimental and theoretically calculated results for samples D6 and D5 when excited to their resonant frequencies at an acceleration level of 100 milli 'g' (≈ 1 m/s^2). Optimum output power for samples D6 and D5 is obtained by driving into resistive loads of 60 kΩ and 39 kΩ respectively.

The required value for the resistive load was found to be a function of the length of the cantilever, as shown in Figure 6-11. This shows that as cantilever length increases the mechanical damping also increases which is reflected by the matched electrical resistive load. At optimum resistive load, the output power increases with cantilever length as shown in Figure 6-12, which is in good agreement with theoretical calculations.
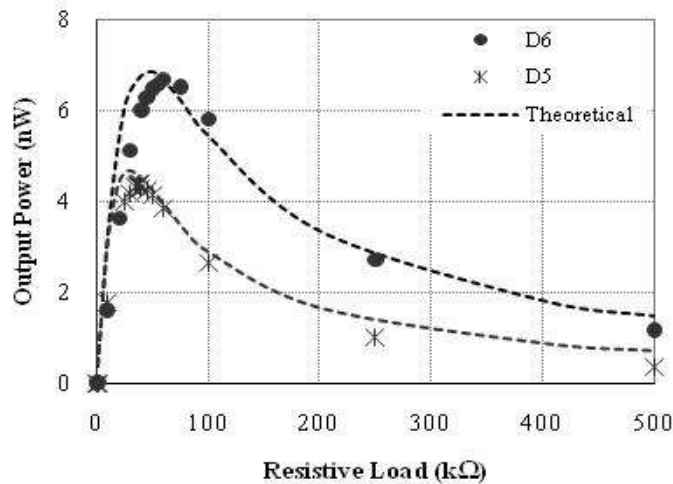
Figure 6-10: Output power at resonant frequency as a function of electrical resistive load when accelerated at a level of 100 milli 'g'.
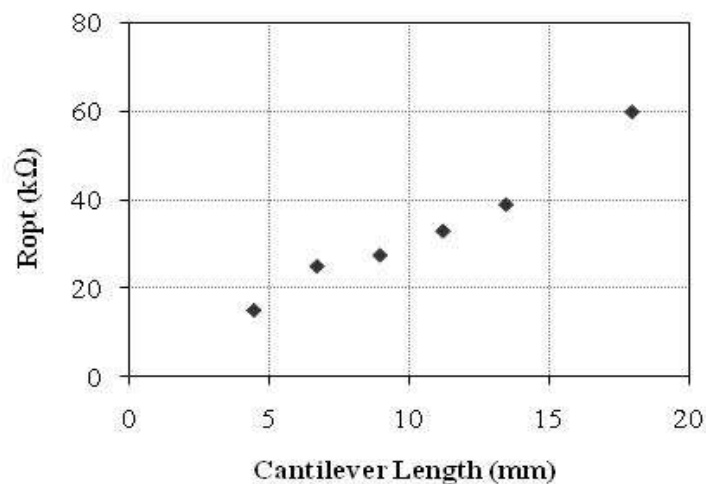
Figure 6-11: Optimum resistive load, R_{opt} as a function of cantilever length.

In another experiment, sample D6 was examined to study the output power levels when it was excited over a range of frequencies around its resonant frequency and at different acceleration levels. Figure 6-13 shows that the output power increases with the acceleration level as expected, but the resonant frequency drops as the acceleration level increases. At an acceleration of 100 milli 'g' (≈ 1 m/s^2), the sample produced an output power of 10.2 nW at a resonant frequency of 235 Hz. The output power increased to 84 nW when the sample was excited at an acceleration level of 1 'g' (≈ 10 m/s^2) at the

139

same frequency. However, by shifting to a new resonant frequency of 229 Hz, the output power increased to 280 nW.
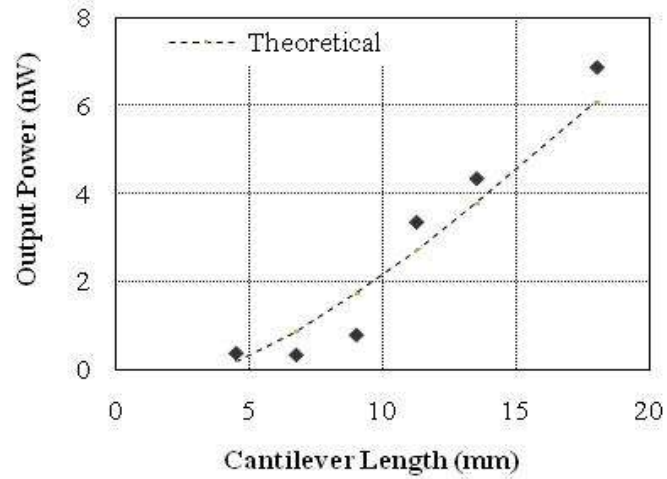
Figure 6-12: Output power at optimum resistive load as a function of cantilever length when excited to their resonant frequency at an acceleration of 0.1 'g'.
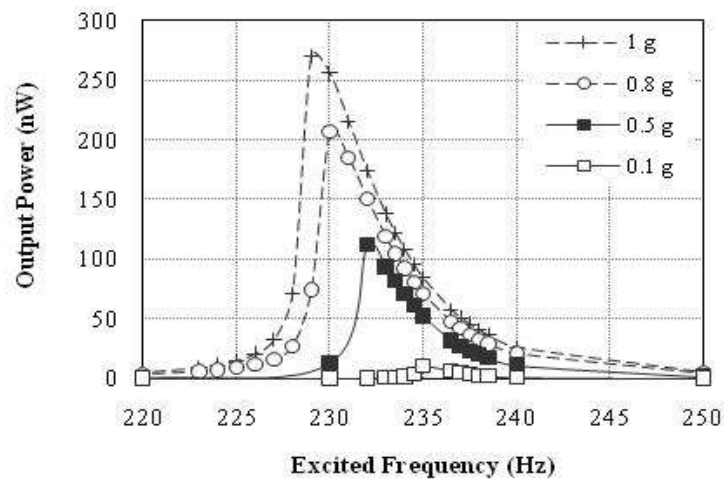
Figure 6-13: Output power as a function of excited frequency at different levels of acceleration for sample D6, where 1 'g' = 10 m/s^2.

6.5.2 Excitation with Proof Mass

The resistive load increased with proof mass, as shown in Figure 6-14. The optimum resistive load for sample D5 saturates at around 240 kΩ, with an added proof mass exceeding 1.5 g. The distribution of the masses does not seem to influence the value of the optimum resistive load. When compared to the mechanical damping loss as shown in Figure 6-9, the pattern of change for mechanical damping and electrical damping with mass increment is different. This shows that, not all the energy loss from mechanical damping is converted into electrical energy. Some of the energy is lost through support and air damping.

The distribution of the proof masses has a significant influence on the output power, as shown in Figure 6-15. Sample D5 with attached proof masses of dimensions M1 produces a maximum output power of about 40 nW, which is more than a factor of 8 higher than a device without the proof mass. M1 has a distribution of masses focused at the tip of the cantilever and appears to have imposed the maximum allowable stress on the cantilever, before a reduction of power due to energy losses from mechanical damping at greater values of added mass (> 1.2g).

For cantilever designs where the distribution of proof masses is over a large proportion of the cantilever beam (e.g. by using proof mass M2), a greater range of proof masses can be added before mechanical damping becomes dominant (cf. Figure 6-14). The larger mass of M2, however, does not show a significant improvement in the output power, and furthermore it is not desirable to stress the fragile ceramic cantilever beyond 8.5 MPa (experimental maximum stress point). In this case, an acceleration level of 1 m/s^2 permits a maximum mass of approximately 2.8 g. Designs M3 and M4 respectively have a mass distribution centred around the centre line of the cantilever and show inferior output power levels of less than a quarter the value of the maximum power stored in the piezoelectric materials.
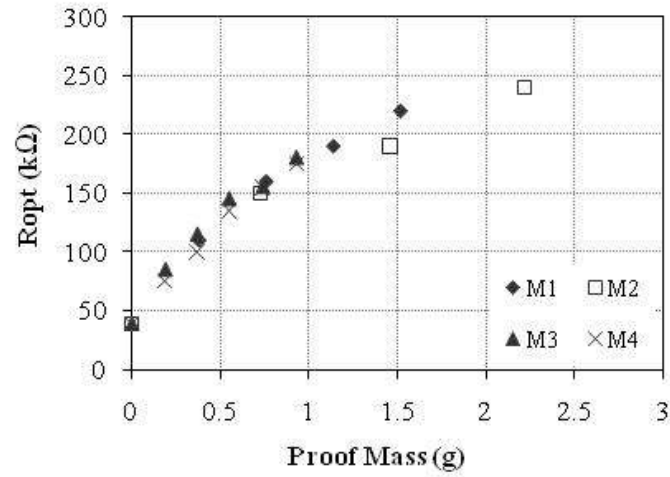
Figure 6-14: Optimum resistive load, R_{opt} as a function of mass for sample D5 with different configurations of proof mass as shown in Figure 6-4.
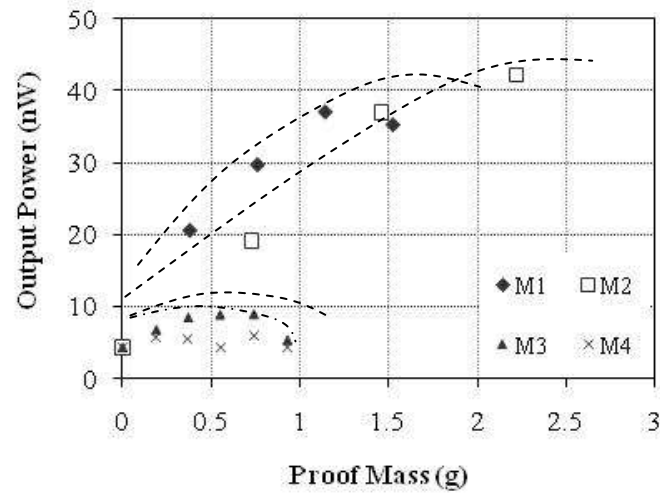
Figure 6-15: Output power at optimum resistive load as a function of mass for sample D5 loaded with different distributions of proof masses. (Dotted lines show general trend).

6.5.3 Comparison between Samples with Different Distance from Neutral Axis

The distance from the centroid of the active piezoelectric layer to the neutral axis of the composite cantilever is also an important factor in determining the electrical output. Figure 6-16 shows a comparison between sample A1, D5 and C3 with same length but different distance from PZT centroid to neutral axis; 7.2 µm, 3.7 µm and approximate to zero respectively.
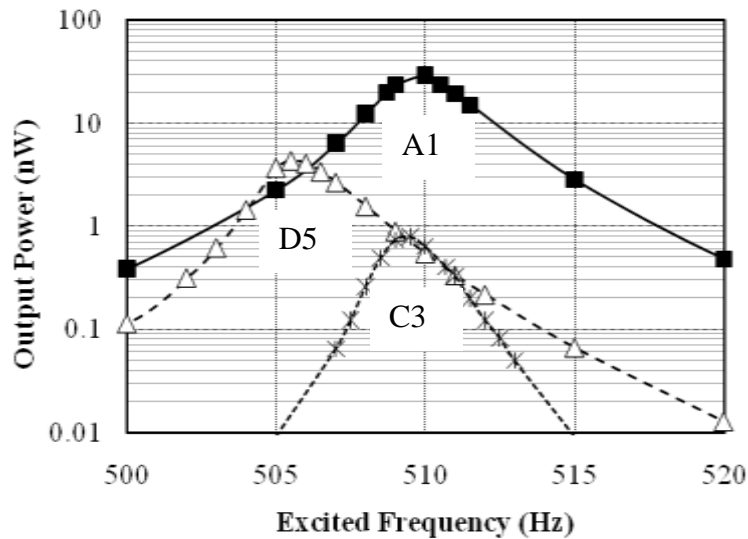
Figure 6-16: Frequency response for sample A1, D5 and C3.

Sample A1 is a non-symmetric unimorph structure, where the lower part of the structure was printed with two additional layers of PZT as a non-electro-active lower protective layer. Sample D5 is another non-symmetric unimorph structure, similar to sample A1 but with an additional layer of non-active PZT as the upper protective layer, while sample C3 is a symmetric unimorph structure with both sides printed with two additional layer of non-active PZT as the lower and upper protective layer.

The measurement results show that the symmetric unimorph structure, sample C3 generates the least output power. This is entirely expected since a symmetric structure

will produce a zero resultant stress at the central of the active piezoelectric layer and therefore produce zero electrical output power. In reality, however, because of fabrication tolerances, the centroid of the active PZT layer is not exactly coincident with the neutral axis and therefore a relatively small electrical output is generated when the structure is operating in a bending mode. Sample A1, which has a greater *d* distance from the neutral axis, generates the greatest output power among these samples. These results verify that the output power can be increased by adjusting the thickness of the non-active component of the unimorph structure according to equations (3-22) and (3-35).

A thinner cantilever theoretically has a lower resonant frequency. However, sample A1 with the thinnest structure has a resonant frequency greater than the thicker sample D5. This discrepancy can be explained by considering the relative shape of the structure; sample A1 is not a flat structure but rather a U-curve shaped cantilever as shown in Figure 4-19, which increases the effective thickness of the structure and it therefore resonates at a higher frequency.

Figure 6-17 shows the relationship of optimum resistive load with different samples. Maximum output powers were generated when driving resistive loads of 30 kΩ, 39 kΩ and 50 kΩ for samples A1, D5 and C3 respectively. This shows that, the thicker the unimorph cantilever structure, the higher the matching electrical resistive load.
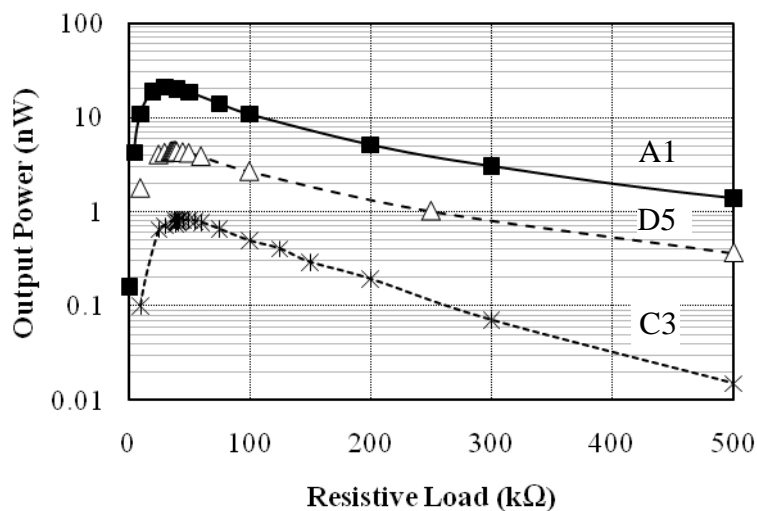
Figure 6-17: Output power as a function of resistive load for samples A1, D5 and C3.

6.5.4 *Interdigitated Cantilever*

An interdigitated electrode (IDE) pattern printed on a 9 mm long piezoceramic cantilever, with gap between the fingers, w_{gap} of 1.95 mm as shown in Figure 6-18 was tested and compared with plated samples. Theoretically, to obtain optimum performance the sample has to be polarised at approximately 5 kV to establish a similar electrical field strength of 2.5 MV/m as used for the plated electrode samples [104]). However, electrical sparking was observed at a polarisation voltage of just 350 V and burnt the area near to the base of the substrate, resulting in a short-circuit between the IDE and the bottom Ag/Pd support layer.
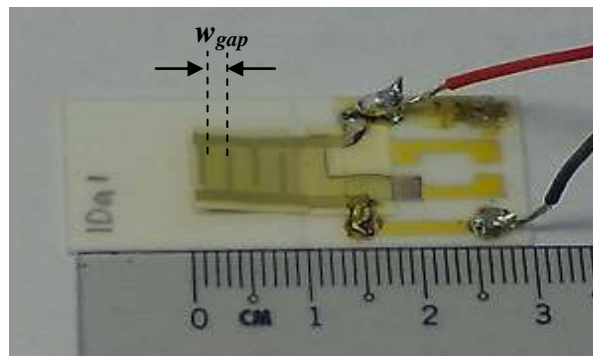
Figure 6-18: Photograph of an IDE sample.

In another experiment, a similar sample, IDa1, was polarised at a lower dc voltage of 300 V, which gives an electric field strength of 154 kV/m for an in-plane polarisation mode. Figure 6-20 shows the experiment output power for the sample at an acceleration level of 0.05 g and 0.5 g. At resonant frequency of 960 Hz, an output power of 5 pW was measured when driving a resistive load of 30 kΩ at an acceleration of 0.05 g. The output power increased by about a factor of 150 to 745 pW when the IDE cantilever was excited to its resonant frequency with an acceleration of 0.5 g, as shown in Figure 6-19.

A relatively small output power was measured at 8.3 pW from the IDE sample (IDa1) compared to plated samples with similar length (D3 and C2) as shown in Figure 6-20, which is attributed to the much lower polarisation voltage used (field strength of 154 kV/m compared to 2.5 MV/m) producing correspondingly lower values for the piezoelectric coefficients.

Figure 6-21 shows a comparison of the maximum output power and resonant frequency for sample D3, C2 and IDa1. Sample D3, with thinner non-active PZT protective layer compared to the other samples, was expected to have the lowest resonant frequency at 875 Hz. Although samples C2 and IDa1 were printed with similar numbers of layers of films, their resonant frequencies are slightly different, at 1155 Hz and 960 Hz respectively. The difference maybe because the effective thickness of an IDE sample is less than the plated sample and therefore resonance occurs at a lower frequency.
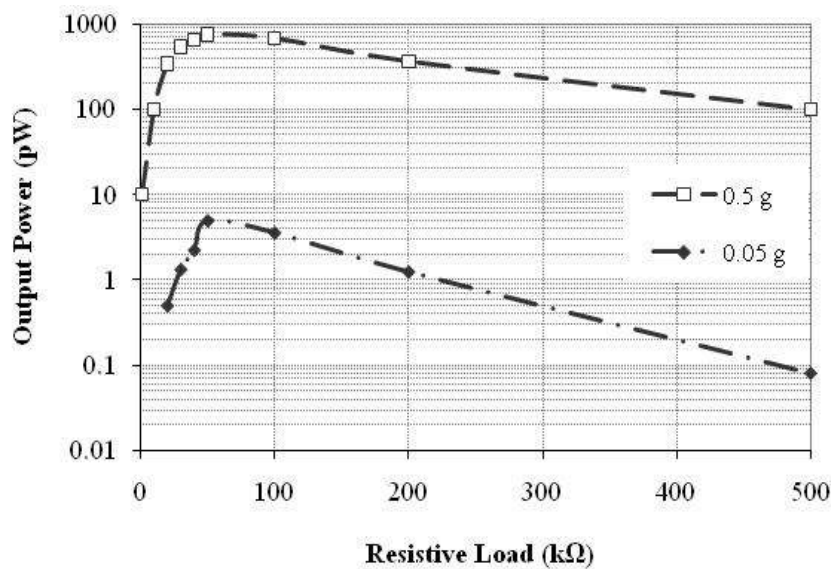
Figure 6-19: Output power of sample IDa1 as a function of resistive load at an acceleration of 0.05 g and 0.5 g.
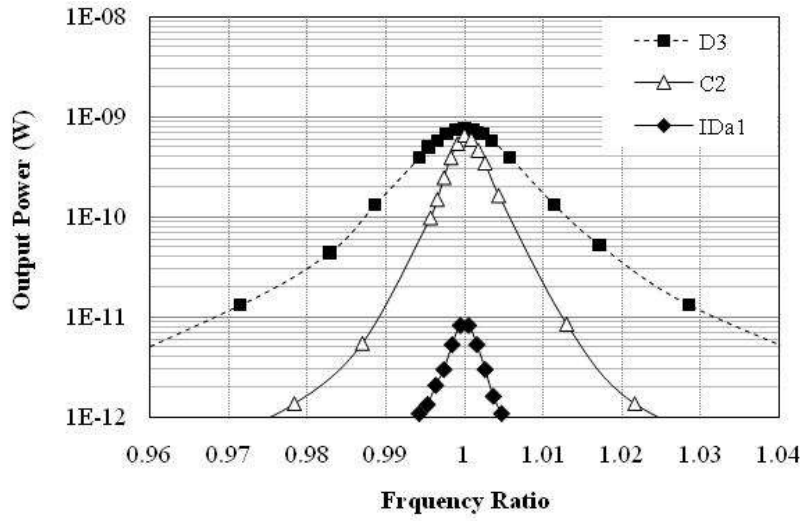
Figure 6-20: Frequency response comparison for sample D3, C2 and IDa1 at an acceleration of 0.1 g and with resistive load of 30 kΩ.
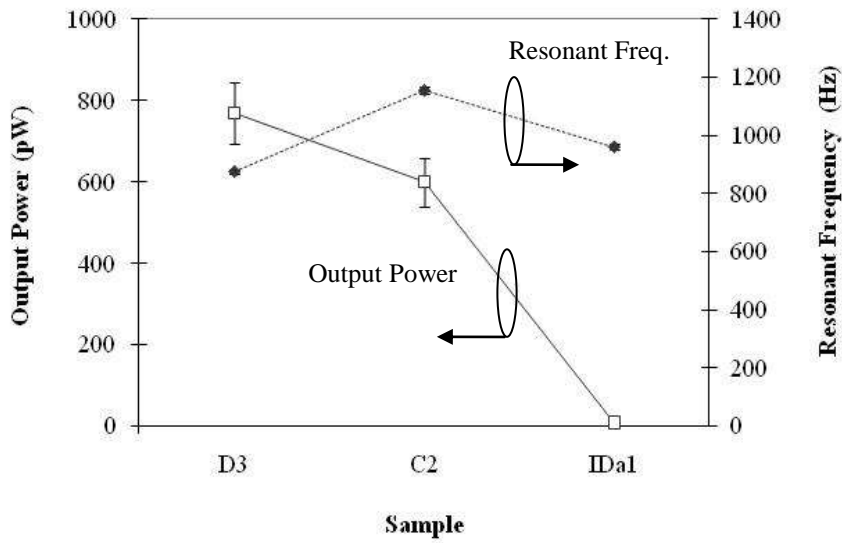
Figure 6-21: Comparison of output power and natural frequency for sample D3, C2 and IDa1 at 0.05 g.

6.6 Energy Conversion Efficiency

The efficiency of energy conversion from mechanical to electrical energy is given by [115],

$$E_{eff} = \left(\frac{k^2}{1-k^2}\right) \bigg/ \left[\frac{2}{Q_T} + \left(\frac{k^2}{1-k^2}\right)\right] \tag{6-10}$$

where k is the actual coupling factor ($< k_{31}$) of the piezoelectric free-standing structure after taking into account its dielectric and mechanical losses, which can be measured from experiment when the optimum electrical resistive load, R_{opt} is known. The value is derived from [12] as,

$$k = \left[\left(\frac{2\xi_T}{R_{opt}\omega_{s0}C_p}\right)^2 - 4\xi_T^2\right]^{\frac{1}{4}} \tag{6-11}$$

where ω_{s0} is the angular resonant frequency, C_p is the capacitance of the material and ξ_T is the total damping ratio. The damping ratio is relatively small (< 0.05) for the ceramic structure, and can be determined experimentally by measuring the Q-factor as shown in equation (6-8).

The optimum electrical resistive load, R_{opt} can be derived from equation (3-35) by differentiating the output power with load resistance. At optimum output power, $dP/dR = 0$, this gives,

$$R_{opt} = \frac{1}{\omega_r C_p} \frac{2\xi_T}{\sqrt{4\xi_T^2 + k^4}} \tag{6-12}$$

Figure 6-22 shows the relationship between coupling factor, k with the optimum resistive load, R_{opt} and total damping ratio, ζ_T. The coupling coefficient is equal to zero when the load resistance is equal to the inverse of the natural frequency multiplied by the capacitance of the material ($R_{opt} = \dfrac{1}{\omega_r C_p}$). For the case of $R_{opt} > \dfrac{1}{\omega_r C_p}$, the coupling coefficient is almost uniform with changing resistive load. The coupling coefficient changes critically in the range of $\dfrac{2}{\sqrt{5}}\dfrac{1}{\omega_r C_p} \le R_{opt} < \dfrac{1}{\omega_r C_p}$, therefore the

coupling coefficient can be improved with adjusting the optimum resistive load in this region, with the assumption that the mechanical damping can be modified.
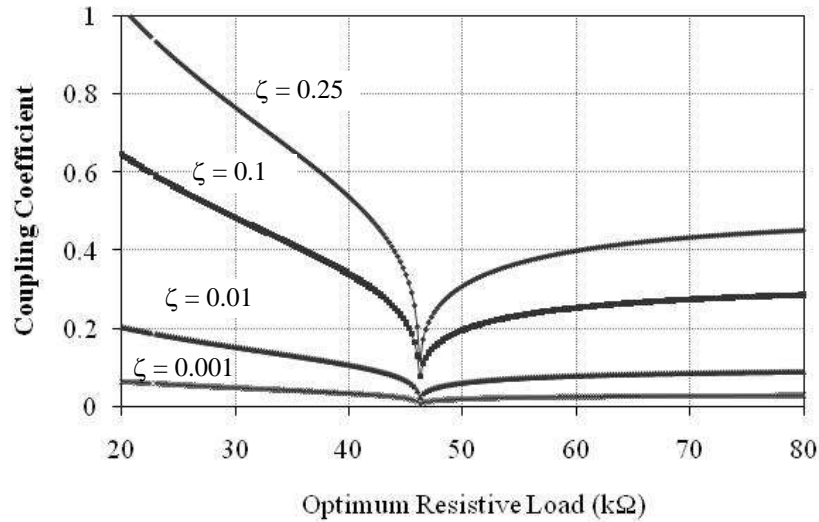
Figure 6-22: Coupling coefficient as a function of optimum resistive load for different damping ratio for sample D5, with resonant frequency at 505.5 Hz and capacitance of 6.82 nF.

Figure 6-23 shows the relationships between the efficiency of energy conversion for a piezoelectric cantilever with the coupling factor and Q-factor. The efficiency can be improved by increasing the coupling factor and the Q-factor of the cantilever structure.
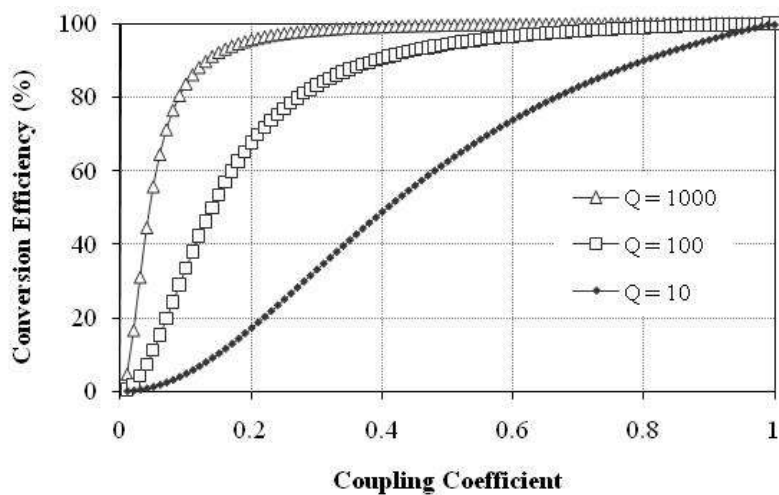
Figure 6-23: Efficiency of energy conversion as a function of coupling coefficient and Q-factor.

In an experiment with sample D as shown in Figure 6-24, the efficiency decreases with increasing cantilever length. The shortest cantilever sample appears to have an initial level of efficiency at about 35 % and the longest sample has an efficiency of about 25 %.
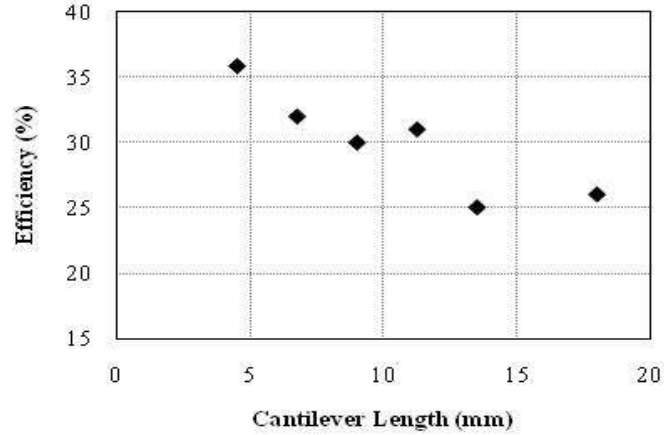
Figure 6-24: The energy conversion efficiency (equation (6-10)) as a function of cantilever length (with 5 % error).

The *Q*-factor of sample D5 was reduced but the coupling factor, *k* increased when proof mass is attached. This shows that more energy is stored in the structure at resonance [111], and hence more electrical energy can be extracted with improved energy conversion efficiency as demonstrated in equation (6.10), which is in good agreement with experimental results shown in Figure 6-25. Sample D5 has as efficiency of 25 % initially, which increases to around 35 % with the addition of a 2.2 g proof mass.
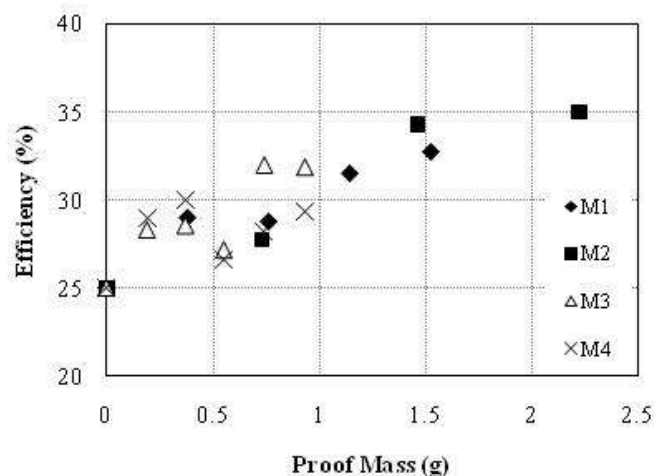
Figure 6-25: The energy conversion efficiency as a function of mass for sample D5.

6.7 Conclusion

The mechanical properties of the cantilever samples were measured. Shorter cantilevers were found to suffer energy loss at the support of the cantilever while the surface loss is dominant for longer cantilevers, which can be explained by the measured Q-factor and the damping ratio of the structures. The Q-factor for the samples with length between 4.5 mm to 18 mm is in the range of $100 - 220$, which results in a calculated damping ratio of 0.002 to 0.0045.

The resonant frequency is inversely proportional to the length of a cantilever while the electrical output power increases gradually with the cantilever length. The improvement, however is not as effective as adding additional proof masses. In order to operate at a low level ambient condition while keeping the overall device size as small as possible, additional proof masses is therefore the preferred method for improving the output power. The present of proof mass also increases the energy conversion efficiency of the device from 25 % to about 35 % when a 2.2 g proof mass was attached.

The electrical output power, however, do not increases infinitely with proof mass. A maximum output power of about 40 nW was measured when a proof mass of 2.2 g with dimension 9 mm $\times$ 5mm $\times$ 1 mm was attached to the tip of a cantilever having a length of 13.5 mm. The power can be further increased by increasing the acceleration level. In a separate measurement, the output power of a cantilever having a length of 18 mm, increases from 10 nW to 280 nW when accelerated to 0.1 g and 1.0 g respectively.

Another factor which is important in increasing the output power is the distance from the centroid of the active piezoelectric layer to the neutral axis of the composite cantilever. The experiment results show that the greater the distance from the neutral axis the great output power it produced which is in good agreement with the theoretical calculation in Chapter 3. The neutral axis factor will be discussed in detail in next chapter.

Chapter 7   Multimorph Cantilevers

7.1 Introduction

A multimorph is a multilayer composite structure consists of more than two active piezoelectric layers separated by electrodes in between them. The main advantage in producing a multimorph structure consisting of alternating layers of PZT and Ag/Pd electrodes, is that it generates larger electrical output than would be possible with a single layer (unimorph) structure having the same total thickness. This is because the individual PZT layer is arranged away from the neutral axis of the whole structure and the resultant stress would be increased when the cantilever structure bends, therefore increasing the electrical output from the piezoelectric materials.

Another advantage of multimorph structures compared to traditional piezoelectric cantilevers fabricated on a substrate is the flexibility offered in the configuration of electrode terminals to operate as either current sources or voltages sources.

A model of a multimorph structure will be discussed in the following section and a series of multimorph structures were fabricated to verify the model. The multimorph structures were fabricated using a co-firing temperature profile with a peak temperature of 950 °C. For simplification the structures were fabricated with three similar laminar sections of PZT having thicknesses of about 40 μm and physically separated by thin layers of Ag/Pd electrodes of equal thickness of 12 μm as shown in Figure 7-1.

Characterisation of the multimorph samples were carried out using the same set-up as described in Chapter 6 and the electrical output from the samples were obtained by connecting their terminals in different configurations to indentify the optimum arrangement.
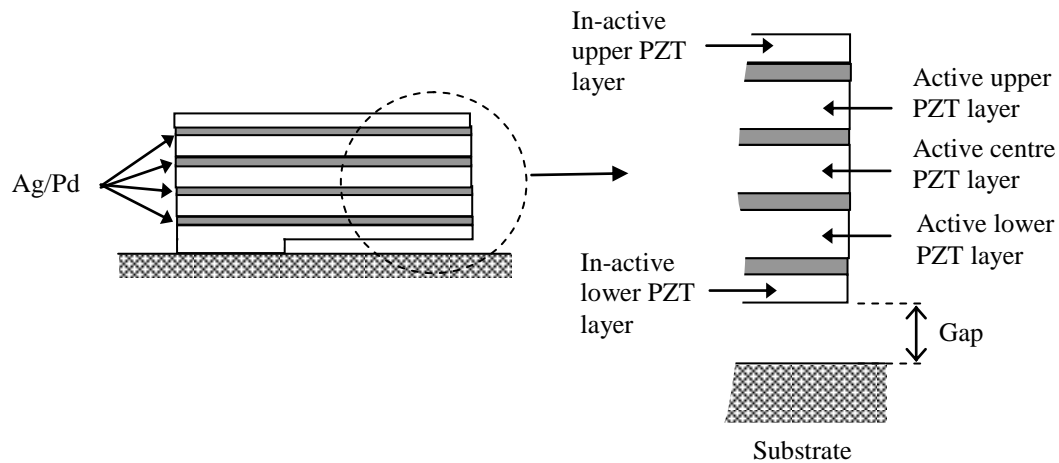
Figure 7-1: Diagram of a side-view of a multimorph cantilever.

7.2 The Functioning Principle
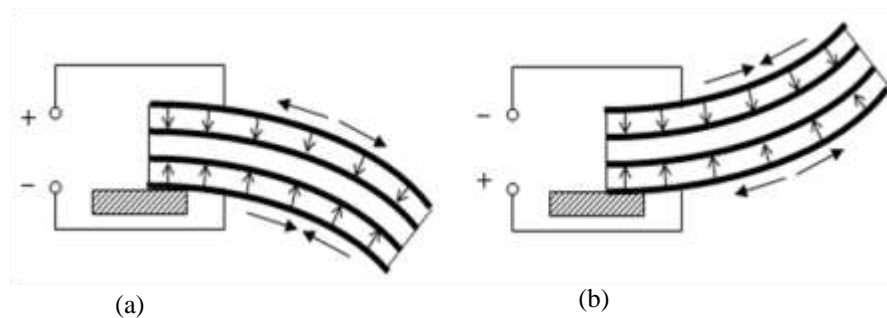
Figure 7-2: A diagram showing (a) downward and (b) upward bending position of a series polarised multimorph cantilever, which produces an alternating output voltage at the output terminal.

An example of a series polarised multimorph structure, with one end rigidly clamped is shown in Figure 7-2. When the structure resonates, an alternating voltage is produced as a consequence of the piezoelectric d_{31} effect. At positions where the cantilever bends downward, tensile forces are induced on the upper piezoelectric elements, thus

generating a voltage of the same polarity as the poling voltage; whereas the compressive forces on the lower piezoelectric elements generate a voltage of opposite polarity to that of the poling voltage.
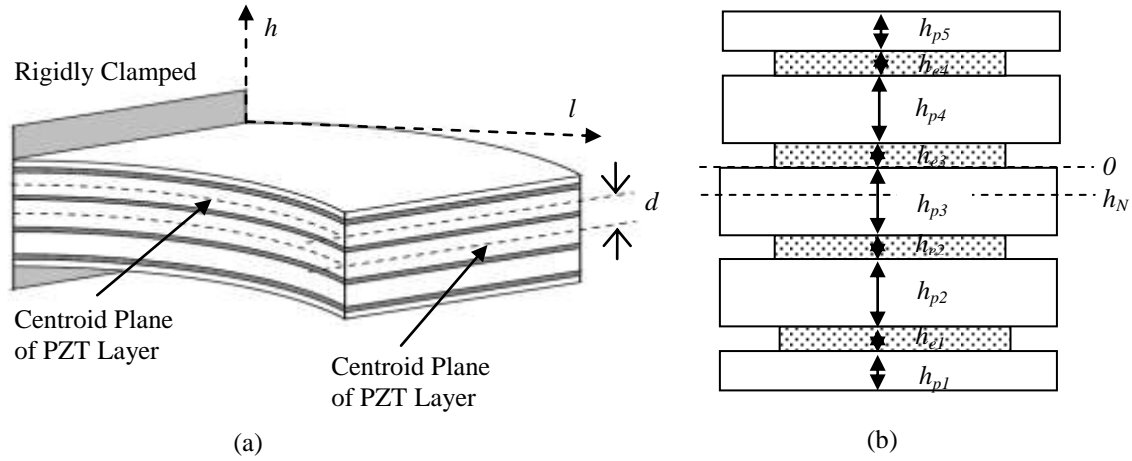
Figure 7-3: Schematic diagram of (a) a multimorph structure and (b) transformed cross-section of a composite multimorph structure.

The output voltage of a piezoelectric cantilever can be estimated with the model developed by Roundy *et al* [12] and is rewritten here,

$$V = \frac{3}{4} \frac{j e_T d_{31} h_p d A_{in}}{\varepsilon\, l_b^2 \left\{ \zeta_T \omega_r^2 - j\left[\frac{\omega_r^2 k_{31}^{\;2}}{2} + \frac{\zeta_T \omega_r}{RC_p} \right] \right\}} \qquad (7\text{-}1)$$

where A_{in} is the base input acceleration, ε is the dielectric constant of the piezoelectric material, ζ_T is the total damping ratio (the sum of electrical and mechanical damping ratios), C_p is the capacitance of the piezoelectric material and E_T is the elastic modulus of the composite structure.

One of the controllable factors that can improve the output voltage is increasing the distance between the PZT layer and the neutral axis of the multimorph structure, d. The neutral axis of the composite multimorph as shown in Figure 7-3 (b) can be determined by the transformed-section method [93] as,

$$h_N = \frac{\left(h_{p3}^2 + h_{p2}^2 + h_{p1}^2 - h_{p4}^2 - h_{p5}^2\right) + 2\left\{h_{p2}\left(h_{p3} + h_{e2}\right) + h_{p1}\left(h_{p3} + h_{p2} + h_{e1} + h_{e2}\right) - h_{p4}h_{e3} - h_{p5}\left(h_{e3} + h_{e4} + h_{p4}\right)\right\} + n_{ep}H_E}{2\left[\sum_{i=1}^{5} h_{pi} + n_{ep}\sum_{j=1}^{4} h_{ej}\right]}$$

(7-2)

where h_{pi} is the thickness of PZT layer-i and h_{ej} is the thickness of electrode layer-j, while H_E is a parameter related to the elastic modular ratio, n_{ep} which is given by,

$$H_E = (h_{e1}^2 + h_{e2}^2 - h_{e3}^2 - h_{e4}^2) + 2\left\{h_{p3}\left(h_{e3} + h_{e1}\right) + h_{p2}h_{e1} + h_{e1}h_{e2} - h_{e3}h_{e4} - h_{p4}h_{e4}\right\}$$

(7-3)

and the elastic modular ratio is,

$$n_{ep} = \frac{e_e}{e_p}$$

(7-4)

where e_e and $\underline{e_p}$ is are the elastic modulus of electrode and PZT respectively. Taking '*0*' as the reference point, the distance for the centroid of PZT of a particular section to the neutral axis of a composite multimorph, as shown in Figure 7-3 (a) can be written as,

$$d_{mm} = \left|\phi\left(\frac{1}{2}h_{pi} + \sum_i h_{pi\pm1} + \sum_{j=i\pm1} h_{ej}\right) - h_N\right|$$

(7-5)

where ϕ is -1 for a layer above and +1 for a layer below the reference point as shown in Figure 7-3 (b). For simplification, the thickness of all the PZT sections and electrode sections are uniform with thickness h_p and h_e respectively as shown in Figure 7-4.
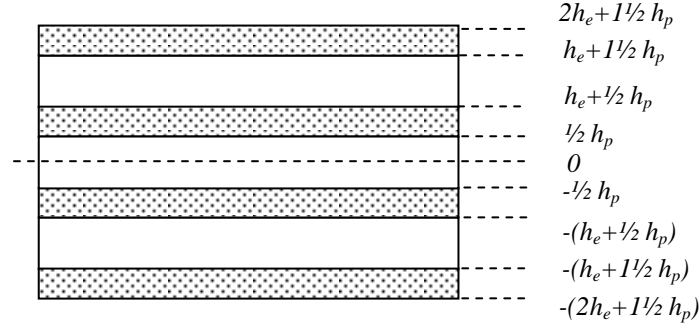
Figure 7-4: Cross-sectional view of a composite multimorph with uniform thickness of PZT and electrode layers.

The bending modulus per unit width for a composite multimorph structure can be simplified as,

$$D_{multimorph} = D_{unimorph} + 2E_p \int_{h_e+\frac{1}{2}h_p}^{h_e+\frac{3}{2}h_p} (z)^2 \, dz + 2E_e \int_{h_e+\frac{3}{2}h_p}^{2h_e+\frac{3}{2}h_p} (z)^2 \, dz \qquad (7\text{-}6)$$

where $D_{unimorph}$ is the unimorph bending modulus per unit width, which is derived from equation (3-13), and therefore the multimorph bending modulus can be written as,

$$D_{multimorph} = \frac{2}{3} \left\{ E_p \left[\frac{27}{8} h_p^{\,3} + 6h_p^{\,2}h_e + 3h_ph_e^{\,2} \right] + E_e \left[8h_e^{\,3} + \frac{15}{2} h_p^{\,2}h_e + 15h_ph_e^{\,2} \right] \right\} \qquad (7\text{-}7)$$

The moment of inertia for the multimorph structure can be obtained by substituting equation (7-7) into equation (3-28),

$$I_{multimorph} = \frac{2}{3} w \left\{ \left(\frac{27}{8} h_p^3 + 6h_p^2 h_e + 3h_p h_e^2 \right) + \frac{E_e}{E_p} \left(8h_e^3 + \frac{15}{2} h_p^2 h_e + 15h_p h_p^2 \right) \right\} \qquad (7\text{-}8)$$

The stress in each section of the PZT can be calculated in a manner similar to that derived for the unimorph structure as shown in equation (3-30).

In order to be more precise when including the non-active PZT protective layers, the total bending modulus is,

$$D_{mm} = D_{multimorph} + \frac{2}{3} E_p \left\{ h_a^3 + 18 h_a h_p h_e + h_a^2 \left(\frac{9}{2} h_p + 6 h_e \right) + h_p^2 \left(\frac{27}{4} h_a \right) + h_e^2 (12 h_a) \right\}$$

$$= \frac{2}{3} \left\{ E_p \left[\frac{27}{8} h_p^3 + 6 h_p^2 h_e + 3 h_e^2 h_p + h_a^3 + 18 h_a h_p h_e + h_a^2 \left(\frac{9}{2} h_p + 6 h_e \right) + h_p^2 \left(\frac{27}{4} h_a \right) + h_e^2 (12 h_a) \right] \right.$$

$$\left. + E_e \left[8 h_e^3 + \frac{15}{2} h_p^2 h_e + 15 h_e^2 h_p \right] \right\}$$

(7-9)

and the moment of inertia is,

$$I_{mm} = \frac{2}{3} w \left\{ \left[\frac{27}{8} h_p^3 + 6 h_p^2 h_e + 3 h_e^2 h_p + h_a^3 + 18 h_a h_p h_e + h_a^2 \left(\frac{9}{2} h_p + 6 h_e \right) + h_p^2 \left(\frac{27}{4} h_a \right) + h_e^2 (12 h_a) \right] \right.$$

$$\left. + \frac{E_e}{E_p} \left(8 h_e^3 + \frac{15}{2} h_p^2 h_e + 15 h_p h_p^2 \right) \right\}$$

(7-10)

7.3 Experimental Samples

A series of composite multimorph structures as shown in Figure 7-5 was fabricated with a co-firing profile at 950 °C. The devices consist of three individual sections of active piezoelectric materials with equal thickness of 40 μm and separated physically and electrically by Ag/Pd conductors with equal thickness of 15 μm. The dimensions of the samples are summarised in Table 7-1, which will also be used for calculation to verify the theoretical model with the experimental results.
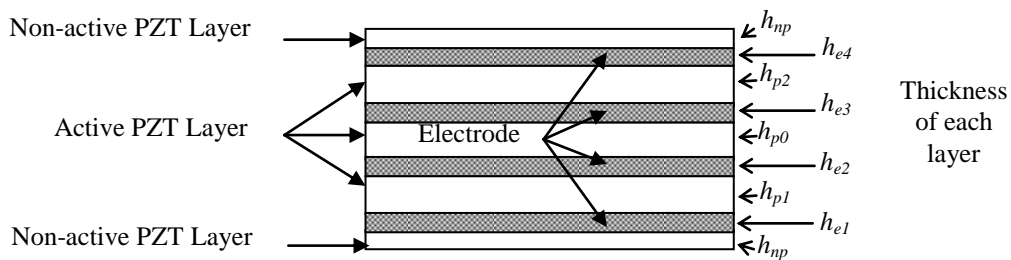
Figure 7-5: Schematic diagram of a cross-sectional view of a composite multimorph structure.

Table 7-1: Fabricated sample dimensions.

Dimension		BA1 (Stress test)	BA2 (Series polarised)	BA3 (Parallel polarised)
PZT Length (mm), $l_p{}^*$		13.5	18	18
Electrode Length (mm), $l_e{}^*$		13	17.5	17.5
PZT Width (mm), $w_p{}^*$		9	9	9
Electrode Width (mm), $w_e{}^*$		8	8	8
PZT Thickness (μm)	h_1	12.5	12.5	12.5
	h_2	40	40	40
	h_3	40	40	40
	h_4	40	40	40
	h_5	12.5	12.5	12.5
Ag/Pd Thickness (μm)	h_{e1}	20	20	20
	h_{e2}	12	12	12
	h_{e3}	12	12	12
	h_{e4}	12	12	12

**Refer to Figure 6-2 (b)*

These samples were polarised with an electric field strength of 5.5 MV/m (220 V dc) on each PZT section of the composite multilayer structure, at an elevated temperature of 200 °C for 30 minutes. Two polarisation modes were studied; series and parallel modes. In the series polarised sample, both the upper and lower PZT sections were polarised in the same direction toward the centre section as shown in Figure 7-6 (a) creating an electrically neutral condition at the centre section. In the parallel polarised sample, the upper section and lower section of the PZT were polarised in opposite directions, as shown in Figure 7-6 (b), where one facing into and the other facing out from the centre section which creates an opposite polarised centre section. When the multimorph structure is operating in a bending mode, charges with different polarity will be produced on the electrode layers, as shown in Figure 7-7. A resultant electrical output equal to the sum of the individual sections of the PZT layers will be produced when a combination of connections is made to the electrode terminals.
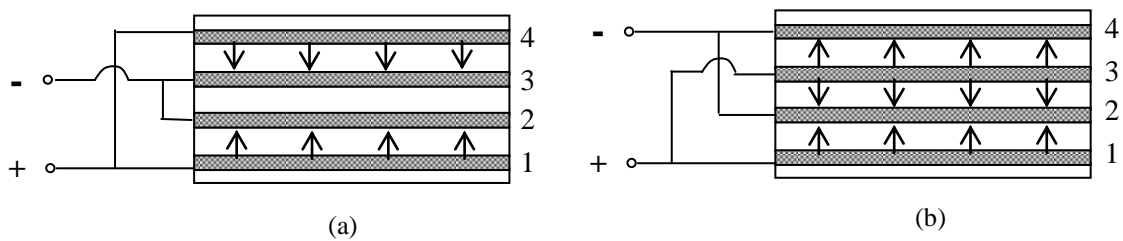
Figure 7-6: Polarisation mode: (a) Series and (b) parallel. The number beside each layer denotes the fabrication sequence of electrode layers.
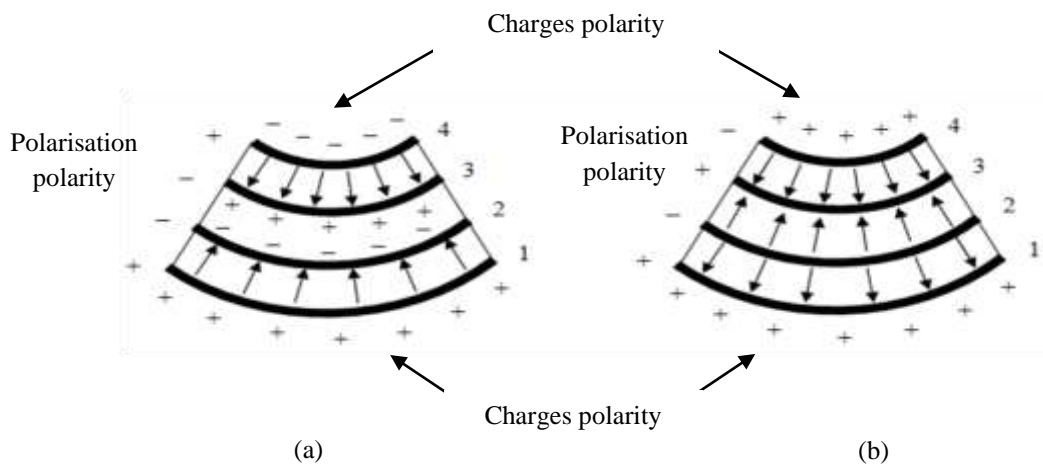
Figure 7-7: Schematic diagram of charges generation when the multimorph structures were in upward bending position for a (a) series and (b) parallel polarised device.

An experiment was also performed with proof masses attached to the tip of the multimorph structures in order to study the dependence of electrical output on the additional mass. However, there is a maximum stress that the structure can withstand before the structure fails to respond accordingly. The maximum stress of a free-standing structure was determined experimentally, as described in the following section.

7.4 Evaluation of Maximum Allowed Excitation with Proof Mass

A series polarised bimorph cantilever (sample BA1) with dimensions as shown in Table 7-1 and with a proof mass of 0.73 g attached was excited to its resonant frequency of 149 Hz at increasing acceleration levels from 0.01 g to 0.75 g. Results show that there is an increase in output power from 81 nW to 32 μW and a slight shift in resonant frequency from 156 Hz to 149 Hz when the acceleration level is increased from 0.01 g to 0.5 g (cf. Figure 7-8). This is because the tip of the cantilever hit the surface of the substrate and displaced the proof mass. The deflection of the cantilever tip is related to the excitation acceleration level and proof mass according to equation (3-33). Once the cantilever reached the maximum gap height, no further improvement of output power is produced.
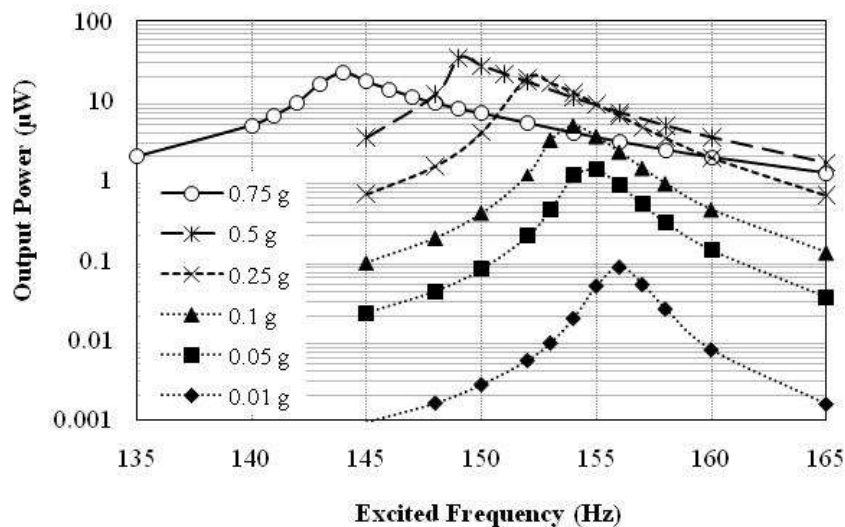
Figure 7-8: Output power as a function of excited frequency at different acceleration levels for sample BA1 (note that output power is displayed on a logarithmic scale).

A dramatic drop of output power and resonant frequency, however, was measured when the sample was excited to a greater acceleration level of 0.75 g as shown in Figure 7-8. This is because fracture starts to develop on the anchor of the cantilever, which connects the free-standing structure to the base, and further increments of acceleration level with the same proof mass may break the free-standing structure completely. The maximum stress that the structure can withstand before failure can be calculated by substituting equations (3-4), (3-18), (7-5) and (7-10) into,

$$\sigma = \frac{M_{eff}\left(\ddot{y} + \ddot{z}\right)d_{mm}l_b}{2I_{mm}} \tag{7-11}$$

From the experiment with sample BA1, the maximum stress allowed was calculated as 115 MPa and 65 MPa on the surface of the electrode and PZT layers respectively.

7.5 Evaluation of Electrical Output

The electrical output from both the series and parallel polarised samples was obtained by connecting the electrode terminals in a configuration that resembles series, parallel and a combination between these two connections. For example, a connection between electrode number 1 and 2 is denoted as 1;2. A connection to make electrode number 2 and 4 as a terminal (shorting 2 and 4) and electrode number 1 and 3 (shorting 1 and 3) as another terminal, is denoted as 2+4; 1+3. The ';' denotes a separation between two terminals.

The PZT network configuration of a multimorph structure can be analysed as a conventional electrical circuit consisting of capacitors, resistors and voltage sources. The resultant capacitance of the configuration was obtained by direct measurement with a Wayne Kerr LCR meter, by connecting a combination of electrode terminals of the multimorph structure. The measurements of the capacitance are summarised in Table 7-2.

The resultant resistance of the PZT layer network corresponds to the optimum resistive load at the maximum output power of the PZT layer when the structure is excited to its

resonant frequency. The resultant voltage is simply the sum of the voltages produced by the network of individual PZT sections.

Table 7-2: Measurement of capacitance of all the possible configurations of terminal connection for series and parallel polarised samples.

Connection configuration	Capacitance (nF)	
	BA2 (Series Polarised)	BA3 (Parallel Polarised)
1;2	21.3	21.3
1;2 (Short 3+4)	21.3	21.3
1;3	10.3	10.1
1;3 (Short 2+4)	14.1	13.8
1;4	7.0	19.8
1;4 (Short 2+3)	10.6	31.0
2;3	20.0	6.9
2;3 (Short 1+4)	30.1	10.7
2;4	10.3	10.2
2;4 (Short 1+3)	14.1	13.9
3;4	21.3	21.1
3;4 (Short 1+2)	21.3	21.1
1+2; 3+4	61.5	63.7
1+3; 2+4	20	19.8
1+4; 2+3	42.8	42.0

7.5.1 *Series polarised multimorph*

A series polarised (Figure 7-6 (a)) sample, BA2, with dimensions as shown in Table 7-1 was excited to its resonant frequency at 403 Hz with a constant acceleration level of 0.5 g. The output power from each of the PZT sections was obtained by measuring the voltages across the electrode terminals sandwiched between each PZT layer when driven over a range of resistive loads from 1 kΩ to 150 kΩ.

The output power from the upper section of PZT was obtained by a configuration of 3;4 (terminal connection of electrode 3 and 4) while the output power for the lower section of PZT was obtained by a configuration of 1;2 (terminal connection of electrode 1 and 2). Figure 7-9 shows that the upper section of PZT produces a higher output power at about 32 µW compared to the lower section which produces about 24 µW. This is due to the fact that the distance from the PZT layer centroid to the neutral axis of a multimorph structure (d_{mm}) for the upper PZT layer is greater than for the lower PZT section, as a result of a thicker electrode being printed on the bottom of the structure. The additional layer of Ag/Pd (two prints with a thickness of 20 µm) was printed as the lower electrode also acts as a physical support to the free-standing structure.

The experiment results are consistent with the calculated results using equation (7-1), as shown in Figure 7-9. The maximum output power for both of the PZT sections were measured when driven through an optimum resistive load of 18.5 kΩ.
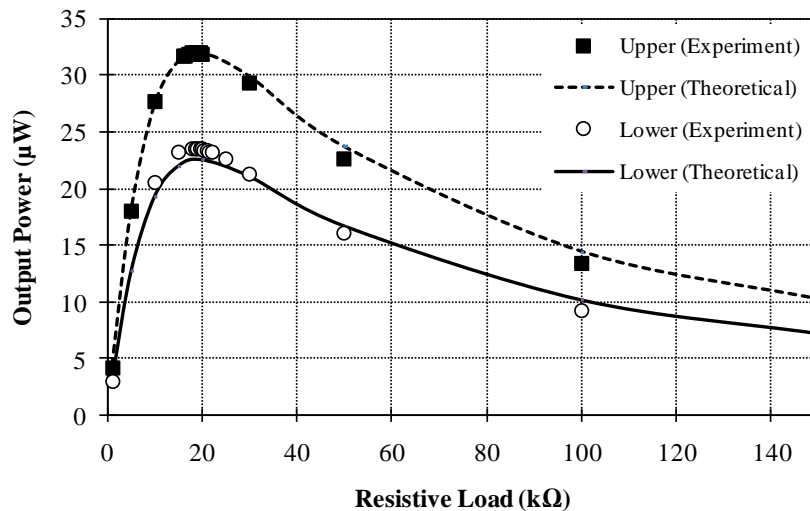
Figure 7-9: Output power as a function of resistive load for upper section and lower section of PZTs for a multimorph structure.

Figure 7-10 shows that the output power is scaled up when connecting the individual lower and upper sections of PZT to make a series configuration (1;4 short 2+3) and this produced a maximum power of about 41 µW, when driving a resistive load of 37.5 kΩ. The magnitude of the output power is significantly improved by a factor of about 400 compared to a unimorph structure with similar length which was reported in Chapter 5. The plot also shows that a configuration of 2+4; 1+3 produces an optimum output

power of 32 μW when driving at a lower resistive load of 7.5 kΩ. Comparing the output open circuit voltage, optimum resistive load and the measured capacitance of this configuration (Table 7-2) to the configurations of 1;2 and 3;4 (individual PZT section), the 2+4; 1+3 configuration resembles a parallel connection of resistors, capacitors and DC voltage sources.

The central section of PZT with the configuration of 2;3 is electrically neutral and no net charge is produced when excited to its resonant frequency. However, a relatively small output power of 9 nW was generated when driving a resistive load of 20 kΩ, which shows that there is a slight difference in the strength of the electrical potential across the electrodes which may be contributed by the upper and lower sections of the PZT. The values of the measured capacitance, as shown in Table 7-2 and the optimum resistive load are similar to those of the individual PZT section, which verified that the central section is electro-active and has the potential to produce an electrical output when the correct configuration of electrode terminals is in place.
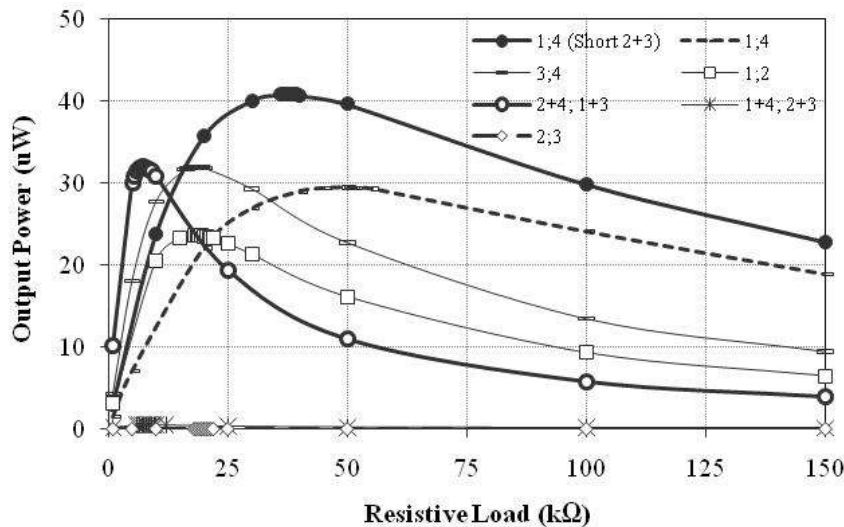
Figure 7-10: Output power as a function of resistive load for a multimorph cantilever with a few different electrode configurations.

Figure 7-11 shows the output current-voltage relationship of the terminal connected configurations. Series configuration (1;4 short 2+3) produces the highest output voltage at a lower output current, while a parallel configuration (2+4; 1+3) produces the highest output current at a lower output voltage. This shows that a series configuration function

is better for applications requiring a higher output voltage, whereas (as will be shown in the following section) a parallel configuration is more suitable for applications that require a higher output current.
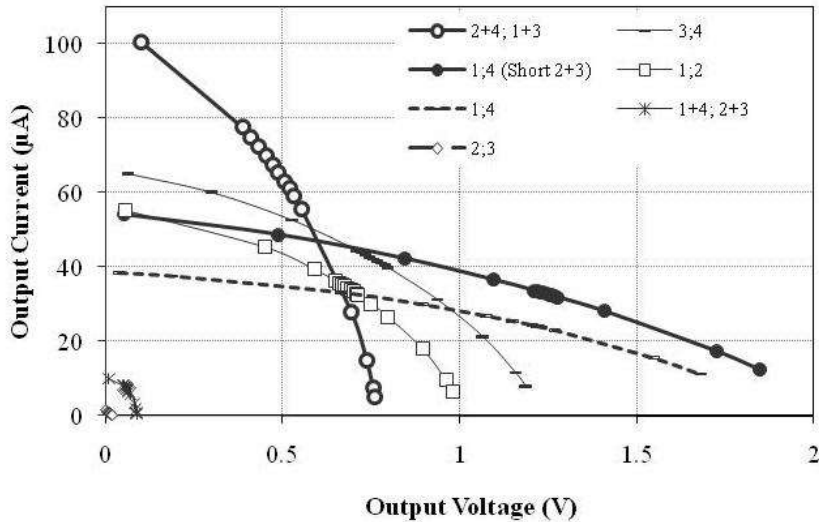
Figure 7-11: Output current-voltage for a series polarised sample.

In another experiment, the resultant voltage for sample BA2 was investigated by measuring the open-circuit voltage at a constant frequency of 403 Hz (a resonant frequency corresponding to an acceleration level of 0.5 g). The open-circuit voltage is increased consistently with acceleration level regardless of configuration with different combination of PZT network, as shown in Figure 7-12. The open-circuit voltage of configuration 1;4 (short 2+3) is equivalent to a series connection of two voltage sources and produces a total output voltage that is equal to the sum of the individual lower (configuration 1;2) and upper (configuration 3;4) sections of the PZT.

Since the central PZT section is electrically neutral, the configuration of 1;4, which is equivalent to a series connection of three voltage sources produced the same voltage output as the configuration where electrode 2 and 3 were shorted, as expected. This is consistent with the result of configuration 2;3, where no obvious increment of open circuit voltage is noticed with increased acceleration level. Configuration 1+4; 2+3 is equivalent to two voltage sources connected in a parallel mode with different polarity resulting in a voltage difference between two voltage sources.An open-circuit voltage of about 2.6 V was measured from a series connection of two voltage sources when

excited to an acceleration of 1.5 g, which is the sum of the voltages produced by the upper (1.45 V) and lower (1.15 V) sections of the PZT.
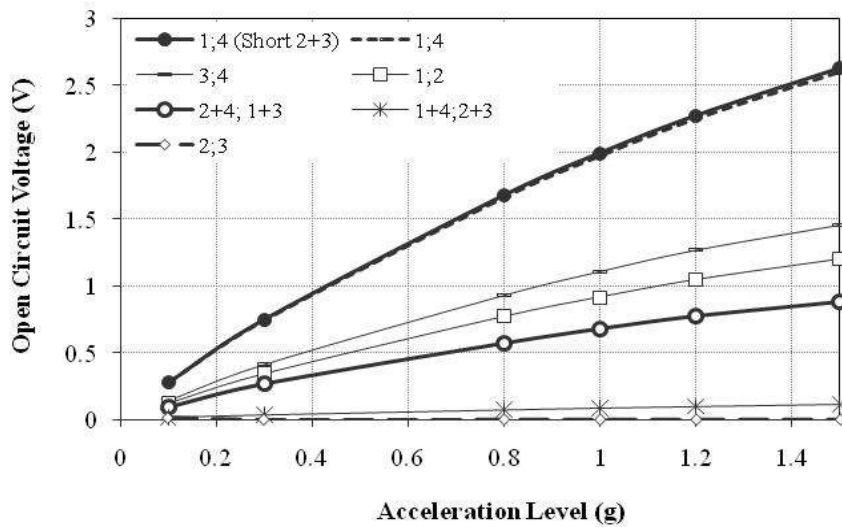
Figure 7-12: Open circuit voltage as a function of acceleration level for a multimorph cantilever with a few different electrode configurations.

Table 7-3 summarises all the major configurations of terminal arrangement for a multimorph structure polarised in series mode. The table is divided into three columns, where the first column is the notation for the configuration, while the second column shows the connection diagram of the multimorph structure and the equivalent circuit of the configuration.

The equivalent circuit of the networks consist of individual components representing a resistor, a capacitor and a voltage source. The polarity of the component shown in the table is the polarity of the charges produced as a result of stress applied on the PZT in bending mode at upward bending position as shown in Figure 7-7 (a). The polarity, however, is not static and is dependent on the bending position of the multimorph structure. In a downward bending position, the polarity will be opposite to that shown in the table.

The third column of the table shows the equivalent circuit equations of capacitance, resistance and open-circuit voltage of the configuration. The equations were verified by the experiment results discussed above.

Table 7-3: Summary of connection configurations for a series polarised sample.

Connection Configuration	Connection Diagram	Equivalent circuits
1; 4 (Short 2+3)		$C_{1;4}^{S} = \dfrac{C_{1,2}C_{3;4}}{C_{1;2} + C_{3;4}}$ $R_{1;4}^{S} = R_{1;2} + R_{3;4}$ $V_{1;4}^{S} = V_{1;2} + V_{3;4}$
1; 4		$C_{1;4} = \dfrac{C_{1;2}C_{2;3}C_{3;4}}{C_{3;4}\left(C_{1;2}+C_{2;3}\right)+C_{1;2}C_{2;3}}$ $R_{1;4} = R_{1;2} + R_{1;3} + R_{1;4}$ $V_{1;4} = V_{1;2} - V_{2;3} + V_{3;4}$
1+4; 2+3		$C_{1+4;2+3} = C_{1;2} + C_{3;4}$ $R_{1+4;2+3} = \dfrac{R_{1;2}R_{3;4}}{R_{1;2} + R_{3;4}}$ $V_{1+4;2+3} = \left|V_{1;2} - V_{3;4}\right|$
2+4; 1+3		$C_{2+4;1+3} = C_{1;2} + C_{2;3} + C_{3;4}$ $R_{2+4;1+3} = \dfrac{R_{1;2}R_{2;3}R_{3;4}}{R_{2;3}R_{3;4} + R_{1;2}\left(R_{2;3} + R_{3;4}\right)}$ $V_{2+4;1+3} = \dfrac{V_{1;2} + V_{2;3} + V_{3;4}}{3}$
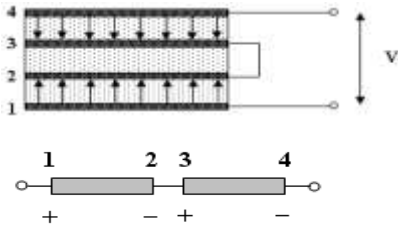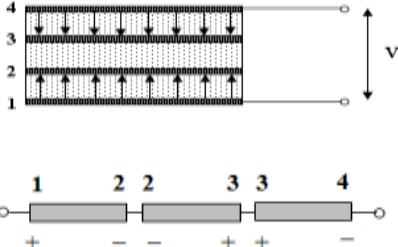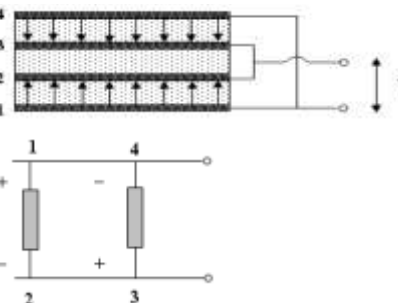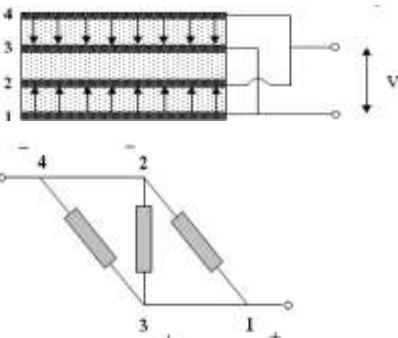
7.5.2 Parallel polarised multimorph

Sample BA3 with similar dimensions and processed in the same way as BA2 was polarised in parallel mode as shown in Figure 7-6 (b). Similar to the case of BA2, the lowest electrode layer is thicker than the rest of the electrodes and therefore results in a greater *d* (equation (7-5)) distance of the upper section of PZT compared to the lower section. As a consequence, the output power for the upper section of PZT with configuration 3;4 is greater than the lower section with configuration 1;2, as shown in Figure 7-13. The output powers are 20.9 nW and 14.6 nW respectively, which is in good agreement with equation (7-5).

The parallel polarised multimorph sample, however, does not have a pure series configuration. The configuration of 1;3 short 2+4 is the nearest arrangement to the series configuration of a series polarised sample, which is actually equivalent to a combination of parallel and series networks of components. This configuration generates a lower output power of 22.5 µW, compared to the series polarised sample, when driving a resistive load of 27.5 kΩ, as shown in Figure 7-13.

A pure parallel connection was established with a configuration of 1+4; 2+3, which resembles the configuration of 2+4; 1+3 of a series polarised sample. This configuration generates an optimum output power of 28.7 µW when driving a resistive load of 9.5 kΩ. All the remaining configurations are hybrid connections of series and parallel which generate output power with a magnitude in between maximum and minimum value.

The maximum output voltage generated by a parallel polarised sample is lower than that generated from a series polarised multimorph sample, as would be expected. Figure 7-14 shows that the open circuit voltage of the hybrid configuration (1;3 short 2+4) is 1.18 V, which is merely 33 % higher compared to its parallel configuration (1+4; 2+3), while the series configuration of sample BA2 (series polarised multimorph) is about 150 % higher when compared to its parallel configuration, as shown in Figure 7-11. This shows that a parallel polarised multimorph is not as effective when operated as a voltage source.

When driving a very low resistive load (≈ short circuit), the upper and lower sections of PZT produce electrical current of 55 μA and 44 μA respectively. An optimum output current of about 88 μA was measured for a parallel configuration (1+4; 2+3), while the hybrid configuration generates 44.2 μA of electrical current. This verifies that a parallel configuration can be an effective current source compared to other possible configuration for the multimorph structure.
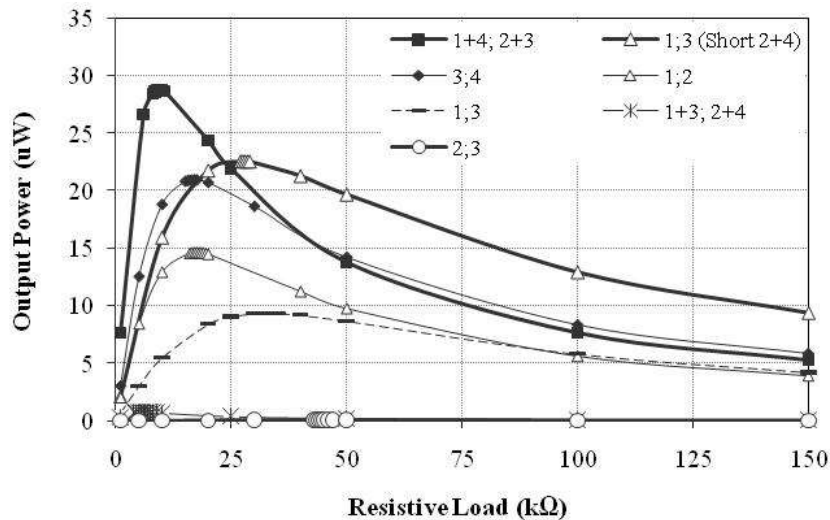
Figure 7-13: Output power as a function of resistive load for a parallel polarised sample.
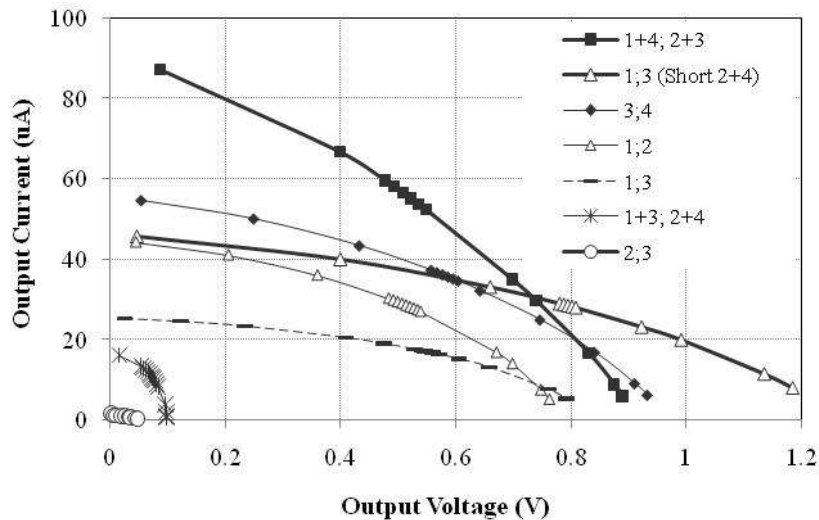
Figure 7-14: Output current-voltage for a parallel polarised sample.

Figure 7-15 shows the dependence of open circuit voltage for sample BA3 on acceleration level. Similar to the results shown in Figure 7-12, the increment of the open circuit voltage is consistent for all the configurations at an increased acceleration level.

169

An open-circuit voltage of about 2.5 V was measured for a configuration of 1;3 (short 2+4), when the multimorph cantilever was excited to its resonant frequency at an acceleration level of 1.5 g. The configuration is equivalent to a network of individual voltage sources with configuration of 2;3 and 3;4 connected in parallel and linked together in series with configuration 1;2.

It is noticed that the central PZT section for sample BA3 is weakly polarised and generates relatively small open-circuit voltage when excited to the resonant frequency of the structure. This is more obvious when the acceleration level increases. An open-circuit voltage of 100 mV was measured from the central PZT section (with configuration 2;3) at an acceleration of 1.5 g, as shown in Figure 7-15.

Since the central PZT section was weakly polarised, it plays a part in the resultant electrical output. When the multimorph is bent downward as shown in Figure 7-7 (b), the polarities of electrodes at the central section are similar to those of the outer layer, e.g. electrode 1 and 2 are at same polarity but with different electric field strength. The difference in electrical potential between them is lower than those of series polarised samples and therefore generates less electrical output. This effect, however, is useful for actuation applications, where a smaller input voltage is required to deflect the cantilever, as a result of converse piezoelectric effect, at the same magnitude as a series polarised samples with higher input voltage.

Table 7-4 summarises all the major configurations of the terminal and the equivalent circuit of the connection for a parallel polarised sample. The equivalent circuits were verified experimentally.
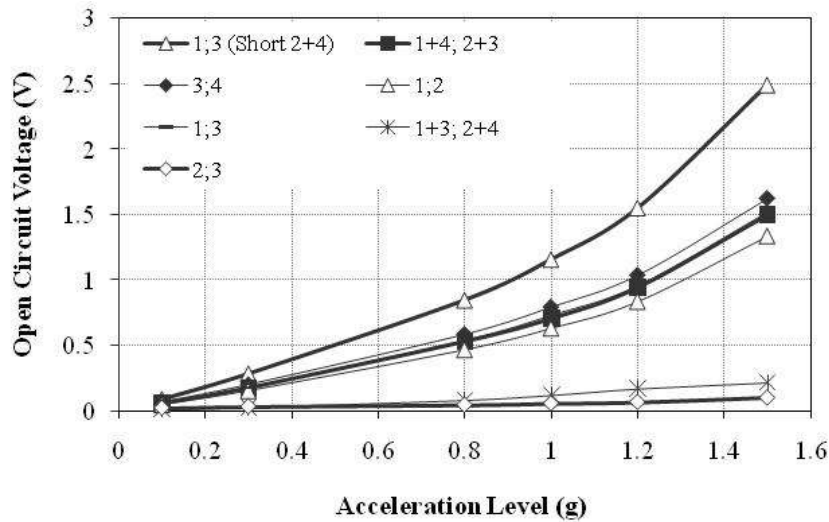
Figure 7-15: Open circuit voltage as a function of acceleration level of a parallel polarised sample.

Table 7-4: Summary of connection configurations for a parallel polarised sample.

Connection Configuration	Connection Diagram	Equivalent circuits
1+4; 2+3		$C_{4+1,2+3} = C_{1,2} + C_{3,4}$ $R_{4+1,2+3} = \dfrac{R_{1,2}R_{3,4}}{R_{1,2} + R_{3,4}}$ $V_{4+1,2+3} = \dfrac{V_{1,2} + V_{3,4}}{2}$
2; 4		$C_{2,4} = \dfrac{C_{3,4}\{C_{1,2}C_{1,3} + C_{2,3}(C_{1,2} + C_{1,3})\}}{(C_{1,2} + C_{1,3})(C_{2,3} + C_{3,4}) + C_{1,2}C_{1,3}}$ $R_{2,4} = R_{3,4} + \left\{\dfrac{R_{2,3}(R_{1,2} + R_{1,3})}{R_{1,2} + R_{1,3} + R_{2,3}}\right\}$ $V_{2,4} = V_{3,4} + \left[\dfrac{(V_{1,2} - V_{1,3}) + V_{2,3}}{2}\right]$

171

2; 4
(Short 1+3)
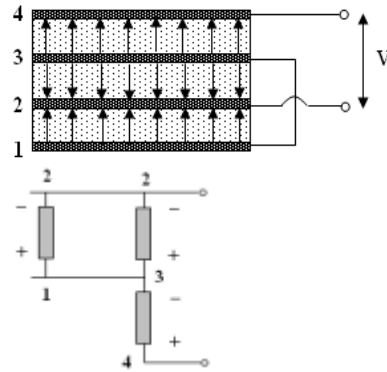
$$C_{2,4}^{S} = \frac{C_{3,4}(C_{1,2} + C_{2,3})}{C_{1,2} + C_{2,3} + C_{3,4}}$$

$$R_{2,4}^{S} = R_{3,4} + \frac{R_{1,2}R_{2,3}}{R_{1,2} + R_{2,3}}$$

$$V_{2,4}^{S} = V_{3,4} + \frac{V_{1,2} + V_{2,3}}{2}$$

1; 3
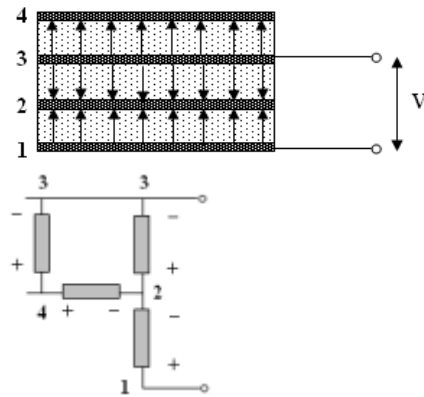
$$C_{1,3} = \frac{C_{1,2}\{C_{2,4}C_{3,4} + C_{2,3}(C_{2,4} + C_{3,4})\}}{(C_{2,4} + C_{3,4})(C_{1,2} + C_{2,3}) + C_{2,4}C_{3,4}}$$

$$R_{1,3} = R_{1,2} + \left\{\frac{R_{2,3}(R_{2,4} + R_{3,4})}{R_{2,3} + R_{2,4} + R_{3,4}}\right\}$$

$$V_{1,3} = V_{1,2} + \left[\frac{(V_{3,4} - V_{2,4}) + V_{2,3}}{2}\right]$$

1; 3
(Short 2+4)
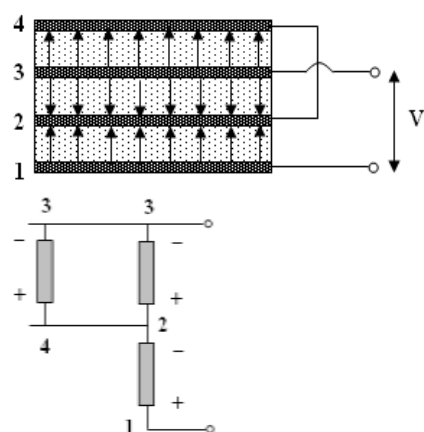
$$C_{1,3}^{S} = \frac{C_{1,2}(C_{2,3} + C_{3,4})}{C_{1,2} + C_{2,3} + C_{3,4}}$$

$$R_{1,3}^{S} = R_{1,2} + \frac{R_{1,3}R_{3,4}}{R_{1,3} + R_{3,4}}$$

$$V_{1,3}^{S} = V_{1,2} + \frac{V_{2,3} + V_{3,4}}{2}$$

7.5.3 Excitation with Proof Mass

In another experiment, the electrical output of a multimorph cantilever sample was increased by attaching a proof mass at the tip of the cantilever. This experiment was carried out to investigate the practical use of the device in energy harvesting. An output voltage of approximately 300 mV to compensate for the voltage dropped across a rectification diode and an electrical output power of 60 μW are the minimum requirement for a micro-system to function properly, as reported in [65]. Consequently, these values are used as the benchmark for this experiment. Sample BA2, a series polarised multimorph, was used in this experiment. It was connected in an optimum series configuration to draw out as much output power and voltage as possible to meet the minimum requirement.

A new resonant frequency was measured at 155 Hz when the multimorph cantilever was attached with a proof mass of 0.38 g. With this proof mass, an output power of 110 μW was generated, which is about a factor of 3 higher compared to the same sample with no proof mass, as shown in Figure 7-16. However this arrangement required a greater resistive load of about a factor of 2.6 compared to excitation without proof mass. The optimum resistive loads for an excitation with and without proof mass for the multimorph structure are 90 kΩ and 35 kΩ respectively as shown in Figure 7-17.

If the resistive load is maintained at 35 kΩ, an output power of 75 μW is produced. Although the value is not up to its maximum, it is good enough to meet the minimum requirement at 60 μW.

In an experiment where the sample was excited with different acceleration levels, the open circuit voltage increases with acceleration level as expected, from about 1.5 V for an acceleration level of 0.1 g to about 5.8 V for an acceleration of 0.6 g, as shown in Figure 7-18. The increment of acceleration level, however, is limited to the maximum allowed stress of 77.0 MPa for the resonant structure before it suffers fracture. With a proof mass of 0.38 g, the maximum allowed acceleration level, according to equation (7-11), is 0.89 g.
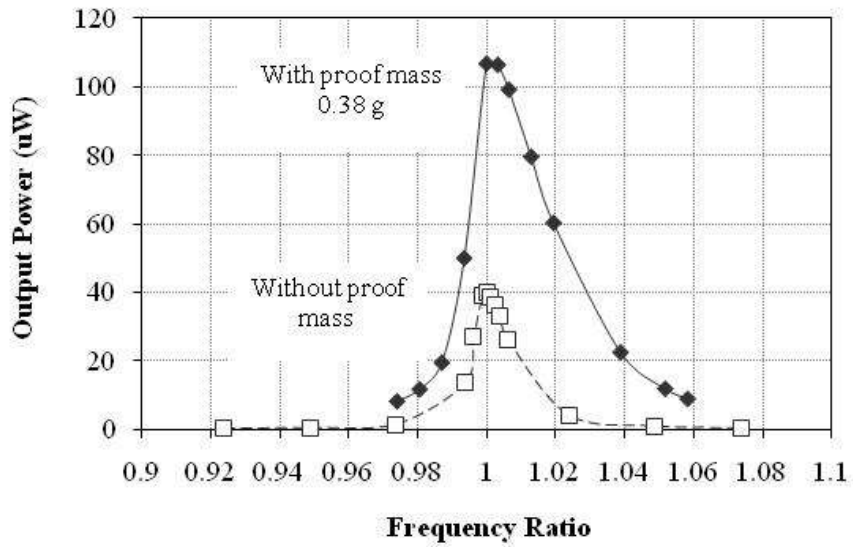
Figure 7-16: Comparison of output power between excitation with and without proof mass for the same multimorph sample (at connection 1;4 short 2+3).
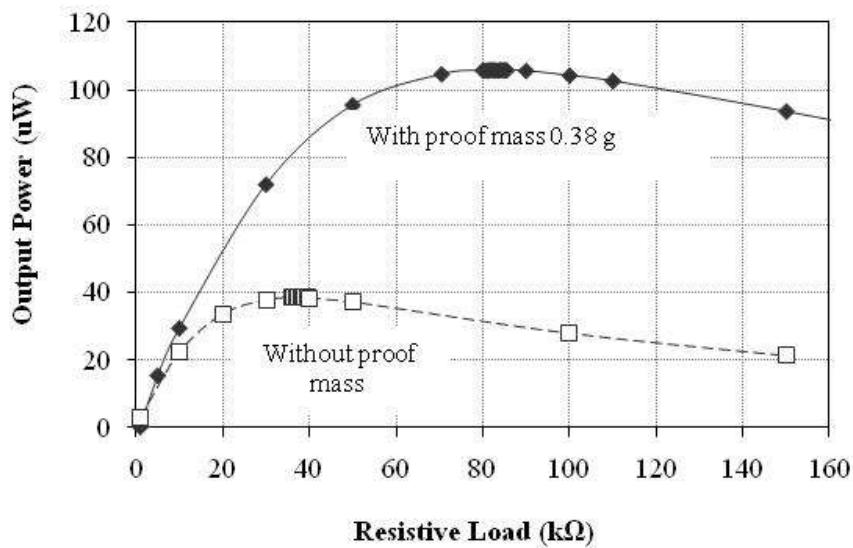
Figure 7-17: Output power as a function of resistive load for the multimorph sample when excited with and without proof mass.
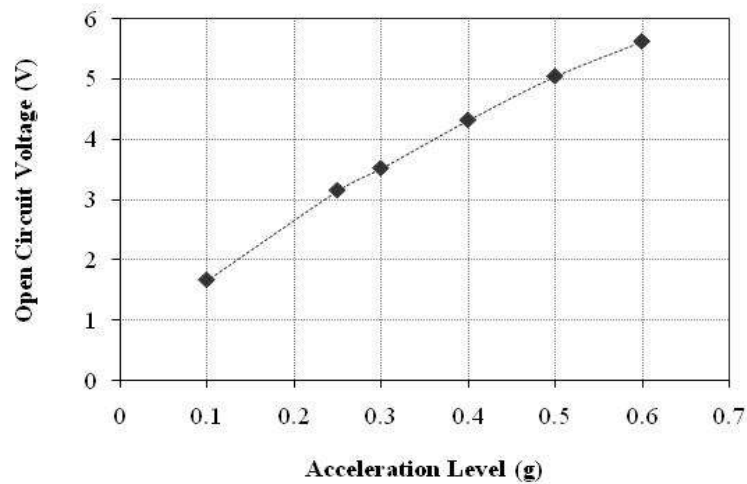
Figure 7-18: Open circuit voltage as a function of acceleration level for the multimorph
cantilever sample.

This experiment shows that the device is able to operate a micro-system application at a
low level ambient vibration condition. However, care must be taken when operating in
certain ambient environments, where the acceleration levels and frequency are changing
randomly with time. Figure 7-19 shows that as the acceleration level increases, the
resonant frequency shifts to a lower value from 156.5 Hz for an acceleration of 0.1 g to
154 Hz for an acceleration of 0.6 g. One of the ways to minimise the effect of
uncertainty is by designing a multi-frequency energy harvester, which will be discussed
in the following chapter.
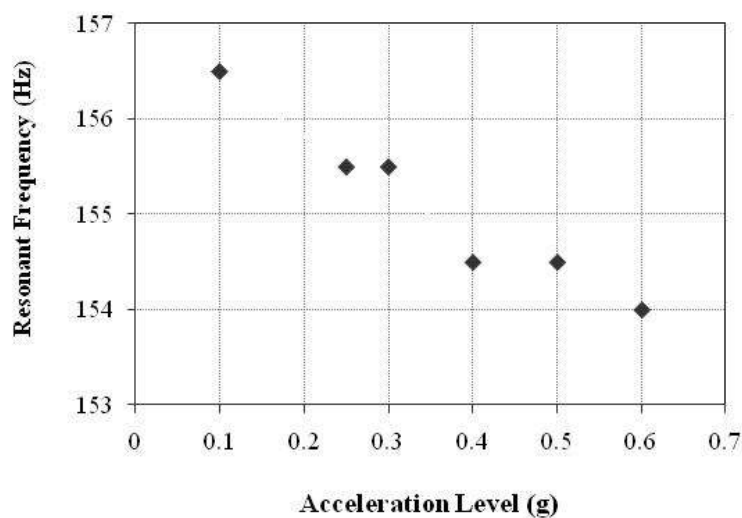
Figure 7-19: Resonant frequency as a function of acceleration level for the multimorph
cantilever sample.

7.6 Conclusion

The distance between the centroid of the PZT layers to the neutral axis, d is one of the important factors in determining the electrical output for a free-standing cantilever structure. In order to increase the d distance, multimorph composite structures were fabricated and characterised. The experimental results are in good agreement with the theoretically calculated results and verify that a multimorph structure performs better than a unimorph structure. A free-standing multimorph structure offers two significant advantages over conventional piezoelectric cantilevers; one of which is its flexibility in fabrication and integration within microelectronic systems and the other one is the flexibility in switching between current and voltage sources for energy harvesting applications by arranging the configuration of the terminals. As expected from the experiment, a series polarised sample is suitable for use as an energy harvester, while a parallel polarised sample is preferred for actuator applications.

Chapter 8   Multi-Frequency Piezoelectric Energy Harvesters

8.1 Introduction

There are a few issues concerning cantilever-type energy harvesters. Of significance is the narrow bandwidth of frequencies, where a small change (±2 Hz) in excitation frequency will lead to a drastic drop in the output power (-3 dB). This is due to the high Q-factor of a piezoelectric cantilever structure, which is typically greater than 100. This characteristic is favourable when operated with a vibration sources of constant excitation frequency. Ambient vibration sources, however, are unpredictable, and therefore a wider bandwidth of operation is desirable.

One of the ways to increase operating frequency is by utilising a self-tuning mechanism, where the energy harvester can tune its resonant frequency to match the vibration source on which it is mounted, thereby optimizing its electrical output. This can be done by altering the parameters of the generator such as the mass, length or the stiffness of the system. Tuneable energy harvesters can be classified into two categories; active and passive [116], or intermittent and continuous as described in [117]

Active tuning techniques involve actuators, which adjust the frequency of the system continuously to match the environmental frequency. By comparison, the actuators for a passive tuning technique are disengaged once the frequencies are matched and are then maintained at that particular frequency until any change in the environmental frequency exceeds a predetermined threshold level, whereupon the actuators are re-engaged to repeat the process of frequency matching. Typically tuning techniques involve complex

processing systems which may require more electrical power to operate than the energy harvester can supply, thereby making them unattractive for microsystem applications.

An alternative method for increasing the operating frequency range is by widening the bandwidth, which can be implemented by fabricating an array of cantilever beam structure with slightly different resonant frequencies, operating as a single system. Each of the individual cantilevers generates maximum electrical output at its resonance and effectively offers a solution for operating in multi-frequency conditions. This method does not involve complex microelectronic components and does not require additional electrical power to operate. Therefore, it is flexible to design and easy to integrate with microsystems.

One of the ways to implement multi-frequency methods is by deploying an array of cantilevers with different lengths as described by Sari *et al* [118]. The model is based on an electromagnetic conversion mechanism, where an array of cantilevers is excited over a band of frequencies centered about the resonant frequency of the device. In this system the electrical coils which are fabricated on the micromachined silicon, will generate a ripple of electrical current according to the resonant frequency of each cantilever. The authors showed that an electrical output power of 0.4 µW was generated across a frequency band of 800 Hz, from 4.2 kHz to 5 kHz. In another publication, Liu *et al* [119] described a MEMS-based array of piezoelectric energy harvesters. The system consists of three cantilevers with lengths from 2 mm to 3.5 mm and width 0.75 mm to 1 mm. When excited to their resonant frequencies (226 – 234 Hz) an average power of 3.98 µW was measured by electrically connecting in series each cantilever.

An alternative approach to the use of different cantilever lengths was described by Ferrari *et al* [120]. Their implementation for multi-frequency concept involved attaching three different proof masses (0.6 g, 0.7 g and 1.4 g) at the tip of bimorph cantilevers with the same dimensions of 15 mm × 1.5 mm × 0.6 mm. Their experiment showed an improvement in the effectiveness of the overall energy generation across a wideband frequency spectrum (113 – 281 Hz) compared to a single cantilever device.

Most of the multi-frequency energy harvesters reported in the literature are either fabricated with silicon micromachining or manual assembly of individual components

into a complete system. Therefore they either have to be operated at very high frequencies or have the constraint of integrating within microsystems. By comparison, thick-film multi-cantilever structures have the advantages of both technologies and offer a better solution for harvesting energy from ambient environments. This chapter discusses the design of, simulation of, and experimental results from multi-cantilever free-standing structures.

8.2 The Functioning Principle

The natural frequency of a cantilever structure can be altered by changing its dimensions and mass according to equation (3-9). When operated in an array of cantilevers with small differences in lengths or masses, they can harvest optimum electrical energy collectively from each of the cantilevers over a wider bandwidth of excitation frequencies as described by Sari *et al* [118].

The operational bandwidth of this multi-cantilever system depends on the number of cantilevers which are integrated within the system. The overlapping effect of resonant frequency of individual cantilever is an important factor to ensure a continuity of operation within a specified spectrum of vibration frequencies. Simulation results of individual cantilevers and a multi-cantilever system performed by Sari *et al* [118] is shown in Figure 8-1.

The results show that the output power increases with the resonant frequency; this is because the experiment was performed at constant vibration amplitude of 1 μm. In order to maintain this level, the acceleration level has to be increased according to $a_{in} = Y\omega^2$. In the case for a resonant frequency of 4.5 kHz, an acceleration of about 800 g should be applied to the system to maintain a vibration amplitude of 1 μm. This level of acceleration is out of the range that the ambient environment could possibly supply.
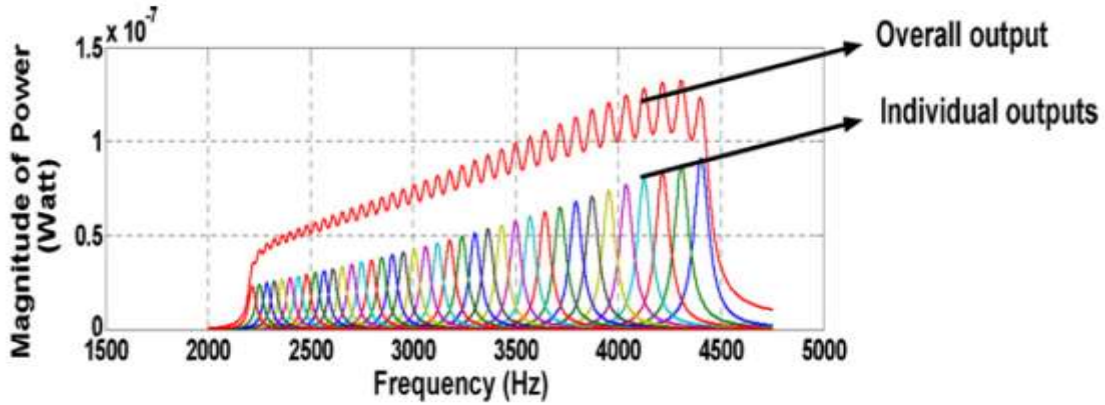
Figure 8-1: Comparison of simulated power output between individual cantilevers and a multi-cantilever system consisting of 40 individual cantilevers at a vibration amplitude of 1 μm [118].

A multi-cantilever system has a few disadvantages. One of which is that the maximum power will be reduced compared to an identical cantilever operating as an individual device, at a constant acceleration level. This is because of charge leakage as a result of the converse piezoelectric effect, where a small amount of charge generated by a resonated cantilever will leak to cantilevers which are at rest. Another weakness is the size of the whole system which tends to increases with the number of cantilevers.

In order to function as an effective wideband energy harvester, the overlapping individual resonant frequencies have to be close enough to produce a continuity in the optimum electrical output within the operation bandwidth. In this work, a figure of merit is used to compare the level of continuity and is given by,

$$C_c = \frac{\sum \Delta f_{\frac{avg}{2}_i}}{\Delta f_B} \tag{8-1}$$

where $\Delta f_{\frac{avg}{2}}$ is the operating bandwidth at half the output voltage of an individual cantilever and Δf_B is the overall operating bandwidth.

8.3 Multi-Cantilever Design

ANSYS[TM] finite element software was used to design and simulate three different models of multi-cantilevers. They are multi-cantilevers with six and three individual cantilevers with different lengths and a multi-cantilever with five individual cantilevers with different width. All of the multi-cantilevers were designed to have similar base width of 35 mm.

Table 8-1: Simulation parameters.

Parameter	Unit	Value
Base excitation	m/s^2	1
Elastic Modulus	GPa	37.8
Poisson's Ratio	Dimensionless	0.35
Density	kg/m^3	7400

The purpose of the simulation was to investigate the harmonic response of the structures at their resonant frequency without the interaction of piezoelectric effect. The resultant stress developed on the structures will be presented as a simulation output, which would give an idea of the magnitude of changes in different cantilever structure at different excitation frequencies. The pattern of changes in the stress will be compared with the pattern of changes in the electrical output from experimental results in the following section.

A multi-cantilever with an array of individual cantilevers (which will be depicted as simple fingers) with different lengths was designed as shown in Figure 8-2. The multi-cantilever consists of six fingers with similar width of 5 mm, having lengths of 20 mm, 19 mm, 18 mm, 17 mm, 16 mm and 15 mm. The dimensions of the multi-cantilever are summarised in Table 8-2.
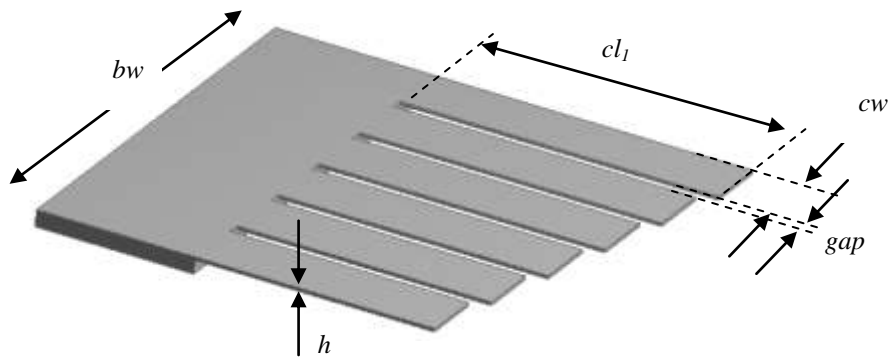
Figure 8-2: A multi-cantilever with different cantilever lengths.

Table 8-2: Summary of dimensions for a multi-cantilever with six fingers of different length.

Parameter	Finger no.					
	1	2	3	4	5	6
Length, *cl* (mm)	20	19	18	17	16	15
Thickness, *h* (mm)	0.2	0.2	0.2	0.2	0.2	0.2
Width, *cw* (mm)	5	5	5	5	5	5
Base width, *bw* (mm)			35			
Gap in between cantilevers (mm)			1			

With a similar total width of the device, an array of cantilevers consisting of 3 fingers with different length of 20 mm, 18 mm and 16 mm was designed as shown in Figure 8-3. A summary of the dimensions of this structure is shown in Table 8-3.

.
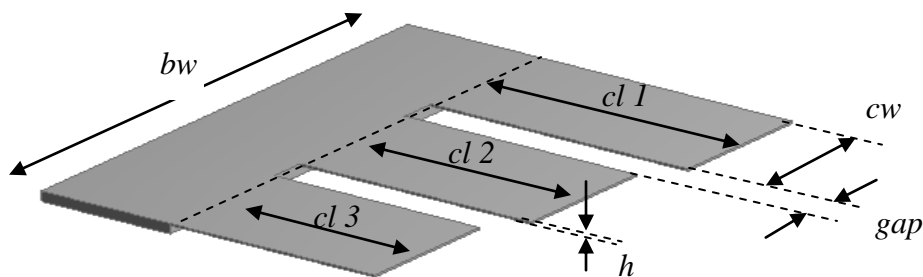
Figure 8-3: An array of cantilevers with three free-standing structures of different length.

Table 8-3: Summary of dimensions for a multi-cantilever with three fingers of different length.

Parameter	Finger no.		
	1	2	3
Length, cl (mm)	20	18	16
Thickness, h (mm)	0.2	0.2	0.2
Width, cw (mm)	10	10	10
Base width, bw (mm)		35	
Gap in between cantilevers (mm)		2.5	

An array of cantilevers with different widths of 2 mm, 4 mm, 6 mm, 8 mm and 10 mm and separation of 1.25 mm between the cantilevers was designed as shown in Figure 8-4. The dimensions of the structure are summarised in

Table 8-4.
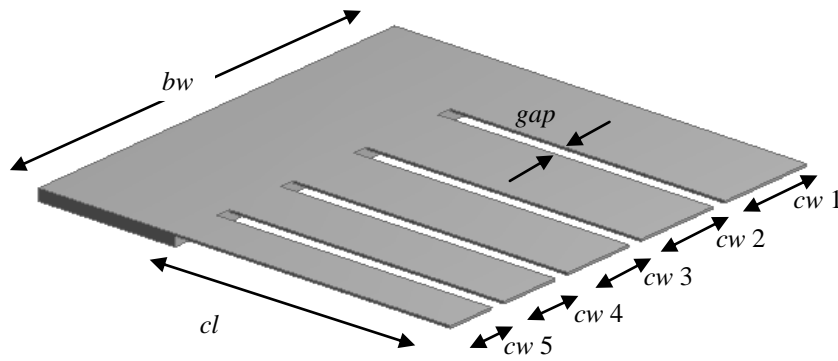
Figure 8-4: Multi-cantilever with an array of free-standing structures of different width.

Table 8-4: Summary of dimensions for a multi-cantilever with five fingers of different width.

Parameter	Finger no.				
	1	2	3	4	5
Length, cl (mm)	20	20	20	20	20
Thickness, h (mm)	0.2	0.2	0.2	0.2	0.2
Width, cw (mm)	10	8	6	4	2
Base width, bw (mm)			35		
Gap in between cantilevers (mm)			1.25		

8.4 ANSYS$^{\text{TM}}$ Simulation Results and Discussion

(a)

(b)

(c)

(d)
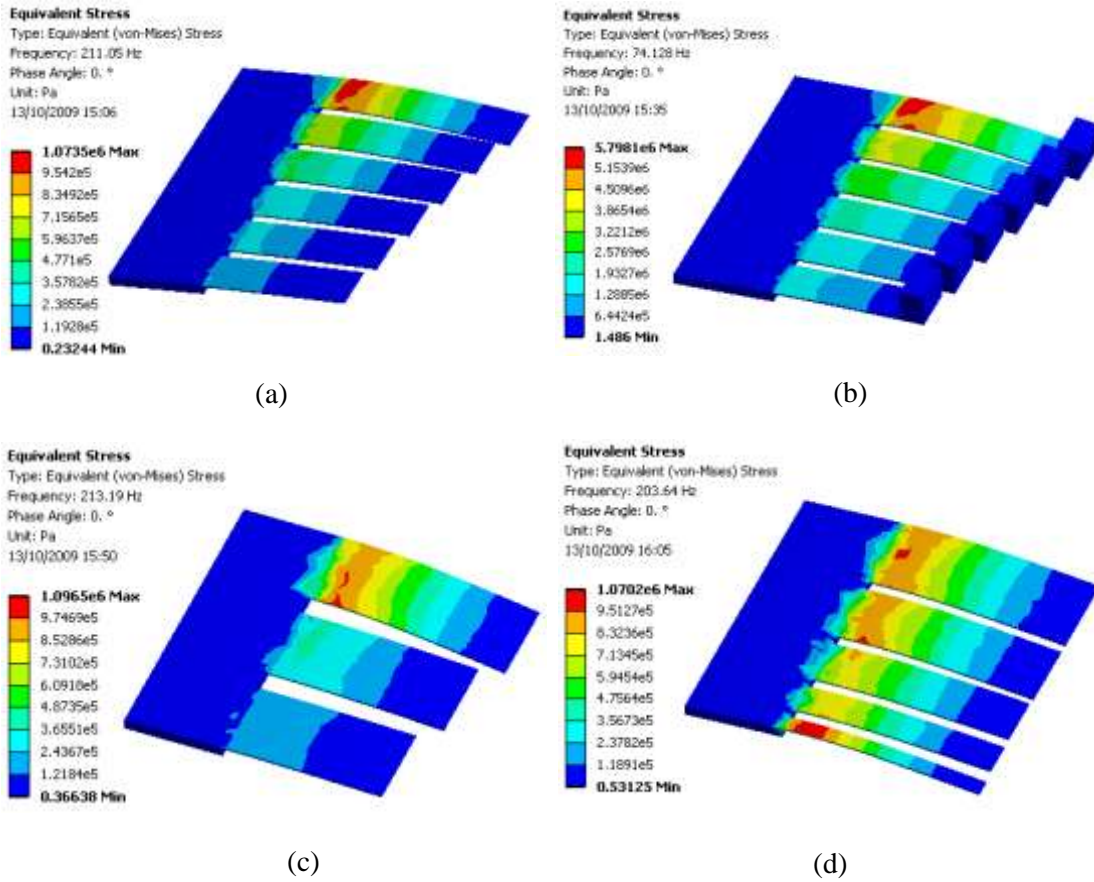
Figure 8-5: ANSYS$^{\text{TM}}$ simulation results showing stress distribution on multi-cantilever structures; (a) model with six fingers with different lengths, (b) cantilevers with masses attached on each finger, (c) model with three fingers with different lengths and (d) model with five fingers of different cantilever width.

Figure 8-5 shows the stress distribution plots for various multi-cantilever structures. For each structure, the stress is concentrated at the clamped end of the cantilever structure near to the base when it is excited to its resonant frequency. For the case of the multi-cantilever with six individual cantilevers as shown in Figure 8-5 (a), a maximum stress of about 1.1 MPa was calculated when excited at 211 Hz, which is the resonant frequency of the longest cantilever. The other cantilevers on this array have a distribution of stresses with magnitudes below the maximum level. The maximum stress distribution pattern shifts toward the second, third (and so on) cantilever, when excited to higher resonant frequencies that are matched to each individual cantilever.

184

The stress distribution pattern is similar for the case when the multi-cantilever is attached with masses as shown in Figure 8-5 (b) but at lower resonant frequencies. The multi-cantilever with three wider free-standing structures but different cantilever lengths appears to have a slightly different first resonant frequency and higher level of stress, as shown in Figure 8-5 (c) compared to the first model. The stress distribution plot also shows that the cantilevers with similar lengths but different width have an almost similar distribution of stress when excited to a resonant frequency of 204 Hz, as shown in Figure 8-5 (d).

Figure 8-6 shows a comparison of a multi-cantilever structure with six fingers of different lengths to a similar set of individual cantilevers. The magnitude of stress of the multi-cantilever is less than that of the identical individual cantilevers and there is a slight frequency shift to lower values. With no interaction of piezoelectric effect on the simulation, the results can be explained as a pure mechanical damping interaction between all the cantilevers in the system. It is noticed that, both of these models displayed a similar pattern of change where the magnitude of stress reduces as the resonant frequency increases corresponding to the length of the cantilevers. This is because, when excited at a constant acceleration level, the amplitude of the excitation decreases at a higher resonant frequency according to $a_{in} = Y\omega^2$, therefore smaller stress is produced.

The same multi-cantilever structure when attached with different proof masses at the end of each of the fingers produces a band of resonant frequencies which is shifting to the left of the plot, as shown in Figure 8-7. Three different arrays of mass were used for the simulation; 0.24 g, 0.48 g and 0.72 g. Multi-cantilevers attached with larger proof mass have a narrower operational bandwidth but with better continuity when compared to smaller masses. The multi-cantilever attached with 0.72 g proof mass has a bandwidth of about 26 Hz (46 – 72 Hz), while 0.48 g and 0.24 g proof mass produced a bandwidth of 35 Hz (53 – 88 Hz) and 49 Hz (72 – 121 Hz) respectively. Since output voltage is proportional to the stress induced on a piezoelectric material, the level of continuity of the multi-cantilever system can be estimated by equation (8-1). The level of continuity for multi-cantilevers attached with proof masses of 0.72 g, 0.48 g and 0.24 g are 23 %, 18.8 % and 13.6 % respectively. A larger proof mass also shows an increase

in the amount of stress that is produced on the structure, which can be translated into a larger output electrical power which is verified by experiment in the following section.
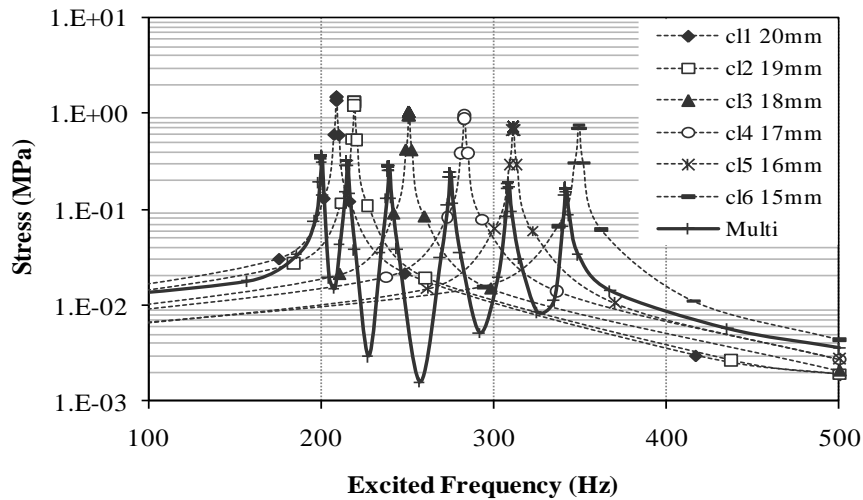
Figure 8-6: Average stress of cantilever structure as a function of excited frequency for multi-cantilever and individual cantilever with different lengths.

By a careful selection of different masses attached to the end of the fingers, the level of continuity can be improved. For example, a combination of proof masses of 0.24 g and 0.48 g attached to the end of finger 1, 2, 3 and 4, 5, 6 respectively resulted in an improvement of the level of continuity to about 25.8 %, as shown in Figure 8-8, with a bandwidth of 18 Hz (72 - 90 Hz). By comparison, a combination of 0.48 g and 0.72 g attached to the end of finger 1, 2, 3 and 4, 5, 6 respectively resulted in an improvement of level of continuity to about 27.3 %, with a slightly narrower bandwidth of 17 Hz (55 – 72 Hz).

A bigger number of individual cantilevers in a multi-cantilever structure would give a better chance in generating more electrical energy for a wider bandwidth of vibration sources but at the expense of the overall electrical output. Comparable to electrical output, Figure 8-9 shows that the overall stress produced by a multi-cantilever with six fingers produces about half of the overall stress produced by one with three fingers, but with a slightly wider bandwidth and a better level of continuity. The former has a bandwidth of 145 Hz and level of continuity of 14%, while the latter has a bandwidth of 125 Hz and level of continuity of 10%.
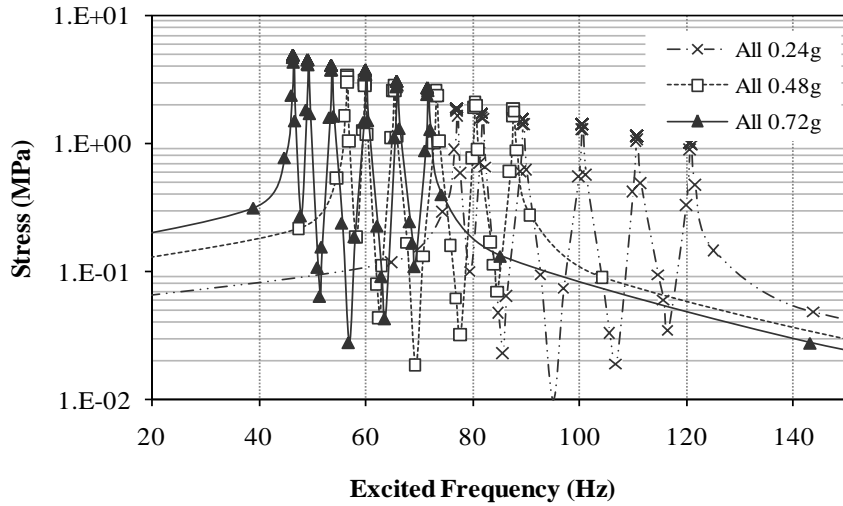
Figure 8-7: Average stress as a function of excited frequency for multi-cantilever attached with proof mass.
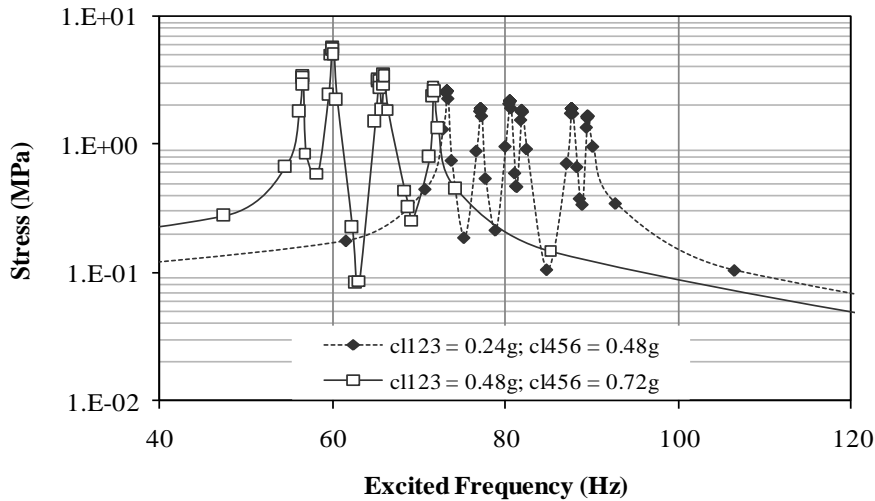
Figure 8-8: Average stress as a function of excited frequency for multi-cantilever attached with a combination of proof masses.

The equation for a pure bending cantilever beam under harmonic base excitation (equation (3-9)) does not predict a modal frequency dependence on the width of the cantilever. From ANSYS^{TM} simulation results, however, it can be shown that the resonant frequency of a multi-cantilever with five fingers varied between 192 – 204 Hz, with optimum response at around 196 Hz, as shown in Figure 8-10. This dependence is due to the coupling between the fundamental and higher order modes of vibration of the interaction of the individual cantilevers. The figure also compares frequency response of the three models. The multi-cantilever of five fingers with different widths shows a

slightly higher magnitude of stress produced compared to the multi-cantilever of three fingers and covers a narrower operating bandwidth of 10 Hz (192 – 202 Hz).
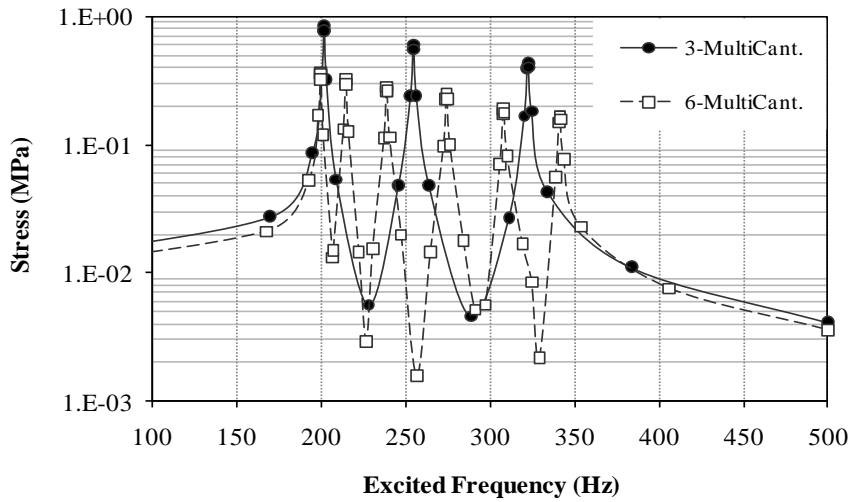
Figure 8-9: Maximum stress induced on the anchor of a cantilever structure as a function of excited resonant frequency for multi-cantilever with 3 and 6 array of individual cantilevers.
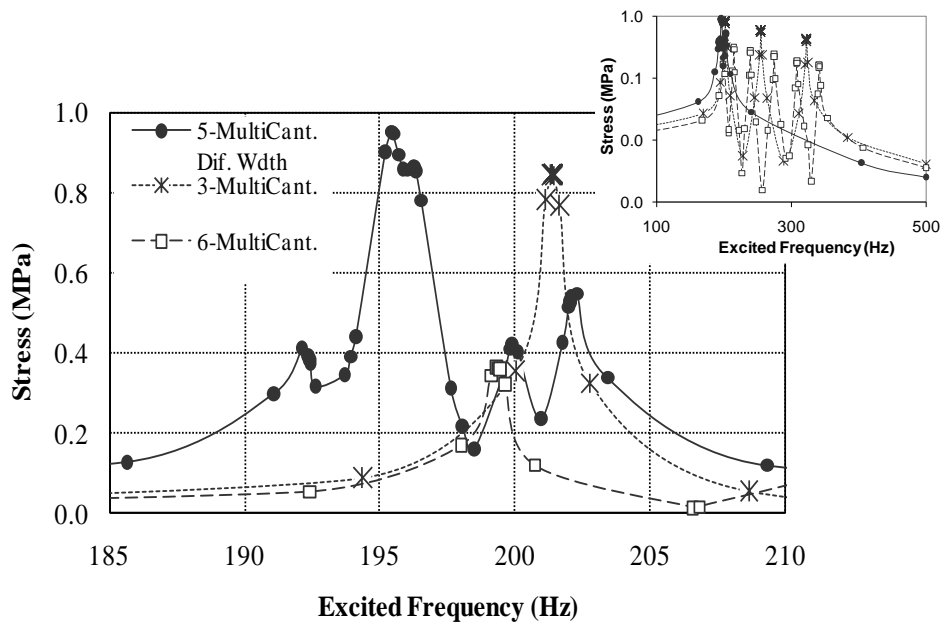
Figure 8-10: Maximum stress as a function of excited resonant frequency for multi-cantilever of five fingers with different widths, three fingers and six fingers. Insert: comparison of frequency response for multi-cantilever with different widths and those with different lengths.

8.5 Experimental Results and Discussions

A series of multi-cantilevers of six fingers with different lengths (Figure 8-11 (a)) and five fingers with different widths (Figure 8-11 (b)) were fabricated using similar method as described in Chapter 4. The composite free-standing structures were fabricated in a sequence of PZT-Ag/Pd-PZT-Ag/Pd-PZT as illustrated in Figure 4-1, with the middle section of PZT sandwiched with upper and lower electrodes. This section of PZT was polarised and functions as an active piezoelectric layer.

The objective of the experiment is to investigate the resonant response of the multi-cantilever and is not intended to optimise the output power. In order to obtain measureable electrical output, however, the neutral axis of the cantilever structure has to be adjusted away from the centroid of the PZT. To do this, the thickness of the lower and upper electrode is varied while maintaining the thickness of lower and upper non-active PZT layers (protective layer to Ag/Pd conductor). Two layers of Ag/Pd were printed as the lower electrode while the upper electrode was printed with one layer of Ag/Pd. The dimensions for the multi-cantilever of six fingers with different lengths and the one with five fingers with different widths are summarised in Table 8-5 and Table 8-6 respectively.

(a)   (b)
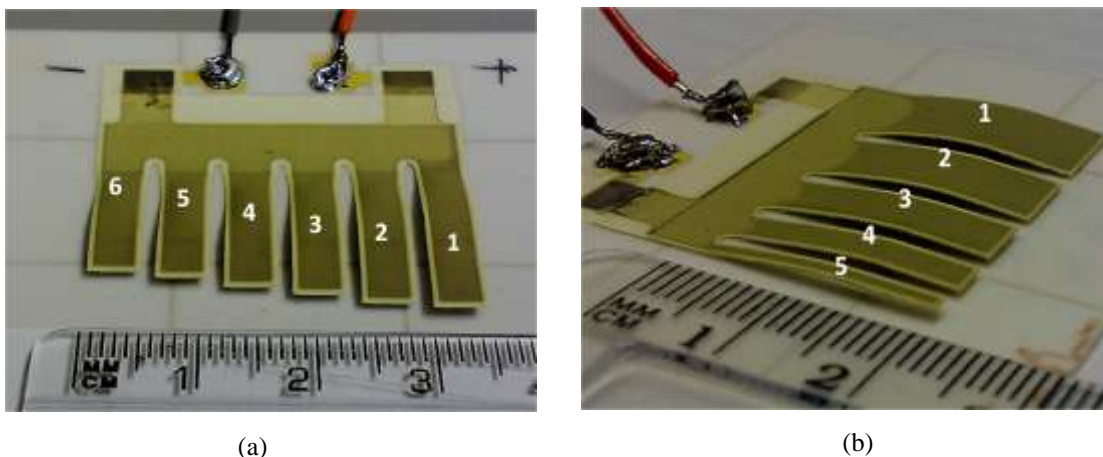
Figure 8-11: A photograph of a multi-cantilever sample of (a) six fingers with different lengths and (b) five fingers with different widths.

(a)

(b)
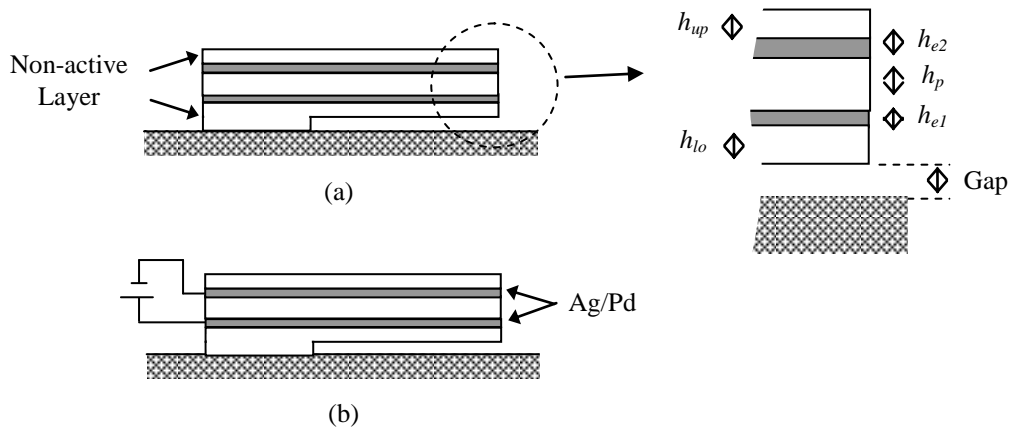
Figure 8-12: Schematic diagram showing the side view of (a) a composite multi-cantilever structure and (b) polarisation arrangement. h_{e1}, h_{e2}, h_p, h_{up} and h_{lo} denotes the thickness of lower electrode, upper electrode, active PZT, upper non-active PZT and lower non-active PZT.

The influence of cantilever number in a multi-cantilever system will be investigated experimentally by breaking off the free-standing cantilevers one at a time to analyse the frequency response at different numbers of cantilever. This process will be carried out in both directions; from longest to shortest and vice versa.

In another experiment, tungsten proof masses of 0.19 g with dimension of $2.5 \times 4.5 \times 1$ mm were attached at the tip of each finger of the multi-cantilever, as shown in Figure 8-13. This experiment was carried out to verify the ANSYS simulation results as shown in Figure 8-7.

5 mm
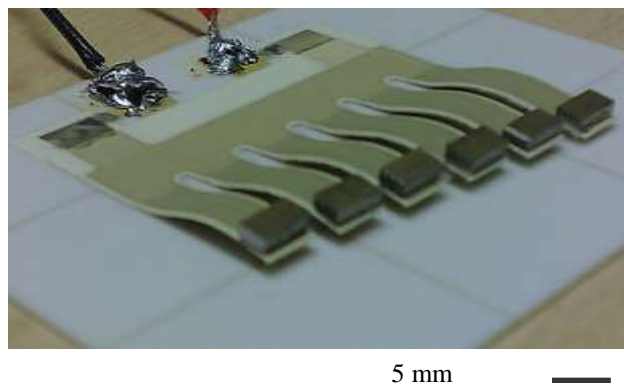
Figure 8-13: Photograph of a multi-cantilever attached with tungsten proof mass, M3.

Table 8-5: Dimensions of a fabricated multi-cantilever of six fingers with different lengths.

Parameter		Finger no.					
		1	2	3	4	5	6
PZT Length (mm)		20	19	18	17	16	15
Ag/Pd Length (mm)		19.5	18.5	17.5	16.5	15.5	14.5
PZT Width (mm)		5	5	5	5	5	5
Ag/Pd Width (mm)		4	4	4	4	4	4
	h_{e1}	0.01	0.01	0.01	0.01	0.01	0.01
	h_{e2}	0.015	0.015	0.015	0.015	0.015	0.015
Thickness (mm)	h_p			Varied			
	h_{up}	0.01	0.01	0.01	0.01	0.01	0.01
	h_{lo}	0.01	0.01	0.01	0.01	0.01	0.01
Base width, bw (mm)				35			
Gap in between cantilevers (mm)				1			

Table 8-6: Dimensions of a fabricated multi-cantilever of five fingers with different widths.

Parameter		Finger no.				
		1	2	3	4	5
PZT Length (mm)		20	20	20	20	20
Ag/Pd Length (mm)		19.5	19.5	19.5	19.5	19.5
PZT Width (mm)		10	8	6	4	2
Ag/Pd Width (mm)		9	7	5	3	1
	h_{e1}	0.01	0.01	0.01	0.01	0.01
	h_{e2}	0.015	0.015	0.015	0.015	0.015
Thickness (mm)	h_p			Varied		
	h_{up}	0.01	0.01	0.01	0.01	0.01
	h_{lo}	0.01	0.01	0.01	0.01	0.01
Base width, bw (mm)				35		
Gap in between cantilevers (mm)				1.25		

8.5.1 *Excitation without Proof Mass*

A series of multi-cantilever samples was tested with unloaded condition under a base excitation within a range of frequencies matched to the maximum and minimum resonant frequencies of the individual cantilevers.

Figure 8-14 shows three multi-cantilever samples with different thickness of active PZT layers; 8, 6 and 4 layers of printed-dried-co-fired PZT, which corresponds to thicknesses of 109.25 µm, 86.5 µm and 53 µm, according to measurement results in Figure 5-2. The resonant frequency increases with thickness as expected from equation (3-14). This shows that the operation frequency bandwidth can be adjusted by varying the thickness of the devices. All the three multi-cantilevers have a bandwidth of about 270 Hz. The multi-cantilever printed with 8 PZT layers has a bandwidth between 375 - 650 Hz, while the one printed with 4 PZT layers has a bandwidth between 205 - 480 Hz.
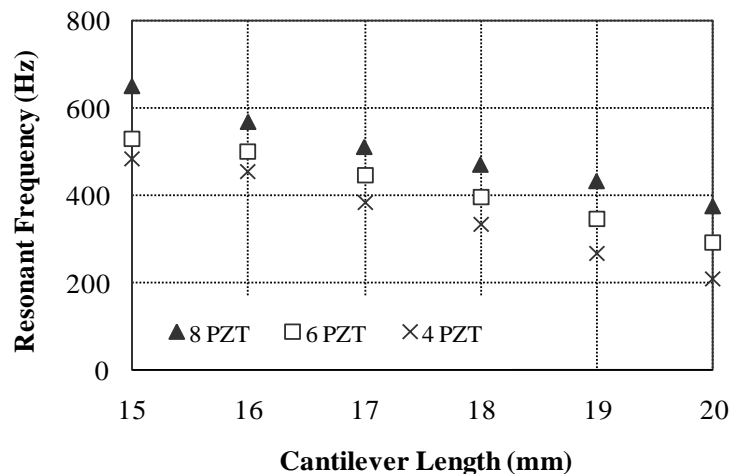
Figure 8-14: Resonant frequency as a function of cantilever length and number of PZT layers for a multi-cantilever structure.

In the following experiment, a series of multi-cantilevers fabricated with 4 layers of PZT were used to investigate the frequency response of the structures in terms of electrical output.

Figure 8-15 shows that the open circuit voltage of a multi-cantilever of five fingers with different lengths (the sample was designed to have six fingers, but during the experiment, the shortest free-standing structure was accidentally broken off). It is noticed that the open circuit voltage drops when excited to higher frequency, at a constant acceleration level, which is the opposite to that shown in Figure 8-1. At a

constant cantilever beam displacement, however, the outcome of the experiment is expected to be in an agreement with the simulation results as reported by Sari *et al* [118].
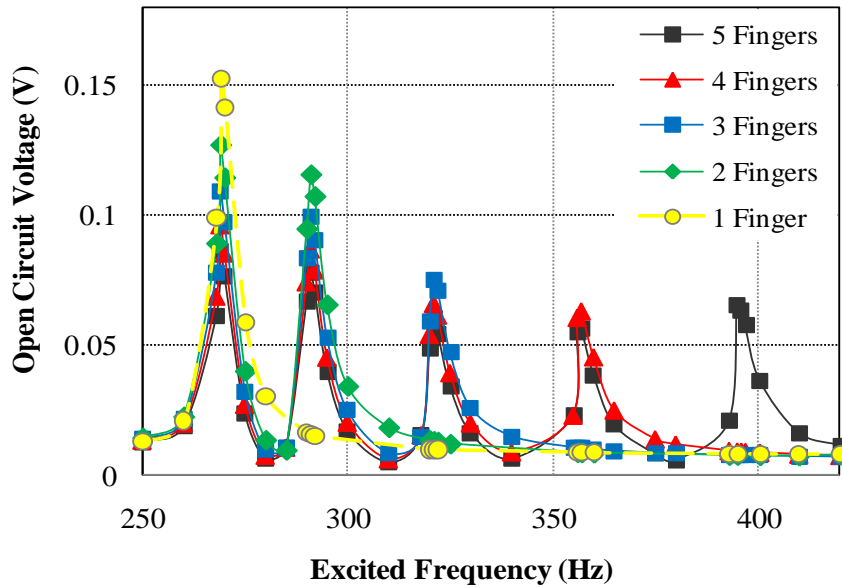
Figure 8-15: Open circuit voltage as a function of excited frequency for a multi-cantilever with reducing number of fingers from the shortest to the longest, when excited at 0.5 g.

In order to investigate the interaction of individual cantilevers to the overall electrical output, a series of measurements was carried out with reducing number of cantilevers by intentionally detaching one at a time from the shortest finger first.

Figure 8-15 clearly shows that as the number of cantilevers reduces, the open circuit voltage increases. It is also noticed that the open circuit voltage drops sharply in between two matched resonant frequencies while a relatively smooth reduction occurs at the "tail" of the resonant frequency.

In another experiment, with the same cantilever number reduction process but in the reverse order (i.e. longest to shortest), an irregular pattern of output power was measured when driving a resistive load of 20 kΩ, as shown in Figure 8-16. The resistive load was approximately matched to the mechanical damping of the cantilever with length 19 mm for a multi-cantilever with six fingers, and therefore produced a relatively high output power compared to the other cantilevers.

This experiment shows that an optimum output power for all the individual cantilever at their resonant frequency can only be produced if the resistive load is tuneable. Such a tuneable system may require some complex processing circuit and consume electrical energy and is not desirable for a micro-system. Therefore a better solution is to use a resistive load which is matched between the maximum and minimum mechanical damping corresponding to the individual cantilevers of the system.
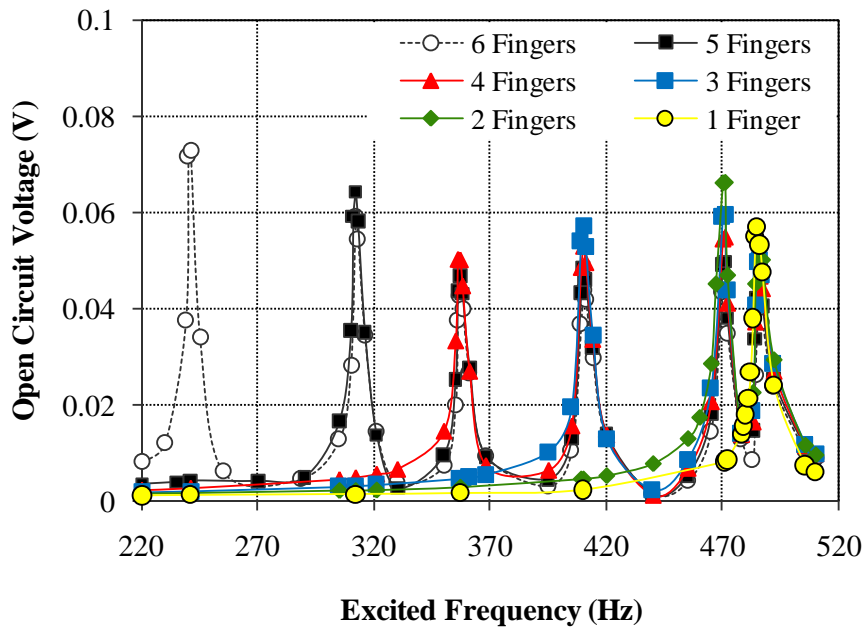
Figure 8-16: Output voltage (at a resistive load of 20 kΩ) as a function of excited frequency for a multi-cantilever with reducing number of fingers from the longest to the shortest, when excited at 0.5 g.

Figure 8-17 shows a clearer picture of the dependence of optimum resistive load to the cantilever length which demonstrates a matching of electrical damping to the mechanical damping of the individual cantilevers when operated as a multi-cantilever system. It is noticed that when one of the individual cantilevers was detached from the system, all other remaining cantilevers experience an increase in the optimum resistive load and the optimum resistive load continues to increase with fewer fingers.
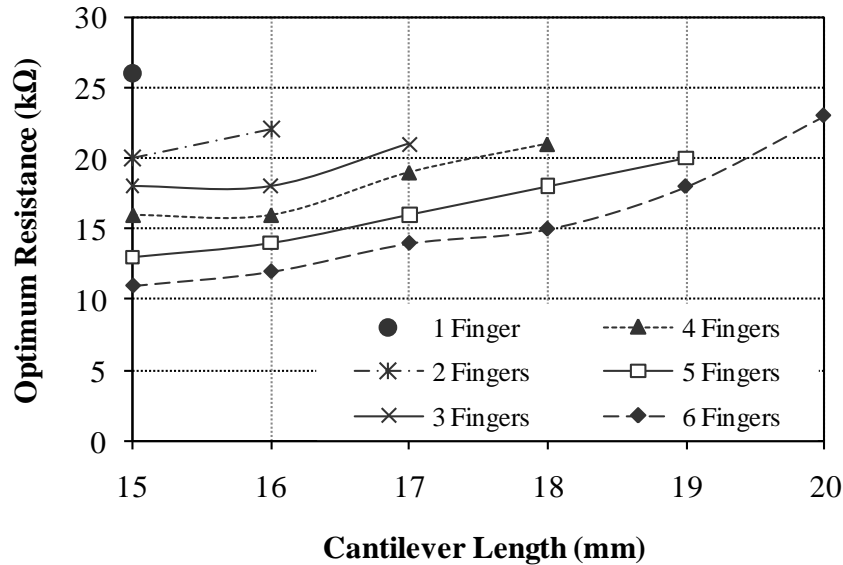
Figure 8-17: Optimum resistive load as a function of cantilever length of a series of multi-cantilever with different number of cantilevers (fingers).

If a system is driven with a consistent resistive load at 20 kΩ, optimum electrical power can be obtained from cantilevers with a length of 19 mm for a multi-cantilever system with six fingers. As the number of the fingers is reduced to 5, 4 and 3 cantilevers, the optimum output powers were obtained from the longest individual cantilever in the systems, as shown in Figure 8-17.

From the experiment results shown in Figure 6-13, as acceleration level increases the resonant frequency of a cantilever shifts slightly to a lower magnitude and at the same time broadens the operation frequency. These effects can be utilised to bring the gap between each operation frequency closer and increase the continuity level. This is clearly shown in Figure 8-18, where a multi-cantilever system of six fingers is excited to an acceleration level of 0.05 g, the bandwidth is about 190 Hz (260 – 450 Hz), while at an acceleration of 1 g, the bandwidth is increased to about 195 Hz (256 – 450 Hz). The continuity level is also increased from 2 % to 4.5 %. The magnitude of the overall output power is increased by a factor of about 35 from an acceleration of 0.05 g to 1 g.
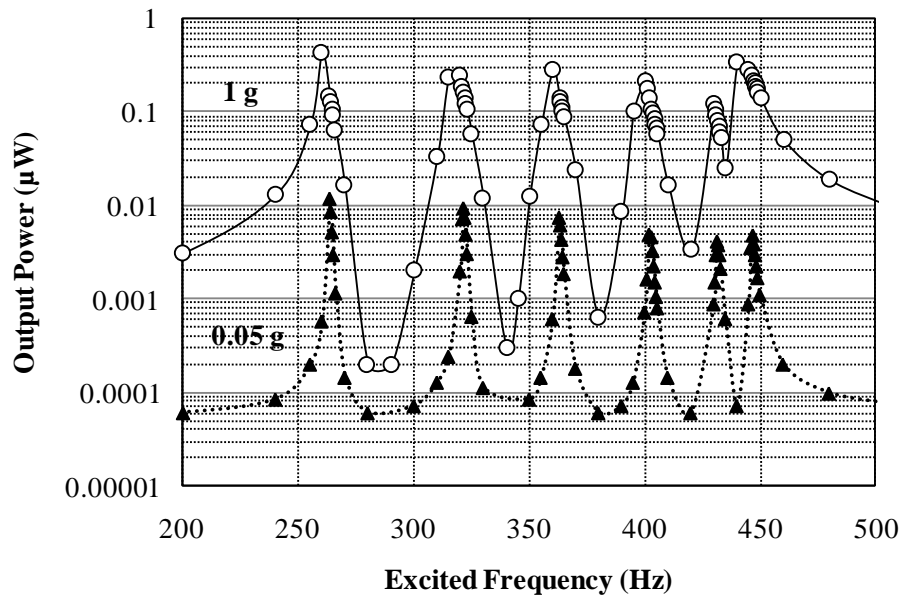
Figure 8-18: Log magnitude of output power as a function of driving frequency at different levels of acceleration.

The overlapping effect of resonant frequencies is prominent when the multi-cantilever is excited at a higher acceleration level and the chance of overlapping is higher at higher resonant frequency which corresponds to a shorter cantilever. Figure 8-19 shows the coverage of operation frequencies which produces a constant output power of 50 nW. At an acceleration level of 1 g, a coverage of frequencies from 435 Hz to 460 Hz (25 Hz) was measured. The lower band of operation frequency for a cantilever with length 15 mm is overlapped with the higher band of operation frequency for a cantilever with length 16 mm. At a lower acceleration level of 0.5 g, however, the coverage of frequencies is reduced to 8 Hz and the tolerance of cantilever length is from 15 to 15.5 mm. This experiment shows that, the length of an individual cantilever is crucial in designing a multi-cantilever. At a low ambient vibration level, the lengths of the individual cantilevers have to be very close to each other in order for the system to operate with high continuity.
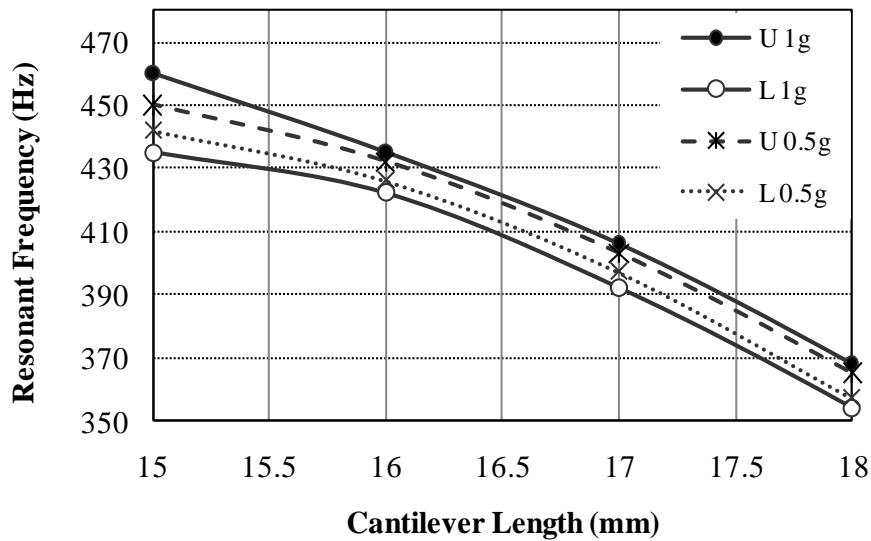
Figure 8-19: Lower and upper band of operation frequencies for an output power of 50 nW with varying cantilever lengths. The measurements were taken at excitation acceleration levels of 1 g and 0.5 g when driving a resistive load of 20 kΩ.

In another experiment, the frequency response of an array of cantilevers with different widths was investigated. A multi-cantilever fabricated with 6 layers (86 μm) of active PZT with dimensions listed in Table 8-6 was used in this experiment. Figure 8-20 shows the modal frequency dependence on the width of a cantilever, which also agrees with the ANSYS simulation results in Figure 8-10, although both results do not show the exact pattern of change, but it is reasonable to deduce that the width of a cantilever influences the resonant frequency of a cantilever. Four peaks of resonance occur within the range of 280 – 340 Hz, with a prominent resonance occurring at 340 Hz, which corresponds to the widest cantilever of the multi-cantilever system. One of the five cantilever's resonant frequency may have been overlapping completely with the one beside it. Interestingly, it is also noticed that, a peak output voltage of 7.5 mV was measured at a frequency of around 520 Hz, which may be produced by the narrowest cantilever of the system operated at a higher mode of resonant frequency.
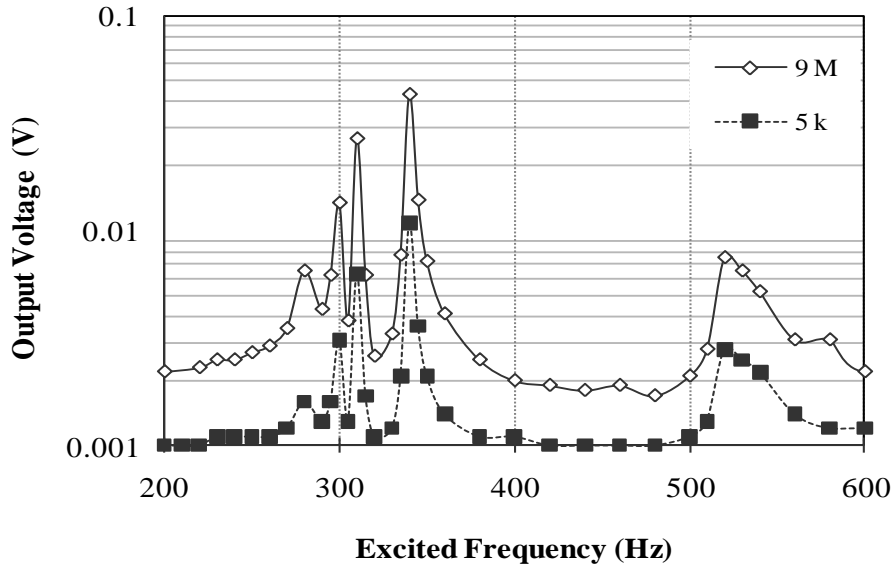
Figure 8-20: Output voltage as a function of excited frequency at resistive load of 5 kΩ and 9 MΩ for a multi-cantilever with different width fingers.

8.5.2 *Excitation with Proof Mass*

The discontinuity of operational frequency of a multi-cantilever system can be reduced by increasing the mechanical damping of the structure. This can be done by attaching proof masses on each of the cantilevers. In this experiment, tungsten blocks of mass 0.19 g each were attached to the tip of the cantilevers as shown in Figure 8-13. A frequency band of 50 Hz (100 – 150 Hz) is produced as shown in Figure 8-21. The continuity level was increased from 3 % to 23.5% at an acceleration of 0.1 g.

It is noticed that at higher frequencies, the frequency spectrum becomes denser, where the resonant peaks tends to overlap with each other, resulting in an increased output power. Further improvements can be achieved by increasing the number of cantilevers with smaller increments in lengths between 15 mm to 20 mm, without compromising the bandwidth of the operational frequency.

Figure 8-22 shows an overall output power at specific frequencies when driving into a resistive load of 20 kΩ at a range of acceleration levels up to 1 g. The plot shows that the multi-cantilever performs at its best when operating at a frequency of 152 Hz across

a wide range of acceleration levels. Generally, by broadening the operational frequencies the multi-cantilever structure tends to reduce the maximum output power compared with a single cantilever of similar dimensions, due to decoupling effects amongst the cantilevers. A major issue is to design a device that can harvest energy over a broader range of frequencies at unpredictable levels of acceleration, whilst at the same time producing useful amounts of electrical energy to an integrated microsystem.
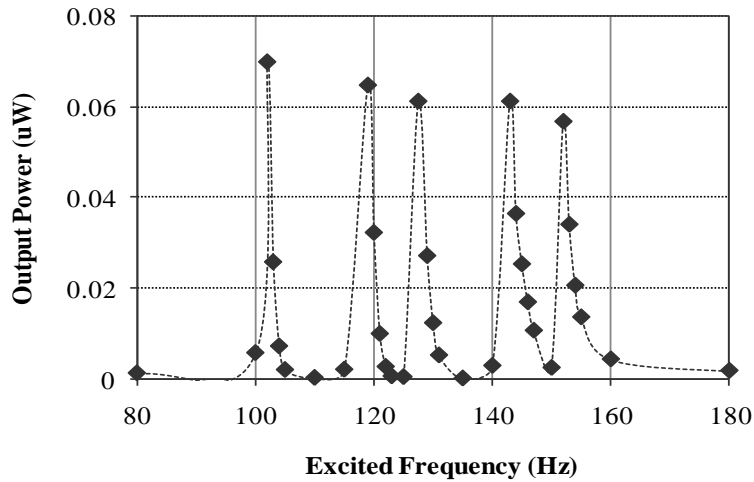
Figure 8-21: Output power of multi-cantilever with each cantilever attached with tungsten proof mass of 0.19 g (M1) when driving resistive load of 20 kΩ at a range of driving frequencies.
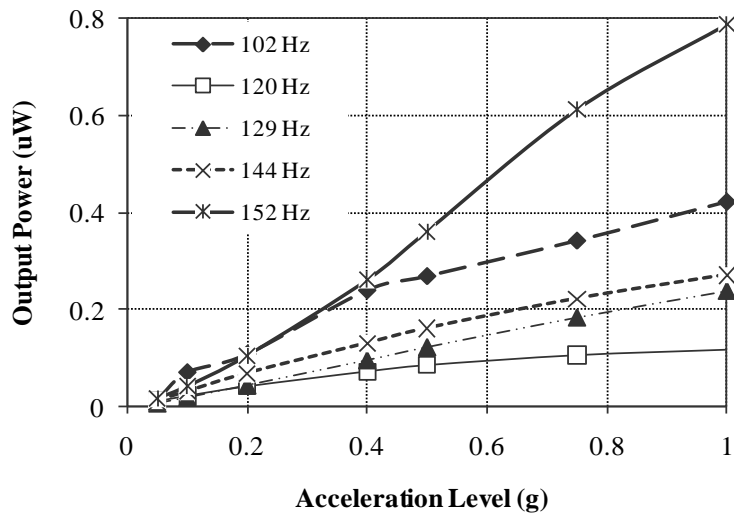
Figure 8-22: Output power for various driving frequencies with a resistive load of 20 kΩ, at a range of acceleration levels up to 1 g ($\approx$ 10 m/s^2).

8.6 Conclusion

Owing to the unpredictable nature of vibration sources, a wider bandwidth of operation is desirable. This can be implemented in two ways; broadening the bandwidth or tuning to match the resonant frequency. The tuning method involves complex processing which requires electrical energy, while the bandwidth broadening method is basically a structural property involving a combination of multi-cantilevers with different stiffness, hence producing multiple frequency responses within an operation bandwidth. The disadvantages of multi-cantilever systems are the discontinuity issue and a low overall electrical output compared to individual cantilevers. A few experiments have been carried out to investigate the continuity level of the system. Increasing the number of cantilevers with very small differences in lengths, is one of the ways to improve the continuity, though this tends to increase the overall size of the device. Proof mass attached to the tips of the multi-cantilever was proven to be a better solution for improving the continuity level within the operation bandwidth.

Appendix A

Specimens from Ferroperm Piezoceramics (Pz26, Pz29 and Pz27) [22] and Morgan Electroceramics (PZT-401, PZT-5H and PZT-5A) [31].

	Properties		Dimension	Material Type					
				Hard		Soft			
				PZT-401	Pz26	Pz29	PZT-5H	Pz27	PZT-5A
Mechanical	Density, ρ		kg/m^3	7600	7700	7450	7400	7700	7750
	Elastic Compliances	s_{11}^{E}	10^{-12} m^2/N	12.7	13	17	17.7	17	16.7
		s_{33}^{E}	10^{-12} m^2/N	15.6	20	23	21.9	23	17.2
		s_{11}^{D}	10^{-12} m^2/N	11.1	12	15	15.5	15	15
		s_{33}^{D}	10^{-12} m^2/N	7.76	11	10	10.5	12	9.4
	Quality Factor	Q_m	Dimensionless	600	1000	90	65	80	60
	Poisson's Ratio	v^E	Dimensionless	NA	0.33	0.34	NA	0.39	NA
Electrical	Curie Temperature, T_c		°C	330	330	235	200	350	370
	Relative Dielectric Constant at 1 kHz, K_{33}^{T}		Dimensionless	1470	1300	2900	3250	1800	1875
	Dielectric Dissipation Factor at 1 kHz, $tan\ \delta$		Dimensionless	0.003	0.002	0.019	0.018	0.017	0.02
Electro-mechanical	Piezoelectric Charge Coefficients	$-d_{31}$	10^{-12} C/N	132	130	240	250	170	176
		d_{33}	10^{-12} C/N	315	330	575	620	425	409
	Piezoelectric Voltage Coefficients	$-g_{31}$	10^{-12} Vm/N	12	11	10	8.7	11	11
		g_{33}	10^{-12} Vm/N	26.8	28	23	21.9	27	25.7
	Coupling Factors	k_p	Dimensionless	0.60	0.57	0.64	0.60	0.59	0.62
		k_t	Dimensionless	NA	0.47	0.52	0.50	0.47	0.45
		k_{31}	Dimensionless	0.35	0.33	0.37	0.35	0.33	0.34
		k_{33}	Dimensionless	0.71	0.68	0.75	0.72	0.70	0.67

Note: k_p and k_t are the planar and thickness coupling factors for thin discs.

Appendix B

Bernoulli-Euler Equation

The natural transverse vibration of a thin cantilever beam in flexural vibration with one end clamped and the other end free, can be derived from the Bernoulli-Euler equation as,

$$\frac{\partial^2}{\partial x^2}\left(D(x)\frac{\partial^2 h}{\partial x^2}\right) + m(x)\frac{\partial^2 h}{\partial t^2} = 0 \tag{B.1}$$

where $D(x)$, $m(x)$ and h are the bending modulus, mass per unit length and the lateral deflection of the beam at longitudinal axis, x, and h is the deflection at the transverse axis of the beam. If the bending modulus and mass per unit length are independent of the position (uniform beam), equation (B.1) can be written as,

$$D\frac{\partial^4 h}{\partial x^4} + m\frac{\partial^2 h}{\partial t^2} = 0 \tag{B.2}$$

In each mode, the vibration amplitude and frequency are independent factors. Hence, the time and space functions will be separable for a natural mode and the deflection can be written in the form,

$$h(x,t) = X(x)T(t) \tag{B.3}$$

Substituting equation (B.3) in equation (B.2), we get,

$$DT(t)\frac{\partial^4 X(x)}{\partial x^4} + mX(x)\frac{\partial^2 T(t)}{\partial t^2} = 0 \tag{B.4}$$

Since x and t are independent parameters, equation (B.4) can be separated and represented by a constant as,

$$\frac{D}{m}\frac{1}{X(x)}\frac{\partial^4 X(x)}{\partial x^4} = \omega^2 \tag{B.5}$$

$$-\frac{1}{T(t)}\frac{\partial^2 T(t)}{\partial t^2} = \omega^2 \tag{B.6}$$

Rearranging equations (B.5) and (B.6), we get,

$$\frac{\partial^4 X(x)}{\partial x^4} - \omega^2 \frac{m}{D} X(x) = 0 \tag{B.7}$$

$$\frac{\partial^2 T(t)}{\partial t^2} + \omega^2 T(t) = 0 \tag{B.8}$$

Defining the wave factor, k as,

$$k^4 = \omega^2 \frac{m}{D} \tag{B.9}$$

The general solution for equation (B.7) is,

$$X(x) = C_1 \sin(kx) + C_2 \cos(kx) + C_3 \sinh(kx) + C_4 \cosh(kx) \tag{B.10}$$

Whereas, equation (B.8) is a harmonic vibration, therefore the general solution is,

$$T(t) = e^{i\omega t} \tag{B.11}$$

Substituting equation (B.10) and (B.11) into (B.3), we obtain the lateral deflection of the cantilever beam as,

$$h(x,t) = \{C_1 \sin(kx) + C_2 \cos(kx) + C_3 \sinh(kx) + C_4 \cosh(kx)\}e^{i\omega t} \tag{B.12}$$

The coefficients of C_1, C_2, C_3 and C_4 are determined by the boundary conditions of the vibrational beam. For the case of a beam rigidly clamped at one end and free at the other, the boundary conditions are,

$$h = 0, \quad \text{at } x = 0 \tag{B.13}$$

$$\frac{dh}{dx} = 0, \quad \text{at } x = 0 \tag{B.14}$$

$$D\frac{d^2h}{dx^2} = 0, \quad \text{at } x = l \tag{B.15}$$

$$D\frac{d^3h}{dx^3} = 0, \quad \text{at } x = l \tag{B.16}$$

Rewriting equation (B.10) and its derivations as,

$$X(x) = C_1 \sin(kx) + C_2 \cos(kx) + C_3 \sinh(kx) + C_4 \cosh(kx) \tag{B.17}$$

$$\frac{dX(x)}{dx} = C_1 k \cos(kx) - C_2 k \sin(kx) + C_3 k \cosh(kx) + C_4 k \sinh(kx) \tag{B.18}$$

$$\frac{d^2X(x)}{dx^2} = -C_1 k^2 \sin(kx) - C_2 k^2 \cos(kx) + C_3 k^2 \sinh(kx) + C_4 k^2 \cosh(kx) \tag{B.19}$$

$$\frac{d^3X(x)}{dx^3} = -C_1 k^3 \cos(kx) + C_2 k^3 \sin(kx) + C_3 k^3 \cosh(kx) + C_4 k^3 \sinh(kx) \tag{B.20}$$

Substituting equations (B.13) to (B.16) in (B.17) to (B.20), we get,

$$C_2 + C_4 = 0 \tag{B.21}$$

$$C_1 + C_3 = 0 \tag{B.22}$$

$$-C_1 \sin(kl) - C_2 \cos(kl) + C_3 \sinh(kl) + C_4 \cosh(kl) = 0 \tag{B.23}$$

$$-C_1 \cos(kl) + C_2 \sin(kl) + C_3 \cosh(kl) + C_4 \sinh(kl) = 0 \tag{B.24}$$

Eliminating C_3 and C_4 in equation (B.23) and (B.24) by substituting equation (B.21) and (B.22), we obtain,

$$[\sinh(kl) + \sin(kl)]C_1 + [\cosh(kl) + \cos(kl)]C_2 = 0 \tag{B.25}$$

$$[\cosh(kl) + \cos(kl)]C_1 + [\sinh(kl) - \sin(kl)]C_2 = 0 \qquad (B.26)$$

Eliminating C_1 and C_2 in equation (B.25) and (B.26), we obtain,

$$[\cosh(kl) + \cos(kl)]^2 - [\sinh(kl) + \sin(kl)][\sinh(kl) - \sin(kl)] = 0 \qquad (B.27)$$

Expanding equation (B.27), we get,

$$\cosh^2(kl) + 2\cosh(kl)\cos(kl) + \cos^2(kl) - \sinh^2(kl) + \sin^2(kl) = 0 \qquad (B.28)$$

From the trigonometric identities,

$$\cosh^2(kl) - \sinh^2(kl) = 1 \qquad (B.29)$$

$$\cos^2(kl) + \sin^2(kl) = 1 \qquad (B.30)$$

Solving equation (B.28) with the trigonometric identities, we get,

$$\cos(kl)\cosh(kl) = -1 \qquad (B.31)$$

Equation (B.31) has an infinite number of solutions depending on k_i, which corresponds to the ith vibration mode of the natural resonant frequencies. The natural resonant frequencies at i^{th} vibration mode is derived from equation (B.9) as,

$$f_i = \frac{\omega_i}{2\pi} = \frac{k_i^2}{2\pi}\sqrt{\frac{D}{m}} \qquad (B.32)$$

Solving $k_i l$ in equation (B.31), we obtain the first three modes as,

$$k_1 l = 1.875104 \qquad (B.33)$$

$$k_2 l = 4.694091 \qquad (B.34)$$

$$k_3 l = 7.854757 \qquad (B.35)$$

Appendix C

Analytical Model of Piezoelectric Unimorph Energy Harvester [121]

A dynamic model for a composite cantilever beam, as shown in Figure C.1, driving a resistive load can be represented by an analogous circuit as shown in Figure C.2.
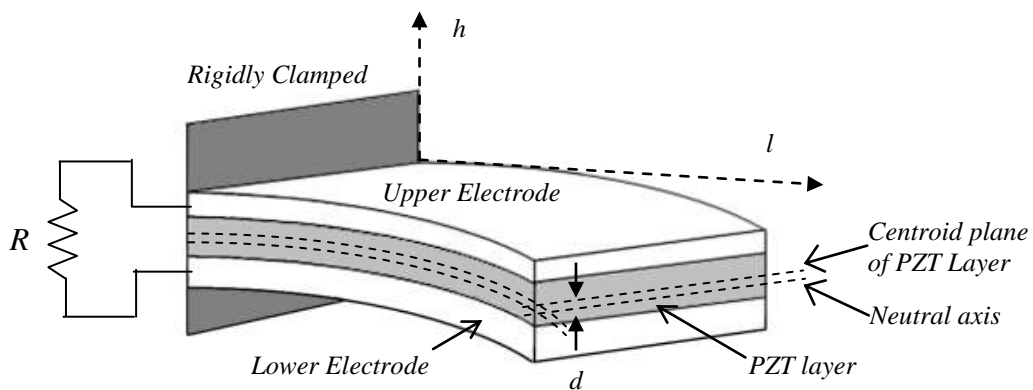
Figure C.1: Schematic diagram of unimorph cantilever.
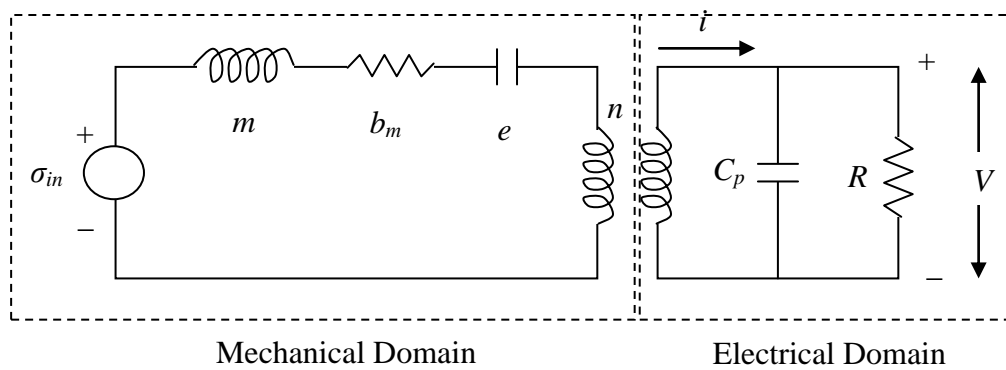
Figure C.2: Circuit representation of piezoelectric unimorph cantilever.

Applying Kirchhoff's Voltage Law (KVL) on the mechanical domain, we have,

$$\sigma_{in} = \sigma_m + \sigma_{bm} + \sigma_e + \sigma_t \tag{C.1}$$

From the Euler beam equation,

$$\frac{d^2 z}{dl^2} = \frac{M(l)}{e_T I_{unimorph}} \tag{C.2}$$

where z is the vertical displacement at the tip of the cantilever, l is the distance from the base of the beam, e_T is the elastic modulus and $I_{unimorph}$ is the effective moment of inertia for the unimorph. The moment at l distance from the tip, is given as,

$$M(l) = m(\ddot{y} + \ddot{z})(l_b - l) \tag{C.3}$$

where m is the effective mass of the cantilever, $\ddot{y}$ is the base acceleration, $\ddot{z}$ is acceleration at the tip of the cantilever. Substitute equation (C.3) into (C.2), the deflection of the cantilever at the tip can be written as,

$$z = \frac{m(\ddot{y} + \ddot{z})l_b^3}{3 e_T I_{unimorph}} \tag{C.4}$$

The average stress in the piezoelectric material is expressed as,

$$\sigma = \frac{1}{l_b} \int \frac{M(l)d}{I_{unimorph}} dl \tag{C.5}$$

Substituting equation (C.3) into (C.5), yields,

$$\sigma = \frac{m(\ddot{y} + \ddot{z})dl_b}{2 I_{unimorph}} \tag{C.6}$$

Rearranging equation (C.6), yields an expression of force in term of stress as,

$$m(\ddot{y} + \ddot{z}) = \frac{2 I_{unimorph}}{dl_b} \sigma \tag{C.7}$$

Substituting equation (C.7) into (C.4), yields,

$$z = \frac{2}{3} \frac{\sigma l_b^2}{e_T d} \tag{C.8}$$

As strain is given by,

$$\delta = \frac{\sigma}{e_T} \tag{C.9}$$

therefore, in term of strain, δ, equation (C.8) can be written as,

$$z = \frac{2}{3} \frac{l_b^2}{d} \delta \tag{C.10}$$

Stress developed as a result of input vibrations,

$$\sigma_{in} = \frac{m d l_b}{2 I_{unimorph}} \ddot{y} \tag{C.11}$$

Stress developed as a result of mass, *m,*

$$\sigma_m = \frac{m d l_b}{2 I_{unimorph}} \ddot{z} \tag{C.12}$$

The acceleration at the tip of the cantilever is 2nd order differentiation of equation (C.10),

$$\ddot{z} = \frac{2}{3} \frac{l_b^2}{d} \ddot{\delta} \tag{C.13}$$

Substituting equation (C.13) into (C.12), yields,

$$\sigma_m = \frac{m l_b^3}{3 I_{unimorph}} \ddot{\delta} \tag{C.14}$$

Stress and strain relationship for the damping element b_m,

$$\sigma_{bm} = \left(\frac{2}{3} \frac{l_b^2}{d} \right) b_m \dot{\delta} \tag{C.15}$$

Stiffness element represents by capacitor as,

$$\sigma_e = e_T \delta \tag{C.16}$$

From the constituency equation, the stress causes by the piezoelectric material at zero strain is,

$$\sigma_t = -d_{31} e_T E \tag{C.17}$$

Electric field is,

$$E = \frac{V}{h_p} \tag{C.18}$$

Substituting equation (C.18) into (C.17), yields,

$$\sigma_t = -d_{31} e_T \frac{V}{h_p} \tag{C.19}$$

Substituting equation (C.11), (C.14), (C.15), (C.16) and (C.19) into (C.1), we get,

$$\left(\frac{dl_b}{2I_{unimorph}} \right) m\ddot{y} = \left(\frac{l_b^3}{3I_{unimorph}} \right) m\ddot{\delta} + \left(\frac{2}{3} \frac{l_b^2}{d} \right) b_m \dot{\delta} + e_T \delta - d_{31} e_T \frac{V}{h_p} \tag{C.20}$$

Given,

$$\frac{2I_{unimorph}}{dl_b} = A \; ; \quad \frac{3}{2} \frac{d}{l_b^2} = B \tag{C.21}$$

Substituting equation (C.21) into (C.20), and rearrange the equation, yields,

$$\ddot{\delta} = -AB \left(\frac{e_T}{m} \right) \delta - A \left(\frac{b_m}{m} \right) \dot{\delta} + AB \left(\frac{d_{31} e_T}{m h_p} \right) V + B\ddot{y} \tag{C.22}$$

The expression of effective spring constant can be obtained by comparing equation (C.22) to (2-11) as,

$$k_s = e_T AB \tag{C.23}$$

Substituting (C.23) into (C.22), we get,

$$\ddot{\delta} = -\left(\frac{k_s}{m}\right)\delta - A\left(\frac{b_m}{m}\right)\dot{\delta} + \left(\frac{k_s d_{31}}{mh_p}\right)V + B\ddot{y} \tag{C.24}$$

Assume that the mechanical side of the circuit is unchanged and applying Kirchhoff's Current Law (KCL) to the electrical domain, yields,

$$\dot{q}_t = \dot{q}_{Cp} + \dot{q}_R \tag{C.25}$$

From the piezoelectric constituent equation, the electrical charge density of piezoelectric is,

$$D_t = \varepsilon E + \left(-d_{31}\right)\sigma \tag{C.26}$$

At $E = 0$, and substituting equation (C.9) into equation (C.26), we get,

$$D_t = -d_{31}e_T\delta \tag{C.27}$$

In term of charge, equation (C.27) becomes,

$$\frac{q_t}{nl_b w} = -d_{31}e_T\delta \tag{C.28}$$

Therefore, the current through the transformer is,

$$\dot{q}_t = -d_{31}e_T nl_b w\dot{\delta} \tag{C.29}$$

and the current through the capacitor is,

$$\dot{q}_{Cp} = \left(\frac{n\varepsilon wl_b}{h_p}\right)\dot{V} \tag{C.30}$$

Current through the resistive load,

$$\dot{q}_R = \frac{V}{R} \tag{C.31}$$

Substituting equation (C.29), (C.30) and (C.31) into (C.25) and rearrange the equation, yields,

$$\dot{V} = -\left(\frac{d_{31}e_T h_p}{\varepsilon}\right)\dot{\delta} - \left(\frac{1}{RC_p}\right)V \tag{C.32}$$

Equation (C.32) and (C.24) can be presented in a form of matrix as,

$$\begin{bmatrix} \dot{\delta} \\ \ddot{\delta} \\ \dot{V} \end{bmatrix} = \begin{bmatrix} 0 & 1 & 0 \\ -\dfrac{k_s}{m} & -\dfrac{b_m A}{m} & \dfrac{k_s d_{31}}{mh_p} \\ 0 & -\dfrac{d_{31}e_T h_p}{\varepsilon} & -\dfrac{1}{RC_p} \end{bmatrix} \begin{bmatrix} \delta \\ \dot{\delta} \\ V \end{bmatrix} + \begin{bmatrix} 0 \\ B \\ 0 \end{bmatrix} \ddot{y} \tag{C.33}$$

Rearranging equation (C.32) in the form of,

$$\dot{\delta} = -\frac{\varepsilon\left(\dot{V} + \dfrac{V}{RC_p}\right)}{d_{31}e_T h_p} \tag{C.34}$$

and using Laplace transform, equation (C.34) can be rewritten as,

$$s\Delta = -\frac{\varepsilon\left(sV + \dfrac{V}{RC_p}\right)}{d_{31}e_T h_p} \tag{C.35}$$

Therefore, Laplace transform for strain is,

$$\Delta = -\frac{\varepsilon}{e_T d_{31} h_p s}\left(s + \frac{1}{RC_p}\right)V \tag{C.36}$$

Similarly, applying Laplace transform to equation (C.24) yields,

$$s^2\Delta = -\frac{k_s}{m}\Delta - \frac{b_m A}{m}\Delta s + \frac{k_s d_{31}}{mh_p}V + Bs^2 Y \tag{C.37}$$

211

In the term of acceleration, $s^2 Y = a_{in}$, equation (C.37) becomes,

$$\Delta\left(s^2 + \frac{b_m A}{m} s + \frac{k_s}{m}\right) = \frac{k_s d_{31}}{m h_p} V + B a_{in} \tag{C.38}$$

Substituting equation (C.36) into (C.38), and rearranging the equation yields,

$$V\left[s^3 + \left(\frac{1}{RC_p} + \frac{b_m A}{m}\right)s^2 + \left\{\frac{k_s}{m}\left(1 + \frac{d_{31}^2 e_T}{\varepsilon}\right) + \frac{b_m A}{m RC_p}\right\}s + \frac{k_s}{m RC_p}\right] = -\frac{e_T d_{31} h_p B s}{\varepsilon} a_{in} \tag{C.39}$$

The piezoelectric coupling coefficient can be written in a term of d_{31} as,

$$k_{31}^2 = \frac{d_{31}^2 e_T}{\varepsilon} \tag{C.40}$$

The natural frequency of the system in term of spring constant is given by,

$$\omega_n^2 = \frac{k_s}{m} \tag{C.41}$$

while the constant of A and the damping element b_m can be written in an expression associate with damping ratio and natural frequency as,

$$\frac{b_m A}{m} = 2\xi\omega_n \tag{C.42}$$

and Laplace variable is given by,

$$s = j\omega \tag{C.43}$$

Substituting equation (C.21) and (C.40) – (C.43) into (C.39), yields,

$$V = \frac{-j\omega\left(\frac{3}{2}\frac{e_T d_{31} h_p d}{\varepsilon\, l_b^{\,2}}\right)a_{in}}{\left\{\frac{1}{RC_p}\omega_n^{\,2} - \left(\frac{1}{RC_p} + 2\xi\omega_n\right)\omega^2\right\} + j\omega\left\{\omega_n^{\,2}\left(1 + k_{31}^{\,2}\right) + \frac{2\xi\omega_n}{RC_p} - \omega^2\right\}} \qquad \text{(C.44)}$$

If resonant frequency matches the driving frequency, equation (C.44) can be simplified to,

$$V = \frac{3}{4}\frac{j e_T d_{31} h_p d a_{in}}{\varepsilon\, l_b^2\left\{\zeta_T \omega_r^2 - j\left[\frac{\omega_r^2 k_{31}^{\,2}}{2} + \frac{\zeta_T \omega_r}{RC_p}\right]\right\}} \qquad \text{(C.45)}$$

Appendix D

Each layer of the multimorph structure was designed with Autodesk Inventor and converted separately into photo-plotter format (e.g Gerber, HPGL, DXF or DWG) that can be translated into a patterned thick-film screen. The layout of a multimorph cantilever is shown in Figure D-23.
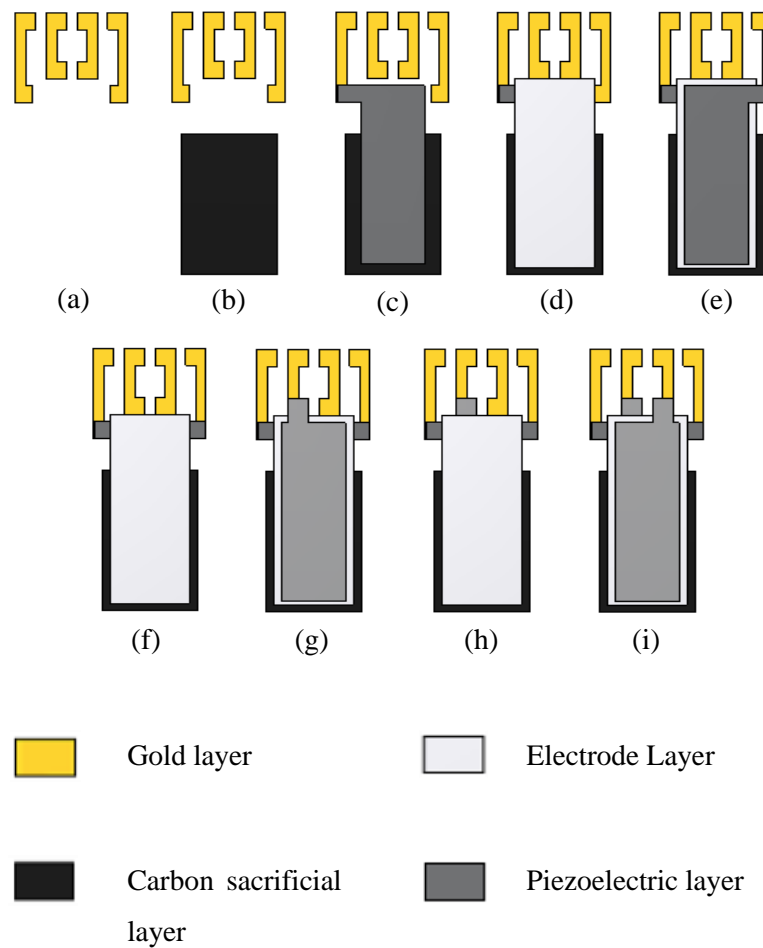
Figure D-23: Diagram of a printing sequence of a multimorph cantilever structure.

The printing sequence of the multimorph structure as shown in Figure D-23 is,

    (a) Gold pad

    (b) Carbon sacrificial layer

    (c) Lower electrode (lower section)

    (d) PZT (lower section)

    (e) Upper electrode (lower section)

    (f) PZT (middle section)

    (g) Lower electrode (upper section)

    (h) PZT (upper section)

    (i) Upper electrode (upper section)

Figure D-24 shows an exploded view of the printing sequence of an enhanced multimorph cantilever structure. Two additional passive PZT layers were printed on the lower and upper part of the structure as protective layers.

The layout of a unimorph multi-cantilever is shown in Figure D-25. Figure D-26 shows an exploded view of the printing sequence as follow,

    Layer 1: Gold pad

    Layer 2: Carbon sacrificial layer

    Layer 3: Lower protective (PZT)

    Layer 4: Lower electrode

    Layer 5: Active PZT layer

    Layer 6: Upper electrode

    Layer 7: Upper protective (PZT)
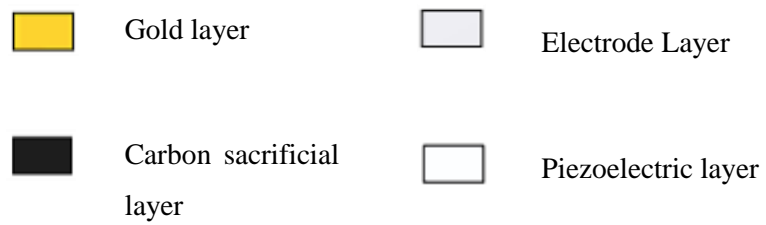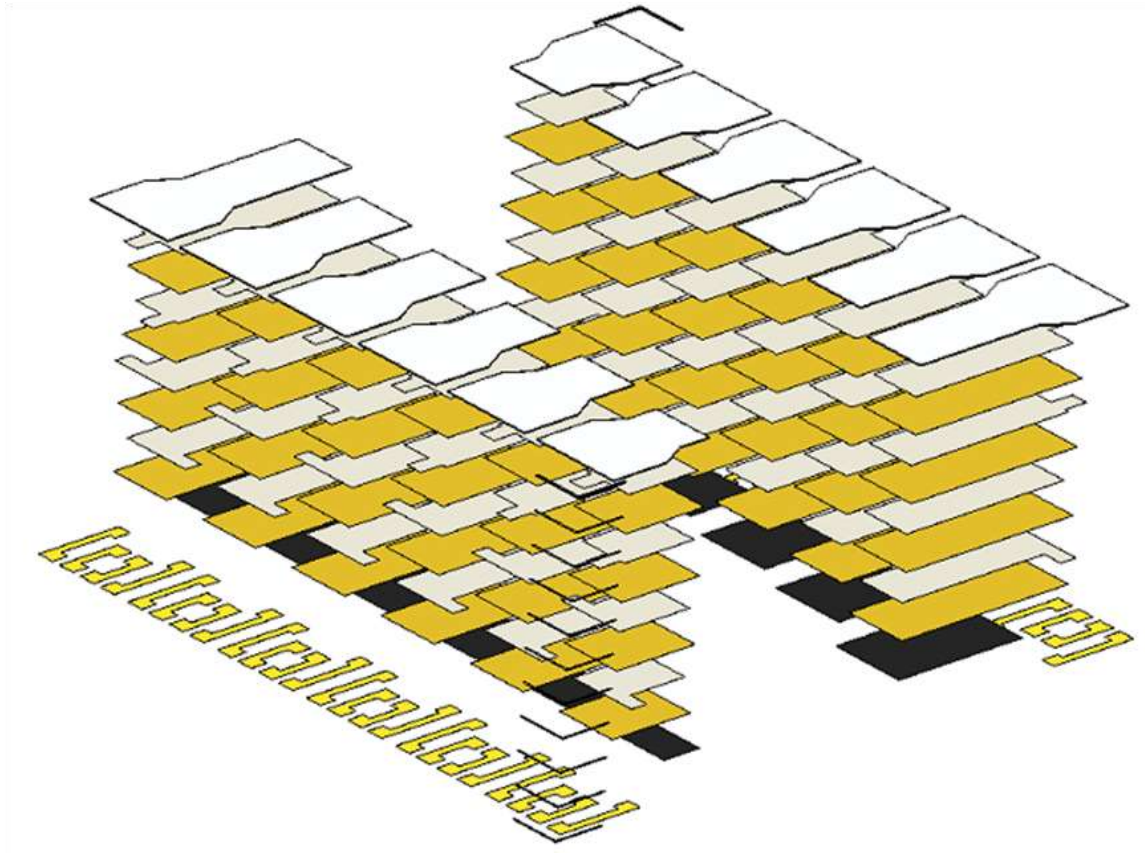
Figure D-24 Exploded view of multimorph cantilever printing sequence
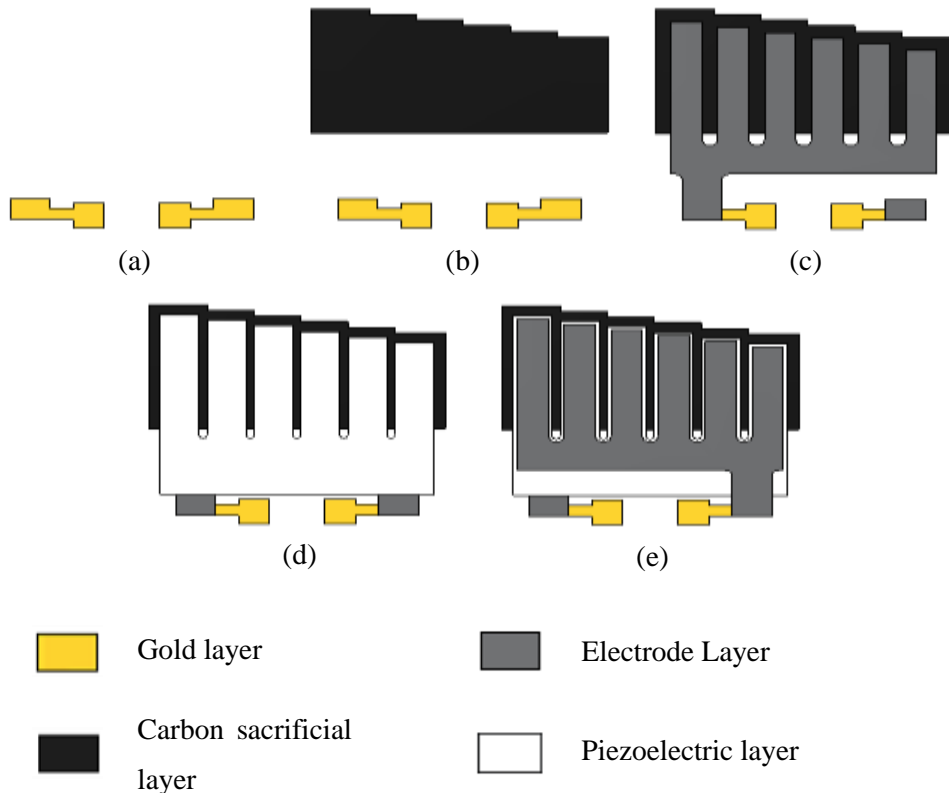
Figure D-25: Multi-cantilever layout of screen mask in printing sequence.
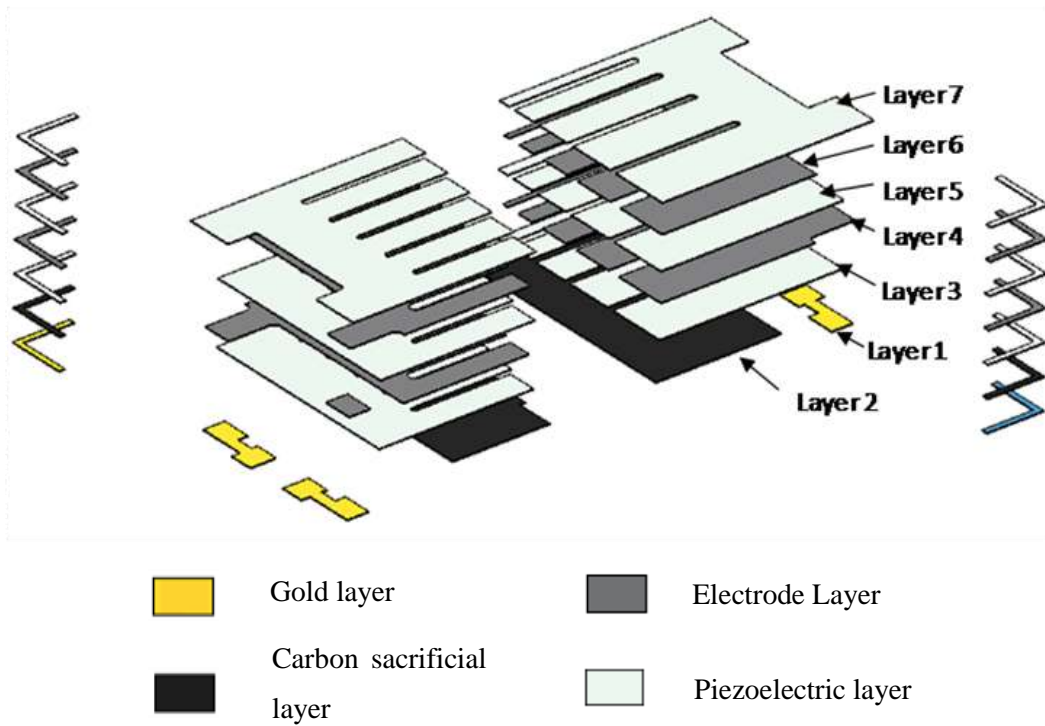
Figure D-26: Exploded view of multimorph cantilever printing sequence.

References

1. Lupu, E., Dulay, N., J. Sventek, and M. Sloman. *Autonomous Pervasive Systems and the Policy Challenges of a Small World!* in *Policies for Distributed Systems and Networks, 2007. POLICY '07. Eighth IEEE International Workshop on.* 2007.

2. Merabti, M., Fergus, P., Abuelma'atti, O., H. Yu, and C. Judice, *Managing Distributed Networked Appliances in Home Networks.* Proceedings of the IEEE, 2008. **96**(1): p. 166-185.

3. Asmare, E., Dulay, N.,, E. Lupu, and M. Sloman. *Towards self-managing unmanned autonomous vehicles.* in *Systems Engineering for Autonomous Systems Defence Technology Centre Conference.* 2007. Edinburgh, UK.

4. *Body Sensor Networks*, ed. G.Z. Yang. 2006: Springer-Verlag.

5. Glynne-Jones, P., S.P. Beeby, and N.M. White, *Towards a piezoelectric vibration-powered microgenerator.* IEE Science Measurement and Technlogy, 2001. **148**(2): p. 68-72.

6. Beeby, S.P., Torah, R. N., Tudor, M. J., Glynne-Jones, P., O'Donnell, T., C.R. Saha, and S. Roy, *A micro electromagnetic generator for vibration energy harvesting.* Journal of Micromechanics and Microengineering, 2007. **17**(7): p. 1257-1265.

7. Mitcheson, P.D., Miao, P., Stark, B. H., Yeatman, E. M., A.S. Holmes, and T.C. Green, *MEMS electrostatic micropower generator for low frequency operation.* Sensors and Actuators A: Physical, 2004. **115**(2-3): p. 523-529.

8. Wang, L. and F.G. Yuan, *Vibration energy harvesting by magnetostrictive material.* Smart Materials and Structures, 2008. **17**(4): p. 045009.

9. Polla, D.L. and L.F. Francis, *Processing and characterization of piezoelectric materials and integration into microelectromechanical systems.* Annual Review of Materials Science, 1998. **28**: p. 563-597.

10. White, N.M. and J.D. Turner, *Thick-film sensors: past, present and future.* Meas.Sci.Technol., 1997. **8**: p. 1-20.

11. Hoffmann, M., Kuppers, H., Schneller, T., Bottger, U., Schnakenberg, U., W. Mokwa, and R. Waser. *A new concept and first development results of a PZT thin film actuator A new concept and first development results of a PZT thin film actuator.* in *Applications of Ferroelectrics, 2000. ISAF 2000. Proceedings of the 2000 12th IEEE International Symposium on.* 2000.

12. Roundy, S. and P.K. Wright, *A piezoelectric vibration based generator for wireless electronics.* Smart Materials and Structures, IOP, 2004. **12**: p. 1131-1142.

13. Sodano, H.A., G. Park, and D.J. Inman, *Estimation of electric charge output for piezoelectric energy harvesting.* Strain, 2004. **40**: p. 49-58.

14. Yalcinkaya, F. and E.T. Powner, *Intelligent Structures.* Sensor Review, 1996. **16**: p. 32-37.

15. Jeon, Y.B., Sood, R., J.h. Jeong, and S.G. Kim, *MEMS Power Generator with Transverse Mode Thin Film PZT.* Sensor and Actuators A, 2005(122): p. 16-22.

16. Fritz, J., et al., *Translating Biomolecular Recognition into Nanomechanics.* Science, 2000. **288**(5464): p. 316-318.

17. Mason, W.P., *Piezoelectric crystals and their application to ultrasonics*. 1950: D. Van Nostrand Company Inc.

18. Bernstein, J.J., Bottari, J., Houston, K., Kirkos, G., Miller, R., Xu, B., Y. Ye, and L.E. Cross. *Advanced MEMS ferroelectric ultrasound 2D arrays*. in *Ultrasonics Symposium, 1999. Proceedings. 1999 IEEE*.

19. Mason, W.P. and H. Jaffe, *Methods for Measuring Piezoelectric, Elastic, and Dielectric Coefficients of Crystals and Ceramics.* Proceedings of the IRE, 1954. **42**(6): p. 921-930.

20. Torah, R. and Thesis, *Optimisation of The Piezoelectric Properties of Thick-film Piezoceramic Devices*. 2004, Thesis, University of Southampton.

21. Jordan, T.L. and Z. Ounaies, *Piezoelectric Ceramics Characterization*. 2001, NASA/CR-2001-211225 ICASE Report, No. 2001-28.

22. *High Quality Components and Materials for The Electronic Industry*. 2003, Ferroperm Piezoceramics.

23. Kawai, H., *The piezoelectricity of poly(vinylidene fluoride).* Jpn.J.Appl.Phys., 1969. **8**: p. 975.

24. Fu, Y., Harvey, Erol C., M.K. Ghantasala, and G.M. Spinks, *Design, fabrication and testing of piezoelectric polymer PVDF microactuators.* Smart Materials and Structures, 2006. **15**(1): p. S141-S146.

25. Arshak, K.I., D. McDonough, and M.A. Duncan, *Development of new capacitive strain sensors based on thick film polymer and cermet technologies.* Sensors and Actuators A., 2000. **79**: p. 102-114.

26. Fang, H.B., Liu, Jing Quan, Xu, Zheng Yi, Dong, Lu, Wang, Li, Chen, Di, B.C. Cai, and Y. Liu, *Fabrication and performance of MEMS-based piezoelectric power generator for vibration energy harvesting.* Microelectronics Journal, 2006. **37**(11): p. 1280-1284.

27. Atkinson, G.M., Pearson, R. E., Ounaies, Z., Park, C., Harrison, J. S., W.C. Wilson, and J.A. Midkiff, *Piezoelectric polyimide MEMS process.* NASA 11th Symposium: May 28 -29, 2003.

28. Jaffe, H., *Piezoelectric Ceramics.* Journal of The American Ceramic Society, 1958. **41**(11): p. 494-498.

29. Jaffe, B., Cook Jr, W. R., Jaffe, H., J.P. Roberts, and P. Popper, *Piezoelectric Ceramics*. 1971, London: Academic Press Inc.

30. Giurgiutiu, V. and S.E. Lyshevski, *Electroactive and Magnetoactive Materials*, in *Micromechatronics: modeling, analysis, and design with Matlab*. 2003, CRC Press. p. 357-415.

31. *Piezoelectric ceramics data book for designers*. 1999, Morgan Electroceramics.

32. Van Lintel, H.T.G., F.C.M. Van De Pol, and S. Bouwstra, *A piezoelectric micropump based on micromachining of silicon.* Sensors and Actuators, 1988. **15**(2): p. 153-167.

33. Karami, M.A. and D.J. Inman, *Analytical Modeling and Experimental Verification of the Vibrations of the Zigzag Microstructure for Energy Harvesting.* Journal of Vibration and Acoustics, 2011. **133**(1): p. 011002.

34. Meiling, Z., E. Worthington, and A. Tiwari, *Design study of piezoelectric energy-harvesting devices for generation of higher electrical power using a coupled piezoelectric-circuit finite element method.* Ultrasonics, Ferroelectrics and Frequency Control, IEEE Transactions on, 2010. **57**(2): p. 427-437.

35. Blom, F.R., Yntema, D. J., Van De Pol, F. C. M., Elwenspoek, M., J.H.J. Fluitman, and T.H.J.A. Popma, *Thin-film ZnO as micromechanical actuator at low frequencies.* Sensors and Actuators A: Physical, 1990. **21**(1-3): p. 226-228.

36. Lee, S.S. and R.M. White, *Piezoelectric cantilever acoustic transducer.* J.Micromech.Microeng., 1998. **8**: p. 230-238.

37. Itoh, T. and T. Suga, *Self-excited force-sensing microcantilevers with piezoelectric thin films for dynamic scanning force microscopy.* Sensors and Actuators A: Physical, 1996. **54**(1-3): p. 477-481.

38. Yi, J.W., W.Y. Shih, and W.H. Shih, *Effect of length, width, and mode on the mass detection sensitivity of piezoelectric unimorph cantilevers.* Journal of Applied Physics, 2002. **91**(3): p. 1680-1686.

39. Umeda, M., K. Nakamura, and S. Ueha, *Analysis of transformation of mechanical impact energy to electrical energy using a piezoelectric vibrator.* Japanese Journal of Applied Physics, 1996. **35**: p. 3267-3273.

40. Shenck, N.S. and J.A. Paradiso, *Energy scavenging with shoe-mounted piezoelectrics.* Micro.IEEE, 2001. **21**(3): p. 30-42.

41. Erturk, A., J. Hoffmann, and D.J. Inman, *A piezomagnetoelastic structure for broadband vibration energy harvesting.* Applied Physics Letters, 2009. **94**(25): p. 254102-3.

42. Anton, S.R. and H.A. Sodano, *A review of power harvesting using piezoelectric materials (2003–2006).* Smart Materials and Structures, 2007. **16**(3): p. R1-R21.

43. Liao, Y. and A. Sodano, *Optimal parameters and power characteristics of piezoelectric energy harvesters with an RC circuit.* Smart Mater.Struct., 2009. **18**(045011).

44. Williams, C.B. and R.B. Yates, *Analysis of a micro-electric generator for microsystems.* Transducers 95/Eurosensors IX, 1995: p. 369-372.

45. duToit, N.E., B.L. Wardle, and S.G. Kim, *Design Considerations for MEMS-Scale Piezoelectric Mechanical Vibration Energy Harvesters.* Integrated Ferroelectrics, 2005(71): p. 121-160.

46. Erturk, A. and D.J. Inman, *A Distributed Parameter Electromechanical Model for Cantilevered Piezoelectric Energy Harvesters.* Journal of Vibration and Acoustics, 2008. **130**(4): p. 041002-041015.

47. Erturk, A. and D.J. Inman, *Issues in mathematical modeling of piezoelectric energy harvesters.* Smart Materials and Structures, 2008. **17**(6): p. 065016.

48. Roundy, S., P.K. Wright, and J. Rabaey, *A study of low level vibrations as a power source for wireless sensor nodes.* Computer Communications, 2003. **26**: p. 1131-1144.

49. Sodano, H.A., D.J. Inman, and G. Park, *Comparison of piezoelectric energy harvesting devices for recharging batteries.* Journal of Materials Science: Materials in Electronics, 2005. **16**: p. 799-807.

50. Wang, Z. and Y. Xu, *Vibration energy harvesting device based on air-spaced piezoelectric cantilevers.* Applied Physics Letters, 2007. **90**(26): p. 263512-263513.

51. Mitcheson, P.D., Yeatman, E. M., Rao, G. K., A.S. Holmes, and T.C. Green, *Energy Harvesting From Human and Machine Motion for Wireless Electronic Devices.* Proceedings of the IEEE, 2008. **96**(9): p. 1457-1486.

52. Glynne-Jones, P., El-Hami, M., Beeby, S., James, E. P., Brown, A. D., M. Hill, and N.M. White. *A vibration-powered generator for wireless microsystems*. in *Proc. Int. Symp. Smart Struct. Microsyst. Hong Kong*. Oct. 2000. Hong Kong.

53. Roundy, S., P.K. Wright, and J.M. Rabaey, *Energy scavenging for wirless sensor networks*. Vol. 1st edition. 2003, Boston, MA: Kluwer Academic.

54. Tanaka, H., Ono, G., T. Nagano, and H. Ohkubo, *Electric power generation using piezoelectric resonator for power-free sensor node*, in *Proc. IEEE Custom Integr. Circuits Conf.* 2005. p. 97 - 100.

55. Reilly, K.E. and P. Wright. *Thin film piezoelectric energy scavenging systems for an on chip power supply*. in *Proc. Int. Workshop Micro Nanotechnlo. Power Generation Energy Conversion Applicat., Berkeley, CA*. Dec. 2006.

56. Lefeuvre, E., Badel, A., Richard, C., Petit, L. and Guyomar, D., *A comparison between several vibration-powered piezoelectric generators for standalone systems*. Sensor and Actuators A, Phys., 2006. **126 (2)**: p. 405 - 416.

57. Ferrari, M., Ferrari, V., D. Marioli, and A. Taroni, *Modeling, Fabrication and Performance Measurements of a Piezoelectric Energy Converter for Power Harvesting in Autonomous Microsystems*. IEEE Trans.on Instrumentation and Measurement, 2006. **55**(6): p. 2096-2101.

58. Mide. *Volture PEH25w online datasheet :http://www.mide.com/pdfs/volture_specs_piezo_properties.pdf*. [cited 2010 11 January].

59. Ching, N.N.H., et al. *PCB integrated micro-generator for wireless*. in *Proc. Int. Symp. Smart Struct., Hong Kong SAR*. Oct. 2000.

60. Li, W.J., Wen, Z., Wong, P. K., G.M.H. Chan, and P.H.W. Leong. *A micromachined vibration-induced power generator for low power sensors of robotic systems*. in *Proc. World Automat. Congr. 8th Int. Symp. Robot. Applicat., Maui, HI*. Jun. 2000.

61. Williams, C.B., Shearwood, C., Harradine, M. A., Mellor, P. H., T.S. Birch, and R.B. Yates, *Development of an electromagnetic micro-generator*. IEE Proceedings - Circuits, Devices and Systems, 2001. **148**(6): p. 337-342.

62. Glynne-Jones, P., *Vibration powered generators for self-powered microsystems*, in *PhD Thesis, School of Electronics and Computer Science*. 2001, University of Southampton.

63. Mizuno, M. and D.G. Chetwynd, *Investigation of a resonance microgenerator*. J. Micromech. Microeng., 2003. **13**: p. 209 - 216.

64. Huang, W.S., Tzeng, K. E., M.C. Cheng, and R.S. Huang, *A silicon MEMS micro power generator for wearable micro devices*. J. Chin. Inst. Eng., 2007. **30**(1): p. 133 - 140.

65. Torah, R., Glynne-Jones, P., Tudor, M., O'Donnell, T., S. Roy, and S. Beeby, *Self-powered autonomous wireless sensor node using vibration energy harvesting*. Measurement Science and Technology, 2008. **19**(12): p. 125202.

66. Ferro-Solutions. *VEH-360 online datasheet: http://www.ferrosi.com/files/VEH360_datasheet.pdf*. 2008 [cited 2010 12 Jan.].

67. Perpetuum. *PMG37 online datasheet: http://www.perpetuum.com/resources/PMG37%20-%20Technical%20Datasheet.pdf*. 2009 [cited 2010 12 Jan].

68. Tashiro, R., Kabei, N., Katayama, K., Ishizuka, Y.,, F. Tsuboi, and K. Tsuchiya, *Development of an electrostatic generator that harnesses the ventricular wall motion*. Jpn. Soc. Artif. Organs, 2002. **5**: p. 239 - 245.

69. Arakawa, Y., Y. Suzuki, and N. Kasagi. *Micro seismic power generator using electret polymer film*. in *Proc. 4th Int. Workship Micro and Nanotechnology for*

Power Generation and Energy Conversion Applicat. Power MEMS, Kyoto, Japan. Nov. 2004.

70. Despesse, G., Chaillout, J., Jager, T., Leger, J. M., Vassilev, A., S. Basrour, and B. Charlot. *High damping electrostatic system for vibraiton energy scavenging.* in *Proc. 2005 Joint Conf. Smart Objects Ambient Intell. -Innov. Context-Aware Services: Usages Technolo., Grenoble, France.* 2005.

71. Miao, P., Mitcheson, P. D., Holmes, A. S., Yeatman, E. M., T.C. Green, and B. Stark, *MEMS inertial power generators for biomedical applications.* Microsyst Technol, 2006. **12**(10-11): p. 1079-1083.

72. Basset, P., Galayko, D., Mahmood Paracha, A., Marty, F., A. Dudka, and T. Bourouina, *A batch-fabricated and electret-free silicon electrostatic vibration energy harvester.* J. Micromech. Microeng., 2009. **19**.

73. Larry, J.R., R.M. Rosenberg, and R.O. Uhler, *Thick-film technology: an introduction to the materials.* IEEE Trans.on Components, Hybrids, and Manufacturing Technology, 1980. **CHMT-3**(3): p. 211-225.

74. Brignell, J.E., N.M. White, and A.W.J. Cranny, *Sensor applications of thick-film technology.* Communications, Speech and Vision, IEE Proceedings I, 1988. **135**(4): p. 77-84.

75. White, N.M. and J.E. Brignell, *A planar thick-film load cell.* Sensors and Actuators, 1991. **25 - 27**: p. 313-319.

76. Arshak, K.I., Ansari, F., McDonagh, D. and D. Collins, *Development of a novel thick-film strain gauge sensor system.* Measurement Science and Technology, 1997. **8**(1): p. 58-70.

77. Baudry, H., *Screen-printing piezoelectric devices.* Proc.6th European Microelec.Conf., 1987: p. 456-463.

78. White, N.M., P. Glynne-Jones, and S.P. Beeby, *A novel thick-film piezoelectric micro-generator.* Smart Mater.Struct., 2001. **10**: p. 850-852.

79. Koplow, M., Chen, A., Steingart, D., P. Wright, and J. Evans. *Thick film thermoelectric energy harvesting systems for biomedical applications.* in *Proceedings of the 5th International Workshop on Wearable and Implantable Body Sensor Networks.* 2008.

80. Hill, M., Townsend, R. J., Harris, N. R., White, N. M., S.P. Beeby, and J. Ding. *An ultrasonic MEMS particle separator with thick film piezoelectric actuation.* in *IEEE International Ultrasonics Symposium, 18-21 Sept 2005, Rotterdam, Netherlands.* Sept. 2005.

81. Hale, J.M., White, J. R., R. Stephenson, and F. Liu, *Development of piezoelectric paint thick-film vibration sensors.* J. Mechanical Engineering Science, 2004. **219**(1/2005).

82. Torah, R.N., S.P. Beeby, and N.M. White, *Experimental Investigation into The Effect of Substrate Clamping on The Piezoelectric Behaviour of Thick-Film PZT Elements.* J.Phys.D: Appl.Phys., 2004. **37**: p. 1-5.

83. Stecher, G., *Free Supporting Structures in Thick-Film Technology: A Substrate Integrated Pressure Sensor.* 6th European Microelectronics Conferences, Bournemouth, 1987: p. 421-427.

84. Steinhausen, R., Hauke, T., Seifert, W., Mueller, V., Beige, H., S. Seifert, and P. Lobmann. *Clamping of piezoelectric thin films on metallic substrates: influence on the effective piezoelectric modulus d_{33}.* in *Proceedings of the Eleventh IEEE International Symposium on Application of Ferroelectrics, ISAF, Montreux, Switzerland.* Aug. 1998.

85. Thornell, G. and S. Johansson, *Microprocessing at the fingertips.* Journal of Micromechanics and Microengineering, 1998. **8**(4): p. 251-262.

86.   Beeby, S.P., J.N. Ross, and N.M. White, *Design and fabrication of a micromachined silicon accelerometer with thick-film printed PZT sensors.* J.Micromech.Microeng., 2000. **10**: p. 322-328.

87.   Papakostas, T., *Polymer Thick-Film Sensor and Their Integration with Silicon: A Route to Hybrid Microsystems*, in *PhD Thesis, University of Southampton, November*. 2000, PhD Thesis, University of Southampton, November: PhD Thesis, University of Southampton, November.

88.   Schmid, S. and C. Hierold, *Two Sacrificial Layer Techniques for The Fabrication of Free-standing Polymer Micro Structures.* MicroMechanics Europe Workshop, Southampton, 2006: p. 177-180.

89.   Saha, C., O'Donnell, T., Godsell, J., Carlioz, L., Wang, N., McCloskey, P., Beeby, S., J. Tudor, and R. Torah. *Step-up converter for electromagnetic vibration energy scavenger*. in *DTIP of MEMS & MEOMS*. 2007. Stresa, Italy, April.

90.   Rao, S.S., *Mechanical vibrations*. 2004: Pearson Prentice Hall.

91.   Li, X., Shih, Wan Y., I.A. Aksay, and W.-H. Shih, *Electromechanical behavior of PZT-brass unimorphs.* J.Am.Ceram.Soc., 1999. **82**(7): p. 1733-1740.

92.   Merhaut, J., *Theory of Electroacoustics*. 1981: McGraw-Hill, New York.

93.   Gere, J.M., *Mechanics of Materials*. 2001: Brooks/Cole.

94.   Wang, S.F. and J.P. Dougherty, *Silver-palladium thick-film conductors.* J.Am.Ceram.Soc., 1994. **77**(12): p. 3051-3072.

95.   *Materials technology and crystals for research, development and production*. 2007, MaTeck GmbH. p. http://www.mateck.de/.

96.   Birol, H., T. Maeder, and P. Ryser, *Fabrication of LTCC Micro-fluidic Devices Using Sacrificial Carbon Layers.* J.Appl.Ceram.Technol., 2005. **2**: p. 345-354.

97.   Torah, R., S.P. Beeby, and N.M. White, *An improved thick-film piezoelectric material by powder blending and enhanced processing parameters.* IEEE Trans.Ultrason.Ferroelectr.Freq, Control, 2005. **52**(1): p. 10-16.

98.   Dorey, R.A., Whatmore, R. W., Beeby, S. P., R.N. Torah, and N.M. White, *Screen printed PZT composite thick films.* Integr.Ferroelectr., 2004. **63**: p. 89-92.

99.   Cotton, D., Chappell, Paul, A. Cranny, and N. White, *A new binderless thick-film piezoelectric paste.* Journal of Materials Science: Materials in Electronics, 2007. **18**(10): p. 1037-1044.

100.   Birol, H., Maeder, T., C. Jacq, and P. Ryser, *3-D Structuration of LTCC for Sensor Micro-Fluidic Applications.* European Microelectronics and Packaging Symposium, 2004.

101.   Harris, N.R., Hill, M., Torah, R., Townsend, R., Beeby, S., N.M. White, and J. Ding, *A multilayer thick-film PZT actuator for MEMs applications.* Sensor and Actuators A, 2006(132): p. 311-316.

102.   Glynne-Jones, P., Beeby, S. P., Dargie, P., T. Papakostas, and N.M. White, *An investigation into the effect of modified firing profiles on the piezoelectric properties of thick-film PZT layers on silicon.* Measurement Science and Technology, 2000. **11**(5): p. 526-531.

103.   Lu, P., Shen, F., O'Shea, S. J., K.H. Lee, and T.Y. Ng, *Analysis of surface effects on mechanical properties of microcantilevers.* Mater.Phys.Mech., 2001. **4**: p. 51-55.

104.   Dargie, P., Sion, R., J. Atkinson, and N. White, *An investigatin of the effect of poling conditions on the characteristics of screen-printed piezoceramics.* J.Meicroelectronics International, 1998. **15**(2): p. 6-10.

105. Walker, W.J., J.S. Reed, and S.K. Verma, *Influence of Granule Character on Strength and Weibull Modulus of Sintered Alumina.* Journal of The American Ceramic Society, 1999. **82**(1): p. 50-56.

106. Shepard, J.J.F., Chu, F., I. Kanno, and S. Trolier-McKinstry, *Characterization and aging response of the d31 piezoelectric coefficient of lead zirconate titanate thin films.* J.Appl.Physics, 1999. **85**(9): p. 6711-6716.

107. Smits, J. and W.S. Choi, *The constituent equations of piezoelectric heterogeneous bimorphs.* IEEE Trans.Ultrason.Ferroelectr.Freq, Control, 1991. **38**: p. 256-270.

108. Yasumura, K.Y., Stowe, T. D., Chow, E. M., Pfafman, T., Kenny, T. W., B.C. Stipe, and D. Rugar, *Quality factors in micron- and submicron-thick cantilevers.* Microelectromechanical Systems, Journal of, 2000. **9**(1): p. 117-125.

109. Jinling, Y., T. Ono, and M. Esashi, *Energy dissipation in submicrometer thick single-crystal silicon cantilevers.* Journal of Microelectromechanical Systems, 2002. **11**(6): p. 775-783.

110. Sandberg, R., lhave, K., A. Boisen, and W. Svendsen, *Effect of gold coating on the Q-factor of a resonant cantilever.* Journal of Micromechanics and Microengineering, 2005. **15**(12): p. 2249-2253.

111. Choi, W., Jeon, Y., Jeong, J. H., R. Sood, and S. Kim, *Energy harvesting MEMS device based on thin film piezoelectric cantilevers.* Journal of Electroceramics, 2006. **17**(2): p. 543-548.

112. Blom, F.R., Bouwstra, S., M. Elwenspoek, and H.J. Fluitman, *Dependence of the quality factor of micromachined silicon beam resonators on pressure and geometry.* J.Vac.Sci.Technol., 1992. **B10**: p. 19-26.

113. Lu, J., Ikehara, T., Kobayashi, T., Zhang, Y., Mihara, T., T. Itoh, and R. Maeda. *High quality factor silicon cantilever driven by PZT actuator for resonant based mass detection.* in *Symposium on DTIP of MEMS & MOEMS* April 2008.

114. Nouira, H., Foltête, E., L. Hirsinger, and S. Ballandras, *Investigation of the effects of air on the dynamic behavior of a small cantilever beam.* Journal of Sound and Vibration, 2007. **305**(1-2): p. 243-260.

115. Richards, C.D., Anderson, Michael J., D.F. Bahr, and R.F. Richards, *Efficiency of energy conversion for devices containing a piezoelectric component.* Journal of Micromechanics and Microengineering, 2004. **14**(5): p. 717-721.

116. Roundy, S., Leland, E. S., Baker, J., Carleton, E., Reilly, E., Lai, E., Otis, B., Rabaey, J., P.K. Wright, and V. Sundararajan, *Improving power output for vibration-based energy scavengers.* IEEE Pervasive Computing, 2005. **4**: p. 28-36.

117. Zhu, D., M.J. Tudor, and S.P. Beeby, *Strategies for increasing the operating frequency range of vibration energy harvesters: a review.* Meas.Sci.Technol., 2010. **21**(2).

118. Sari, I., T. Balkan, and H. Kulah, *An electromagnetic micro power generator for wideband environmental vibrations.* Sensors and Actuators A: Physical, 2008. **145-146**: p. 405-413.

119. Liu, J.Q., Fang, Hua Bin, Xu, Zheng Yi, Mao, Xin Hui, Shen, Xiu Cheng, Chen, Di, H. Liao, and B.C. Cai, *A MEMS-based piezoelectric power generator array for vibration energy harvesting.* Microelectronics Journal, 2008. **39**(5): p. 802-806.

120. Ferrari, M., Ferrari, Vittorio, Guizzetti, Michele, D. Marioli, and A. Taroni, *Piezoelectric multifrequency energy converter for power harvesting in autonomous microsystems.* Sensors and Actuators A: Physical, 2008. **142**(1): p. 329-335.

121. Roundy, S., *Energy scavenging for wireless sensor nodes with a focus on vibration to electricity conversion*, in *Engineering-Mechanical Engineering*. 2003, University of California, Berkeley.

Vibration-based energy harvesting is one of the attractive solutions for powering autonomous microsystems, due to the fact that vibration sources are ubiquitous in the ambient environment. Basically, the vibration to-electricity conversion mechanism can be implemented by piezoelectric, electromagnetic, electrostatic, and magnetostrictive transductions. In this book, piezoelectric transduction is investigated due to its high electrical output density, compatibility with conventional thick-film and thin-film fabrication technologies, and ease of integration in silicon integrated circuits. A three dimensional thick-film structure in the form of a free standing cantilever incorporated with piezoelectric materials is proposed in this work. The advantages of this structure include minimising the movement constraints on the piezoelectric, thereby maximising the electrical output and offering the ability for integration with other microelectronic devices.

Swee-Leong Kok

Swee-Leong Kok obtained his Ph.D degree in 2010 from University of Southampton, UK. He is currently affiliated with Universiti Teknikal Malaysia Melaka (UTeM) as a senior lecturer. His research interests include energy harvesting, thick-film technology and microelectromechanical systems (MEMS).